Wax Deposition from Single-Phase Oil Flows and Water-Oil Two-Phase Flows in Oil Transportation Pipelines

by

Sheng Zheng

A dissertation submitted in partial fulfillment
of the requirements for the degree of
Doctor of Philosophy
(Chemical Engineering)
in The University of Michigan
2017

Doctoral Committee:

Professor H. Scott Fogler, Chair
Professor Ronald G. Larson
Professor Margaret S. Wooldridge
Professor Robert M. Ziff

Sheng Zheng
shzheng@umich.edu
ORCID iD: 0000-0001-5948-7325

To my wife, Huiguan “Lydia” Zheng

and

my parents, Xuesu Zheng and Yao Zhang

Acknowledgement

My first acknowledgement goes to my thesis advisor, Professor H. Scott Fogler. I'm very grateful to have the opportunity to conduct my Ph.D. research under Professor Fogler's guidance. Professor Fogler is constantly dedicated to cultivate my critical thinking skills and my ability to conduct independent research. He never tells me exactly what to do while he has been giving the maximal possible supports from all aspects when I came up with ideas I would like to test. I think these are the two best attributes of a Ph.D. advisor and Professor Fogler has them both at the same time. Professor Fogler is a true care taker of all his students and I think I feel his care more strongly as an international student. Beyond academic advice, he has given me his absolute supports on immigration issues, work authorizations, English language and many other matters relevant only to international students. Without Professor Fogler's dedication, this thesis work will certainly be impossible.

I would like to thank my thesis committee, Professors Ronald Larson, Margaret Wooldridge and Robert Ziff for the enlightening discussions we had along the thesis work and their valuable inputs.

I would like to thank our industrial partners for funding the University of Michigan Industrial Affiliates Program within which I carried out my thesis reach. Without their generous supports, the completion of this thesis work will literally be impossible. Our industrial partners include AssuredFlowSolutions, LLC., BP, Chevron, ConocoPhillips, Multichem – A Halliburton Service, Nalco Champion - An Ecolab Company, Phillips66, Shell, Statoil, TOTAL and

Woodgroup Kenny. I would like to specifically thank the subject matter experts from these companies that I had extensive discussions with: Dr. Zhenyu "Jason" Huang (AFS), Dr. Taras Makogon (BP), Drs. Probjot Singh, Steve Appleyard and Yaqin Wu (ConocoPhillips), Drs. Rama Venkatesan and Jefferson Creek (Chevron), Dr. Thierry Palermo (TOTAL), Dr. Shuxin Hou (Statoil), Drs. Moniraj Ghosh, Mark Jemmett and Keith Lawson (Phillips66). Drs. Probjot, Rama and Jason are in fact my academic brothers.

Among these industrial partners, I would like to thank TOTAL and Woodgroup Kenny, who had offered me intern positions during the course of my Ph.D. thesis. These two internships are extremely beneficial for my career development. Good technical work was done in collaboration with colleagues at TOTAL and Woodgroup Kenny which led to the development of Chapters 2 and 7 in this thesis. I would like to specifically thank the colleagues I had the honor to work with at TOTAL and Woodgroup Kenny: Mr. Khalid Mateen, Dr. Mayela Rivero, Mr. Mohamed Saidoun, Dr. Thierry Palermo, Dr. Moussa Kané, Dr. Kun Ma and Dr. Guangwei Ren (TOTAL); Dr. Prabu Parthasarathy and Mr. Reaz Kabir (Woodgroup Kenny).

Teaching is an integral part of the Ph.D. training. I had great teaching experience under the guidance by Professors Fei Wen and Suljo Linic. I'm grateful for the opportunities they provided for me to enjoy my child-time dream, teaching. I'm also grateful for the class of '16 chemical engineering undergraduates. They were very patient listening to my lectures and always laughed when I tried to tell a joke. I wish them all the best for their future endeavors.

I would also like to Thank Dr. Susan Montgomery for her advices on teaching and engaging students. Dr. Montgomery was my undergraduate program advisor as well. Her dedication to the undergraduate program is unmatchable.

I would like to thank the undergraduate, master and visiting students who had provided substantial help during my research: Fan Zhang, Yimeng Lyu, Yiyu Ren, Kasidit "Tua" Smathwitthayawech, Thanaphoom "A" Khrutphisit and Tunya Ketjuntiwa. Without their help, it will take perhaps another 5 years for me to complete all the simulations and experimental work.

I would like to thank the excellent staff of the department of chemical engineering: Laura Bracken, Susan Hamlin, Shelley Fellers, Pablo LaValle, Chris Barr, Laurel Neff and Michael Africa. They have provided indispensable supports from virtually all aspects to the keep the department functioning and for my research to be smooth.

I would like to thank the Fogler group family: Claudio Vilas Boas Favero, Luqman Mahir, Drs. Nasim Hadji Arkbari Balou, Yingda "Alex" Lu, Michael Hoepfner and Zhenyu "Jason" Huang for the discussions, critiques, encouragements and supports they provided during my study.

I would like to also extend my acknowledgement to several special parties. I would like to thank 5 world-renowned soccer clubs from England, Germany, France, Italy and Spain: Arsenal FC (Premier League), Borussia Dortmund (Bundesliga), Paris Saint-German (Ligue 1), AC Milan (Serie A) and Real Madrid (La Liga). They play on weekend afternoons so that I could listen to the game broadcast while working in the lab, which makes a 7-day work week as enjoyable as a 5-day work week. I would also like to thank my soccer friends in Ann Arbor. I sincerely think that weekly soccer games kept me at a healthy fitness level so I could handle heavy-duty lab work, e.g., running and servicing the flow loop apparatus.

I would like to thank my parents and grandparents for their endless love. Without the education and training they have provided since I was a child, I won't even have a chance to come to the US to pursue a Ph.D. degree. Although emotionally difficult for them, they support my decision

to stay and explore in the US. I appreciate their sacrifices and I'm sure I can only understand this challenge when myself become a parent.

My final acknowledgement goes to my girlfriend (yr. 2008-2016) and wife (since 2016), Huiguan "Lydia" Zheng. Lydia has been extremely patient with me during my Ph.D. program and has given me unconditional love. I understand that it is not easy to be together with a Ph.D. candidate because of the long time-commitment it takes to finish a Ph.D., financial burden, uncertainties in job opportunities after graduation, the emotional ups and downs associated with the ups and downs of the instrument readings and many other challenges. None of these challenges has come in between Lydia and me and we had spent the wonderful past 8 years together. When I got some nice results from the lab, I would show it to her before showing to Professor Fogler. When I got frustrating results from the lab, I would call Lydia and we would have happy talks so I would forget about the frustration and be brave again to carry on. I enjoy explaining to her my research in plain words and now she understands what "pigging" means in the context of flow assurance. I proposed to Lydia on a Delta flight to New Orleans for a vacation and we are married since September 2016. I look forward to the endless happiness with Lydia in the many decades to come.

Table of Contents

List of Figures

List of Tables

List of Appendices

Abstract

Paraffin deposition is a severe challenge facing the oil and gas industry. Wax deposition risks in oil production are usually characterized by the wax deposition rate, wax deposit thickness and hardness. Research efforts have been dedicated to establishing modeling methodologies to predict the severity of wax deposition during oil production. In this thesis, wax deposition modeling investigations were carried out in single-phase oil flow as well as water-oil two phase flow.

Firstly, the existing "single-component" wax deposition model was enhanced to simulate the precipitation and deposition of paraffin molecules covering a wide range of carbon numbers. The enhanced model predicts the carbon number distribution of the wax deposit in addition to the deposit thickness. For a waxy crude oil with a paraffin carbon number distribution covering C_{15} to C_{45}, the enhanced model can predict the carbon number of the most abundant component in the deposit within an error of 2 carbon numbers. The composition of the deposit provides insights to the hardness of the deposit as well as its responsiveness to polymeric inhibitors.

Modeling methodologies were also established for wax deposition process in water-oil dispersed flow by analyzing the roles of the dispersed water droplets on the heat and mass transfer aspects of wax deposition. NMR techniques were implemented to uncover and quantify the hindrance to wax molecular diffusion caused by dispersed water droplets. It was discovered that the confusion about the wax diffusivity in water-oil dispersion in the industry can lead to underestimation of the wax diffusivity by as much as 300%. Simulations also revealed the different impacts of the dispersed water phase on heat transfer in a laboratory set-up and in field operations. Dispersed water droplets can also be entrapped in the deposit. It was discovered experimentally that the water content of the deposit depends not only on the water content of the bulk but also the size of the droplets. Incorporation of the droplets in the wax deposit lowers the yield strength of the deposit and causes the deposit to slough-off frequently during wax deposition. In a laboratory flow loop test, the pressure drop across the test section increased by more than 10 psi during a single-phase wax deposition experiment. However, the pressure drop did not increase by more than 5 psi due to frequent sloughing of the deposit when only 10 vol.% of water was dispersed in the oil phase.

In contrary to the complex effects of the dispersed water phase on the heat and mass transfer characteristics of wax deposition from water-oil dispersed flow, the water phase has minimal impact on heat and mass transfer in water-oil stratified flow regime, as was discovered by wax deposition experiments.

Eventually, the long-existing simplified wax deposition model assuming Newtonian fluid mechanics was enhanced to consider the non-Newtonian fluid characteristics. A comprehensive workflow was established to perform hydrodynamics, heat and mass transfer as well as deposit formation simulations based on fundamental analysis with advanced Computational Fluid

Dynamics. It was discovered that for a highly waxy (>15 wt.% wax) and thus highly non-Newtonian crude oil, the wax deposit thickness predicted by the Newtonian model can be 1/3 that of the thickness predicted by the non-Newtonian model. Therefore, misuse of the Newtonian wax deposition model for highly waxy oils can lead to over-optimistic assessments of the wax risk.

Chapter 1

Introduction

1.A Wax Deposition in Oil Transportation Pipelines

Over 40% of the total energy consumed by the world is generated from oil while other sources for energy, e.g., coal, natural gas, biofuels, electricity etc., only contribute less than half of the energy contributed by oil[1]. Surprisingly, renewable sources contribute less than 5% of the total energy consumed[1]. Although there has been a persistent advocate to transit the energy dependence away from fossil fuels, crude oil continues to be a dominating source of energy. The United States alone produces approximately 10,000,000 barrels of oil daily in order to meet the growing need for energy[2]. Therefore, oil production is critical to the growth of economy. Consequently, research campaigns to tackle challenges associated with oil production, such as paraffin deposition, are of great economical value.

Crude oil usually contains high molecular weight normal paraffins ranging from n-C_{16} to as high as n-C_{50}+. This family of molecules are also known as waxes[3]. Because of their ordered molecular structure, paraffin molecules can easily crystallize to form solids when temperature decreases. The solubility of wax molecules in oil is a strong function of temperature[4]. Paraffin molecules remain dissolved at reservoir conditions, e.g., pressure ranging from 8000 to 15000 psi and temperature ranging from 70 to 150 °C[5]. When temperature decreases, the concentration of the dissolved wax in oil reaches the solubility limit and consequently, wax molecules

precipitate out of solution to form solid particles. During oil transportation, heat loss from the oil flow to the ambient constantly occurs, leading to a gradual decrease of the oil temperature and subsequent wax precipitation. The precipitated wax particles form an interlocking network with a "house-of-card" configuration[4], shown in Figure 1-1.

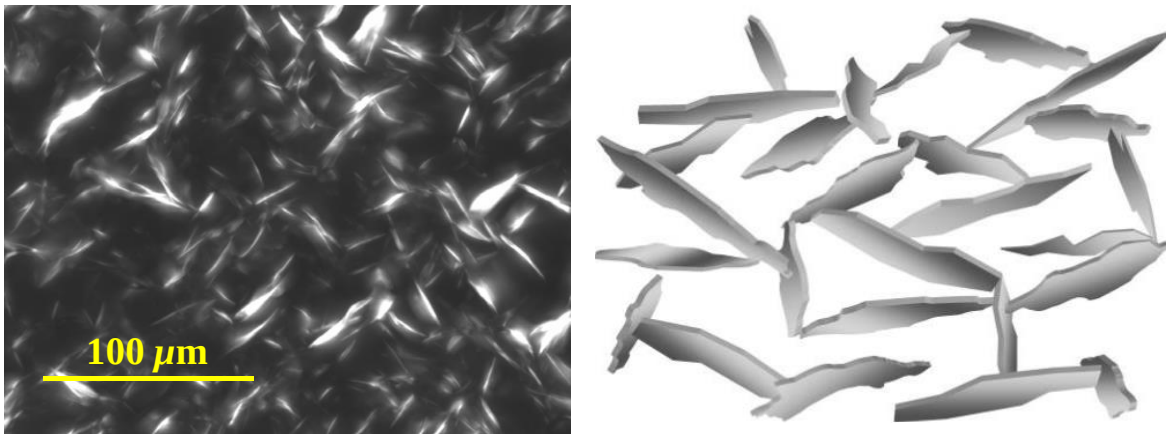

Figure 1-1: (a) A cross-polarized microscopic picture of an interlocking wax solid network; (b) A schematic of the "house-of-card"configuration of wax particles

Such an entangled solid network of wax particles can trap a substantial amount of liquid oil and form a stationary gel on the pipe wall[3]. Early researchers discovered that a waxy gel can surprisingly contain as less as 2-4 wt.% solid wax with the rest 98-96 wt.% of the gel being entrapped oil[6,7]. Wax deposit can continue to grow and harden during oil transportation, reducing the effective pipeline diameter and posing severe risks to the pipeline. Figure 1-2 shows a pipeline cross section with a substantial amount of wax deposit and a very limited effective diameter.

Figure 1-2: A pipe cross section with a significant amount of wax deposit attached to the pipe wall and a very limited effective diameter

Under extreme circumstances, wax deposition can even clog the pipeline completely, leading to abandonment of oil fields and loss of hundreds of millions of dollars[8]. The reduction in the effective diameter of oil transportation pipelines requires increased pump power to maintain a prescribed production rate, generating uneconomical operational costs of oil production. In order to maintain safe and cost-efficient production, the wax deposit needs to be remediated by pipeline heat tracing[9], injection of wax inhibitors and/or pour point depressants[10] and/or mechanical removal[11], further worsening the financial burden of oil production. For example, Figure 1-3 shows the operational cost associated with typical pigging operations to mechanically scrap deposit off the pipe wall[11].

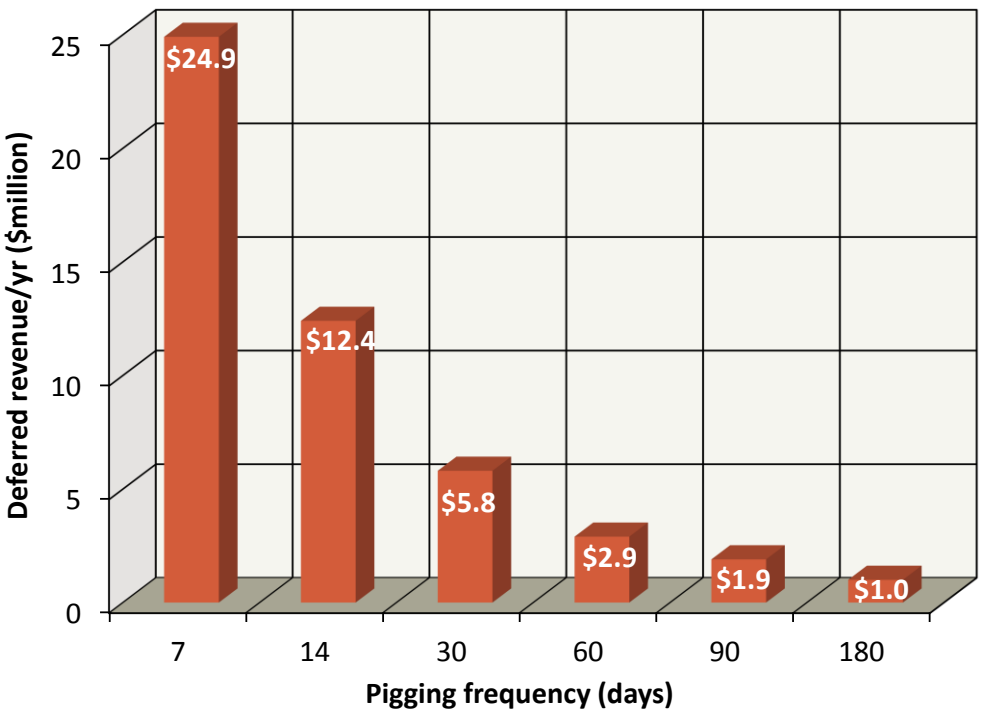

Figure 1-3: Cost of pigging operation as a function of pigging frequency

As oil production gradually moves from on-shore to off-shore, wax deposition becomes more and more common as oil pipelines of tens of kilometers in length need to sit on the sea bed at 4 °C, shown in Figure 1-4.

Figure 1-4: Offshore oil production with oil pipelines sitting on the sea bed and gradually cooled by the surrounding sea water

Consequently, wax deposition has become a challenge facing the oil and gas industry globally. Figure 1-5 shows the distribution of reported wax deposition issues around the world

Figure 1-5: An overview of locations around the world where wax deposition issues were reported

This thesis is dedicated to advancing our understanding of the wax deposition phenomena from multiple aspects and presenting important knowledge and tools to assess and tackle wax deposition issues.

1.B Overview of the Wax Deposition Process and Modeling

Wax deposition models have been developed to predict the growth of wax deposit during oil production. Such prediction is of great value for the design of wax remediation operations. For example, the pigging operation is usually implemented to mechanically remove the wax deposit attached to the inner surface of the pipe. Excessively frequent pigging operations are costly while insufficient pigging can lead to complete clogging of the pipeline. Therefore, it is important to determine an appropriate pigging frequency during oil production. A pigging operation is usually implemented when the deposit thickness reaches a threshold. The accepted

threshold varies from different oil producers but is usually on the order of 2 millimeters. Wax deposition models can be used to predict the time it takes for the deposit to grow to this threshold thickness and thereby providing guidance to the design of pigging operations.

Based on the investigations carried out since early 1980s, multiple mechanisms causing wax deposition, including molecular diffusion, shear dispersion, Brownian diffusion and gravitational settling, have been proposed[12]. Follow-up experimental investigations have confirmed that among these proposed mechanisms, molecular diffusion is the main mechanism of wax deposition[3]. According to the molecular diffusion mechanism, wax deposition occurs via the following three steps:

- Precipitation of wax at the pipe wall
- Radial diffusion of wax from the bulk towards the deposit interface
- Internal diffusion of wax into the deposit layer

Wax deposition is initiated by precipitation of wax at the pipe wall to form an incipient layer of deposit. The heat loss of the oil flow to the ambient causes the temperature drop of the oil flow, leading to precipitation and initiation of wax deposition. In order to model the heat loss and predict the pipe wall temperature, wax deposition models numerically solve the heat transfer governing system, shown in Equations (1-1)- (1-2). It should be noted that Equation (1-1) is a simplified version of the unsteady state conduction-convection equation under the pseudo-steady state assumption that a steady state temperature profile can be reached rapidly given the relative fast heat transfer compared to the slow deposit growth process. A detailed analysis on the validity of the pseudo-steady state assumption is included in Appendix A.

$$V_z \frac{\partial T_o}{\partial z} + \frac{1}{r}\frac{\partial}{\partial r}\left[-r\left(\alpha_o + \varepsilon_T\right)\frac{\partial T_o}{\partial r} \right] = 0 \qquad (1\text{-}1)$$

T_o = oil temperature,(K)

ρ_o = density of oil,(kg/m^3)

α_o = thermal diffusivity of oil,(m^2/s)

ε_T = turbulent thermal diffusivity,(m^2/s)

V_z = axial velocity,(m/s)

z = axial position,(m)

r = radial position,(m)

$$\begin{cases} T_o = T_{o,inlet}, \text{ at } z = 0 \\ \dfrac{\partial T_o}{\partial r} = 0, \text{ at } r = 0 \\ U_{extn}(T_{ambient} - T_{o,interface}) = k_o \dfrac{\partial T_o}{\partial r}, \text{ at } r = r_{interface} \end{cases} \tag{1-2}$$

$T_{o,inlet}$ = oil temperature at the inlet,(K)

U_{extn} = overall external heat transfer coefficient,$(W/m^2/K)$

$T_{ambient}$ = ambient temperature,(K)

$T_{o,interface}$ = oil temperature at the fluid/deposit interface,(K)

$r_{interface}$ = the effective pipe radius,(m)

Precipitation of wax molecules and formation of an incipient gel deposit on the pipe wall creates a radial concentration gradient of the dissolved wax in oil, resulting in a net radial diffusive flux of wax. The radial diffusion of wax can be modeled by solving the mass transfer governing system, shown in Equations (1-3)- (1-4).

$$V_z \frac{\partial C_{wax}}{\partial z} + \frac{1}{r}\frac{\partial}{\partial r}\left[-r\left(D_{wo} + \varepsilon_M\right)\frac{\partial C_{wax}}{\partial r} \right] + k_{precipitation}\left(C_{wax} - C_{wax,eq}\right) = 0 \tag{1-3}$$

C_{wax} = concentration of dissolved wax in oil,(kg/m^3)

D_{wo} = diffusivity of wax in oil,(m^2/s)

ε_M = turbulent mass diffusivity,(m^2/s)

$k_{precipitation}$ = bulk precipitation rate constant,$(1/s)$

$C_{wax,eq}$ = equilibrium concentration of wax in oil,(kg/m^3)

$$\begin{cases} C_{wax} = C_{wax,inlet}, \text{ at } z = 0 \\ \dfrac{\partial C_{wax}}{\partial r} = 0, \text{ at } r = 0 \\ C_{wax} = C_{wax,eq,interface}(T_{o,interface}), \text{ at } r = r_{interface} \end{cases} \tag{1-4}$$

$C_{\text{wax,inlet}}$ = concentration of dissolved wax at the inlet,(kg / m^3)

$C_{\text{wax,eq,interface}}$ = equilibrium concentration of dissolved wax at the interface,(kg / m^3)

Two extreme cases were considered for the rate of precipitation, i.e., no precipitation of wax in the bulk and instantaneous precipitation of wax in the bulk. In order to represent these two limiting cases, the bulk precipitation rate constant is set to two limiting values, i.e., zero and infinity (a large number in numerical simulations), shown in Equation (1-5).

$$\begin{cases} \text{no precipitation: } k_{\text{precipitation}} = 0 \\ \text{instantaneous precipitation: } k_{\text{precipitation}} \to \infty \end{cases} \tag{1-5}$$

A fraction of the wax molecules reaching the deposit-fluid interface via molecular diffusion precipitate on the deposit-fluid interface, causing the deposit to grow towards the centerline of the pipe. Simultaneously, some wax molecules continue to diffuse into the deposit that has already formed, causing the wax deposit to harden. The growth of the deposit generated by the radial diffusive flux reaching the fluid-deposit interface is calculated with Equation (1-6).

$$\begin{aligned} \rho_{\text{deposit}} \Omega_{\text{deposit}} \frac{\mathrm{d}\delta}{\mathrm{d}t} = & \left(-D_{\text{wo}} \frac{\mathrm{d}C_{\text{wax}}}{\mathrm{d}r} \Big|_{\text{from oil to interface}} \right) \\ & - \left(-D_{\text{eff}} \frac{\mathrm{d}C_{\text{wax}}}{\mathrm{d}r} \Big|_{\text{from interface to deposit}} \right) \end{aligned} \tag{1-6}$$

ρ_{deposit} = density of wax deposit,(kg / m^3)

Ω_{deposit} = solid wax fraction of the depositing layer

δ = deposit thickness,(m)

t = time,(s)

D_{eff} = effective diffusivity of wax in waxy gel,(m^2 / s)

The increase of the wax content of deposit due to internal diffusion of wax can be calculated using Equation (1-7).

$$\rho_{\text{deposit}} \left(R^2 - r_{\text{interface}}^2 \right) \frac{\mathrm{d}\Omega_{\text{deposit}}}{\mathrm{d}t} = 2 r_{\text{interface}} \left(-D_{\text{eff}} \frac{\mathrm{d}C_{\text{wax}}}{\mathrm{d}r} \Big|_{\text{from interface to deposit}} \right) \tag{1-7}$$

R = pipe radius,(m)

The aforementioned numerical calculations are compiled in the premium wax deposition model, i.e., the Michigan Wax Predictor (MWP) through four Ph.D. theses[3,8,13,14]. The MWP can generate reliable predictions for the change of deposit thickness and wax content over time[3,13], as well as the change of deposition rate with varying operating conditions[14]. The MWP has been accepted as the most theoretically advanced wax deposition model available to the oil and gas industry.

1.C Imperative Enhancements to Wax Deposition Models

Although a substantial volume of wax deposition research has been generated over the past decades, there are still non-negligible gaps between the wax deposition models developed by the academia and the needs from oil producers. Several imperative enhancements that will help close this gap between academic investigations and field applications are discussed in this section.

Firstly, existing wax deposition models lump all precipitating normal paraffin molecules into one single pseudo-component. However, precipitating wax usually covers a wide range of carbon numbers. It should be noted that the carbon number of the wax depositing in the wellbore tubing can be significantly different from the deposit in the transport pipeline. Wax with different chain lengths requires different remediation strategies. For example, wax with certain lengths are responsive to polymeric inhibitors while others are not. As a result, prediction of the carbon number distribution of depositing wax can provide additional guidance during the design of wax remediation operations. Unfortunately, existing wax deposition models cannot generate this prediction due to the lumping of wax molecules into a single pseudo-component. Consequently, there is a need to enhance the existing wax deposition models to enable the prediction of the carbon number distribution of the deposit.

Secondly, contemporary wax deposition models have been developed based on single phase oil flow. It should be noted that multiphase flow is commonly encountered during real-world oil production. Consequently, it is difficult (if possible) to directly apply an existing wax deposition model to simulate real field productions. Among the relevant multiphase flow regimes in oil production, water-oil two phase flows continue to gain interests from the industry as the water content of the production stream increases as time elapses. For example, the Daqin oil field in China produces as much as 90 % of water together with 10% of oil[15]. As a result, there is an imperative need to advance the understanding of wax deposition in presence of water and develop modeling methodologies that consider the co-produced water.

Thirdly, the effect of the complex rheology of waxy crude oil on wax deposition has been long neglected during the previous development of wax deposition models. It should be noted that the wax-in-oil suspension due to wax precipitation possesses non-Newtonian fluid characteristics, including plasticity and shear thinning. Such non-Newtonian characteristics can affect the modeling of hydrodynamics, heat and mass transfer as well as deposit growth rate. The impact of non-Newtonian fluid characteristics on wax deposition is expected to be significant when the oil of interest has a high wax content, e.g., the Mangala crude oil from India[16], the Black Wax Crude from Utah[17], etc.

The aforementioned complexities prevent the direct application of existing wax deposition models to field-scale wax deposition modeling. These complexities are addressed in this thesis.

1.D Research Objectives and Thesis Overview

The goal of this thesis is to advance our understanding of wax deposition beyond established knowledge on the heat and mass transfer characteristics of single phase oil flow. Such

advancements will close the gap between academic wax deposition modeling investigations and analysis for real-world wax deposition issues during oil and gas productions.

Chapter 2 focuses on the prediction of deposit carbon number distribution in wax deposition modeling. This predication is achieved by combining the most advanced wax deposition model, the Michigan Wax Predictor with the most theoretically comprehensive thermodynamic model, the Coutinho's model[18]. The algorithm to predict the carbon number distribution of the deposit is validated by comparing the predictions with results from lab-scale flow loop wax deposition experiments. This enhancement will provide additional insights to understand the mechanical properties of wax deposit, which in turn depends on the carbon number distribution of the deposit. In addition, predicted carbon number distribution of the depositing wax can guide the selection of wax inhibitors to target these waxy components and achieve optimal inhibitor efficacy. Chapter 3 – Chapter 6 are dedicated to both experimental and modeling investigations of wax deposition in water-oil two phase flows. Chapter 3 studies wax deposition in water-oil stratified flow. Wax deposition experiments were performed with the state-of-the-art flow loop apparatus. The role of the stratified water on wax deposition was uncovered. Chapter 4 - Chapter 6 are dedicated to analyzing wax deposition in water-in-oil dispersed flow. Chapter 4 provides a fundamental characterization of the diffusion characteristics of wax in water-in-oil dispersion. This experimental characterization clears the persistent confusion in literature about the modeling of wax diffusion in water-in-oil dispersion. Chapter 5 presents a comprehensive heat and mass transfer analysis on wax deposition from water-in-oil dispersed flow. A wax deposition model for water-in-oil dispersed flow was developed and validated by comparisons between lab-scale wax deposition experiments and model predictions. Further experimental investigations on wax deposition from water-in-oil dispersions were carried out in Chapter 6.

The phenomena of droplets entrapment by deposit formation was characterized experimentally. The impact of entrapped droplets on the rheological properties of the resulting deposit and the subsequent sloughing of deposit is presented, which serves as considerations beyond heat and mass transfer analysis during the assessment of wax deposition risk from water-in-oil dispersed flow. Chapter 7 presents the incorporation of non-Newtonian fluid mechanics of waxy crude oil on wax deposition modeling. Non-Newtonian fluid characteristics are expected to complicate the modeling of hydrodynamics, heat and mass transfer as well as deposit growth. Such complication is non-negligible when the oil of interest contains a substantial amount of wax. Incorporation of the non-Newtonian fluid mechanics leads to the development of a next-generation wax deposition model, which can generate reliable wax deposition rate predictions in a real-world field pipeline.

Chapter 2

Effects of Operating Conditions on Wax Deposit Carbon Number Distribution: Theory and Experiment

2.A Introduction

Wax deposition in subsea oil pipelines is a significant economic problem in petroleum industry because it can lead to a reduction in oil production, pipeline shutdown, increased operational costs and Health, Safety and Environment problems[13,19–21]. In extreme cases, the pipeline may become completely plugged by the wax deposit, requiring the plugged portion of the pipeline to be removed and replaced in order for the production to continue[22]. In most cases, remediation operations are periodically conducted to maintain the crude oil transport in subsea pipelines. One of the most conventional remediation techniques is called "pigging" where an inspection gauge, also known as "pig", is sent into the pipeline to scrape off the wax[23]. In the case of "pigging", it is vital to determine a pigging frequency because the cost of "pigging" increases exponentially as the pigging frequency increases[11]. Insufficient pigging frequency can result in the buildup of a thick wax deposit that causes the pig to get stuck. The only way to remove this blockage is to send divers down to replace the pipe section with the stuck pig at a cost of several million dollars[11]. Knowledge of deposition rate is critical in order for one to determine a suitable pigging frequency. In the past decade, multiple wax deposition models have been developed for the prediction of deposition rate and to provide recommendations on pigging frequency[21,24–29].

In addition to the wax deposition rate, the wax's rheological properties, specifically the yield stress of the deposit is also an important element in pigging operations. The force generated by the pig needs to overcome the deposit yield stress in order to remove the deposit. Therefore, as the deposit yield stress increases, it becomes more difficult to remove the deposit with pigging[30]. The deposit yield stress depends on deposit's carbon number distribution. In a study by Senra et al. using model mixtures, it was found that [2% n-C_{32}+ 2% n-C_{36}] in C_{10} produces a much weaker deposit than [2% n-C_{28}+2% n-C_{36}] in C_{10} because of the co-crystalization of C_{32} and C_{36}[31]. More recently, Bai and Zhang reported that the variation in the n-paraffin distribution with a wide range of carbon numbers (C_{17}-C_{55}) can significantly change the deposit yield stress[32]. Consequently, the knowledge of deposit carbon number distribution forms the basis for the estimation of the deposit yield stress and thus is potentially important to pigging design. Understanding the evolution of deposit carbon number distribution during wax deposition requires fundamental knowledge of the mechanism by which the deposit is formed. It is widely accepted that molecular diffusion is the main mechanism responsible for deposit formation[20,21,24,25,27,28,33–35]. In the molecular diffusion mechanism, wax, chemically known as n-alkane, precipitates at the pipe wall when the surface temperature is below the wax appearance temperature. The precipitated wax crystals form a gel network with oil trapped by the wax. Precipitation of n-alkane molecules creates a concentration gradient in the boundary layer for each of the diffusing wax components. The resulting concentration gradients from the bulk towards the wall drive more molecules to diffuse towards the wall to form deposit. Depending on the carbon number, different n-alkanes will have different physical properties, e.g. solubility and molecular diffusivity, and thus can have different mass transfer and precipitation characteristics. This variation in characteristics for different n-alkanes could potentially cause a

distribution of n-alkanes in the deposit formed by molecular diffusion of multiple n-alkane components.

While the deposit thickness has been extensively studied in the past few decades, much fewer investigations have been carried out on the composition of the wax deposit on the pipe wall. In this study, an unprecedented extensive analysis on the carbon number distribution (CND) of the wax deposit was carried out.

In this study, the Michigan Wax Predictor (MWP)[26–28], a fundamental wax deposition model based on the mechanism of molecular diffusion is used to model the diffusion and deposition of multiple n-alkane components and to study the deposit carbon number distribution. For the first time, the critical factors that affect the deposit carbon number distribution are identified from fundamental thermodynamic and transport modeling. The identified critical factors are verified by flow-loop experiments. A modeling approach is developed based on the Michigan Wax Predictor in order to predict the carbon number distribution in wax deposit. The prediction of carbon number distribution from MWP can potentially provide insights for pigging design.

2.B Fundamentals of Transport Modeling Using the Michigan Wax Predictor (MWP)

In this section, the fundamental equations used by the MWP to model mass transfer of wax from the liquid bulk towards the wall/interface are briefly revisited [26–28]. Additionally, the method of incorporating Coutinho's thermodynamic model into the MWP to simulate the mass transfer of multiple species is developed.

The MWP numerically solves the fundamental transport equation, shown in Equation (2-1) , with the boundary conditions shown in Equation (2-2), in order to predict the concentration profiles of wax.

$$V_z \frac{\partial C_{\text{wax}}}{\partial z} = \frac{1}{r}\frac{\partial}{\partial r}\left[\left(\varepsilon_{\text{M}} + D_{\text{wo}}\right) r \frac{\partial C_{\text{wax}}}{\partial r}\right] \tag{2-1}$$

$$\text{at } z = 0,\ C_{\text{wax}} = C_{\text{wax,inlet}}$$

$$\text{at } r = 0,\ \frac{\partial C_{\text{wax}}}{\partial r} = 0 \tag{2-2}$$

$$\text{at } r = R,\ C_{\text{wax}} = C_{\text{wax,eq,interface}}$$

$V_z =$ axial velocity,(m/s)

$C_{\text{wax}} =$ concentration of dissolved wax in oil,(kg/m^3)

$z =$ axial position,(m)

$r =$ radial position,(m)

$\varepsilon_{\text{M}} =$ turbulent mass diffusivity,(m^2/s)

$D_{\text{wo}} =$ diffusivity of wax in oil,(m^2/s)

$C_{\text{wax,inlet}} =$ concentration of dissolved wax at the inlet,(kg/m^3)

$R =$ pipe radius,(m)

$C_{\text{wax,eq,interface}} =$ equilibrium concentration of dissolved wax at the interface,(kg/m^3)

Based on the predicted concentration profiles, the MWP calculates the mass flux of wax towards the wall/interface and then predicts the deposition rate. It has been shown in previous studies[26–28] that the MWP provides reliable predictions for:

- The magnitude of wax deposition rate
- The effects of operating conditions

However, in the previous studies based on MWP[26–28], n-alkanes with different carbon numbers were lumped into one pseudo-component, termed as "wax". Because of this lumping, it was impossible to resolve the mass transfer of different species and thus impossible to predict the deposit carbon number distribution. A prediction of the carbon number distribution in the deposit is possible using the MWP by modeling the mass transfer of each component.

The fundamental transport equation and boundary conditions shown in Equations (2-1)-(2-2) are universally applicable to the modeling of mass transfer for all species. However, the following species-dependent mass transfer characteristics need to be accounted for:

- Different molecular diffusivities of n-alkanes with different chain lengths
- Different inlet and wall concentration boundary conditions of n-alkanes due to different solubility

Species-dependencies are emphasized with the subscript *i* in the terms in the transport equation and the boundary conditions, resulting in Equations (2-3)-(2-4).

$$V_z \frac{\partial C_{\text{wax,i}}}{\partial z} = \frac{1}{r}\frac{\partial}{\partial r}\left[\left(\varepsilon_{\text{M,i}} + D_{\text{wo,i}}\right) r \frac{\partial C_{\text{wax,i}}}{\partial r}\right] \tag{2-3}$$

$$\text{at } z = 0,\ C_{\text{wax,i}} = C_{\text{wax,i,inlet}}$$

$$\text{at } r = 0,\ \frac{\partial C_{\text{wax,i}}}{\partial r} = 0 \tag{2-4}$$

$$\text{at } r = R,\ C_{\text{wax,i}} = C_{\text{wax,i,eq,interface}}$$

These modifications to the current MWP incorporate the aforementioned two species-dependent characteristics of diffusivity and solubility, and will be discussed separately in more detail in the following sub-sections.

2.B.1 Molecular Diffusivities of n-Alkane Molecules with Different Chain Lengths

In the modeling of molecular diffusion of multiple components, the difference in diffusivities due to the difference in molecular sizes needs to be considered. As the chain length increases, the molecular diffusivity decreases due to the increasing bulkiness of the molecules. In order to be consistent with the previous studies based on the MWP, the Hayduk-Minhas equation[36] is used in this study to calculate the diffusivity of n-alkanes, as shown below:

$$D_{\text{wo,i}} = 13.3\times10^{-12}\ \frac{T_{\text{o}}^{1.47}\,\mu^{(10.2/V_{\text{A,i}}-0.791)}}{V_{\text{A,i}}^{0.71}} \tag{2-5}$$

$D_{\text{wo,i}}$ = the molecular diffusivity of wax in oil,(m^2/s)

T_{o} = the temperature of the fluid,(K)

μ = the viscosity of the fluid,$(c.P.)$

V_A = the molar volume of the diffusing n-alkane,(cm^3/mol)

One notes in Equation (2-5) that the effect of molecular size on diffusivity is taken into consideration by the molecular volume term, $V_{A,i}$, and that a larger molecular volume results in a smaller diffusivity.

2.B.2 Concentration Boundary Conditions at Inlet and Wall

It is assumed that the concentrations of species at the inlet and the wall are in thermodynamic equilibrium at the inlet and wall temperatures respectively. The liquid phase equilibrium concentration of a particular n-paraffin species n-C_iH_{2i+2} depends on the total amount of n-C_iH_{2i+2} in the crude oil and its solubility at a particular temperature. As a result, the equilibrium concentrations of components, n-C_jH_{2j+2} ($j \neq i$) will be different from each other. Consequently, the inlet and wall concentration boundary conditions for each n-alkane component need to be specified individually. A thermodynamic model is needed to calculate the equilibrium concentrations. Among the existing thermodynamic models[18,37,38], Coutinho's thermodynamic model is the most comprehensive one because it considers both the liquid phase and solid phase non-idealities. Consequently, Coutinho's thermodynamic model was chosen for this study. It should be noted that branched and cyclic components were not included in thermodynamic modeling as they have melting points lower than their normal isomers with the same carbon number and thus does not precipitate. Details regarding the equations used by Coutinho's model are discussed in the previous studies by Coutinho and are summarized in Appendix B.

With the species-dependent diffusivities and concentration boundary conditions incorporated, the MWP can now be used to model the diffusion of multiple n-alkane components and provide predictions for the deposit carbon number distribution.

2.C Experimental

Flow-loop experiments were performed using a North Sea crude oil (Oil S) on a pilot-scale flow-loop at the Herøya Research Center of Statoil ASA in Porsgrunn, Norway. Deposits formed under different operating conditions were collected and the deposit carbon number distributions were measured to verify the results obtained from theoretical analysis. A detailed analysis of these experiments is discussed below.

2.C.1 Crude Oil Characterization

2.C.1.a Compositional Information

The composition of the oil needs to be determined by experiments in order to be used as input to Coutinho's model. The following two distributions can be used to characterize the oil composition for the purpose of predicting wax precipitation characteristics:

- **The Single Carbon Number (SCN) distribution:** A single carbon number fraction with carbon number *i* includes branched paraffin, cyclic paraffin, aromatics and n-paraffin with carbon number *i*. Therefore, the molecular formula of the components in SCN with carbon number *i* can be written as C_iH_j, where $j = 2i+2$ represents paraffinic components and $j \neq 2i+2$ represents the un-saturated fractions.
- **The n-paraffin distribution:** the mole/mass fraction of only n-paraffin, n-C_iH_{2i+2}, as a function of carbon number *i*

The "SCN distribution" provides information regarding the total amount of hydrocarbon components C_iH_j (including both n-paraffin and non-n-paraffin with carbon number *i*) contained by the oil. Only the n-paraffin (n-C_iH_{2i+2}) portion of component C_iH_j can precipitate. For a typical crude oil, the non-normal n-paraffins usually do not precipitate as their melting points are usually significantly lower than the n-paraffin with the same carbon number. In this study, both

the SCN distribution and the n-paraffin distributions of the oil were measured using a Hewlett-Packard 6890A HTGC equipped with capillary column coated with DB-1. Figure 2-1 shows the measured SCN composition along with the n-paraffin distribution of Oil S.

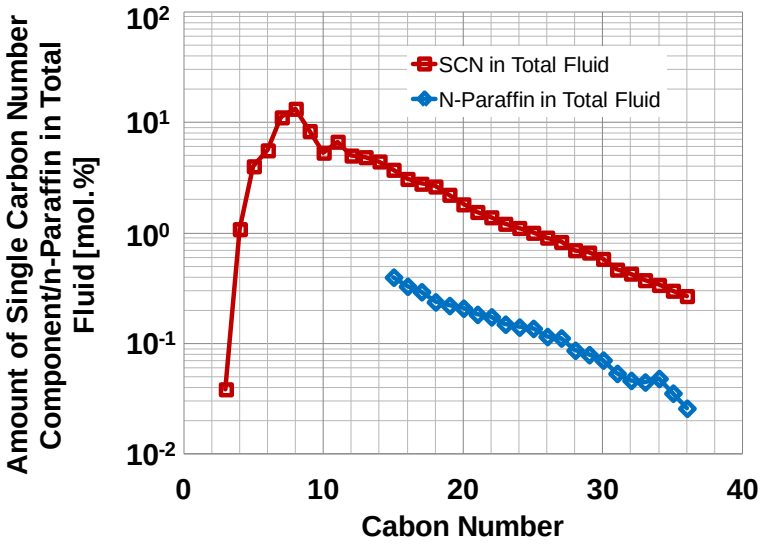

Figure 2-1: Composition of the crude oil including n-paraffin distribution of Oil S measured by HTGC

It should be noted that n-paraffin species with carbon numbers lower than 15 have melting points lower than 5 °C and thus usually do not precipitate[39,40]. Therefore, it is not necessary to differentiate between n-paraffin and non-n-paraffin for C_{15}- components and as seen from Figure 2-1 that the n-paraffin distribution is not measured for C_{15}- components.

2.C.1.b Wax Precipitation Information

Wax precipitation information of North Sea Oil S, shown Table 1, was measured experimentally in the study by Hoffmann and Amundsen[39]. The wax precipitation information obtained from these experiments will be compared with predictions with Coutinho's model in order to verify the applicability of Coutinho's model to Oil S.

Table 2-1: Summary of wax precipitation information obtained from experiments[39,40]

Property	Method	Value
Wax Appearance Temperature	Cross-Polarized Microscope	30°C
Wax Content	Acetone Precipitation (UOP Method 46-64)	4.5 wt.%
Precipitation Curve	Centrifugation/HTGC, Beckman Instruments centrifuge (model L8-70) and Hewlett-Packard 6890A HTGC equipped with a CPSimDist Ultimetal column	Discussed in detail in later sections
Composition of Solid Cakes Obtained from Precipitation Experiments	HTGC, Hewlett-Packard 6890A HTGC equipped with a CPSimDist Ultimetal column	Discussed in detail in later sections

It should be noted that the measured temperature-solubility curve and the composition of the solid cakes will be presented later when compared with predictions by Coutinho's model.

2.C.1.c Physical Properties

Physical properties of the oil that are important to heat and mass transfer include viscosity, thermal conductivity and heat capacity. These properties of Oil S were either measured or estimated. The viscosity of Oil S was measured with a Physica MCR 301 rheometer and the results are shown in Figure 2-2[39].

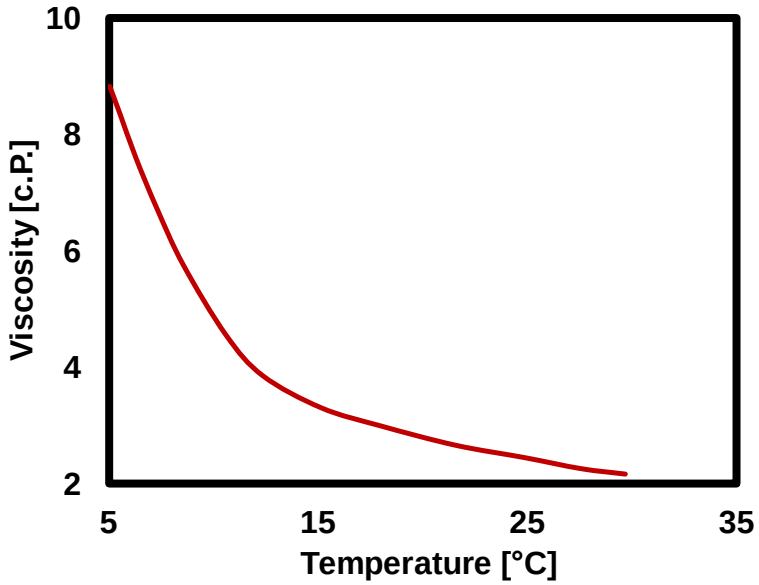

Figure 2-2: Viscosity curve of Oil S measured by rheometer

The thermal conductivity and heat capacity were estimated based on the density of the oil, 809 kg/m^3 using Perry's handbook[41]. Table 2-2 summarizes the estimation for thermal conductivity and heat capacity.

Table 2-2: Estimation for oil thermal conductivity and heat capacity

Property	Value
Oil Thermal Conductivity	0.13 W/m/°C
Oil Heat Capacity	2100 J/g/°C

2.C.2 Flow Loop Experiments

A series of flow-loop experiments were performed using the pilot-scale flow-loop at the Herøya Research Center of Statoil ASA in Porsgrunn, Norway shown schematically in Figure 2-3[39].

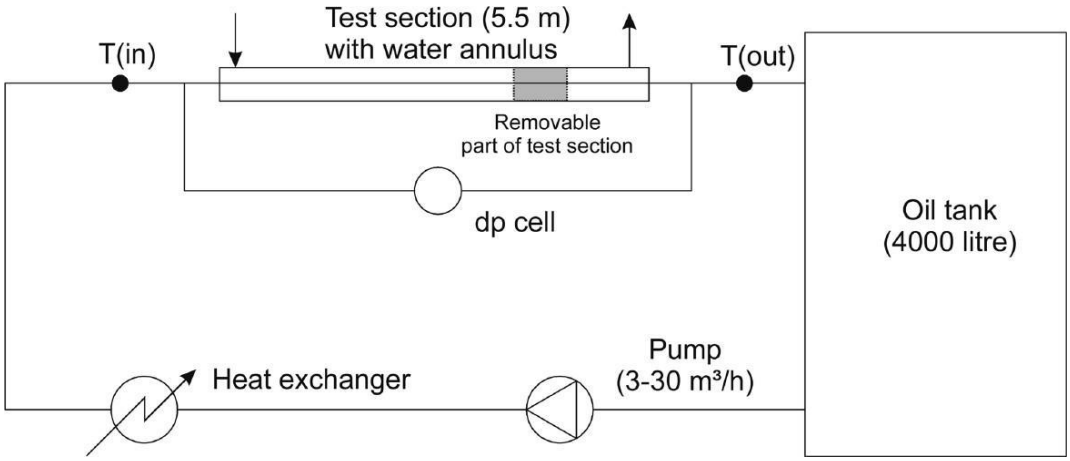

Figure 2-3: The layout of the flow-loop apparatus at Statoil ASA in Porsgrunn

After each deposition experiment, the flow was first stopped and N_2 was blown through the test section to remove residual oil adhered to the deposit surface. The deposit was then collected from a removable spool piece and characterized by gas chromatography. Other details regarding the procedures of flow-loop experiments were provided in a previous study by Hoffmann and Amundsen[39].

2.D Results and Discussions

2.D.1 Verification of Application of Coutinho's Model to North Sea Crude Oil S

As boundary conditions, the concentrations at the inlet and the wall are specified to be equal to the equilibrium concentrations predicted by Coutinho's model. Therefore, it is necessary to verify that for the particular crude oil in this study, Coutinho's model provides reliable prediction for the wax precipitation characteristics including:

- precipitation curve
- composition of the precipitated solid

The composition of the crude oil will be used as the input to Coutinho's model and thus needs to be available from experimental measurements.

In this study, the mole fraction of each alkane component (including normal paraffin and isomers) as well as the n-paraffin fraction of each alkane component was measured by HTGC, as was previously shown in Figure 2-1.

Figure 2-1 shows both the mole fraction hydrocarbon components and their n-paraffin fractions that were measured up to C_{36}. However, for components with carbon number greater than 36, the accuracies of the measured mole fractions and n-paraffin fractions become susceptible to experimental errors due to the low absolute amounts of the C_{36}+ fractions (<~ 0.02 mol%). On the other hand, wax precipitation characteristics in terms of the precipitation curve and the composition of the precipitated solid phase are sensitive to the heavy end composition because heavy components are the first to precipitate as temperature falls below the WAT[37].

Consequently, the mole fractions of the C_{36}+ components and the corresponding n-paraffin fractions need to be properly estimated and included in thermodynamic modeling so that model predictions better represent the actual crude oil precipitation characteristics.

Based on field experience, Pederson et al. suggested extrapolating the SCN and n-paraffin distribution of the heavy end to a certain limiting carbon numbers by assuming that the amount of hydrocarbon component C_iH_j and n-paraffin n-C_iH_{2i+2} decreases logarithmically as the carbon number *i* increases. Pedersen's method of extrapolation has provided satisfactory modeling results for multiple crude oils[42]. Pedersen's method was used to estimate the mole fraction and n-paraffin fraction for components with carbon numbers greater than 36. On the other hand, the computational intensity increases as more C_{36}+ components are included in modeling. For each alkane component n-C_iH_{2i+2}, the MWP solves a 2-D mass transport equation to determine its concentration profiles. Therefore the number of equations that need to be solved increases as the upper limit of extrapolation increases. Moreover, a sensitivity analysis showed that for the particular crude oil in our study, including C_{50}+ alkane components in thermodynamic modeling affects the predicted precipitation curve by less than 0.1%. Consequently, extrapolation of the heavy end composition is performed only up to C_{50} while C_{50}+ components are not included in modeling. Figure 2-4 shows the composition of the oil with the mole fractions of C_{36}-C_{50} components extrapolated using Pedersen's method.

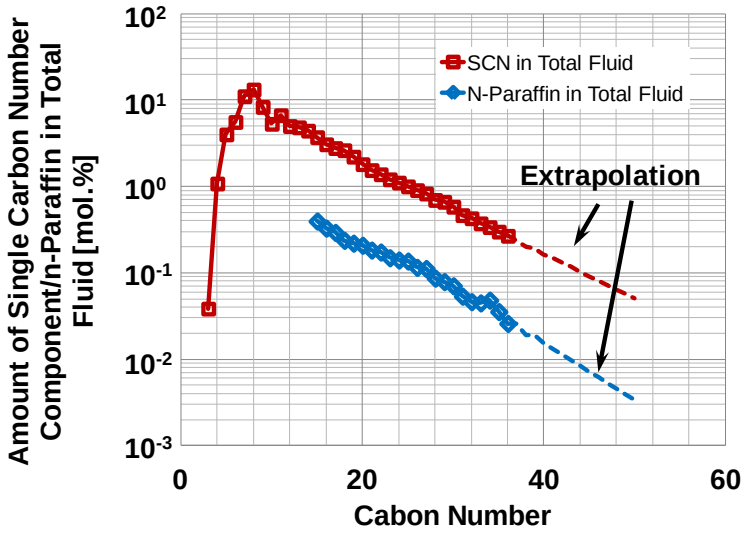

Figure 2-4: Extrapolation of SCN composition and n-paraffin distribution by assuming a logarithmic decrease in mole % as a function of carbon number

Based on the composition shown in Figure 2-4, the solubility curve was predicted and compared with the solubility curve measured by the Centrifugation/HTGC method by Han et al.[40], as is shown in Figure 2-5.

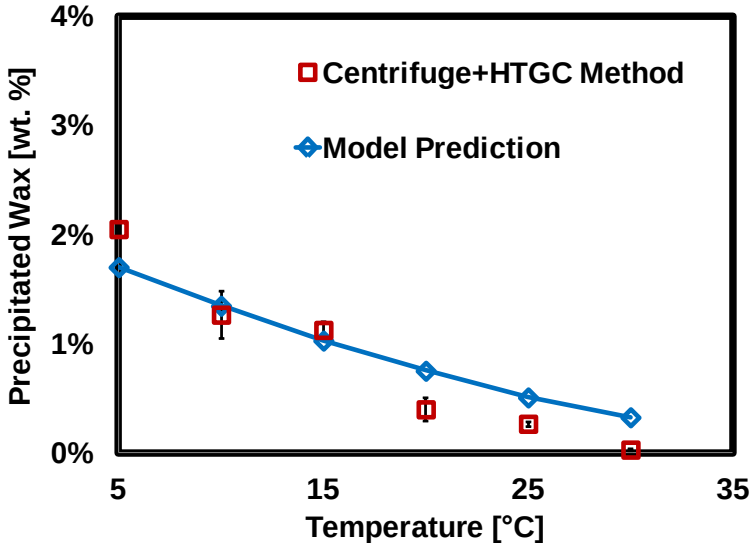

Figure 2-5: Predicted precipitation curve in comparison with measure precipitation curve

It should be noted that uncertainties exist in the procedures to obtain both the predicted and the experimentally measured solubility curve. For example, the crude oil composition used as the input for solubility curve predictions can vary depending on the integration method used to

obtain the mole fraction of the alkane components based on gas chromatography. The uncertainties in the oil composition can thus cause as a much as 2 wt.% difference in the predicted solubility curve[43]. Due to the likely uncertainties, *absolutely no tuning* was performed and as can be seen from Figure 2-5, the predicted precipitation curve is in close agreement with the measured precipitation curve. It should be pointed out that accurate prediction of the precipitation curve indicates Coutinho's model can accurately predict the total amount of all precipitating n-alkane, n-C_iH_{2i+2} that has precipitated at a particular temperature, i.e. $\sum_i w_{\text{n-}C_iH_{2i+2},\text{precipitated}}(\%)$. However, the purpose of incorporating Coutinho's model in the MWP is to specify boundary conditions for all diffusing n-alkanes. Therefore, it needs to be further verified that Coutinho's model can predict the amount of precipitation for each precipitating n-alkane, n-C_iH_{2i+2}, i.e. each $w_{\text{n-}C_iH_{2i+2},\text{precipitated}}(\%)$. This further verification was carried out by comparing the predicted and experimentally measured composition of the precipitated solid phase. Figure 2-6 shows the measured composition of the solid cake at different temperature.

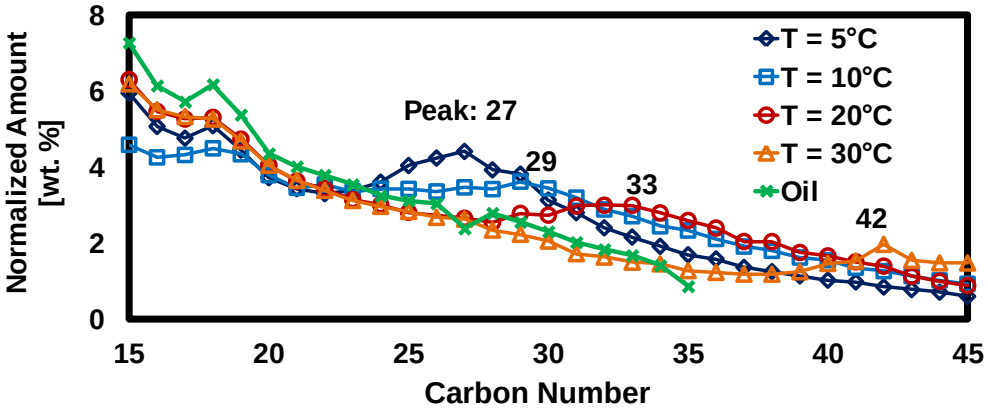

Figure 2-6: Measured composition of the solid cake obtained at 5°C, 10°C 20°C and 30°C

However, it should be noted that the carbon number distribution of the centrifuged solid cake shown in Figure 2-6 does not represent the composition of the precipitated solid phase because

liquid oil is entrapped as the solid cake forms and therefore cannot be removed by centrifugation[40].

Consequently, in order to obtain the "true" composition of the precipitated solid phase, oil composition is subtracted from the cake composition. The procedure of obtaining the "true" composition of the precipitated solid was previously used by Hoffmann et al.[39], and is explained in detail in Appendix C. Figure 2-7 shows the "true" composition of the precipitated solids phase.

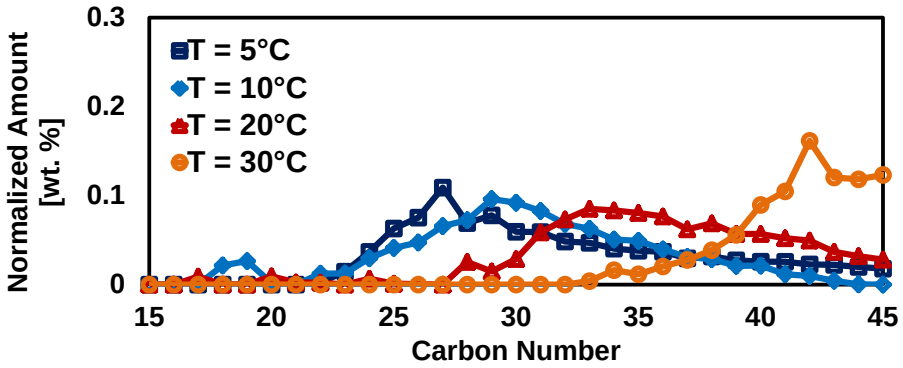

Figure 2-7: "True" precipitated solid phase composition at temperatures, *T* = 5 °C, 10 °C, 20 °C and 30 °C

Two trends can be observed from the measured solid phase composition:

- At a particular temperature, as carbon number *i* increases, the weight fraction of n-C_iH_{2i+2} first increases, reaches a maximum then decreases.
- As temperature increases, the peak in the carbon number distribution shifts towards greater carbon number.

It should be noted that the first trend characterizes the relative amount of n-C_iH_{2i+2} that precipitates at a particular temperature. The second trend characterizes the effect of temperature on the overall deposit carbon number distribution.

Figure 2-8 shows the comparison between predicted solid composition and the solid phase composition obtained from subtracting the oil composition from the cake composition.

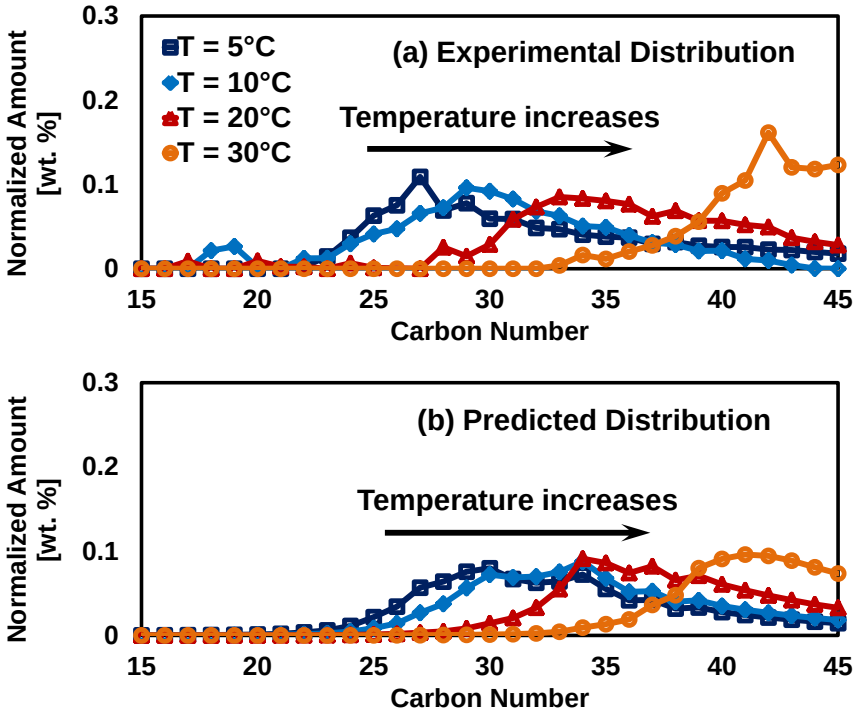

Figure 2-8: Predicted solid compositions at 5°C, 10°C, 20°C and 30°C in comparison with measured composition

It should be emphasized that Coutinho's thermodynamic model does not contain adjustable parameters that allow tuning to produce exact matches between model predictions and experimental data. Consequently, *absolutely no tuning* was performed in this study in order for the predicted carbon number distribution to closely match the measured carbon number distribution.

As can be seen from Figure 2-8, Coutinho's model predicts consistent trends in the weight fractions compared with that obtained by experimental measurements.

Consequently, Coutinho's model can be used to accurately specify the boundary conditions. Using the composition of the oil as model input, the liquid phase equilibrium concentration for each component is calculated using Coutinho's thermodynamic model. The resulting liquid phase equilibrium concentrations were used as the boundary condition for transport modeling.

2.D.2 Identifying the Dominant Factors in the Deposit CND Evolution – Part I: Theoretical Analysis

The evolution of the carbon number distribution in the wax deposit is a result of the differences in the mass fluxes of different components to the interface. The components with larger mass fluxes towards the wall/interface are expected to be more enriched in the deposit compared with those components with relatively lower mass fluxes. The difference in the diffusive mass fluxes for different components is due to the differences in:

- Concentration driving force
- Diffusivity

Differences in mass fluxes caused by the differences in concentration driving force and the differences in the diffusivities can be quantified separately by first de-dimensionlizing the transport equations. The ratios as defined in Equation (2-6) were used to de-dimensionalize the mass transport equation and the boundary conditions, Equation (2-1)-(2-2), resulting in Equations (2-7)-(2-8).

$$\theta_{\text{wax,i}} = \frac{C_{\text{wax,i}} - C_{\text{wax,i,interface}}}{C_{\text{wax,i,bulk}} - C_{\text{wax,i,interface}}}, \nu = \frac{V_z}{U}, \lambda = \frac{z}{L},$$
$$\eta = \frac{r}{R}, Gz_{\text{i}} = \frac{D^2 U}{L(\varepsilon_{\text{M,i}} + D_{\text{wo,i}})} \tag{2-6}$$

$C_{\text{wax,bulk}}$ = the concentration of dissolved wax in the bulk,(kg / m^3)

U =is the average velocity of the bulk fluid,(m / s)

L =is the length of the entire test section,(m)

D =is the inner diameter of the test section,(m)

$$\nu \frac{\partial \theta_{\text{wax,i}}}{\partial \lambda} = \frac{1}{\eta} \frac{\partial}{\partial \eta} \left(\frac{4}{Gz_{\text{i}}} \eta \frac{\partial \theta_{\text{wax,i}}}{\partial \eta} \right) \tag{2-7}$$

$$\text{at } \lambda = 0,\ \theta_{\text{wax,i}} = 1$$
$$\text{at } \eta = 0,\ \frac{\partial \theta_{\text{wax,i}}}{\partial \eta} = 0 \tag{2-8}$$
$$\text{at } \eta = 1,\ \theta_{\text{wax,i}} = 0$$

Based on the defined de-dimensionalized ratio shown in Equation (2-6), the mass flux of each component *i*, initially calculated by $J_{wax,i} = D_{wo,i}\partial C_{wax,i} / \partial r$, can be re-written as shown in Equation (2-9).

$$J_{wax,i} = \underbrace{\frac{\partial \theta_{wax,i}}{\partial \eta}|_{wall}}_{\textbf{Term 1}} \cdot \underbrace{\frac{D_{wo,i}}{R}}_{\textbf{Term 2}} \cdot \underbrace{\left(C_{wax,i,bulk} - C_{wax,i,interface}\right)}_{\textbf{Term 3}} \qquad (2\text{-}9)$$

$$J_{wax,i} = \text{the diffusive mass flux of wax,} (kg/m^2/s)$$

As can be seen from Equation (2-9), three terms are separated from each other and the potential variations in these three terms caused by varying diffusivity and concentration driving force are summarized in Table 2-3.

Table 2-3: Summary of potential variation in Terms 1, 2 and 3 caused by varying diffusivity and concentration driving force

Term	Changes with
Term 1: $\frac{\partial \theta_{wax,i}}{\partial \eta}|_{wall}$	Diffusivity
Term 2: $D_{wo,i}/R$	Diffusivity
Term 3: $C_{wax,i,bulk}$ -$C_{wax,i,interface}$	Concentration driving forces

It is apparent that *Term 2* only changes with diffusivity and *Term 3* only changes with concentration driving force. Although listed in Table 2-3, it is not so apparent at this point why *Term 1* only changes with diffusivity and doesn't change with the concentration driving force.

Term 1: $\frac{\partial \theta_{wax,i}}{\partial \eta}|_{wall}$ is calculated by evaluating the gradient of the solution profiles of the de-dimensionalized transport equations. In addition, one notes that the solution profiles of the de-dimensionalized transport equations are independent of both $C_{wax,i,bulk}$ and $C_{wax,i,interface}$. Consequently, *Term 1* only changes with the diffusivity.

By separately investigating the variation in *Terms 1, 2 and 3* as the carbon number changes, one can study whether the resulting change in diffusivity or the concentration driving forces dominates the corresponding change in mass flux. The variation of *Term 1*, $\frac{\partial \theta_{wax,i}}{\partial \eta}|_{wall}$, was evaluated for a base case with Q_{oil} = 5m^3/hr, T_{oil} = 25°C and $T_{coolant}$ = 5 °C. Using this set of input operating conditions, de-dimensionalized concentration profiles for each component was obtained by numerically solving the transport equations using the MWP. Figure 2-9 shows the predicted de-dimensionalized radial concentration profiles for components with carbon numbers ranging from 20 to 50 with an interval of 5 carbon numbers.

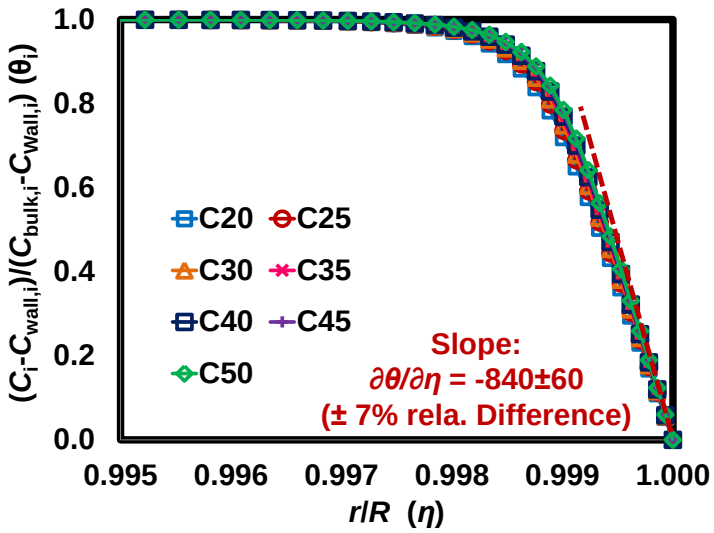

Figure 2-9: De-dimensionalized radial concentration profiles

The slope of the de-dimensionalized concentration profile at wall ($r = R$ or $\eta = r/R = 1$) corresponds to $\frac{\partial \theta_{wax,i}}{\partial \eta}|_{wall}$. It can be seen from Figure 2-9 that for the n-alkane components with carbon number ranging from 20-50, the variation of $\partial\theta/\partial\eta$ is within 7%. Therefore, one can conclude that the difference in *Term 1* caused by the difference in diffusivities does not result in a significant difference in mass fluxes. The difference in mass fluxes can be further investigated

by evaluating the product of the two remaining terms in the expression to calculate mass flux: and $(C_{\text{wax,i,bulk}} - C_{\text{wax,i,interface}})$.

The variation in *Term 2*: ($D_{\text{wo,i}} / R$) is due to the variation in molecular diffusivity. Figure 2-10 shows the variation in molecular diffusivity as carbon number *i* varies.

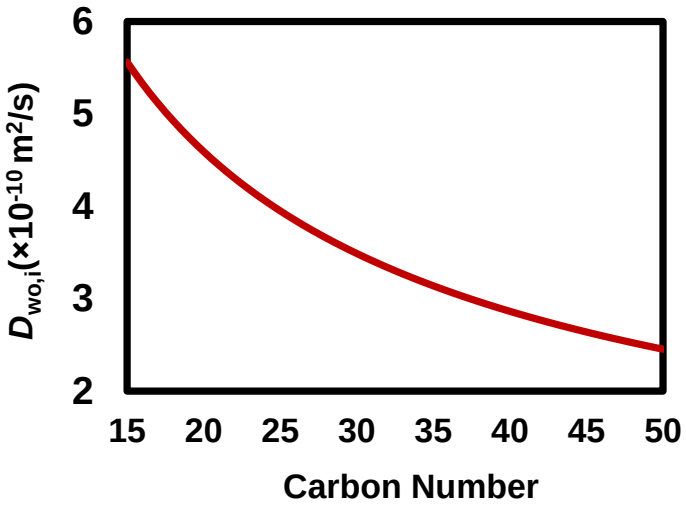

Figure 2-10: Variation in molecular diffusivity, $D_{\text{wo,i}}$, as a function of carbon number

It is seen from Figure 2-10 that molecular diffusivity varies by a factor of 2 as carbon number increases from 15 to 50.

In order to calculate *Term 3*, $(C_{\text{wax,i,bulk}} - C_{\text{wax,i,interface}})$, Coutinho's model was first used to calculate $C_{\text{wax,i,bulk}}$ (at $T_{\text{o,bulk}}$) and $C_{\text{wax,i,interface}}$ ($T_{\text{o,interface}}$) individually. *Term 3* was then determined by calculating the difference between $C_{\text{wax,i,bulk}}$ and $C_{\text{wax,i,interface}}$. Figure 2-11 shows the variation of *Term 3*, the concentration driving force: $(C_{\text{wax,i,bulk}} - C_{\text{wax,i,interface}})$ as a function of carbon number *i*.

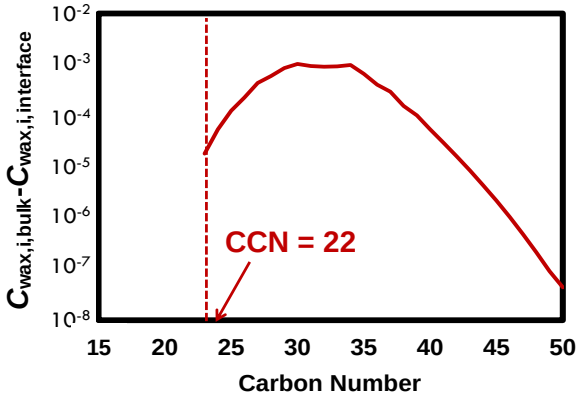

Figure 2-11: Bulk and wall concentration differences for different n-alkane components

According the study by Singh et al., a critical carbon number (CCN) exists such that components having carbon number greater than CCN diffuse towards the interface/wall while those having carbon number less than CCN diffuse away from the interface/wall[44]. The CCN in this study was determined by comparing the relative magnitudes between $C_{wax,i,bulk}$ and $C_{wax,i,interface}$. $C_{wax,i,bulk} > C_{wax,i,interface}$ indicates a concentration gradient for diffusion towards the wall/interface while $C_{wax,i,bulk} < C_{wax,i,interface}$ indicates counter-diffusion away from the interface/wall. Consequently, the CCN should satisfy the following two conditions:

- For $i <$ CCN, $C_{wax,i,bulk} < C_{wax,i,interface}$
- For $i >$ CCN, $C_{wax,i,bulk} > C_{wax,i,interface}$

The CCN in this model case is determined to be at 22. The concentration difference $(C_{wax,i,bulk} - C_{wax,i,interface})$ for n-alkanes with a carbon number lower than 22 are not shown in the figure because they diffuse away from the wall/interface and therefore are not responsible for deposit formation[44].

It is seen from Figure 2-11 that as the carbon number increases, the concentration driving force first increases, reaches a maximum and then decreases. This trend in the concentration driving force as a function of carbon number can be explained as follows:

For a particular n-paraffin, n-C_iH_{2i+2}, the concentration driving force, $(C_{\text{wax,i,bulk}} - C_{\text{wax,i,interface}})$ is determined by the following two factors:

- The solubility limit of n-C_iH_{2i+2} precipitated at the wall, quantified by $C_{\text{wax,i,interface}}$
- The concentration of molecules available for diffusion in the liquid phase, $C_{\text{wax,i,bulk}}$

$C_{\text{wax,i,interface}}$ decreases as *i* increases because n-C_iH_{2i+2} has a lower solubility as *i* increases. Therefore, one might expect as carbon number *i* increases, the concentration driving force for molecular diffusion also increases. However, as carbon number increases, $C_{\text{wax,i,bulk}}$ also decreases because the oil contains less n-C_iH_{2i+2} as *i* increases. Consequently the difference, $(C_{\text{wax,i,bulk}} - C_{\text{wax,i,interface}})$, first increases then decreases as *i* increases.

Moreover, the concentration driving force varies over 5 orders of magnitude as the carbon number varies from 20 to 50.

One notes that the product of *Term 2*, ($D_{\text{wo,i}}/R$), and *Term 3*, $(C_{\text{wax,i,bulk}} - C_{\text{wax,i,interface}})$, as shown in Equation (2-10), $J_{\text{wax,i}}$,

$$J_{\text{wax,i}} = \frac{D_{\text{wo,i}}}{R} \cdot (C_{\text{wax,i,bulk}} - C_{\text{wax,i,interface}}) \tag{2-10}$$

was previously defined by Huang et al.[27] as the "characteristic mass flux" of wax deposition. Based on the previous findings, one can compare the relative magnitude of wax deposition rate by comparing the characteristic mass fluxes among experiments. Similarly, we here compare the characteristic mass fluxes of different components in any give experiment to evaluate the relative contributions of different components to wax deposition.

Figure 2-12 shows the calculated characteristic mass fluxes for different components aligned with the variation in concentration driving forces.

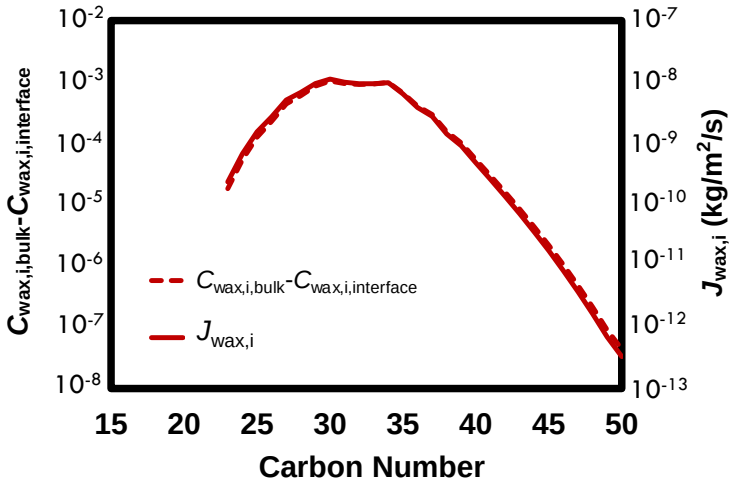

Figure 2-12: The characteristic mass flux in comparison with the concentration driving force

One notes that as the carbon number increases, the trend in mass flux is virtually identical to the trend in the concentration driving force. Therefore, the concentration driving force as a function of carbon number *i* can be used to evaluate the relative magnitude of the mass fluxes of the different components and thus can be correlated to the deposit carbon number distribution. From this point on, the concentration driving force as a function of carbon number *i* is defined as the "concentration driving force distribution" (ΔC distribution). Additionally, in order to better represent the relative magnitude of the concentration driving forces for different components, the "ΔC distribution" can be normalized by dividing each ΔC_i by the sum of all the concentration driving forces, $\sum \Delta C_i$, resulting in a "normalized ΔC distribution". The conclusion that the CND in the deposit is closely related to the "normalized ΔC distribution" was verified based on flow loop experiments and presented in the following section.

2.D.3 Identifying the Dominant Factors in the Evolution of Deposit CND– Part II: Experimental Verification

2.D.3.a Similar "Normalized ΔC Distributions" Lead to Similar Deposit Carbon Number Distributions

The theoretical analysis presented in the previous section showed that the deposit carbon number distribution can be correlated to the "normalized Δ*C* distribution". Consequently, experimental conditions resulting in similar "normalized Δ*C* distributions" are expected to produce similar carbon number distribution in the deposit, even though the operating conditions are different. Table 2-4 summarized two sets of operating conditions that produce similar deposit carbon number distributions.

Table 2-4: Summary of two sets of flow loop operating conditions: A and B, which lead to similar deposit CND

	Condition A	**Condition B**
Q_{oil} (m^3/hr)	5.00	21.00
T_{oil} (°C)	20.17	15.24
$T_{coolant}$ (°C)	5.00	10.00
T_{wall} (°C)	8.39	12.49

It is seen from Table 2-4 that the operating conditions for these two experiments are significantly different. However, the resulting deposit carbon number distributions from these two experiments are indeed quite similar, as can be seen in Figure 2-13.

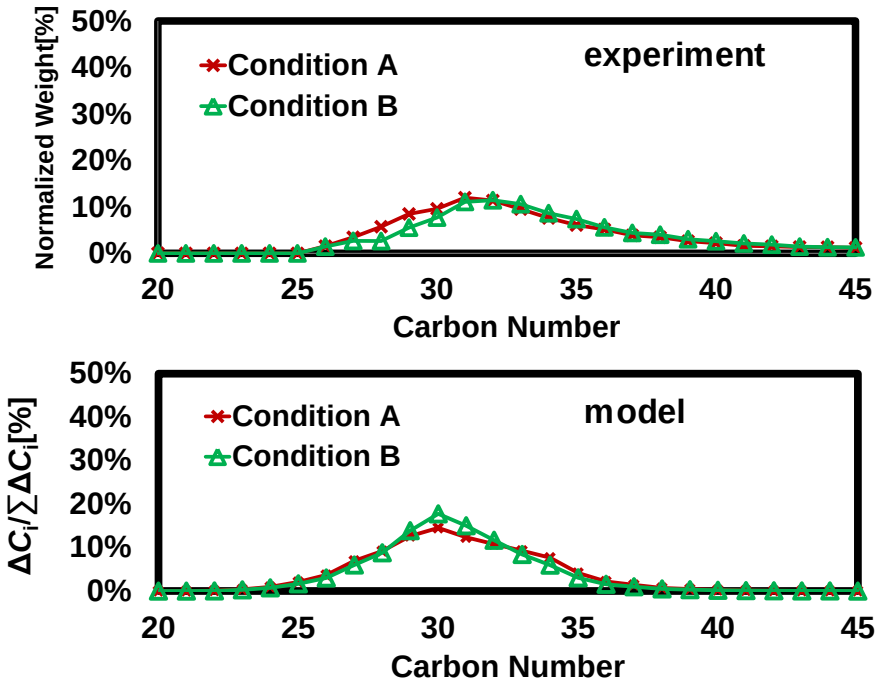

Figure 2-13: Comparison of the deposit carbon number distribution generated by the two sets of operating conditions

It should be noted that in Figure 2-13, the effect of entrapped oil on deposit composition was eliminated by subtracting the oil composition from the deposit composition. The resulting weight fraction as a function of carbon number represents the distribution of n-paraffin in the solid deposit. The similarity in the experimentally measured deposit carbon number distribution can be easily seen by calculating and comparing the "normalized ΔC distributions" for these two sets of experiments.

Figure 2-13 also shows the calculated "normalized ΔC distributions" based on the operating conditions of these two experiments.

It is seen from Figure 2-13 that although the operating conditions in these two experiments are *very* different, the ΔC distributions are similar and therefore resulting in nearly identical carbon number distribution curves in the deposit.

2.D.3.b The Effects of Operating Conditions on Deposit Carbon Number Distribution

The theoretical analysis and experimental verification presented in the previous two subsections show that the deposit's carbon number distribution evolution is driven by diffusion of n-alkanes with different concentration driving forces and can be correlated to the "normalized ΔC distribution". The concentration difference of each component, $\Delta C_{i,}$ can be calculated by taking the difference between the equilibrium concentration of component *i* at the bulk temperature and at the wall temperature. Therefore the different bulk and wall temperatures at various operating conditions can potentially result in different "normalized ΔC distributions" and thus different carbon number distributions in the deposit. The effects of operating conditions on T_{bulk} and T_{wall} and thus on the deposit's carbon number distribution will now be analyzed

To study the effects of operating conditions on T_{wall} (at a fixed T_{bulk}) and the resulting deposit's carbon number distribution, one can vary Q_{oil} or $T_{coolant}$ while keeping $T_{o,inlet}$ fixed. Because of the limited axial length of the flow loop test section, the axial difference in T_{bulk} is negligible. Consequently, T_{bulk} is sufficiently close to the $T_{o,inlet}$ regardless of the oil flow rate Q_{oil} and/or the coolant temperature $T_{coolant}$.

Due to the aforementioned experimental uncertainties, it is practically not possible to achieve exact matches between the predicted and observed CND without applying tuning parameters. Introducing tuning parameters to the model can potentially reduce the reliability of model predictions. On the other hand, it is important to note that *without any tuning*, the trends in carbon number distribution with changing operating conditions can be predicted. These model predictions can then provide insights to the changes in the carbon number distribution when scaling up to from lab-scale testing to field operations. Consequently, we focused on comparing the predicted trends in carbon number distribution with the observed trends without tuning.

Figure 2-14 shows the comparison between the experimentally observed and predicted carbon number distribution in the deposit as T_{wall} changes due to changing Q_{oil}.

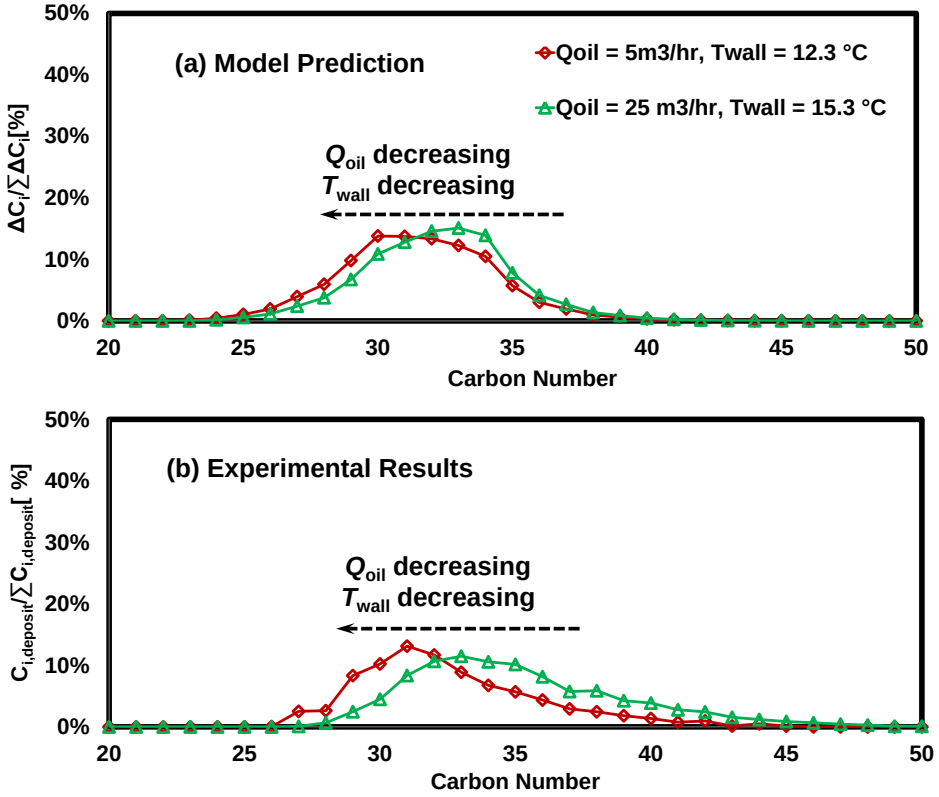

Figure 2-14: Effect of oil flow rate on the deposit carbon number distribution

It should be noted that as Q_{oil} decreases, the thermal mass entering the test section decreases. Therefore, the fluid is cooled down to a lower wall temperature, T_{wall}. As can be seen in Figure 2-14, both experimental results and model predictions show that as Q_{oil} and T_{wall} decreases, the peak in the deposit's carbon number distribution shifts towards small carbon numbers. This trend can be explained by the fact that n-C_iH_{2i+2} with different "*i*'s" do not precipitate at the same time as the wall temperature gradually goes from above WAT to below WAT[45–47]. When the wall temperature is lowered to just below WAT, the heaviest n-paraffin fractions precipitate first and thus create concentration gradients for diffusion of the heaviest fractions. As temperature is further lowered, n-paraffins with lower molecular weight start to precipitate. Consequently, as

T_{wall} decreases, n-paraffins with lower molecular weights precipitate resulting in a shift in the peak of the deposit carbon number distribution to smaller carbon numbers.

Similar to the case of decreasing Q_{oil}, as the $T_{coolant}$ decreases, T_{wall} decreases. Based on the same reasoning presented in the case of decreasing Q_{oil}, the deposit's carbon number distribution shifts to smaller carbon numbers as T_{wall} decreases as can be seen in Figure 2-15.

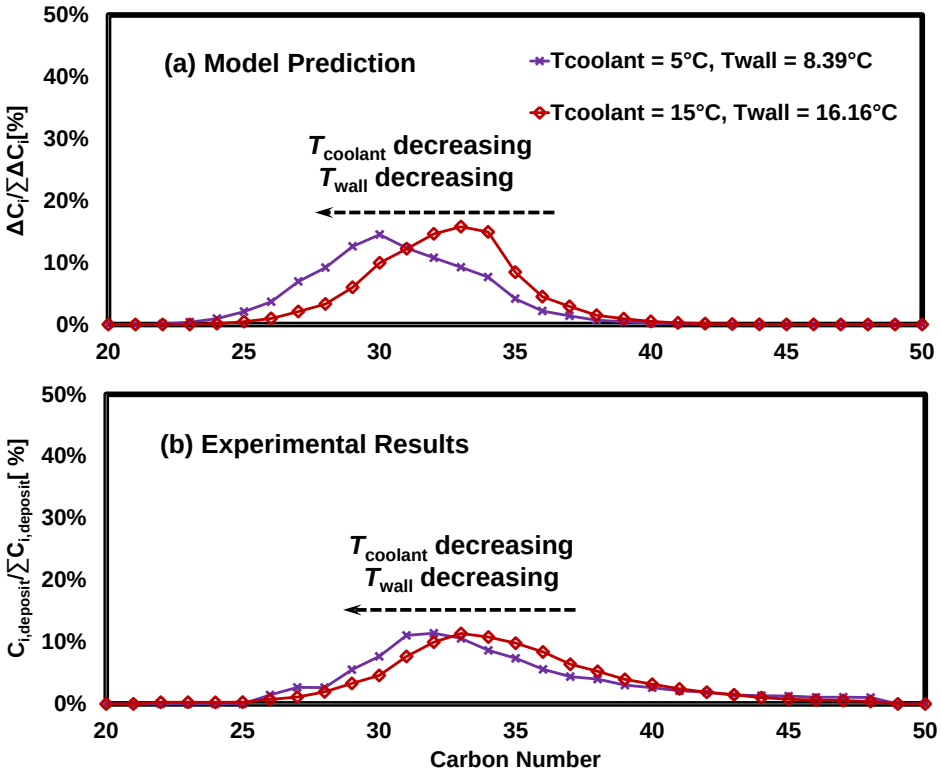

Figure 2-15: Effect of coolant temperature on the deposit carbon number distribution

2.E Conclusions

In this study, the Michigan Wax Predictor is combined with Coutinho's thermodynamic solubility model to identify the important parameters that affect the carbon number distribution in the deposit. It was found that the evolution of carbon number distribution is driven by the molecular diffusion of n-alkanes each with a different concentration driving force. A critical indicator, "the normalized concentration difference (ΔC) distribution", is defined and used to predict the deposit's carbon number distribution. It was predicted and experimentally verified by

flow-loop experiments, that the peak in deposit carbon number distribution shifts towards higher carbon numbers as either the oil flow rate or the coolant temperature increases. The predicted effects of operating conditions on deposit carbon number distribution are consistent with the observed trends in flow-loop experiments.

Chapter 3

Wax Deposition Experiments in Stratified Oil/Water Flows

3.A Introduction

3.A.1 Wax Deposition in Oil/Water Stratified Flow

Wax deposition from stratified oil/water flow is of great interest because most fields will produce a significant amount of water in their late life. Wax deposition experiments of oil/water stratified flow provide significant insights to the role of water in wax deposition characteristics. To this end, a state-of-the-art 2 inch flow loop was constructed at the Statoil Research Centre Porsgrunn where real waxy gas condensate from a North Sea field flows through a test section where a surrounding water annulus simulates the conditions sub-sea[39]. This flow-loop was used to study wax deposition from stratified oil/water flow. This study investigates how an increasing water cut[i] will influence wax deposition.

3.A.2 Different Steps for Wax Deposit Formation

Wax deposit can be formed by two steps: 1) diffusion of wax molecules from the bulk oil to the oil-deposit interface[21] and 2) gelation due to crystallization of wax molecules in the immediate vicinity of the pipe wall/deposit-fluid interface[5,48–56]. These two steps will be further discussed in detail.

[i] The term "water cut" describes the fraction of the water flow rate based on the total flow rate, $[Q_w/(Q_w + Q_o)]$, as an operating condition for the experiments.

3.A.2.a Diffusion of Wax Molecules towards the Oil/Deposit Interface[21]

Due to the heat loss of the oil to the surroundings, the temperature of the wall decreases and wax molecules start to precipitate at the wall to form an incipient layer of deposit. This precipitation reduces the concentration of wax at the oil-deposit interface and generates a radial diffusion of wax molecules from the bulk towards the oil-deposit interface. The wax molecules that diffuse to the oil-deposit interface can either precipitate at the interface to increase the thickness of the existing deposit or continue to diffuse into the deposit and contribute to the increase of wax fraction in the deposit. This diffusion of the wax molecules (the heavy components) into the deposit is accompanied by the counter-diffusion (the light components) of the oil molecules from the deposit back to the oil phase. Consequently, the deposit resulted from diffusion is enriched with heavy components. The trend was originally found by the study by Singh and Fogler, as shown in Figure 3-1.

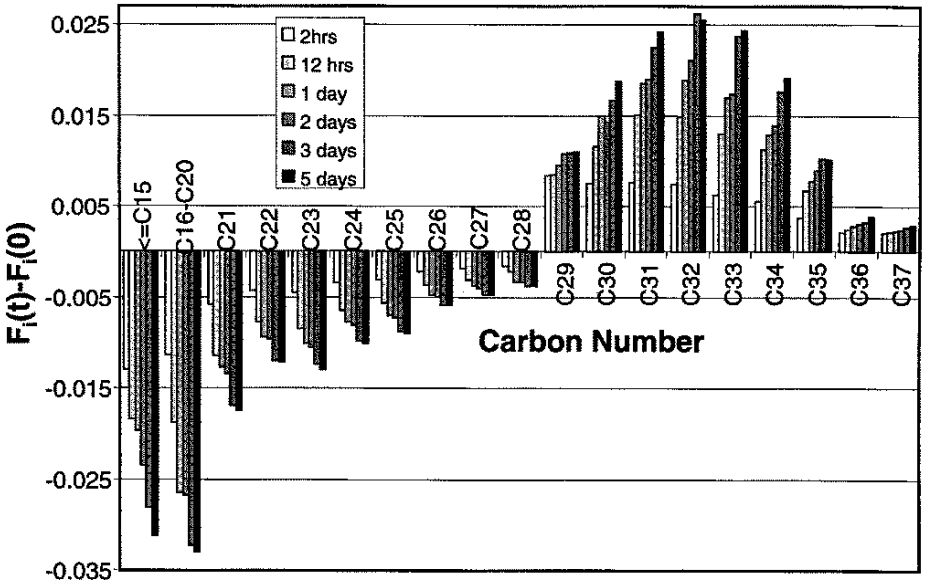

Figure 3-1: Change in carbon number distribution of gel deposits from flow loop with time[21]

3.A.2.b Gelation due to the crystallization of wax molecules at the immediate vicinity of the pipe wall/deposit-fluid interface

The crystallization of wax in oil has been studied since the 1920s[48]. The crystal structures observed from optical microscopy for the n-paraffins formed under static conditions are mainly platelet-like crystals with the diameters of 30-100 μm[5,48–50], although the existence of the branched and cyclic paraffins can significantly alter the structure and the crystallinity of the gel[51,52]. Kane et al. has used cryofixation with transmission electron microscopy (TEM) to reveal the micro-structure of the wax crystals[54], as shown in Figure 3-2.

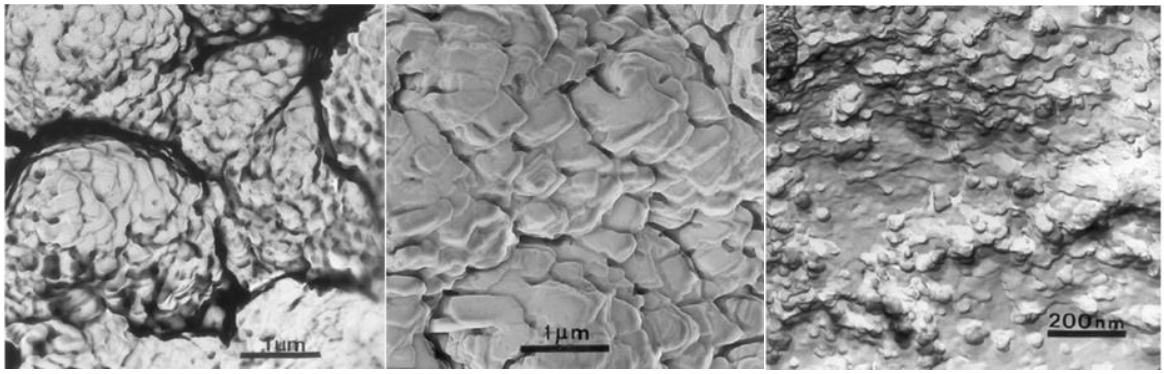

Figure 3-2: The micro-structure of the wax crystals observed by Kane, et al. (a) The "pine cone" structure of paraffin crystallized from in the crude oil. (b) The wax platelet lamellas observed on each "pine cone" structures (c) The disc-like sub-units that form the platelet lamellas

It was found that the wax crystals consist of smaller "pipe cone" blocks of around 3-5μm. Each block includes the platelet structure with stratified lamellas of area around 0.5-1μm[19]. A closer examination at the surface of the lamella reveals that the platelet consists of disc-like sub-units with diameters of 20-40 nm, which is considered to be the locations of the nucleation as the initial stage of wax crystallization. It is believed that the aggregation of these disc-like sub-units forms the platelet lamellas, while the overlapping of the platelet lamellas forms the "pine cone" structures. It is believe that the aggregation of the "pine cone" structures forms the platelet crystals that one frequently sees in an optical microscope[5,48–50].

As temperature further decrease from the cloud point, the degree of wax crystallization becomes sufficient to form a crystal network so that the entrapped oil is no longer able to flow. The mixture of the solid network and its entrained oil forms a gel. A number of studies on the structure of the network of wax crystals reveal that the growth of the wax crystals and the aggregation of the existing crystals occur simultaneously and that the network is connected by the attractive interactions between the wax crystals[57].

Although wax gelation has been frequently observed in quiescent conditions, recent studies have focused on the investigation on the wax gel formed under shear/flow conditions[5,53–55]. Venkatesan et al. has shown that a model wax-oil system was still able to gel when the shear stress is as high as 5 Pa (corresponding to a flow rate of 16,000 barrels per day in a 10-inch pipeline with an oil viscosity of 10 cp)[5]. The imposed shear rate is known to delay or suppress gelation, as reported by several rheological studies[53–56]. Kane et al. found that the shear stress can significantly reduce the gelation temperatures. This conclusion was found from the drastic increase of the apparent viscosity from their rheometer measurements as shown in Figure 3-3.

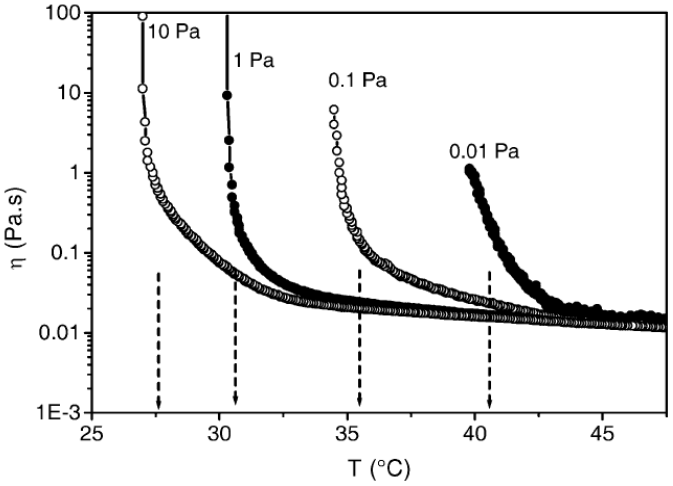

Figure 3-3: The impact of impose shear stress on gelation temperature, the gelation temperatures are highlighted with vertical dash lines where steep increase of the apparent viscosity is observed. The cooling rate is 0.5ºC/min

Deposit formation at the pipe wall/deposit-fluid interface is due to both the diffusion of wax molecules towards the pipe wall and the subsequent precipitation-gelation of the wax molecules. Depending on the shear stress condition, the amount of solid wax required to gel the deposit varies. The deposit formed under a higher shear stress is richer in solids. In this experimental investigation, it was observed that the deposit solid fraction characterized by an HTGC analysis responds sensitively to the water cut of the water-oil mixture. Such variation is explained by the effect of the water cut on the shear stress at the pipe wall/deposit-fluid interface.

3.B Experimental

3.B.1 Wax Deposition Flow Loop Apparatus

The state-of-the-art flow loop apparatus, also called a test rig, used for the experimental program is located in the Multiphase Flow-Loop Laboratory at Statoil's Research Centre Porsgrunn, Norway. It is used to study wax deposition mechanisms and to develop technologies for wax removal, wax prevention and wax thickness measurements. A schematic layout of the flow loop apparatus is shown in Figure 3-4.

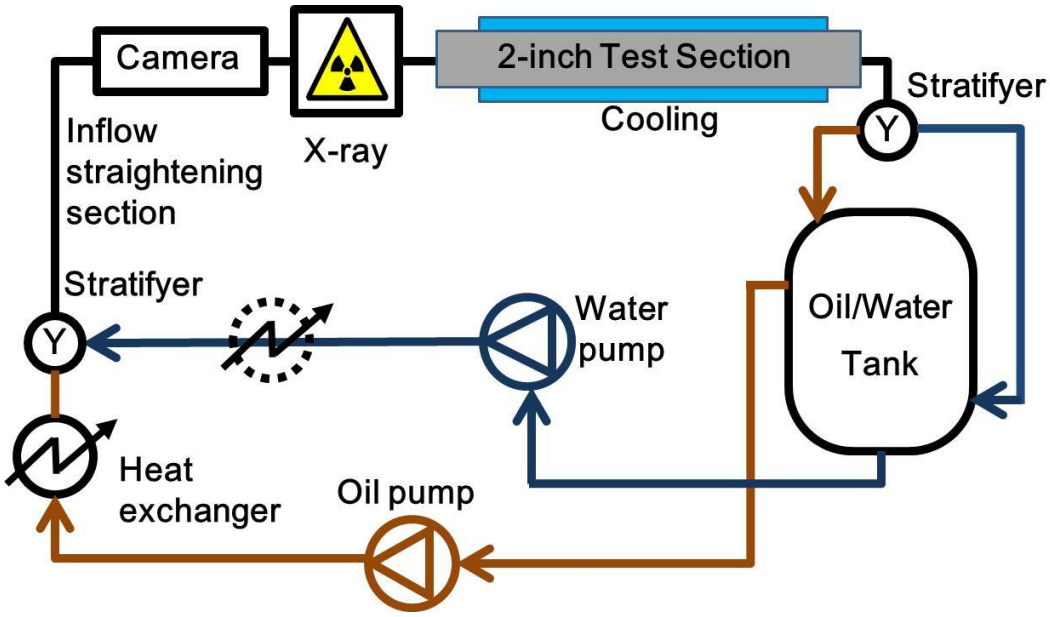

Figure 3-4: Overview of the wax deposition flow-loop

Before an experiment begins, the water and oil phases are pre-heated separately using an oil heat exchanger. Pre-heated oil and water are continuously circulated in the flow loop using the water and oil pumps. The oil phase is circulated through the heat exchanger during the experiment to keep the oil temperature constant. Because there is no separate heat exchanger to keep the water temperature constant, the water temperature drops slightly during the course of an experiment to a lower level. In a future modification, an additional heat exchanger for the water flow shall be implemented to avoid this drawback. The oil and water are unified in a Y-shaped stratifier which initializes stratified flow by avoiding excessive mixing of the phases. Oil and water then flow through a 17-m long pipe section to ensure fully developed flow before entering the test section. After the inflow section, the flow enters first a window section for visual observations of the flow structure followed by an X-ray tomograph for measuring the phase distribution. Next, the fluids enter the 2-inch test section where they are cooled by water that is circulating in an annulus surrounding the oil pipe, simulating the conditions subsea. The coolant water is provided from the communal network and is heat exchanged with steam to achieve the specified temperature before entering the test section annulus.

Two test sections (one 2-inch and one 3-inch inner diameter) are available to investigate the scale-up behavior of wax deposition. However for this study only the 2-inch section was used. Before the oil and water return to the main separator, the phases are pre-separated in a splitter. The two streams from the splitter enter the main separator in two different locations. Having both a pre-separation and a main separator improves the separation and hence lowers the total separation time. The large main separator with a maximum volume of 4.2 m^3 was designed to give a long retention time (up to 1 hour for the lowest flow rates) and to prevent wax depletion of

the circulating oil. Density measurements in front of each pump are used to monitor the separation quality of the phases. Some key data for the rig may be found in Table 3-1.

Table 3-1: Dimensions and the range of the operating conditions for the flow loop

Pipe material	Stainless steel	X2CRNi17-13-2	Parameter	Range
Oil pipe	Inner diameter	$52.5mm$	Oil temperature	$10°C - 60°C$
Oil pipe	Outer diameter	$60.6mm$	Water temperature	$10°C - 60°C$
Water annulus	Inner diameter	$131.3mm$	Oil flow rate	$2\frac{m^3}{h} - 20\frac{m^3}{h}$
Whole test section	Length	$5.31m$	Water flow rate	$2\frac{m^3}{h} - 20\frac{m^3}{h}$
Removable test section	Length	$0.63m$	Cooling flow rate	$3\frac{m^3}{h} - 16\frac{m^3}{h}$
Tank	Max. volume	$4200l$	Pressure	$1bar$

3.B.2 X-ray Tomography

An X-ray tomograph was used to measure the vertical phase distribution in the pipe before the flow enters the test section. The tomograph was built by Innospexion AS and consists of two pairs of X-ray sources and detectors, so that both the horizontal and the vertical phase distribution can be measured. The X-ray source is a water-cooled MB70 MCA 450 monoblock X-ray source with a maximum energy of 60 kVp. The detectors consist of CdTe CMOS detector arrays with 1500 pixel resolution.

The water volume fraction was calculated from X-ray measurements which were performed over 30 seconds to average over all transient flow phenomena. A sketch of the X-ray measurement is shown in Figure 3-5. The water volume fraction for a two-phase flow $\phi(x)$ as a function of the vertical position x is obtained by comparing the measured x-ray intensities for oil-water flow $I_{ow}(x)$ with the intensities for single-phase oil flow $I_o(x)$ and single-phase water flow $I_w(x)$, as shown in Equation (3-1)

$$\phi(x) = \frac{\ln \frac{I_{ow}(x)}{I_o(x)}}{\ln \frac{I_w(x)}{I_o(x)}} \tag{3-1}$$

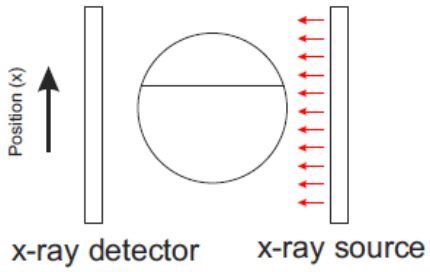

Figure 3-5: Layout of vertical X-ray measurement

The logarithm in Equation (3-1) stems from the attenuation of the X-ray beam passing through the fluid. A more in-depth description of the theory can be found in the research by Hoffmann and Johnson[58].

3.B.3 Gas Chromatography

Gas chromatography was used to measure the carbon number distributions of the deposit. The crude oil is measured using high temperature gas chromatograph (HTGC) Hewlett-Packard 6890A equipped with a CP-SimDist Ultimetal column (25m x 0.53mm x 0.09mm). The oven temperature was initiated at 40˚C and increased to 430˚C at a rate of 10˚C/min.

3.B.4 Fluid Characteristics

3.B.4.a Oil and Water Composition

The North Sea gas condensate utilized in this research is the same as in the previously reported single-phase study (4.7 wt% wax content, 30°C WAT, η = 3cP @ 20°C)[39]. The salt concentration of the water phase was chosen to be equal to the formation water from that field. The ion concentrations are listed in Table 3-2.

Table 3-2: Water composition of the aqueous phase used in water/oil stratified flow wax deposition experiments

Ion	Concentration [mg/l]
Sodium, Na	158
Calcium, Ca	16
Potassium, K	204
Chloride, Cl	735
Sulphate, SO4-	33

3.B.4.b Emulsion Breaker to Encourage Water/Oil Stratified Flow

Short-time deposition tests have shown that gravity separation in the tank is not sufficient to encourage oil/water phase separation to occur at lower temperatures and higher flow rates. It was therefore decided to add a commercially available emulsion breaker (DMO 86538, 500 ppm) to improve separation.

3.C Results and Discussions

3.C.1 Hydrodynamics

The most interesting parameter in two-phase oil/water flow is of course the water cut. To investigate its influence and to define the matrix of most relevant wax deposition experiments, a pre-study was performed where the influence of the water cut on the flow regime was investigated.

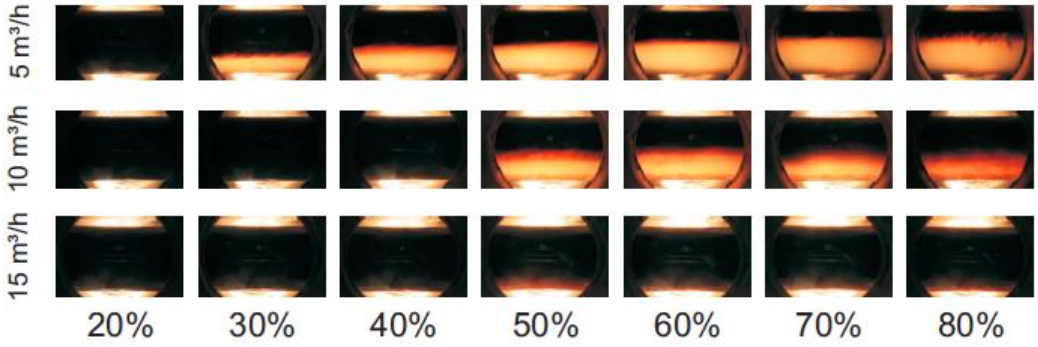

Figure 3-6: Side view camera picture of the oil/water two phase flow pattern at different total flow rates and water cuts

Experiments were carried out for three different total volumetric flow rates. These two-phase flow rates were $Q_{total} = Q_o + Q_w = 5m^3/h$, $Q_{total} = 10\ m^3/h$, and $Q_{total} = 15\ m^3/h$, corresponding to mixture velocities of $V_{total} = 0.64m/s$, $V_{total} = 1.28m/s$, and $V_{total} = 1.92m/s$. Experiments were carried out with water cuts ranging from 20% to 80%. Figure 3-6 shows the camera pictures for these flow regimes. It is observed that completely stratified flows occur for the cases of water cut from 30% to 70% when the total flow rate is $5m^3/h$, while completely stratified flows occur in a smaller range of water cut (50%-70%) as the total flow rate increases to $10m^3/h$. This observation indicates that the degree of dispersion increases with increasing total flow rate. Visual impression however can be misleading because relatively small amounts of dispersed oil in water make the mixture appear dark. It is therefore important to measure the water volume fraction using the X-ray instrument. Figure 3-7 shows the water fraction distribution for the three flow rates.

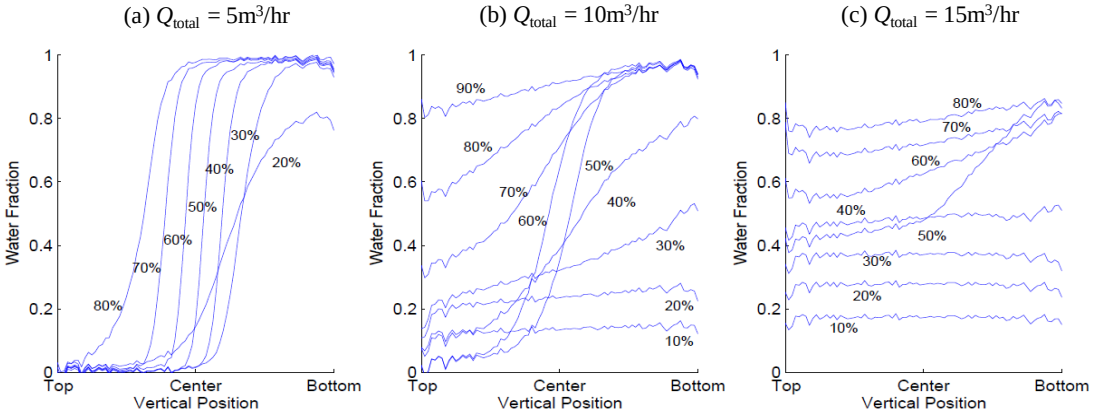

Figure 3-7: Water fraction at different water cuts measured by X-ray tomography

Correspondingly to the reflex camera pictures, the lowest flow rate, 5 m^3/h, gave fine stratified flow regimes except water cuts = 20% and 80%, where some dispersion was observed. For the flow rate of $10m^3/h$ there is a clear transition from fully dispersed flow at 10% and 20% water cut to stratified flow (around 40% to 70% water cut) and further on to water continuous flow. The highest flow rate of 15 m^3/h shows almost always fully dispersed flow with the exception of

50% water cut which appears to be stratified flow of a water continuous and an oil continuous phase (albeit with a high amount of dispersion in each of the phases).

Because the scope of this study focuses on stratified flow it was decided to perform one series of wax deposition experiments with varying water cut at a total flow rate of $5m^3/h$ and one series at a total flow rate of $10m^3/h$. In the later study we hope to extend this investigation also to higher flow rates and dispersed flow. Dispersed phase flow will however require modifications of the rig since it proved to be impossible to maintain a sufficiently high separation quality for the duration of a whole wax deposition experiment (typically several days). This drawback will lead to the build-up of a significant amount of emulsion as the experiments are running at highest flow rates.

3.C.2 Wax Deposition Experiments

Two lists of deposition experiments are shown in Table 3-3 and Table 3-4 for different total flow rates. It can be seen that the inlet temperatures for the oil and the coolant are not the same, which is due to the limited number of heat-exchangers available in the flow-loop.

Table 3-3 List of operating conditions for the deposition experiments with different water cuts for the total flow rate of $5m^3/h$

Total Flow Rate (m^3/h)	5.0					
Water Cut (%)	0.0[ii]	25.0	50.0	65.0	75.0	80.0
Oil Flow Rate(m^3/h)	5.0	3.7	2.5	1.7	1.2	1.0
Water Flow Rate (m^3/h)	0.0	1.3	2.5	3.3	3.8	4.0
Duration (days)	2.0	2.6	2.7	2.7	2.7	2.7
Oil Inlet Temperature(°C)	24.0	24.0	24.0	24.7	25.0	24.4
Water Inlet Temperature(°C)	-	23.1	21.6	22.0	21.3	20.5
Coolant Temperature (°C)	15.0					

[ii] The GC measurement is not available for these experiments.

Table 3-4 List of operating conditions for the deposition experiments with different water cuts for the total flow rate of 10m^3/h

Total Flow Rate (m^3/h)	10.0				
Water Cut (%)	0.0[ii]	10.0	50.0	75.0	85.0
Oil Flow Rate(m^3/h)	10.0	9.0	5.0	2.5	1.5
Water Flow Rate (m^3/h)	0.0	1.0	5.0	7.5	8.5
Duration (days)	1.8	2.8	1.8	1.7	1.8
Oil Inlet Temperature(^{o}C)	25.0	25.0	25.0	24.9	24.8
Water Inlet Temperature(^{o}C)	-	24.6	23.5	22.9	22.5
Coolant Temperature (^{o}C)	15.0				

3.C.2.a Effect of Water Cut on the Pipe Wall Area Covered by the Deposit

Figure 3-8 shows the cross-sectional view of the coverage of wax deposit on the pipe wall circumference.

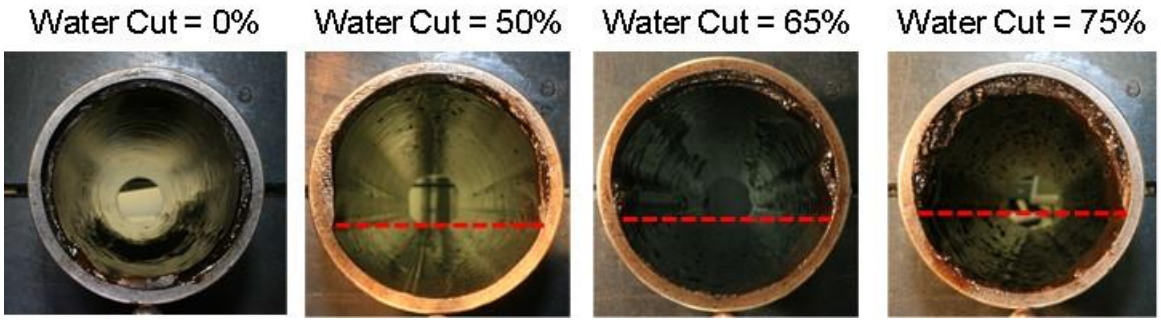

Figure 3-8: Cross sectional view of the coverage of wax deposit on the pipe wall circumference for wax deposition experiments with a total flow rate, Q_{total}, of 5 m^3/hr and water cut varying from 0% to 75%

As can be seen from Figure 3-8, in water/oil stratified flow regime, wax only deposits on the top part of the pipe circumference that is wetted by oil. On the other hand, wax does not deposit on the bottom part of the pipe cross section that is wetted by water. As a result, the existence of a water phase reduces the pipe wall area available for wax deposition.

3.C.2.b Deposition Characteristics under High Flow Rate, Q_{total} = 10 m^3/hr (Equivalently, High Shear Stress)

The amount of wax deposit accumulated on the pipe wall is a critical variable of interest during wax deposition experiments. Since the pipe wall surface area covered by the wax deposit varies with changing water cut, the amount of wax attached to the pipe wall needs to be normalized with respect to the surface area covered by the deposit. The specific deposit mass on a per-area basis can then be compared from run to run with different water cuts to understand the role of the water phase on wax deposit mass. Figure 3-9 compares the wax mass per area obtained from different wax deposition runs performed at a fixed total flow rate of 10 m^3/hr and varying water cuts.

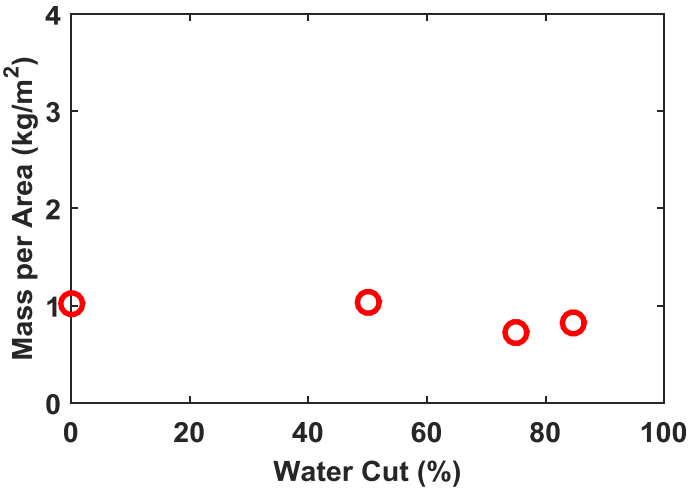

Figure 3-9: Wax deposit mass per area observed in wax deposition experiments performed at a fixed total flow rate of 10 m^3/hr and various water cuts

As can be seen from Figure 3-9, the deposit mass per area remains at a virtually constant level, suggesting that the water phase has minimal impact on the heat and mass transfer characteristics on wax deposition in this set of experiments while merely reduces the pipe surface area available for wax deposition.

3.C.2.c Deposition Characteristics under Low Flow Rate, Q_{total} = 5 m^3/hr (Equivalently, Low Shear Stress)

Comparison among the wax mass per area generated from wax deposition experiments with various water cuts were also performed for the runs conducted at a fixed total flow rate of 5 m^3/hr, shown in Figure 3-10.

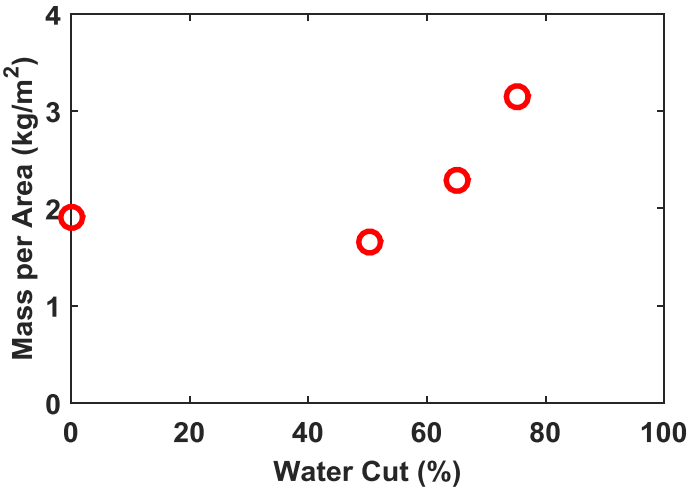

Figure 3-10: Wax deposit mass per area observed in wax deposition experiments performed at a fixed total flow rate of 5 m^3/hr and various water cuts

As can be seen from Figure 3-10, the wax deposit mass per area increases as the water cut increases, suggesting that the wax deposition risk becomes more and more severe as the water cut increases. In order to further understand this trend, the compositions of the wax deposits obtained under various water cuts were analyzed with HTGC, shown in Figure 3-11.

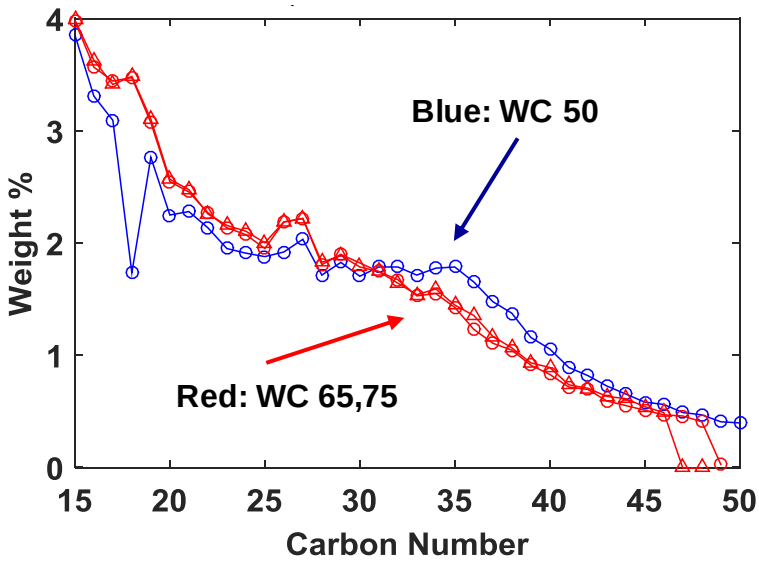

Figure 3-11: Carbon number distributions of the wax deposits generated under a fixed total flow rate of 5m^3/hr and various water cuts

As can be seen from Figure 3-11, the deposits from the experiments with the water cut of 65% and 75% have smaller fractions of the heavy components. Their carbon number distributions are more similar to that of the oil compared to the deposits from the experiments with water cut of 50%, which indicates that the deposit formed at a water cut of 50% contains more solid wax than the deposits formed under water cuts of 65% and 75%. A possible explanation for this difference in solid content of the deposit can be found from the difference in the shear stress in the oil phase. Because the oil and the water used in this study are mainly Newtonian fluids, the shear stress is directly proportional to the viscosity of the fluid. The viscosity of the oil is approximately twice of that of the water for the temperature within the operating range in this study. Therefore the increasing amount of water in the water-oil mixture can help to reduce the shear stress of the oil phase, thereby leading to a lower solid content of the wax deposit.

3.D Conclusions

In this research, wax deposition experiments in oil/water two-phase stratified flow were carried out in order to investigate the effect of the presence of water on wax deposition. First, a flow

map study was performed to identify the flow regimes for oil/water stratified flow. The X-ray measurement showed that completely stratified flow was achieved in the cases of water cut ranging from 30% to 60% at low total flow rate (Q = 5m^3/h). As the total flow rate further increases, the formation of the oil/water droplets reduces the degree of stratification and even prevents stratified flow to occur.

Wax deposition experiments were carried out at various water cuts for the total flow rate of 5m^3/h and 10m^3/h. The complex effects of the water phase on wax deposition were revealed. Firstly the water phase reduces the pipe wall surface area available for wax deposition. At a total flow rate of 10 m^3/hr, the wax deposition characteristics is not sensitive to the water volume fraction, indicating negligible effects of the water phase on the heat and mass transfer characteristics. At a total flow rate of 5 m^3/hr, the water deposition severity increases as the water content increases. As the water cut increases, the shear stress at the pipe wall decreases, leading to a lower solid content of the wax deposit and thereby a thicker deposit. The effect of the wall shear stress on wax deposit thickness will be further discussed and modeled from first principles of rheology in Chapter 7.

Chapter 4

A Fundamental Investigation of Wax Diffusion Characteristics in Water-in-Oil Emulsion

4.A Introduction

Wax deposition in subsea oil pipelines is one of the major challenges in upstream engineering and flow assurance. The build-up of a wax deposit on the inner surface of subsea pipelines reduces the cross-sectional area available for oil transportation and leads to a decrease in oil production. In extreme cases, a particular section of the pipeline may become completely plugged by wax deposits and cannot be restarted[11]. In order to prevent the pipeline from plugging completely, remediation operations such as pigging are conducted on a regular basis to remove the wax deposit before it becomes too thick and too hard and impossible to remove. However frequent pigging to remove the deposits may not be always economically beneficial because it generates not only the costs from the pigging operation itself but also production down time. Determination of a suitable pigging frequency thus becomes a critical element in the remediation of wax deposition[59,60]. The optimum pigging frequency is usually determined based on model predictions in combination with field experiences.

In the past decade, multiple wax deposition models have been developed for the prediction of wax deposition rate and thickness that can be used to provide recommendations on pigging frequency[21,24–27,29,33,34,61]. Most existing wax deposition models predict wax deposition rates in

single phase oil flow, while with the exception of stratified flow[35], wax deposition in two phase oil/water flows has not been modeled using first principles of transport phenomena.

In the early stages of a well's production, the water content of the production stream can be 10 % or lower and the effects of water on wax deposition may often be neglected[62]. However, the water content of the production stream can increase significantly as production continues. In the later stages of oil production, water is injected into the well to force out oil, further increasing the water content in the production stream. To predict wax buildup on subsea pipelines in water/oil two phase flow requires extending a fundamental single phase wax deposition model, the Michigan Wax Predictor (MWP)[26–28,61], to two phase flow and this extension is a non-trivial project.

Two phase flow of water and oil can generate various flow patterns[63]. Figure 4-1 summarizes the possible flow patterns of water/oil two phase flows under various water/oil flow rate conditions.

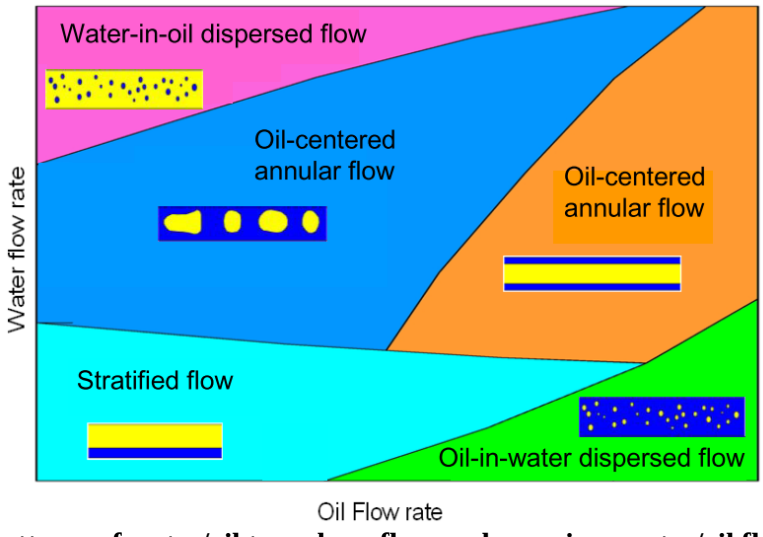

Figure 4-1: Flow patterns of water/oil two phase flow under various water/oil flow rate conditions[63]

Having different flow patterns in the production stream complicates the wax deposition modeling. Based on a series of deposition experiments performed using a state-of-art flow loop

apparatus, Hoffmann et al., confirmed that in stratified flow where the top part of the pipe is in contact with the lower density oil, wax deposit forms on the top of the pipe cross section[64]. Huang et al. developed a fundamental wax deposition model to investigate the impact of water on the heat/mass transfer characteristics and to model wax deposition in water/oil stratified flow[35].

It should be noted that the water/oil stratified flow pattern can only exist at low water and oil flow rates where virtually no mixing of oil and water occurs. In actual field productions, the flow is usually in the turbulent flow regime which promotes the mixing of oil and water to form water-in-oil dispersions. Additionally, crude oils are usually rich in natural surfactants, which stabilize water-in-oil dispersion[65–68]. Because of the common occurrence of water-in-oil dispersed flow in the field, there is a growing interest to carry out a fundamental study on wax deposition in water-in-oil dispersed flow. On the experimental side, Bruno et al. and Panacharoensawad et al. performed flow loop wax deposition studies to provide evidence of wax deposit formation in water-in-oil dispersed flow and also to correlate the deposition rates to operating conditions[69,70]. Despite these two experimental studies, no one has yet developed a fundamental wax deposition model to predict the wax deposition rate in water-in-oil dispersed flow. The only existing water-in-oil dispersed flow wax deposition model is based on an empirical pseudo-single phase approach that was developed by Bruno et al. to model their experimental results[69]. In this pseudo-single phase model, the physical properties of the water-in-oil dispersion, such as viscosity, density, heat capacity and thermal conductivity are calculated by simply averaging the corresponding water and oil physical properties based on mixing rules. The averaged physical properties are then used in the single phase governing equations to model wax deposition in water-in-oil two phase flows. While this approach might be a first

approximation to characterize heat transfer for oil-water dispersed flow, it can have significant limitations when describing the mass transfer characteristics of wax deposition and result in incorrect estimates of the severity of wax deposition and lead to unreliable field predictions. The complexity imposed by dispersed water droplets on the mass transfer characteristics of wax will now be discussed.

It has been widely accepted that molecular diffusion is the dominating mass transfer mechanism of wax deposition[21,24–26,33,34,61]. In the molecular diffusion mechanism, wax molecules precipitate at the pipe wall when the surface temperature is below the wax appearance temperature. The precipitation of wax generates a concentration gradient in the boundary layer, causing more wax molecules to diffuse towards the wall to form a deposit. In single phase flow regime, wax diffuses along the concentration gradient through a straight diffusion pathway as shown in Figure 4-2 (a).

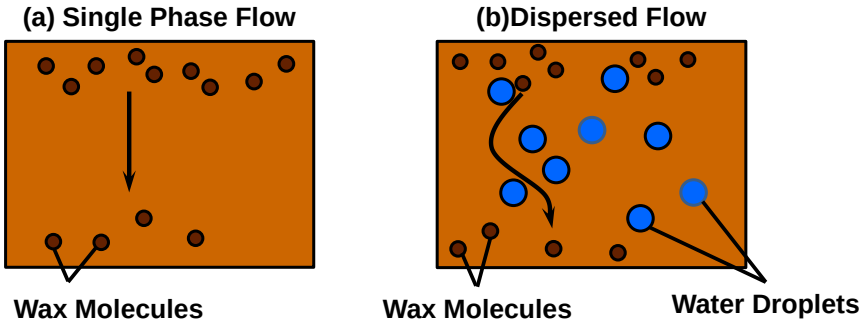

Figure 4-2: Comparison between diffusion of wax in (a) single phase flow and (b) water-in-oil dispersed phase flow

Contrary to wax diffusion in single phase flow, wax diffusion in water-in-oil dispersions is partially blocked because the wax molecules are insoluble in water and they cannot diffuse through the water droplets. Therefore, in order to reach the pipe wall to form deposit, wax molecules must diffuse around water droplets, resulting in more tortuous diffusion pathways as shown in Figure 4-2 (b). Intuitively, this effect of water droplets partially blocking wax

diffusion pathway results in a reduction in the diffusivity of wax and leads to a reduction in the deposition rate.

However, it is experimentally difficult to 1) verify the inhibitive effect of water droplets on wax diffusion and 2) quantify the reduction of diffusivity caused by the dispersed water droplets. Therefore, no existing wax deposition models address the effect of dispersed water on wax diffusion from a fundamental perspective of view. Empirical approaches have been proposed to incorporate the effect of water droplets on wax diffusion in wax deposition modeling[69,71]. However, not only is the correctness of these empirical approaches questionable[72], inappropriate attempts to include this effect of diffusivity reduction in wax deposition modeling can also lead to over-optimistic predictions for the wax deposition rate. These questionable predictions are potentially dangerous during the design of wax remediation operations. Some of these inappropriate applications will be analyzed in this manuscript. This manuscript presents the first fundamental investigation on the wax diffusion characteristics in water-in-oil dispersion.

4.B Pulse Field Gradient NMR Characterization of Molecular Diffusion

The effect of dispersed water droplets on molecular diffusion can be probed by measuring the effective diffusivity of a particular oil-soluble and water insoluble molecule (a "tracer"). Figure 4-3 shows the hypothetical path of (a) a tracer diffusing in a single-phase oil along with (b) a hypothetical pathway of a tracer diffusing in a water-in-oil dispersion.

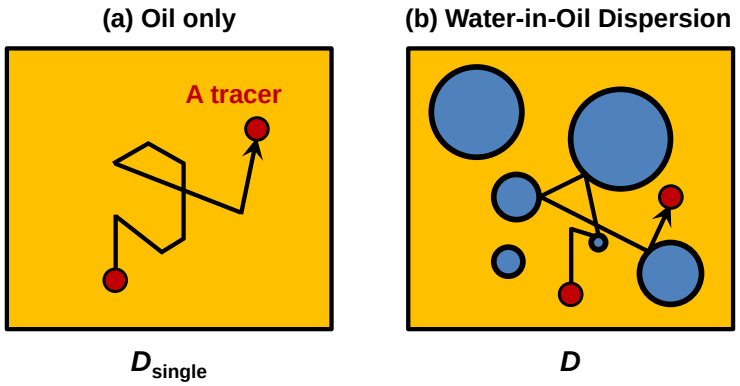

Figure 4-3: Comparison of (a) the scenario of a tracer diffusion in single-phase oil and (b) the scenario of a tracer diffusing in water-in-oil dispersion

If the dispersed water droplets partially block the diffusion path of the tracer, one expects a decrease in the effective diffusivity of the tracer in the water-in-oil dispersion, D, when compared to its original diffusivity in the single-phase oil, D_{single}. In this study, both of the diffusivities, D and D_{single} were measured using NMR diffusometry techniques[73] along with various types of tracers to investigate the effect of water droplets on the molecular diffusion through the oil phase of the water-in-oil dispersion.

In a NMR diffusion experiment, the magnetization of the ^{1}H nuclear spin is manipulated by a Stejskal-Tanner pulse sequence composed of two radio frequency pulses and two pulse field gradients[74]. The magnetization is first excited by a 90° pulse. After a time period with a typical length of 50-300 ms, a 180° pulse is applied. The second pulse causes the refocusing of the magnetization and gives rise to an echo signal. Moreover, at the beginning of each radio frequency pulse, one pulse field gradients with length δ and magnitude G are applied to probe the molecular motion of the tracer. Due to the molecular motion of a tracer, its NMR signal attenuates after a Stejskal-Tanner pulse sequence[74]. The extent of attenuation is related to the net displacement of the tracer during the time period between the 90° and the 180° pulses, which in turn depends on the diffusivity of the tracer according to Equation (4-1).

$$\ln \frac{I}{I_0} = -\gamma^2 \delta^2 G^2 D(\Delta - \frac{\delta}{3}) \quad (4\text{-}1)$$

where I/I_0 characterizes the signal attenuation. γ is the gyromagnetic ratio of the ^{1}H nucleus. δ is the length of the pulse field gradient. G is the magnitude of the pulse field gradient. Δ, also called diffusion time, is the time available for molecular diffusion. D is the diffusivity of the tracer.

The experimentally measured attenuation of the NMR signal can be used to determine the diffusivity of the tracer according to Equation (4-1). A diffusion gradient length δ of 4 ms and a diffusion time Δ of 50-300 ms were used in this study to obtain a sufficient extent of signal attenuation based on which the tracer diffusivity can be calculated to a high level of confidence. A detailed description of the governing principles of experimental measurements of molecular diffusivity using NMR techniques can be found in "*High-Resolution NMR Techniques in Organic Chemistry*" by Claridge[75].

It should be noted that NMR diffusometry on one water-in-oil dispersion sample requires ~10 – 30 minutes to perform. The microstructure of the water-in-oil dispersions might not remain unchanged during the course of NMR diffusometry owing to particle loss mechanisms such as Brownian flocculation, sedimentation flocculation and creaming[76]. Without proper methods to retard these particle loss mechanisms, the microstructure of a water-in-oil dispersion can change rapidly, making it impossible to obtain reliable evaluations of the effect of water droplets on the diffusion characteristics in the continuous phase. In order to avoid rapid change in the dispersion microstructure, model water-in-oil emulsion systems were prepared to represent water-in-oil dispersion and the NMR diffusometry was performed based on the model water-in-oil emulsions.

4.C Experimental

4.C.1 Preparation of Model Water-in-Oil Emulsions

Water-in-oil emulsions with varying water cut (WC) from 10% to 70% were prepared in this investigation. Preparation of the model emulsions followed the procedures provided by Delgado-Linares et al., where similar model emulsions were used in the investigation of hydrate formation[77]. Crystal Plus 70T mineral oil purchased from STE Oil Company was used as the continuous oil phase. Detailed compositional and rheometric information of this particular mineral oil can be found in ref.77 by Delgado-Linares et al. Distilled (DI) water was used as the dispersed water phase. The emulsifying agent was composed of two chemicals: sorbitan monooleate (known as Span 80) and bis(2-ethylhexyl) sulfosuccinate sodium salt (known as AOT). Both chemicals were purchased from Fisher Scientific. In order to prepare the oil continuous phase containing surfactant, 5wt.% of the surfactant mixture (Span 80:AOT = 9:1 wt./wt.) with respect to the total weight of the emulsion was first dissolved in the oil phase. Flocculation of water droplets was observed in the emulsions prepared with Span 80 as the only surfactant. Addition of AOT as a second surfactant prevents flocculation. It is believed that the ionic characteristics of AOT introduces electrostatic repulsion between droplets and prevents flocculation. It should be noted that mineral oil does not contain asphaltenes which stabilize water-in-crude oil emulsions[65–68]. Therefore, an appreciable amount of the surfactant was used for the preparation of model emulsions. Heating of the oil continuous phase was applied to facilitate the dissolution of the surfactant mixture. DI water with volume fraction ranging from 10% to 70% (WC = 10% - 70%) was then added to the surfactant-containing oil phase under constant agitation by a Scilogex D160 homogenizer at 8000 rpm to form water-in-oil emulsion.

3mL of the emulsions were prepared in each batch and the prepared emulsions were used for microscopic, rheometric and diffusometry experiments.

It should be noted that in the preparation of water-in-oil emulsion, the water phase should be added slowly to prevent undesired phase inversion and the resulting formation of an oil-in-water emulsion. In this study, water was added drop wise over a period of 4 minutes. After water addition, the water-in-oil mixture was further agitated using the same homogenizer for 2 minutes.

4.C.2 Characterization of Emulsion Microstructure

The emulsion microstructure was characterized by microscopy experiments. One liquid drop of the emulsion was placed on a 25 mm × 25 mm glass slide. An 18 mm × 18 mm cover slide was then placed on the top of the liquid drop to deform it into a liquid film. The microstructure of the emulsion liquid film was inspected by a Nikon Eclipse E600 microscope with a 50× objective lens and a 10× eyepiece. A Sony AVC-D7 CCD camera was used to take photos of the emulsion microstructure.

Based on experimental experiences, the micrographs of un-diluted WC30-70 emulsion samples are hazy, as shown in Figure 4-4

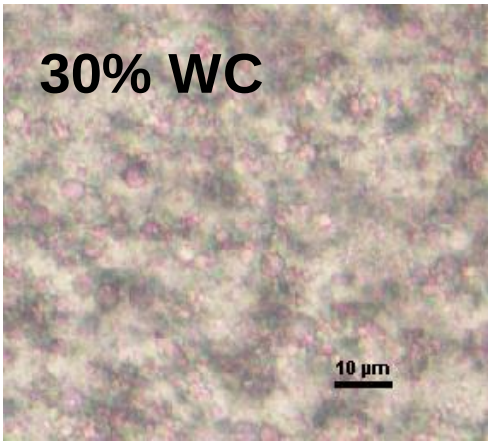

Figure 4-4: A hazy micrograph of the 30% water cut model emulsion

In a hazy micrograph, the boundaries of the water droplets overlap, making it difficult to determine the mean droplet diameter and the droplet size distribution. This haziness is due to the high number density of the droplets in these un-diluted emulsions. Calculations show that one drop of the emulsion (0.05mL) can contain millions of dispersed water droplets. Layers of droplets can thus overlay on top of each other, causing the haziness of the micrograph. In order to obtain a micrograph suitable for the determination of mean droplet diameter and droplet size distribution, the original emulsion samples had to be diluted with mineral oil according to the procedures recommended by Opedal et al.[78]. Figure 4-5 shows a sample micrograph of the diluted emulsion in comparison with the micrograph of an undiluted emulsion.

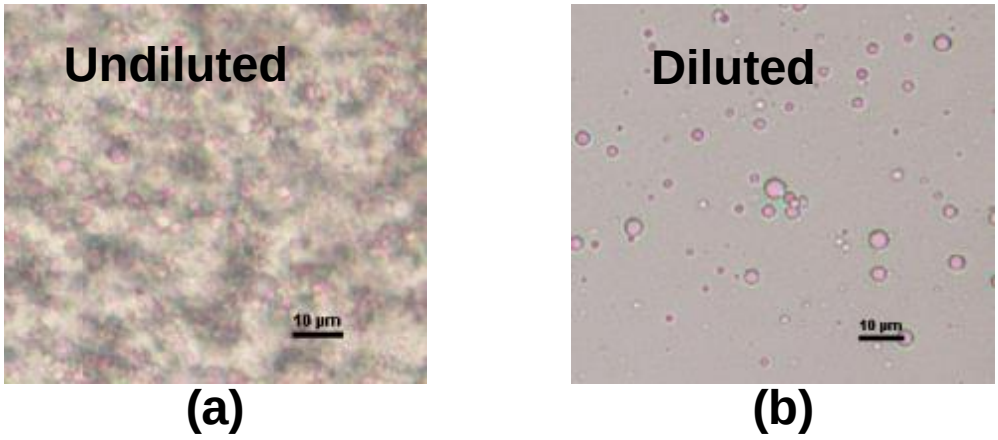

Figure 4-5: Comparison between the micrograph of (a) an undiluted 30% WC model emulsion with the micrograph of (b) the diluted 30% WC model emulsion

As can be seen from Figure 4-5, after dilution of the emulsion, the dispersed droplets can be clearly identified. Based on the micrographs of diluted emulsions, the mean droplet diameter and the droplet size distribution were determined using image processing software called ImageJ.

4.C.3 Characterization of Diffusion Using Pulse Field Gradient – Nuclear Magnetic Resonance Spectroscopy (PFG-NMR)

Two types of NMR experiments were performed: regular $^{1}H/^{19}F$-NMR spectroscopy and $^{1}H/^{19}F$-NMR diffusometry. Based on regular $^{1}H/^{19}F$-NMR spectroscopy, one identifies an NMR signal

from the tracer molecule. In the following diffusometry experiments, one gradually increases the magnitude of the pulse field gradient and tracks the corresponding attenuation of the tracer NMR signal to measure its molecular diffusivity. Both types of NMR experiments were performed on a 400 MHz Varian MR400 NMR Spectrometer at the University of Michigan NMR facility.

In the acquisition of ^{1}H-NMR spectrum, NMR-grade trimethylsilane (TMS, purity > 99.0%) purchased from TCI America was added to the NMR sample and the proton signal from TMS was used as the standard for the 0-ppm chemical shift.

Before NMR diffusometry experiments to measure tracer diffusivity, the NMR pulse field gradient was calibrated based on the known self-diffusion coefficients of H_2O, HDO and n-dodecane.

4.D Results and Discussions

4.D.1 The Macro- and Microscopic Stability of the Model Emulsion

Before the characterization of tracer diffusivity, it is important to evaluate the stability of the model emulsions and confirm that they have undergone negligible structural change during the time period of diffusometry experiments. Such stability needs to be evaluated on both the macro- and microscopic scales.

The macroscopic stability of the emulsions was evaluated by visual detection for signs of bulk phase separation. Figure 4-6 shows the macroscopic appearance of the emulsions after standing for 48 hours (t = 48hr) in comparison with that right after the samples were prepared (t = 0 hr).

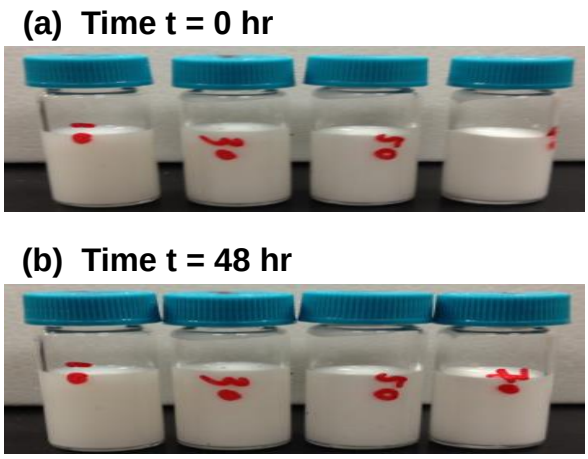

Figure 4-6: Comparison between the macroscopic appearances of the model emulsions (10%, 30%, 50%, 70% WC) (a) Right after they were prepared (*t* = 0hr) and (b)after standing for 48 hours (*t* = 48 hrs)

As can be seen from Figure 4-6, there was no sign of bulk phase separation after 48 hours. However, unchanged macroscopic appearances do not necessarily guarantee unchanged emulsion microstructures. Consequently, microscopic characterizations were also performed in which the mean droplet diameter and size distribution of the emulsions were measured after 48 hours and compared to those of the initial samples right after emulsions preparation. Figure 4-7 shows the comparison between the mean droplet diameters of the model emulsions right after emulsion preparation and after 48 hours.

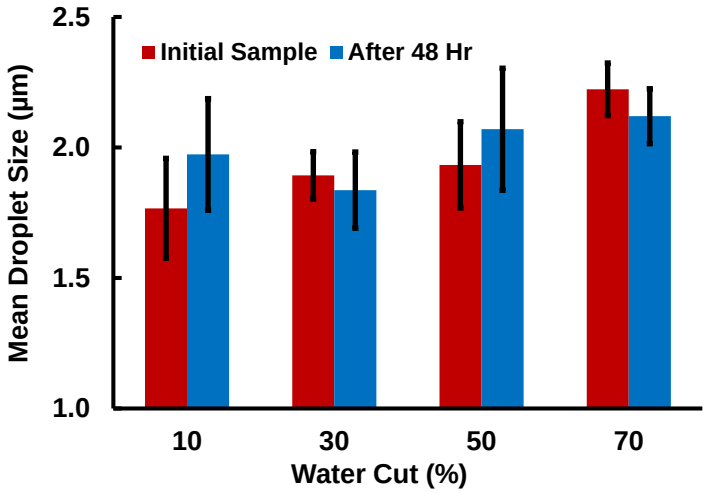

Figure 4-7: Comparisons between the mean droplet diameter of the model emulsions (10%, 30%, 50%, 70% WC) right after emulsion preparation and after standing for 48 hours

It can be seen that no statistical change in the mean droplet diameter was observed after the model emulsions were let stand for 48 hours. During a period of 48 hours, the mean droplet diameters of all model emulsions remain at a virtually constant level of ~2μm. Moreover, no significant variation in the droplet size distribution was observed over a time period of 48 hours as shown in Figure 4-8.

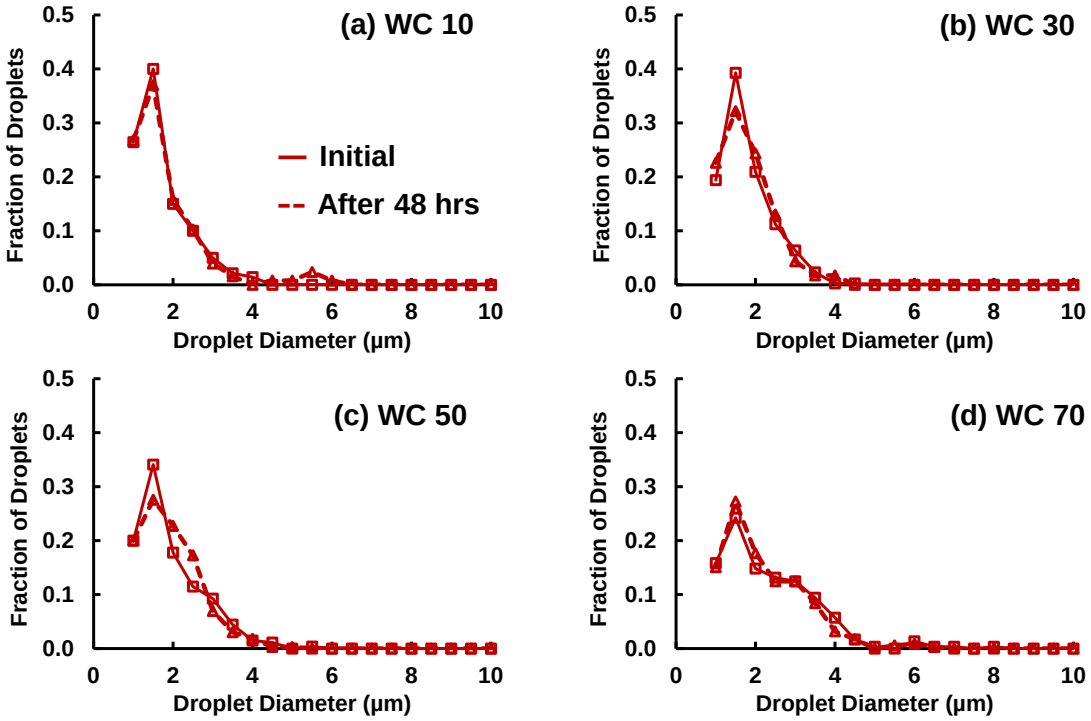

Figure 4-8: Comparison of the droplet size distribution of model emulsions 10%, 30%, 50% and 70% WC right after emulsion preparation and after standing for 48 hours

These results confirm that the emulsions undergo negligible structural change over a period of 48 hours during which diffusivity of tracer molecules can be characterized using NMR techniques.

4.D.2 Observing the Reduction in the Molecular Diffusivity in Water-in-Oil Emulsions

In this phase of the research, various tracers were used to study the molecular diffusivity in water-in-oil emulsions. NMR diffusometry measures the diffusivity of a molecule by tracking the attenuation of its proton NMR signal with varying magnitudes of the NMR pulse field gradient. It should be noted that besides the tracer molecule, both mineral oil and DI water as the

two major constituents of the model emulsions contain protons. ^{1}HNMR signals associated with the protons in mineral oil and DI water can also be detected by the NMR spectrometer. Consequently, in order to differentiate the NMR signal of the tracer to measure its diffusivity, one has to select a tracer whose ^{1}HNMR signal does not overlap with the mineral oil and DI water ^{1}HNMR signals. In our first investigation, toluene was chosen as a tracer and its NMR signal was identified by comparing the NMR spectrum of the emulsion containing tracer with the spectrum of the mineral oil and DI water, as shown in Figure 4-9.

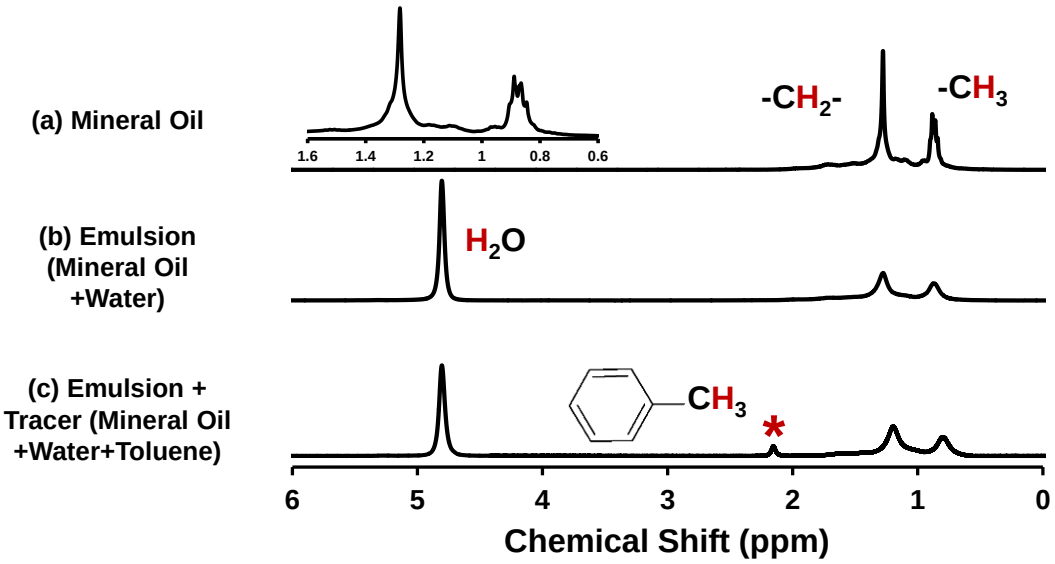

Figure 4-9: Comparison between the NMR spectrum of (a) mineral Oil, (b) model emulsion and (c) model emulsion containing toluene as a tracer

Two major signals: 0.89 ppm and 1.28 ppm are displayed on the mineral oil NMR spectrum, Figure 4-9(a). These two signals correspond to the protons in the methyl group ($-CH_3$) and the methylene group ($-CH_2-$) respectively. Comparing the mineral oil ^{1}HNMR spectrum, Figure 4-9 (a), with the emulsion NMR spectrum, Figure 4-9 (b), one identifies the signal associated with water: 4.81 ppm. In addition to the NMR signals associated with mineral oil and water, the signal associated with the methyl group in toluene (2.17 ppm) is displayed on the spectrum of the emulsions containing toluene, Figure 4-9(c). Therefore, because the toluene methyl group signal

does not overlap with the signals in mineral oil and in water, toluene can be used as a tracer and its diffusivity in water-in-oil emulsions can be measured based on this signal.

In order to emphasize the fractional reduction in diffusivity caused by dispersed water droplets, the ratio of the toluene diffusivities in emulsions to its diffusivity in single phase oil, i.e. (D/D_{single}), is reported instead of the absolute diffusivity of toluene (D). Figure 4-10 shows the measured reduction in toluene diffusivity ratio (D/D_{single}) as a function of water cut.

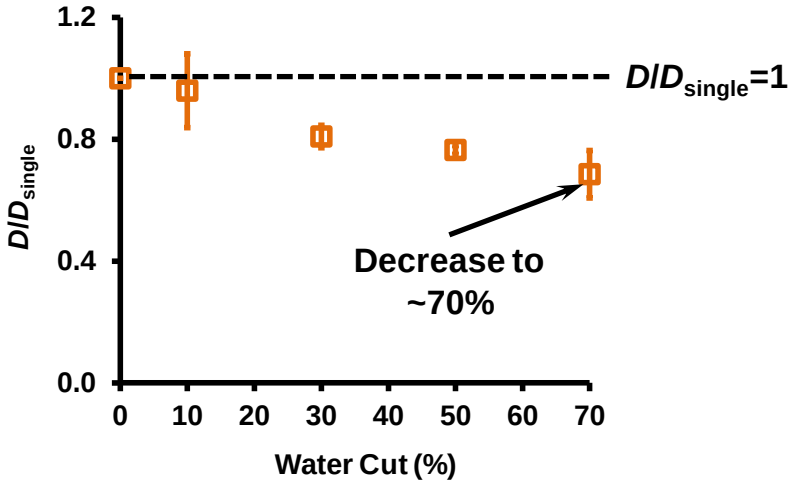

Figure 4-10: The measured reduction in toluene diffusivity in water-in-oil emulsions with water cut = 10%, 30%, 50% and 70%

As can be seen from Figure 4-10, the molecular diffusivities of toluene in WC10-70 emulsions are lower than its single phase molecular diffusivity. This observation indicates that the dispersed water droplets *indeed* partially inhibit the diffusion of toluene molecules in the continuous phase. Additionally, one observes a monotonically decreasing trend in the ratio (D/D_{single}) with increasing water cut, indicating the inhibition of toluene diffusion by the water droplets becomes more profound as the water cut increases.

It should be noted that as the diffusivity reduction is due to the partial blockage of the diffusion path by the water droplets, the trend in (D/D_{single}) as a function of the water cut should only depend on the microstructure of the emulsion while does not depend on the chemical nature of the tracer. Consequently, the trend in (D/D_{single}) measured using different types of tracers should

be consistent with one another. To verify this expectation, the trend in (D/D_{single}) as a function of water cut was also characterized with mineral oil as the tracer and shown in Figure 4-11.

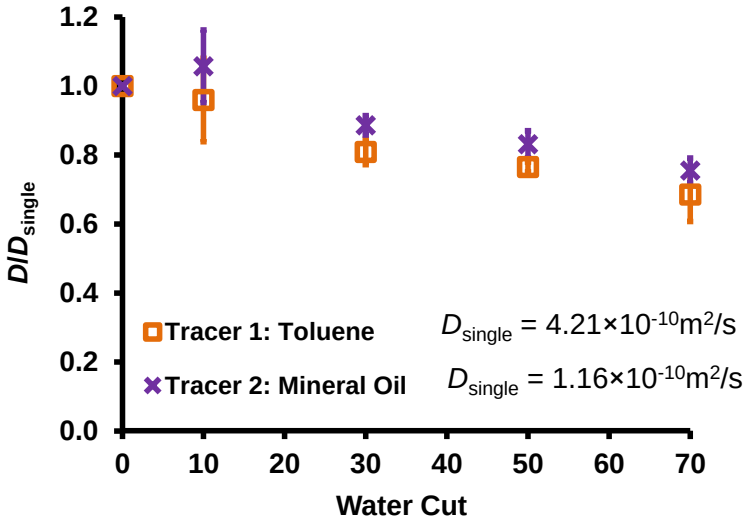

Figure 4-11: Comparison of the trends in (D/D_{single}) as a function of water cuts characterized based on diffusometry using toluene and mineral oil as tracers

Two important observations can be made from Figure 4-11:

- In absence of water droplets, the diffusivity of mineral oil in the oil phase[iii] ($D_{single,\ mineral\ oil}$ = 1.16×10^{-10} m^2/s) is approximately 25% that of toluene in the oil phase ($D_{single,\ toluene}$ = 4.21×10^{-10} m^2/s).
- Despite the significant difference in mineral oil and toluene diffusivities in the oil phase, the trend and magnitude in the diffusivity reduction (D/D_{single}) observed using both tracers are consistent and comparable to each other.

These two observations indicate that the reduction of tracer diffusivity in emulsions is independent of the chemical nature of the tracer while is only dependent on volume fraction of the dispersed water.

[iii] The diffusivity of mineral oil in the single-phase oil is equivalent to the mineral self-diffusivity.

Consequently, the observed trend in (D/D_{single}) as a function of water cut provides a reliable quantification of the inhibitive effect of the water droplets on the molecular diffusion in the continuous phase.

4.D.3 Characterization of Wax Effective Diffusivity in Model Emulsions

The previous sections presented an experimental method developed in this study for the quantification of the inhibitive effect of water droplets on the molecular diffusion through the continuous phase. It would be ideal if this methodology can be extended to characterize the diffusivities of wax molecules (straight alkane molecules) in water-in-oil emulsions. However, due to the similarities in the molecular structures of wax and mineral oil, their ^{1}HNMR signals overlap, posing a difficulty to directly measure the diffusivity of the wax molecules.

In order to overcome this difficulty in wax ^{1}HNMR diffusometry, one of the protons in the methyl group of the wax molecules is replaced with a fluorine atom. The fluorine atom attached to the straight hydrocarbon chain can be detected using ^{19}FNMR spectroscopy, while mineral oil does not display any signal on the ^{19}FNMR spectrum. The fluorine-substituted wax is noted as "F-Wax" in this study. Without the interference from the mineral oil NMR signals, the diffusivity of F-Wax in can be measured. Figure 4-12 shows the trend in (D/D_{single}) characterized with F-Wax as a tracer in comparison with the trends in (D/D_{single}) obtained previously using toluene and mineral oil as tracers.

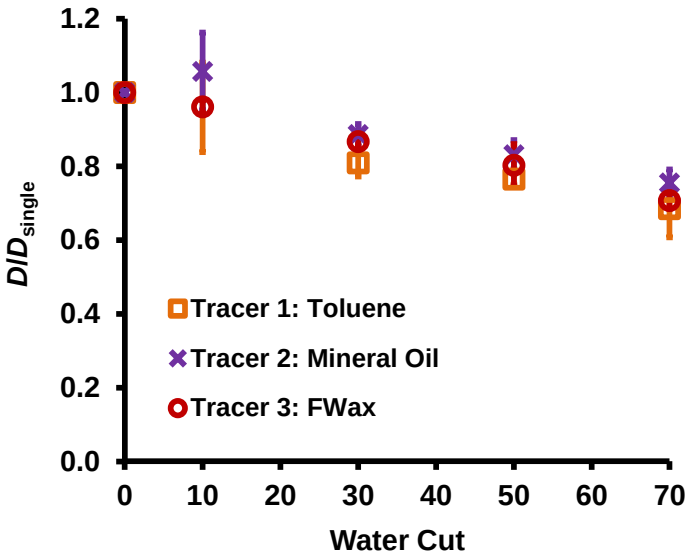

Figure 4-12: The trend in (D/D_{single}) characterized with F-Wax as a tracer using ^{19}FNMR diffusometry in comparison with the trends in (D/D_{single}) obtained previously with toluene and mineral oil as tracers using ^{1}HNMR diffusometry

As can be seen from Figure 9, the trends in (D/D_{single}) observed with toluene, mineral oil and F-Wax are all consistent with one another. This observation indicates that the diffusivity reduction (D/D_{single}) in emulsions also holds for the case of wax diffusion in emulsion.

4.D.4 Evaluation and Improvements of Current Methods for the Modeling of Wax Diffusivity Reduction in Water-in-Oil Emulsion

The diffusivity of wax is an important parameter in wax deposition modeling to predict the severity of wax deposition for the field. For two phase flow wax deposition modeling, two empirical methods have been proposed to obtain the effective diffusivity of wax in water-in-oil dispersion[72].

- Method 1: Calculate the effective diffusivity of wax in water-in-oil emulsion based on Hayduk-Minhas/Wilke-Chang equations with the emulsion viscosity replacing the oil viscosity.
- Method 2: Assume that the effective diffusivity of wax in water-in-oil emulsion equals the single-phase diffusivity in oil.

Neither of the methods has been validated in previous wax deposition studies[72]. In this section, the validity of each of these approaches will be analyzed.

4.D.5 Validation of the First Method: Replacing the Oil Viscosity in the Hayduk-Minhas/Wilke-Chang Equations with Emulsion Viscosity

We will first calculate the wax effective diffusivity in water-in-oil emulsion using the Hayduk-Minhas and Wilke-Chang equations which are used to calculate the diffusivity in single phase wax deposition modeling.

$$\text{Hayduk-Minhas: } D_{\text{single}} = 13.3\times10^{-12}\times\frac{T_{\text{o}}^{1.47}}{\mu_{\text{o}}^{0.791-10.2/V_{\text{w}}}V_{\text{w}}^{0.71}} \tag{4-2}$$

$$\text{Wilke-Chang: } D_{\text{single}} = 7.4\times10^{-8}\frac{T_{\text{o}}(\phi_{\text{o}}M_{\text{o}})^{1/2}}{\mu_{\text{o}}V_{\text{w}}^{0.6}} \tag{4-3}$$

In order to account for the inhibitive effect of water droplets on wax diffusion, the oil viscosity, μ_{o}, in Equation (4-2)or (4-3) is replaced with the emulsion viscosity, μ_{e}. The drawback of this approach is that the emulsion viscosity, μ_{e}, is usually significantly higher than the oil viscosity, μ_{o}, therefore the calculated diffusivity of wax in emulsion based on the emulsion viscosity, $D(\mu_{\text{e}})$, can be lower than its actual value, leading to underestimates of wax deposition severity. The degree of underestimation is investigated in this study based on the dependence of the diffusivity on the viscosity: The Hayduk-Minhas/Wilke-Chang equations predict the following dependency of diffusivity on emulsion viscosity.

$$\text{Hayduk-Minhas: } D\sim\frac{1}{\mu_{\text{e}}^{0.8}} \tag{4-4}$$

$$(\text{assume } V_{\text{w}} = 400 mL/mol, \text{ a typical molar volume of wax})$$

$$\text{Wilke-Chang: } D\sim\frac{1}{\mu_{\text{e}}} \tag{4-5}$$

Based on these dependencies of diffusivity on viscosity, the diffusivity reduction (D/D_{single}) can be calculated using Equations (4-6)and (4-7).

$$\text{Hayduk-Minhas: } \frac{D(\mu_e)}{D_{single}(\mu_o)} = \frac{1/\mu_e^{0.8}}{1/\mu_o^{0.8}} = \left(\frac{\mu_o}{\mu_e}\right)^{0.8} \quad (4\text{-}6)$$

$$\text{Wilke-Chang: } \frac{D(\mu_e)}{D_{single}(\mu_o)} = \frac{1/\mu_e}{1/\mu_o} = \frac{\mu_o}{\mu_e} \quad (4\text{-}7)$$

In order to carry out this calculation, the viscosities of the oil and emulsions were measured using an AR-1000 rheometer with a cone and plate geometry. Viscosity measurements were performed in the temperature range from 30°C to 0°C. Figure 4-13 shows the measured viscosities of oil and emulsions with water cut ranging from 10% to 70%.

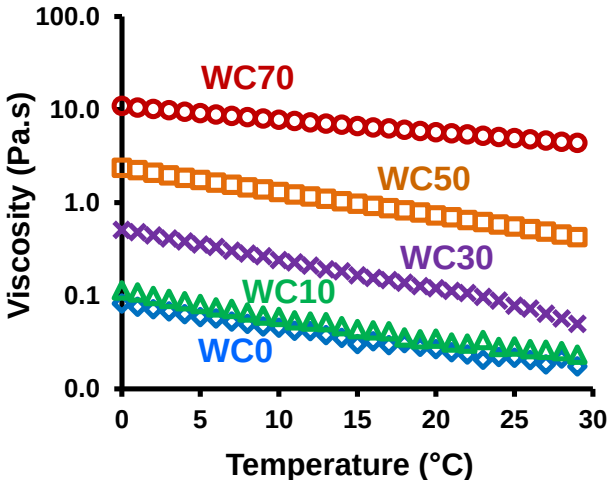

Figure 4-13: Viscosity of emulsions with 10%, 30%, 50%, 70% WC in comparison with the viscosity of the oil (denoted as water cut = 0% in the figure)

One observes that the emulsion viscosity increases drastically as water cut increases. For example, at 25°C, the viscosity of the 70% WC emulsion ($\mu_e = 4.91 Pa{\cdot}s$) is 200 times greater than the oil viscosity ($\mu_o = 0.02 Pa{\cdot}s$). Consequently, when one substitutes the emulsion and oil viscosities into Equations (4-6)and (4-7), one observes a reduction in the diffusivity in 70% WC emulsion by a factor of 200 when compared to the wax diffusivity in oil., Figure 4-14 shows the predicted diffusivity reduction as a function of water cut using Equation (4-6)and (4-7)in comparison with experimentally measured diffusivity reduction.

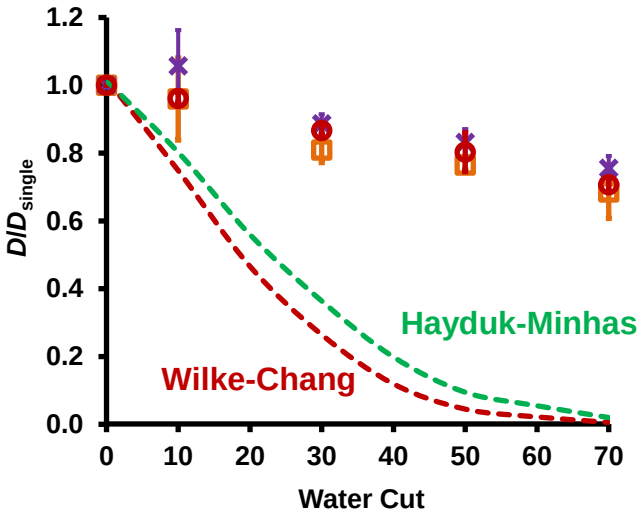

Figure 4-14: Comparison between the predicted diffusivity reduction by inserting the emulsion viscosity into the Hayduk-Minhas Equation/Wilke-Chang Equation and the measured diffusivity reduction by NMR diffusometry

As can be seen from Figure 4-14, Equations (4-6) and (4-7) significantly under-predict the diffusivity in emulsion, especially at high water cuts. In the emulsion with a water cut of 70%, it was measured that the effective diffusivity equals approximately 70% of the diffusivity in absence of water droplets, invalidating the 200 times diffusivity reduction as predicted by Equations (4-6) and (4-7). This under-prediction of the diffusivity in water-in-oil emulsion is due to the fact that the real reason for the reduction in wax diffusivity in water-in-oil emulsions is the increase in transport path cause by the partial blockage of the water droplets. Therefore, the approach of simply modifying the viscosity does not have the correct physical representation. It can further lead to a significant under-prediction in the wax deposition rate and can lead to specifying incorrect pigging frequencies.

4.D.6 Validation of the Second Method: Assume that the Effective Diffusivity of Wax in Water-in-Oil Emulsion Equals its Diffusivity in the Oil Phase

The second method assumes that the effective diffusivity of wax in emulsions equals its diffusivity in the oil phase and then uses the diffusivity of wax in the oil phase for two phase wax deposition modeling. This assumption is based on the argument that wax diffusion only occurs

in the continuous oil phase. However, no diffusivity reduction can be captured using this method. Consequently, this approach of assuming that the effective diffusivity of wax in emulsion equals its diffusivity in the oil phase is inconsistent with the diffusivity reduction observed in experiments. This approach for diffusivity calculation can lead to conservative prediction of the wax deposition rate and thickness.

4.D.7 A Fundamentally Correct Method to Calculate the Effective Wax Diffusivity in Water-in-Oil Dispersion to Predict Wax Buildup in Subsea Pipelines

In order to be consistent with the physics of wax diffusion in water-in-oil emulsion, a fundamentally correct method to account for the inhibitive effect of dispersed water on wax diffusion should be developed based on the following two considerations:

- Wax can only diffuse through the continuous phase. Therefore, its effective diffusivity in the water-in-oil emulsion (D) should depend on its diffusivity in the oil phase (D_{single}).
- Dispersed water droplets act as barriers to wax diffusion and the resulting decrease in the diffusivity in emulsion (D/D_{single}) can be related to the volume fraction of the water droplets (Φ).

Based on these two considerations, Jönsson investigated the effect of spherical transport barriers on the tortuosity of molecular diffusion by solving the diffusion equation analytically[79]. In this study, the obstruction to diffusion was accounted for by imposing a "zero-flux" boundary condition at the surface of the spherical transport barriers, i.e. the diffusive flux normal to the surface of the spheres equals zero. By solving the diffusion equation analytically, the effective diffusivity of molecules in a porous media with spherical transport barriers can be calculated

from first principles. Jönsson's calculation for the effective diffusivity is shown in Equation (4-8).

$$D = D_{\text{single}} \frac{2}{2+\Phi} \tag{4-8}$$

In this study, the comparison between the theoretical derivation and experimental measurements was carried out, as shown in Figure 4-15.

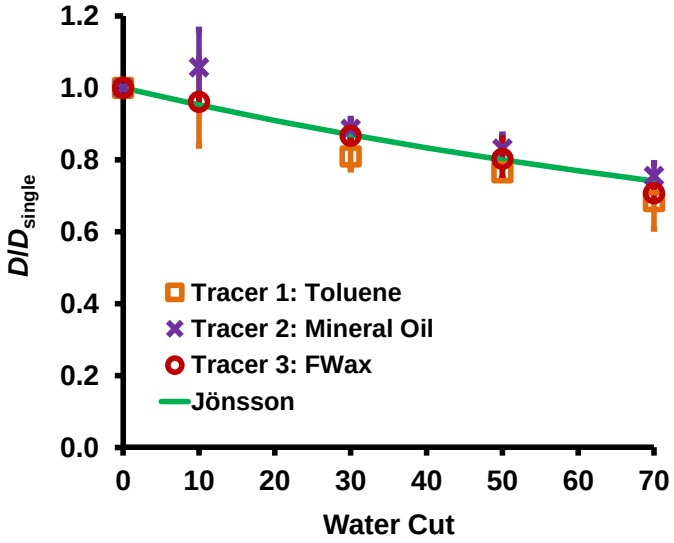

Figure 4-15: The trend in (D/D_{single}) predicted by Jönsson's equation in comparison with the measured trend in (D/D_{single})

As can be seen from Figure 4-15, the predicted trend in (D/D_{single}) using Jönsson's equation is in excellent agreement with the measured trends with increasing water cut. Consequently, Jönsson's method can be a potential candidate as a fundamental approach to model wax diffusion in water-in-oil dispersed phase flow.

4.E Conclusions

In this study, the diffusivities of wax in water-in-oil emulsions were experimentally characterized for the first time. It was discovered that dispersed water droplets inhibit wax diffusion by partially blocking its diffusion path. The inhibitive effect of dispersed water droplets on wax molecular diffusion was quantified by NMR diffusometry.

Two previously proposed empirical methods to model the diffusion of wax in water-in-oil emulsion were reviewed and the validity of each of these empirical methods was questioned. It was found that the method of calculating wax effective diffusivity in emulsion by using an emulsion viscosity in the Hayduk-Minhas/Wilke Chang equations significantly under-predicts the diffusivity of wax in emulsion. Using this method for wax diffusivity calculation in water-in-oil dispersed phase flow wax deposition modeling will lead to a significant under-prediction of wax deposition rate and can be dangerous during the design of pigging. Different from the two empirical methods, Jönsson's approach calculates the diffusivity of wax in emulsion from first principles and its prediction was found to be in close agreement with NMR diffusometry measurements in this study.

Chapter 5

A Fundamental Wax Deposition Model for Water-in-Oil Dispersed Flows in Subsea Pipelines

5.A Introduction

Wax deposition in subsea oil pipelines is a challenging problem in off-shore oil transportation as it causes a reduction in the cross-sectional area available for oil flow, thereby increasing the required pump pressure to maintain a specified production rate. If the wax deposit is not removed periodically by the costly pigging operations, it can grow to too thick and hard and become virtually impossible to be removed by pigging, such as the case shown in Figure 5-1.

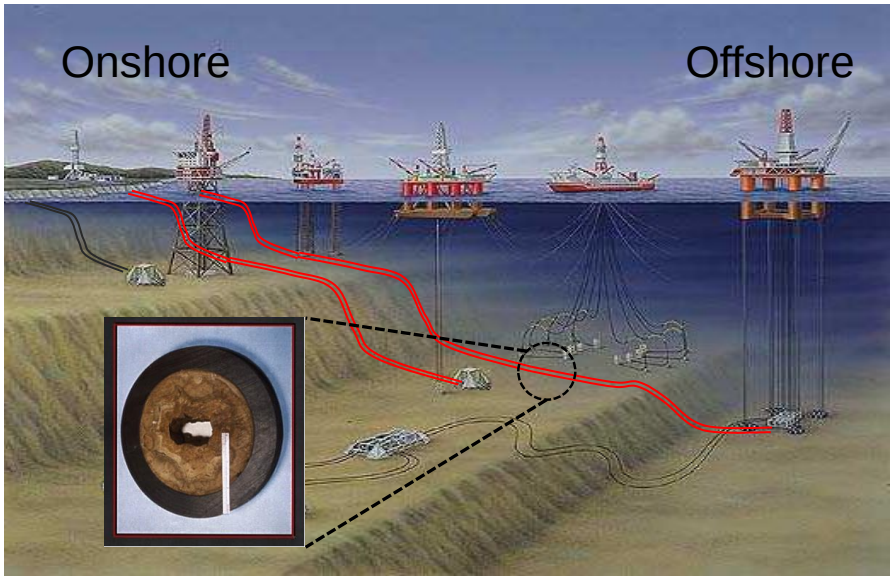

Figure 5-1: A schematic of the layout of subsea pipelines and a cross section of the pipeline plugged by wax deposit[21]

Under such extreme circumstances, the only way to resume production is to dispatch deep sea divers to cut off the clogged pipe section at the cost of tens of millions of dollars[11]. However, excessively frequent pigging operations pose a severe economic burden on the upstream oil industry. With the status of the global oil market, even the major operators must be extremely cautious when determining the pigging frequency. Knowledge of wax deposition rates and thicknesses in subsea pipelines is crucial to the proper scheduling of pigging operations. As a result, a substantial number of theoretical and experimental studies[21,24–29,33,34,61] have been conducted in order to understand the physics of wax deposition and to predict the deposit growth rate and thickness. Previous modeling studies focused mostly on single phase oil flows[21,26–28,61]. However, multiphase flows, including oil-gas/oil-water two phase flows and oil-gas-water three phase flows can occur in oil field operations. Fundamental wax deposition models for multiphase flow patterns have not been developed. Among the multiphase flow scenarios, oil-water two phase flows have gained increasing interests from the upstream oil industry as the water content of the production stream continues to increase as production time of a reservoir elapses. Among the possible oil-water flow patterns, such as water-in-oil dispersed flow, oil-centered annular flow, stratified flow and oil-in-water dispersed flow[63], wax deposition can occur from water-in-oil dispersed phase flow and stratified flow because in these two flow patterns, the pipe wall is completely or partly in contact with the oil phase. Huang et al. developed a fundamental wax deposition model for oil-water stratified channel flow[35]. The transportation of oil in most pipelines occurs in turbulent flow regime and the turbulent eddies intensively mix oil and water. In comparison with water-oil stratified flow, water-in-oil dispersed flow is a common flow pattern in field operations as intensive mixing and the presence of natural surfactants[65–

[68] together promote the formation of water-in-oil dispersion. Nevertheless, no fundamental wax deposition model for this flow pattern has been developed. The only wax deposition modeling study regarding water-in-oil dispersed flow, by Bruno et al., uses the pseudo-single phase (PSP) approach to model flow loop deposition experiments[69]. In this investigation, the heat and mass transfer characteristics of wax deposition were analyzed using first principles from transport theories. For heat transfer simulation, in addition to the pseudo-single phase approach used by Bruno et al.[69], the two phase Eulerian-Eulerian method was applied. Comparisons between the simulation results from the two approaches for heat transfer modeling provide a guideline to select heat transfer model in wax deposition analysis. For mass transfer simulation, reliable approaches to calculate the radial diffusive flux of wax were established based on the unique diffusion characteristic of wax in water-in-oil dispersion, i.e., diffusion occurs around the water droplets. The wax deposition model combining the heat and mass transfer characteristics in water-in-oil dispersed flow was applied not only to model lab scale wax deposition experiments but also field scale wax deposition. The roles of the water volume fraction and droplet size on wax deposition are uncovered with theoretical analysis.

5.B Introduction of Wax Deposition Modeling for Water-in-Oil Dispersed Flows

The wax deposition model developed in this work is based on the Michigan Wax Predictor[26] and consists of four sequential calculation steps: 1) a hydrodynamic calculation, 2) a heat transfer calculation, 3) a mass transfer calculation and 4) a deposit growth calculation. At each time step *t*, the velocity profile of the oil-water mixture is first obtained based on the universal velocity profile for turbulent flow and the parabolic velocity profile for laminar

flow. The velocity profile together with the water content and the droplet size distribution will be used as input parameters for the heat and mass transfer calculations to determine the temperature and dissolved wax concentration profiles. Figure 5-2 shows a schematic of the unique heat and mass transfer characteristics associated with the water-in-oil dispersed flow.

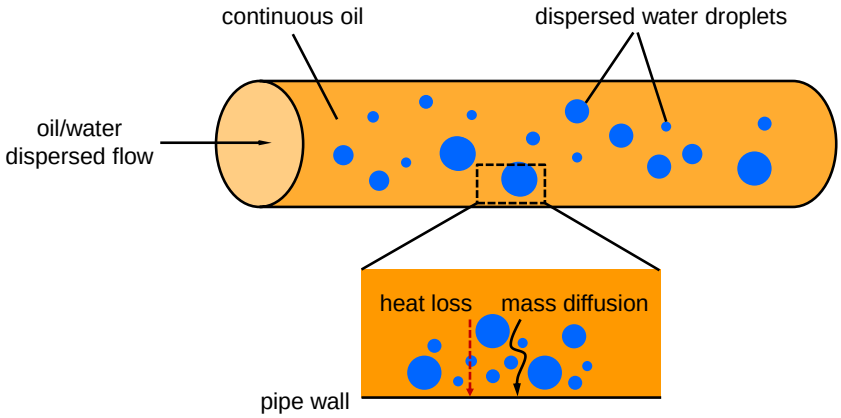

Figure 5-2: A schematic summarizing the heat and mass transfer characteristics for wax deposition in water-in-oil dispersed flow

As can be seen from Figure 5-2, heat conduction from the flow to the cold wall can occur through water droplets. Different from heat transfer, mass transfer *cannot* occur through the droplets as wax molecules cannot dissolve in water droplets and therefore must diffuse around them. Based on the dissolved wax concentration profile, the radial flux of wax is calculated to obtain the deposit growth rates. The computational grid is updated at the end of each cycle to account for the formation of a deposit layer and a new computational grid is used in the next time step, $t + \Delta t$. This calculation procedure is repeated until the simulation time reaches a specified duration for wax deposition. Detailed mathematical formulations of the modifications for the two-phase heat and mass transfer characteristics will be presented in the following sections.

5.C Hydrodynamic Calculations

Predicting the velocity profile in water-in-oil dispersions is essential to subsequent heat and mass transfer calculations because "velocity" is an input parameter to solve the governing heat and mass transfer equations. In carrying out the hydrodynamic calculations, it can be assumed that, owing to their small sizes, the dispersed water droplets move at the same velocity as the continuous oil phases. This assumption is realistic and significantly simplifies the mathematical formulation of the hydrodynamic calculations. This assumption can be justified by the following argument. Hypothetically, if a water droplet moves at a velocity different from that of the surrounding oil, the drag force from the oil phase will quickly accelerate or decelerate the droplet until the velocity difference is eliminated. For example, with a typical oil phase viscosity of 10 c.P., it requires only ~0.1 second to accelerate a 1 mm-diameter droplet from stationary to reach 99% the velocity of the surrounding oil. A typical water-in-crude oil emulsion contains droplets that are smaller than 1 mm[80,81] and it then requires even less than 0.1 seconds for the droplet to be accelerated to the same velocity as the surrounding oil.

Because of the negligible local velocity difference between the oil and water phases, these two phases can be lumped into a single pseudo-phase whose velocity profile can be used to represent the velocity profiles of both phases. Equations from the original single phase MWP were used to calculate the velocity profile with the viscosity of the water-in-oil dispersion mixture replacing that of the oil. Detailed equations for the hydrodynamic calculations can be found in the study by Huang et al.[26] and thus will not be repeated here. These equations were also included in Appendix D.

5.D Heat Transfer Calculations

Heat transfer models are used to calculate the temperature profile of the oil, which will be used as the input for the calculation of concentration profile of dissolved wax. Two approaches can be used to perform the heat transfer modeling: the pseudo-single phase (PSP) approach[69] and the Eulerian-Eulerian (E-E) approach[82]. Detailed mathematical formulations of both approaches will be introduced in the subsections. The E-E approach is theoretically rigorous although computationally intensive. Under certain operating conditions, such as fine droplet diameter and slow heat loss rate to the ambient, the computationally efficient PSP model can be used without causing significant error. Comparison between the PSP and E-E models under various operating conditions will be shown in this section as well.

5.D.1 Eulerian-Eulerian (E-E) Approach

5.D.1.a The Heat Transfer Governing Equations and Boundary Conditions

The Eulerian-Eulerian (E-E) approach uses two variables, $T_o(r,z)$ and $T_w(r,z)$ to describe the oil and water temperature profiles. To determine T_o and T_w, two sets of governing heat transfer equations and boundary conditions need to be solved. The governing equation of the oil phase is:

$$\text{oil phase:} \quad \rho_o Cp_o \phi_o V_z \frac{\partial T_o}{\partial z} + \phi_o \frac{1}{r}\frac{\partial}{\partial r}\left[-r\left(k_o + Cp_o \frac{\mu_T}{Pr_T} \right)\frac{\partial T_o}{\partial r} \right] - h_{inter}(T_w - T_o) = 0 \tag{5-1}$$

T_o = oil temperature,(K)

T_w = water temperature,(K)

ρ_o = density of oil,(kg/m^3)

Cp_o = heat capacity of oil,$(J/kg/K)$

ϕ_o = volume fraction of oil

V_z = axial velocity,(m/s)

z = axial position,(m)

r = radial position,(m)

k_o = thermal conductivity of oil,$(W/m/K)$

μ_T = turbulent viscosity,$(Pa \cdot s)$

Pr_T = turbulent Prandtl number

h_{inter} = heat transfer coefficient between oil and water,$(W/m/K)$

The first term on the left-hand side of Equation (5-1) represents the energy flow by advection in the axial direction. The second term represents the heat transfer in the radial direction. Enhanced heat transfer due to turbulent eddies is accounted for by the addition of eddy thermal conductivity, $k_{o,T} = Cp_o \frac{\mu_T}{Pr_T}$, to the material thermal conductivity, k_o.

The first two terms in Equation (5-1) are also present in the heat transfer governing equation for single phase wax deposition modeling[26]. In addition to the convective and conductive heat transfer modes, heat exchange can also occur between oil and water droplets if the local temperatures of the two phases are different. The third term in Equation (5-1) represents the local heat exchange between the oil and water phases.

The boundary conditions associated with Equation (5-1) are shown in Equation (5-2).

$$\begin{cases} T_o = T_{o,inlet}, \text{ at } z = 0 & \text{(a)} \\ \dfrac{\partial T_o}{\partial r} = 0, \text{ at } r = 0 & \text{(b)} \\ U_{extn}(T_{ambient} - T_{o,interface}) = k_o \dfrac{\partial T_o}{\partial r}, \text{ at } r = r_{interface} & \text{(c)} \end{cases} \quad (5\text{-}2)$$

$T_{o,inlet}$ = oil temperature at the inlet,(K)

U_{extn} = overall external heat transfer coefficient,$(W/m^2/K)$

$T_{ambient}$ = ambient temperature,(K)

$r_{interface}$ = effective radius,(m)

For the simplicity of coding, the overall heat transfer coefficient, U_{extn}, is used in the third boundary condition, i.e. boundary condition (5-2c), to lump the thermal resistances due to the sea water flow/coolant flow outside the pipe and the insulation by the wax deposit layer.

The governing equation and the boundary conditions for the water phase are similar to those of the oil phase but with physical properties of water, seen in Equations (5-3) and (5-4).

$$\text{water phase: } \rho_w Cp_w \phi_w V_z \frac{\partial T_w}{\partial z} + \phi_w \frac{1}{r}\frac{\partial}{\partial r}\left[-r\left(k_w + Cp_w \frac{\mu_T}{Pr_T}\right)\frac{\partial T_w}{\partial r}\right] - h_{inter}(T_o - T_w) = 0 \quad (5\text{-}3)$$

$$\begin{cases} T_w = T_{w,inlet}, \text{ at } z = 0 & \text{(a)} \\ \dfrac{\partial T_w}{\partial r} = 0, \text{ at } r = 0 & \text{(b)} \\ \dfrac{\partial T_w}{\partial r} = 0, \text{ at } r = 0 \text{ and at } r = r_{interface} & \text{(c)} \end{cases} \quad (5\text{-}4)$$

ρ_w = density of water,(kg/m^3)

Cp_w = heat capacity of water,$(J/kg/K)$

ϕ_w = volume fraction of water

T_w = water temperature,(K)

k_w = thermal conductivity of water,$(W/m/K)$

Note that a zero-flux boundary condition, i.e. boundary conditions (5-4c), is imposed on the water phase at the pipe wall. This boundary condition is used in order for the heat transfer characteristics to be consistent with the flow pattern. As the water phase is assumed to be dispersed, water droplets are not in direct contact with the wall and therefore do not conduct heat through the pipe wall[83].

The governing equations are discretized and solved numerically using the numerical techniques provided by Oosthuizen and Naylor[84]. The two governing equations are coupled as the heat exchange terms contain both T_o and T_w. Consequently, iterations are necessary to solve for T_o and T_o simultaneously, causing the E-E approach to be more computationally intensive than the PSP approach.

5.D.1.b Modeling the Heat Exchange between the Oil and Water Phases

It should be noted that the heat transfer model is not completed at this point as the calculation of heat transfer coefficient between the oil and water phases, h_{inter}, has not been specified. The interphase heat transfer coefficient, h_{inter}, between the continuous oil phase and the dispersed water phase with a volume fraction of ϕ_w and uniform droplet diameter of d_w can be calculated using Equation (5-5)[85–88].

$$h_{inter} = \frac{12 k_o \phi_w}{d_w{}^2} \tag{5-5}$$

$$d_w = \text{droplet diameter}, (m)$$

As can be seen from Equations (5-5), h_{inter} scales with d_w^{-2}. When the dispersed water droplets have a size distribution specified by the probability density function, $P(d_w)$, for the droplet size d_w, the heat transfer coefficient between two phases can be calculated by the integral shown in Equation (5-6).

$$h_{inter} = 12 k_o \phi_w \frac{\int_0^\infty d_w P(d_w) \mathrm{d}d_w}{\int_0^\infty d_w{}^3 P(d_w) \mathrm{d}d_w} \tag{5-6}$$

The derivations of Equations (5-5) and (5-6) are included in Appendix E in the supporting information. As can be seen from Equations (5-5) and (5-6), inputting an accurate droplet size distribution is essential to accurately modeling the inter-phase heat transfer. The droplet size distribution thus becomes an additional input parameter required for water-in-oil two

phase wax deposition modeling when compared to single phase wax deposition modeling. Pulsed-NMR techniques[81] or microscopy experiments[89] can be used to measure the water droplet size distribution. When experimental characterization is not feasible, the droplet size can be estimated based on dimensional analysis reported in the studies by Grace[90], Hinze et al.[91], Brauner et al.[92] or Cai et al.[93]. Unfortunately, using the methods in these studies, one can only determine the upper and lower limits of the droplet diameter while the entire droplet size distribution cannot be predicted. A sensitivity analysis on the droplet diameter should then be performed to estimate the uncertainties in the deposit thickness due to the varying droplet diameter.

5.D.2 Pseudo-Single Phase (PSP) Approach

The pseudo-single phase (PSP) approach treats the water-in-oil dispersion as a single pseudo-fluid whose physical properties are calculated by averaging the corresponding physical properties of oil and water, as given in Equations (5-7) to (5-9).

$$\text{density: } \bar{\rho}_{\text{mix}} = \rho_{\text{o}}\phi_{\text{o}} + \rho_{\text{w}}\phi_{\text{w}} \tag{5-7}$$

$$\text{heat capacity: } \overline{C\text{p}}_{\text{mix}} = \frac{\rho_{\text{o}}\phi_{\text{o}}C\text{p}_{\text{o}} + \rho_{\text{w}}\phi_{\text{w}}C\text{p}_{\text{w}}}{\rho_{\text{o}}\phi_{\text{o}} + \rho_{\text{w}}\phi_{\text{w}}} \tag{5-8}$$

$$\text{thermal conductivity: } \bar{k}_{\text{mix}} = \frac{k_{\text{w}} + 2k_{\text{o}} + 2\phi_{\text{w}}(k_{\text{w}} - k_{\text{o}})}{k_{\text{w}} + 2k_{\text{o}} - \phi_{\text{w}}(k_{\text{w}} - k_{\text{o}})}k_{\text{o}} \tag{5-9}$$

$\bar{\rho}_{\text{mix}}$ = average density of the oil-water mixture,(kg / m^3)

$\overline{C\text{p}}_{\text{mix}}$ = average heat capacity of the oil-water mixture,$(J / kg / K)$

$\bar{k}_{\text{mix}}$ = average thermal conductivity of the oil-water mixture,$(W / m / K)$

The density of the pseudo-fluid is calculated by volume-based averaging. The heat capacity is calculated by weight-based averaging. The thermal conductivity is calculated using Maxwell's correlation[94]. These averaged physical properties are then used in the heat transfer governing equation and the corresponding boundary conditions, as shown in Equations (5-10)and (5-11).

pseudo-single phase:

$$\overline{\rho_{\text{mix}} Cp_{\text{mix}}} V_z \frac{\partial T}{\partial z} + \frac{1}{r}\frac{\partial}{\partial r}\left[-r\left(\bar{k}_{\text{mix}} + \overline{Cp}_{\text{mix}} \frac{\mu_T}{\text{Pr}_T} \right) \frac{\partial T}{\partial r} \right] = 0 \tag{5-10}$$

$$\begin{cases} T = T_{\text{inlet}}, \text{ at } z = 0 & \text{(a)} \\ \dfrac{\partial T}{\partial r} = 0, \text{ at } r = 0 & \text{(b)} \\ U_{\text{extn}}(T_{\text{ambient}} - T_{\text{interface}}) = \bar{k}_{\text{mix}} \dfrac{\partial T}{\partial r}, \text{ at } r = r_{\text{interface}} & \text{(c)} \end{cases} \tag{5-11}$$

T_{inlet} = inlet temperature of the oil-water mixture,(K)

$T_{\text{interface}}$ = interface temperature of the oil-water mixture,(K)

By lumping of the oil and water phases into one pseudo-fluid, only one temperature variable, *T*, is needed to describe the temperature distributions in both phases, which intrinsically assumes that the inter-phase heat exchange between oil and water is instantaneous. It should be noted that under certain conditions, the PSP approach becomes superior to the E-E approach due to its computational efficiency. For example, when the droplet size is fine, a large interfacial area is available for inter-phase heat transfer, resulting in rapid heat transfer between the oil and water phase. The prediction from the PSP approach is then consistent with those from the E-E approach. In the next subsection, the applicability of the E-E and PSP approaches under typical field and lab conditions will be assessed in order to provide guidelines to select the heat transfer model for water-in-oil dispersed phase flow wax deposition modeling.

5.D.3 Comparison between the PSP and E-E Approaches

The comparison between the PSP and E-E approach is performed based on typical parameters in a field scale pipeline as well as a lab scale flow loop. These parameters can be found in Appendix F of the supporting information.

5.D.3.a Field Scale Simulations

The axial evolutions of the oil and water phase temperatures at the wall were calculated and shown in Figure 5-3. Note that the dimensionless oil and water phase temperatures, θ_o and θ_w, defined in Equation (5-12), instead of the actual temperatures were plotted for a clearer comparison between the different simulations.

$$\theta_o = \frac{T_o - T_{ambient}}{T_{o,inlet} - T_{ambient}},\ \theta_w = \frac{T_w - T_{ambient}}{T_{w,inlet} - T_{ambient}},\ \zeta = \frac{z}{R} \tag{5-12}$$

θ_o = dimensionless temperature of oil

θ_w = dimensionless temperature of water

ζ = dimensionless axial position

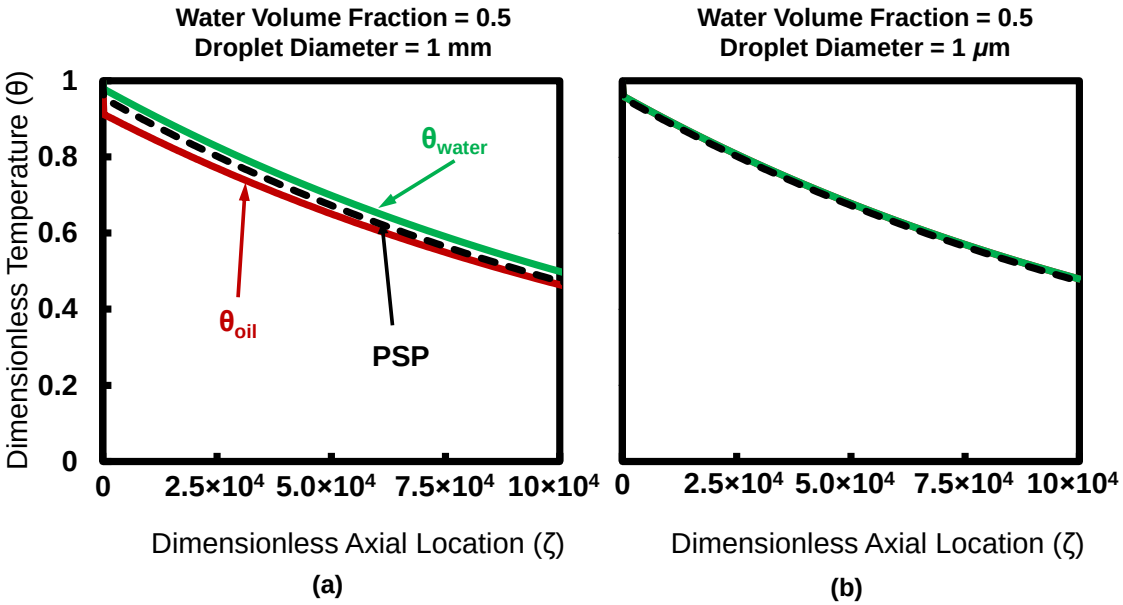

Figure 5-3: Dimensionless oil/water temperature profiles at wall predicted using the E-E approach and the PSP approach by assuming (a) d_w = 1mm and (b) d_w = 1μm. The water volume fraction in these simulations is fixed at 0.5.

Figure 5-3 shows the axial evolutions of the dimensionless temperatures generated with a droplet diameter of (a) 1mm and (b) 1μm. One observes from Figure 5-3 that the predicted temperature profiles evolutions are not sensitive to the droplet diameter. It should be noted that the external heat transfer coefficient of a field scale pipeline is usually small (on the order of 10 W/m^2/K)[59] and as a result, the axial temperature profile evolution of the water

phase will be limited by the heat loss rate to the ambient while is not limited by the heat transfer rate between oil and water even when the droplet diameter is as large as 1 mm. Under these conditions, the PSP approach will generate temperature profile predictions similar to the E-E approach for both fine droplets (d_w = 1μm) and coarse droplets (d_w = 1mm). *The take-away from this analysis is that the pseudo-single phase approach can be used for field scale simulations.*

5.D.3.b Lab Scale Simulations

Unlike field operations, lab scale flow loop wax deposition experiments usually require forced convection of a coolant stream in the test section to induce wax deposition. The external heat transfer coefficient associated with this setting is usually on the order of 1 kW/m^2/K[39]. The evolution of the axial temperature profiles of the oil and water phases with different droplet diameters and an external heat transfer coefficient of 1 kW/m^2/K are shown in Figure 5-4.

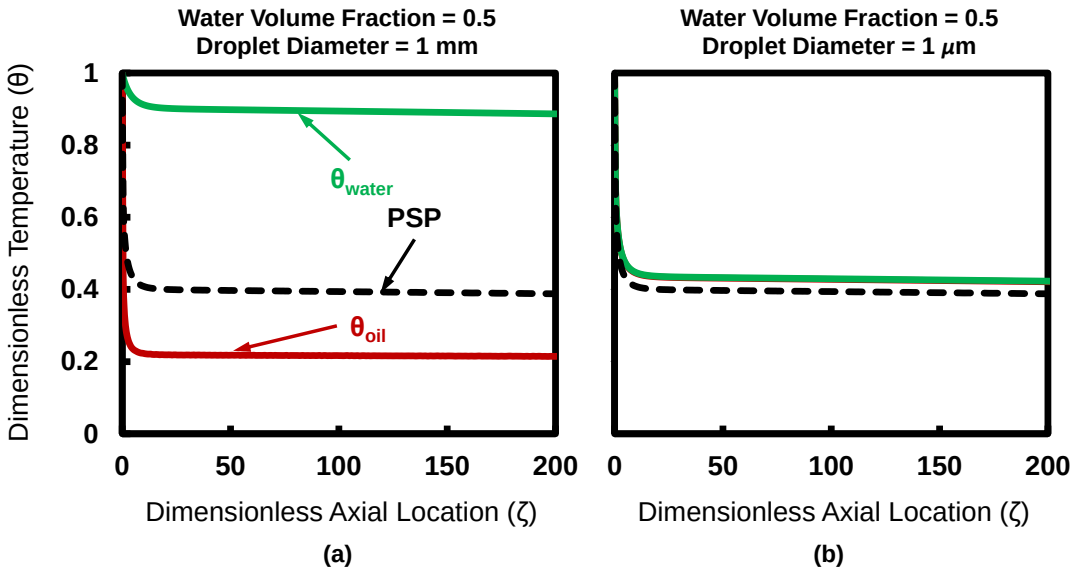

Figure 5-4: Dimensionless oil/water temperature profiles at wall predicted using the E-E approach and the PSP approach by assuming (a) d_w = 1mm and (b) d_w = 1μm. The water volume fraction in these simulations is fixed at 0.5.

As can be seen from Figure 5-4, the droplet diameter has a significant impact on the predicted temperature profiles. *The take-away from this analysis is that when the droplet diameter is large, the temperature profile evolution is limited by the heat transfer between the oil and water phases, causing the PSP approach to break down as it cannot resolve this heat exchange*. The lab scale heat transfer model showed good performance when applied to predict the heat transfer rate in a laboratory rectangular channel[70,95]. Details with respect to this application of the heat transfer model is included in Appendix G.

5.D.3.c Dimensionless Analysis

A dimensionless analysis was performed in order to 1) identify the dimensionless groups that govern the heat transfer characteristics, 2) explain the different heat transfer characteristics between field scale and lab scale simulations based on the different characteristic values of the dimensionless numbers encountered in these simulations and 3) to propose reliable rules of thumb to select a more appropriate heat transfer approach between the PSP and E-E approaches.

De-dimensionalization of the heat transfer governing equations and boundary conditions was performed using the following definitions for dimensionless variables.

$$\lambda = \frac{V_z}{U}, \zeta = \frac{z}{R}, \xi = \frac{r}{R}, \theta_o = \frac{T_o - T_{ambient}}{T_{o,inlet} - T_{ambient}}, \theta_w = \frac{T_w - T_{ambient}}{T_{w,inlet} - T_{ambient}} \quad (5\text{-}13)$$

The dimensionless form of the oil phase heat transfer equation is shown in Equation (5-14).

$$\phi_o \lambda \frac{\partial \theta_o}{\partial \zeta} + \phi_o \frac{1}{\xi} \frac{\partial}{\partial \xi} \left(-\frac{1}{\mathrm{Pe}_R} \xi \frac{\partial \theta_o}{\partial \xi} \right) - \mathrm{St}_R (\theta_o - \theta_w) = 0 \quad (5\text{-}14)$$

Two dimensionless numbers, i.e., the Péclet number, Pe_R and the Stanton number, St_R, surfaced through the de-dimensionalization of Equation (5-1) and are given in Equations (5-15) and (5-17), respectively.

$$\mathrm{Pe}_R = \frac{UR}{(\varepsilon_o + \alpha_o)} \tag{5-15}$$

$$\text{with } \varepsilon_o = 0 \text{ for laminar flow, } \varepsilon_o > 0 \text{ for turbulent flow} \tag{5-16}$$

$$\mathrm{St}_R = \frac{h_{inter} R}{\rho_o Cp_o U} \tag{5-17}$$

The subscript "R" in the definitions for the Péclect and Stanton numbers represents that the radius of the pipe is used as the characteristic length scale. The dimensionless boundary condition is shown in Equation (5-18).

$$\begin{aligned} &\mathrm{Nu}\theta_o + \frac{\mathrm{d}\theta_o}{\mathrm{d}\xi} = 0, \text{ at } \xi = 1 \\ &\mathrm{Nu}_R = \frac{U_{extn} R}{k_o} \end{aligned} \tag{5-18}$$

The boundary conditions have been given in dimensionless form with the external heat transfer coefficient, thermal conductivity of the oil and pipe radius grouped in the Nusselt number Nu_R. Among the three dimensionless numbers, St_R and Nu_R directly affect the heat transfer characteristics. St_R characterizes the rate of heat exchange between the oil phase and the water droplets phase while Nu_R characterizes the rate of heat loss from the oil phase to the coolant stream or the surrounding sea water through the pipe wall. In order to present the roles of St_R and Nu_R on the temperature profile predictions, the dimensionless governing equations and boundary conditions were solved with various combinations of these two parameters, i.e., different pairs of (St_R, Nu_R). The maximal differences between the dimensionless oil and water temperatures, $\Delta\theta_{max} = (\theta_w - \theta_o)$, generated with different pairs of (St_R, Nu_R) were shown in Figure 5-5. $\Delta\theta_{max}$ is an efficient indicator of the validity of the PSP model. A large $\Delta\theta_{max}$ suggests that the PSP model is invalid as it cannot resolve this difference between the oil and water phase temperatures.

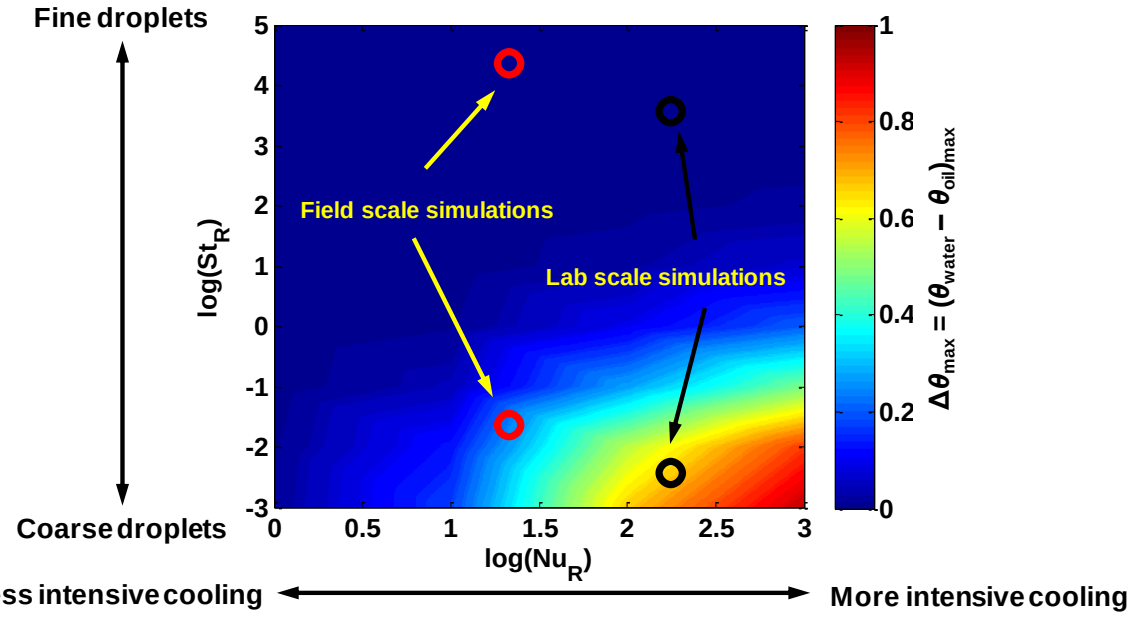

Figure 5-5: Assessment of the applicability of the pseudo-single phase (PSP) approach for heat transfer calculation under various (St_R, Nu_R) conditions

In Figure 5-5, a difference between the dimensionless water and oil temperatures of 0.5, i.e. $\Delta\theta_{max} = 0.5$ represents that the maximal difference between the water and oil phase interface temperatures among all axial positions is 50% that of the difference between the inlet temperature and the ambient/coolant temperature. As can be seen from Figure 5-5, the effect of droplet size on heat transfer becomes less profound as Nu_R decreases because at low values of Nu_R, the temperature profile evolution is no longer limited by the heat transfer rate between oil and water but limited by the heat loss rate to the coolant stream/surrounding sea water. Such heat transfer characteristics at low Nu_R can usually be encountered with small external heat transfer coefficients such as the ones used in field scale simulations. As can be seen in Figure 5-5, the PSP approach is likely to breakdown at high Nu_R and low St_R conditions, which can be encountered with intensive cooling by the ambient/coolant in lab scale simulations. Table 5-1 provides some quantitative rules of thumb to select the appropriate heat transfer approach depending on the magnitude of dimensionless numbers.

Table 5-1: Recommended selection for heat transfer model based on the characteristics dimensionless number, Nu_R and St_R

	Field Scale Cooling ($Nu_R \sim 10^1$)	Lab Scale Cooling ($Nu_R \sim 10^2$)
Coarse Droplet Diameter ($St_R < 10^{-1}$)	PSP	E-E
Fine Droplet Diameter ($St_R > 10^0$)	PSP	PSP

5.E Mass Transfer Calculations

It is accepted that molecular diffusion is the main mechanism responsible for wax deposition[11,21,24–28,33,34,61]. In order to calculate the radial diffusive flux of wax molecules and the deposit growth rate, the concentration profile dissolved wax in the oil phase needs to be determined by solving the governing equations, i.e., Equations (5-19).

$$V_z \frac{\partial C_{\text{wax}}}{\partial z} + \frac{1}{r}\frac{\partial}{\partial r}\left[-r(\varepsilon_{\text{M}} + D_{\text{wo}})\frac{\partial C_{\text{wax}}}{\partial r} \right] + k_{\text{precipitation}}(C_{\text{wax}} - C_{\text{wax,eq}}) = 0 \qquad (5\text{-}19)$$

C_{wax} = concentration of wax in the liquid phase,(kg / m^3)

$C_{\text{wax,eq}}$ = equilibrium concentration of wax at local temperature,(kg / m^3)

D_{wo} = molecular diffusivity of wax in oil,(m^2 / s)

ε_{M} = turbulent mass diffusivity of wax in oil,(m^2 / s)

$k_{\text{precipitation}}$ = bulk precipitation kinetic constant,(s^{-1})

The boundary conditions to Equation (5-19) are

$$\begin{cases} C_{\text{wax}} = C_{\text{wax,inlet}}, \text{ at } z = 0 & \text{(a)} \\ \dfrac{\partial C_{\text{wax}}}{\partial r} = 0, \text{ at } r = 0 & \text{(b)} \\ C_{\text{wax}} = C_{\text{wax,eq,interface}}(T_{\text{o,interface}}), \text{ at } r = r_{\text{interface}} & \text{(c)} \end{cases} \qquad (5\text{-}20)$$

The bulk precipitation kinetic constant, $k_{\text{precipitation}}$, cannot be easily characterized in a flowing system such as in a field pipeline or a laboratory flow loop. Consequently, wax deposition simulations are usually performed by assuming one of the two limiting situations:

- no precipitation of wax in the bulk ($k_{\text{precipitation}} = 0$), also known as the Chilton-Colburn method[21]

- instantaneous precipitation of wax in the bulk ($k_{\text{precipitation}} \to \infty$ and $C_{\text{wax}} \to C_{\text{wax,eq}}$), also known as the solubility method[96]

These two simulations are expected to provide reliable estimations for the most conservative (the largest deposit) and optimistic (the smallest deposit) estimations of deposit thickness respectively. Two methods to calculate the diffusivity of wax were proposed for these two limiting cases for bulk precipitation kinetics. These two methods will be explained in detail in the subsections to follow.

5.E.1 The Chilton-Colburn Method

It should be noted that in water-in-oil dispersed phase flows, diffusion of wax can only occur in the oil continuous phase as the wax molecules are insoluble in water droplets. In order to incorporate these mass transfer characteristics in the governing equations, the following boundary condition needs to be imposed on the oil-water interfaces of *each and every* water droplet.

$$\vec{n}\cdot\vec{J}_{\text{wax}} = \vec{n}\cdot(-D_{\text{wo}}\vec{\nabla}C_{\text{wax}}) = 0, \text{ on oil-water interfaces} \quad (5\text{-}21)$$

$\vec{n}$ = the local normal vector to the oil-water interface

$\vec{J}_{\text{wax}}$ = the diffusive flux of wax in oil, $(kg / m^2 / s)$

The governing equations and the boundary conditions shown in Equations (5-19)- (5-21) appear to be mathematically simple and one might be tempted to solve this system using conventional computational fluid dynamics (CFD) techniques. However, before going down this path, we first need to estimate the computational intensity of a conventional CFD model by estimating the number of cells in the computational domain of the entire pipe. We will perform this estimation by considering a 1-km, 12-in. (0.305 m) pipe section filled with a water-in-oil dispersion at a water volume fraction of 0.1. If the droplets have a uniform diameter of 10 microns, we can calculate that this imaginary pipe section contains as many as

10^{15} water droplets. In order to resolve the diffusion of wax molecules around the water droplets, the computational cells in the vicinity of the droplet-oil interfaces should be finer in size than the water droplets, resulting in even more than 10^{15} computational cells to be constructed for the entire computational domain. Such computational intensity forbids naive" CFD simulations without any "tailor-made" modifications. Strategies to reduce computational intensity were developed in this study and will now be presented in the upcoming subsections.

5.E.1.a Approach I – Method of Volume Averaging

In order to reduce computational intensity, the method of volume averaging technique uses effective transport properties to account for the impact of transport barriers, such as water droplets. It should be emphasized that the method of volume averaging is applicable when the droplet diameter (e.g. ~ 1μm) is significantly smaller than the mass transfer boundary layer thickness (e.g. ~100 μm). Under this condition, the boundary layer contains a sufficient number of droplets and has a homogeneous microstructure, which guarantees that volume averaging can generate representative effective transport properties.

One can account for the partially blocked wax diffusion by using D_{eff} in place of D_{wo} in the governing equation. The effective diffusivity in dispersion can be predicted with the method of volume averaging by first solving the mass balance in a control volume with a sufficient number of water droplets and the integrated volume-averaged flux can then be compared with the flux in absence of droplets, shown in Equation (5-22).

$$\frac{D_{\text{eff}}}{D_{\text{wo}}} = \frac{J_{\text{wax}}}{J_{\text{wax,single}}} = \frac{\frac{1}{V_{\text{oil}}} \iiint_{V_{\text{oil}}} -D_{\text{wo}} \nabla C_{\text{wax}} \, \mathrm{d}V_{\text{oil}}}{J_{\text{wax,single}}} \tag{5-22}$$

D_{eff} = effective diffusivity of wax in the water-oil mixture

J_{wax} = diffusive flux of wax in the direction of

the macroscopic concentration gradient in water-oil mixture,$(kg / m^2 / s)$

$J_{wax,single}$ = diffusive flux of wax in the direction of

the macroscopic concentration gradient in single phase oil,$(kg / m^2 / s)$

V_{oil} = volume of the continuous oil phase in the control volume,(m^3)

The predicted effective diffusivity by CFD is compared with the predictions by the Maxwell-Garnett equation in Figure 5-6. Other computational details regarding the CFD model can be found in Appendix H of the supporting information.

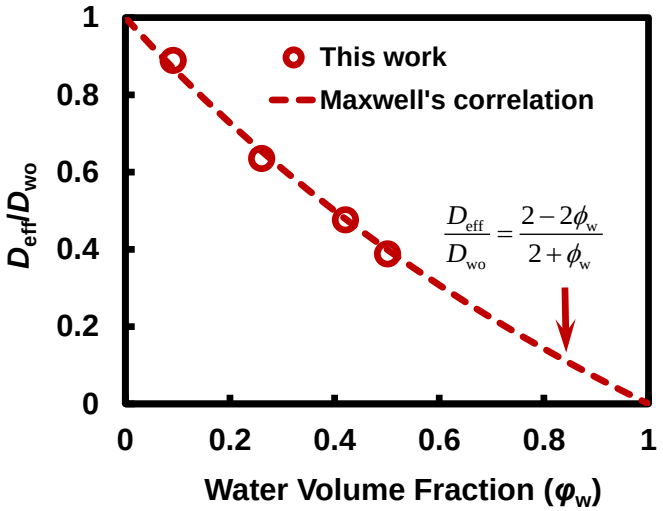

Figure 5-6: Comparison between the effective diffusivity estimated by the microscopic model and theoretical values by Maxwell-Garnett correlation

As can be seen from Figure 5-6, excellent agreement is achieved between (D_{eff}/D_{wo}) predicted by the Maxwell-Garnett equation and by the CFD model and thereby validating the CFD model. The variation of the effective diffusivity with water volume fraction is also consistent with the effect of water volume fraction on the tortuosity of the continuous oil phase measured by NMR[89].

5.E.1.b Approach II – Method of Ensemble Averaging

The method of volume averaging fails when the droplet size is comparable to or larger than the boundary layer thickness. When the droplet diameter is larger than the mass transfer

boundary layer thickness, droplets will not fit into the mass transfer boundary layer. Consequently, the mass transfer boundary layer has a lower water volume fraction than the bulk. The volume fraction of the entire flow is thus not representative of the water volume fraction of the boundary layer. Under this circumstance, a novel method, the method of ensemble averaging is proposed to model the mass transfer around droplets. This method of ensemble averaging is initiated by solving the mass transfer equation at the pipeline scale by assuming $D_{eff} = D_{wo}$ as an initial guess, shown as "Step-1" in Figure 5-7

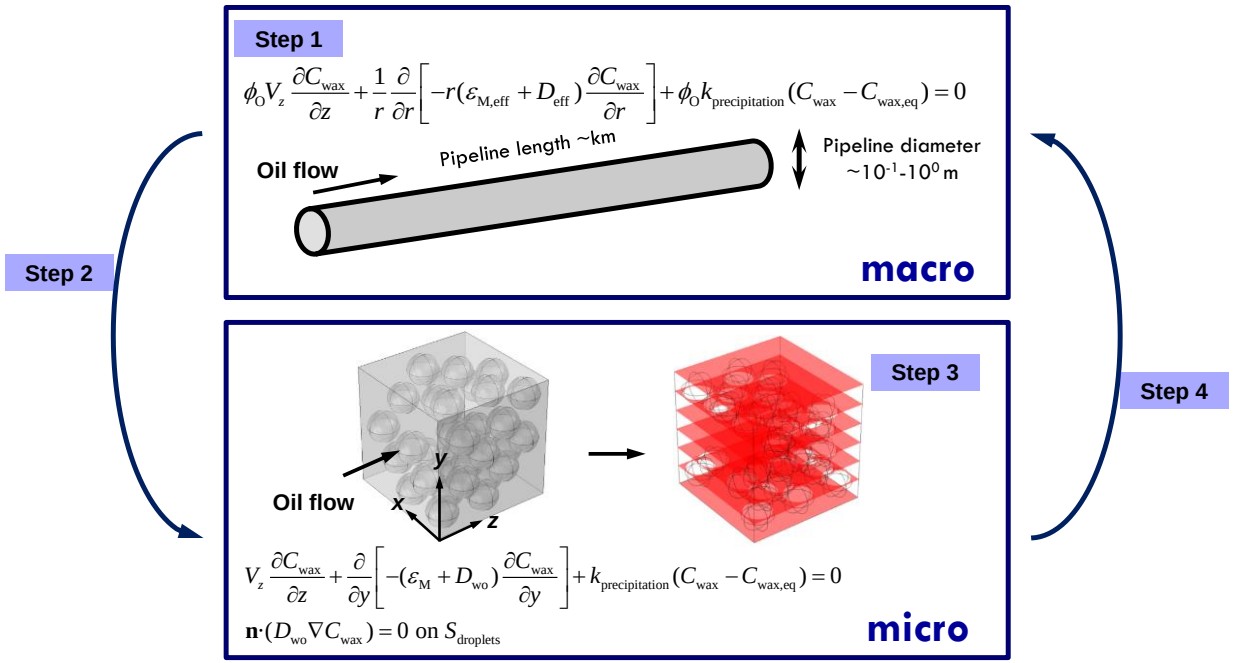

Step 1: Solve the macroscopic mass transfer equation with initial guesses: $D_{eff} = D_{wo}$, $\varepsilon_{M,eff} = \varepsilon_M$

Step 2: Use the concentration profiles from macroscopic simulations from step 1 as inputs to microscopic simulations as boundary conditions.

Step 3: Solve the microscopic mass transfer equation. A series of parallel cut-planes are then constructed and the diffusive mass transfer rate across each plane calculated based on the solution to the concentration profile.

Step 4: Compare the mass transfer rate across the cut-plane in presence of droplets with that in absence of droplets to calculated effective diffusivity. The effective diffusivity is then used in a second macroscopic simulation to determine mass flux of wax to the interface.

Step 5: Repeat Step 1 through Step 4 until the predicted macroscopic radial concentration profile does not change.

Figure 5-7: The algorithm to evaluate the effective diffusivity in the vicinity of the wall when the droplet size is larger or comparable to the boundary layer thickness

The preliminary concentration profiles obtained by the macroscopic simulation are then used as the boundary conditions for a microscopic CFD simulation carried out at a region in the immediate vicinity of the pipe wall, shown as "Step-2" in Figure 5-7. A series of cut planes are then constructed in parallel with the wall and the diffusive mass transfer rates across each cut plane, $\iint J_{\text{wax}} \mathrm{d}A_{\text{cutplane}}$, are calculated and compared to the mass transfer rate in absence of the water droplets, $\iint J_{\text{wax},0} \mathrm{d}A_{\text{cutplane},0}$, shown as "Step-3" in Figure 5-7. Based on the comparison between the calculated mass transfer rates with and without droplets, a local diffusivity reduction parameter can be defined according to Equation (5-23).

$$\lambda(y) = \frac{\int\int J_{\text{wax}} \mathrm{d}A_{\text{cutplane}}}{\int\int J_{\text{wax,single}} \mathrm{d}A_{\text{cutplane,single}}} = \frac{\int\int D_{\text{wo}} \nabla C_{\text{wax}} \mathrm{d}A_{\text{cutplane}}}{\int\int D_{\text{wo}} \nabla C_{\text{wax,single}} \mathrm{d}A_{\text{cutplane,single}}} \tag{5-23}$$

This reduction in diffusivity is then incorporated into the macroscopic modeling with the effective diffusivity, replacing the molecular diffusivity, shown as "Step-4" in Figure 5-7. Steps 1-4 are repeated until the predicted macroscopic concentration profile no longer changes. This converged concentration profile is then used to calculate the flux toward the wall/interface. Figure 5-8 shows the calculated diffusivity reduction parameter for cases with various droplet diameters.

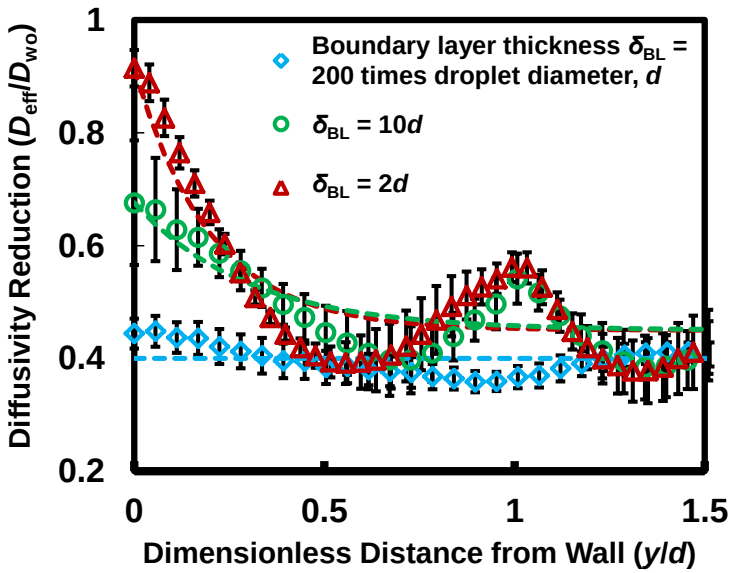

Figure 5-8: Diffusivity reduction parameter calculated with three varying droplet diameters: 1) the boundary layer thickness being 200 times the droplet diameter, 2) the boundary layer thickness being 10 times the droplet diameter and 3) the boundary layer thickness being 2 times the droplet diameter

As can be seen from Figure 5-8, the reduction in diffusivity at the interface/wall (y/d = 0) becomes less significant as the droplet diameter increases. It should be noted that the droplet configurations in the control volume is generated by packing spheres into a cubic simulation box with Monte Carlo simulation[97,98]. Therefore, periodic oscillations in the diffusivity reduction are observed due to the oscillations in the local porosity of the sphere packing. Several microscopic configurations of the droplets were generated to form an ensemble and the predicted diffusivity reduction was averaged over all configurations to obtain an ensemble-average of the diffusivity reduction. Details of the ensemble average method to obtain the effective diffusivity can be found in Appendix I of the supporting information.

In summary, when the boundary layer thickness is much larger than the droplet diameter, the retarded molecular diffusion in the boundary layer due to droplets can be accounted for using the effective diffusivity calculated by the Maxwell-Garnett equation. When the boundary layer thickness is comparable or smaller than droplet diameter, the method of volume averaging

overestimates the hindrance of droplets to molecular diffusion. The method of ensemble averaging is more reliable for mass transfer modeling.

5.E.2 The Solubility Method

For the case of instantaneous bulk precipitation, it was discovered through CFD simulation that the concentration of dissolved wax within the oil phase is at the equilibrium concentration at local temperature and is not affected by the presence of the water droplets. Details regarding the CFD simulation were provided in Appendix J. *As a result, mass transfer calculations are not necessary to determine the dissolved wax concentration profile for the case of instantaneous precipitation.* The diffusive flux of wax reaching the oil/deposit interface (or oil/wall interface at $t = 0^+$) can be calculated based on the wax equilibrium concentration gradient and the molecular diffusivity at the interface, as shown in Equation (5-24).

$$J_{\text{wax}}\,|_{r=r_{\text{interface}}} = -D_{\text{wo}}\,\frac{\partial C_{\text{wax,eq}}}{\partial r}\,|_{r=r_{\text{interface}}} \tag{5-24}$$

The calculated flux of wax can then be used to determine the deposit growth rate.

5.F Applications of the Algorithm in Wax Deposition Modeling

5.F.1 Case Study 1: Wax Deposition in a Lab Scale Flow Loop Apparatus

Although multiple experimental studies[69–71] have showed that wax deposit thickness tends to decrease with increasing water volume fraction, a detail theoretical analysis of this experimental observation is lacking. In this section, a theoretical analysis is performed to understand the role of the water phase on the deposit thickness from fundamentals of heat and mass transfer. The input parameters for simulation are based on the experimental conditions of the flow loop experiments by Bruno et al[69]. These input parameters were summarized in Appendix K of the supporting information. The water volume fraction of the simulation is varied from 0% to as high as 75%. The solubility method, i.e., instantaneous bulk precipitation kinetics, is used for

this set of simulations. The comparison between the deposit thickness predictions and the experimentally measured thickness is shown in Figure 5-9.

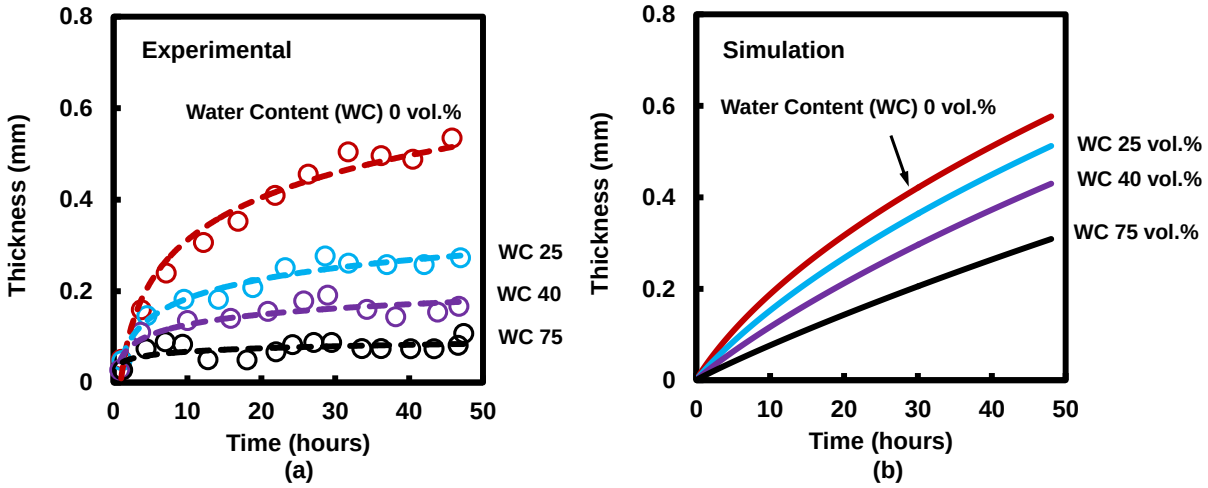

Figure 5-9: Comparison between predicted and measured deposit thickness-time trajectory with varying water volume fractions

As can be seen from Figure 5-9, the model predicts the experimental trend of decreasing deposit thickness as a function of increasing water volume fraction, which serves as a first validation of the model. It can also be observed from the experimental thickness-time trajectories that the deposit thickness decreases with time on several occasions, suggesting slough-off of deposit by the shear force. The slough-off of deposit is random and cannot be accounted for in wax deposition modeling. Now we will analyze the trend of decreasing deposit thickness with increasing water volume fraction based on heat and mass transfer analysis. The thickness of wax deposit can be correlated with the mass flux of wax reaching the interface, shown in Equation (5-25).

$$\text{growth rate } \frac{\mathrm{d}\delta}{\mathrm{d}t} \sim J_{\text{wax}} = -D_{\text{wo}} \frac{\partial C_{\text{wax}}}{\partial r}\Big|_{\text{wall}} \sim D_{\text{wo}} \frac{C_{\text{bulk}} - C_{\text{wall}}}{\delta_{\text{BL}}} \qquad (5\text{-}25)$$

The water phase can affect the concentration driving force, (C_{bulk}-C_{wall}) and the boundary layer thickness δ_{BL}. The effect of water volume fraction on the boundary layer thickness is first investigated by inspecting the radial dissolved wax concentration profiles predicted with

different water volume fractions. As can be seen from the predicted radial concentration profiles of dissolved wax shown in Figure 5-10, the concentration boundary layer thickness increases with increasing water volume fraction due to the increase in viscosity of the water-oil mixture, leading to a decrease in the concentration gradient of wax and deposition rate.

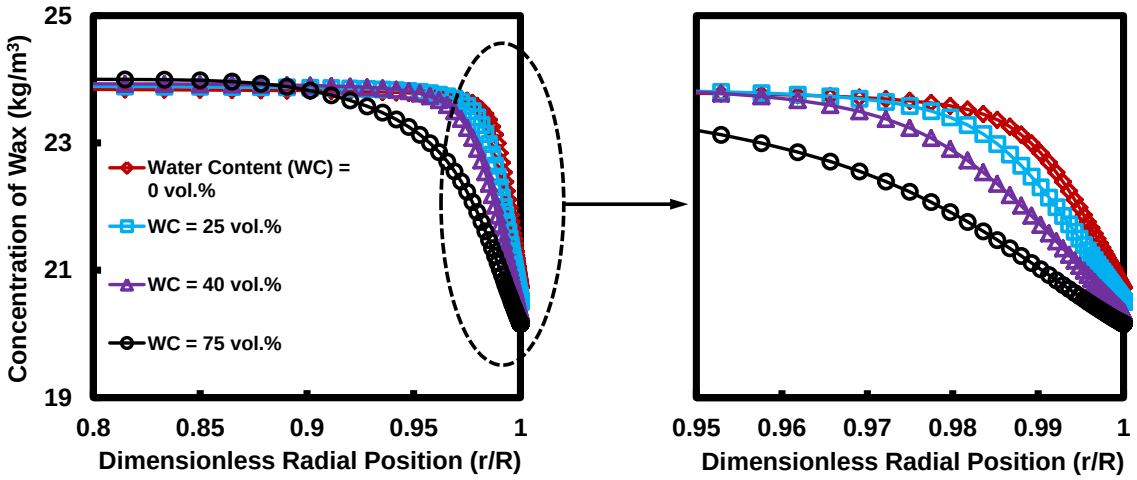

Figure 5-10: Predicted radial concentration profiles of dissolved wax with varying water volume fractions

Now let's consider the effect of the water phase on the concentration driving force for wax deposition, (C_{bulk}-C_{wall}), which depends on the concentrations of wax dissolved in the bulk and at the wall, C_{bulk} and C_{wall} respectively. Due to the short length of the experimental test section, the bulk temperature remains almost unchanged across the test section, as evidenced by the fact that the bulk temperature at the outlet remained within 1 °C from the inlet temperature. The wall temperature is also insensitive to the water volume fraction. The oil temperature at the interface varied between 12.6°C and 10.5°C when the water volume fraction was varied between 0 vol.% and 75 vol.%. It should be noted that the oil temperature at the interface is close to the coolant temperature due to the large external heat transfer coefficient, h_{extn}. Because of the negligible changes in the bulk and interface temperatures with varying water volume fraction, the concentration driving force is also insensitive to the water volume fraction. *The decreased*

deposit thickness with increasing water volume fraction is explained by the retarded heat transfer due to the increase in viscosity when there are water droplets dispersed in oil.

5.F.2 Case Study 2: Field Scale Wax Deposition Predictions

The goal of this model development is to predict wax deposition rates in field scale oil pipelines. Therefore, it is desirable to bench-mark our model with wax deposition data from actual subsea pipelines. Unfortunately, no such wax deposition data is available in the public domain. The performance of this model will be evaluated by simulating wax deposition under the field scale operating conditions included in Appendix L. The wax solubility and viscosity curves used in this case study are identical to those used in the previous lab scale case study.

The water volume fraction in the feed is varied from 0 vol.% to 50 vol.%. Figure 5-11 shows the predicted deposit thickness.

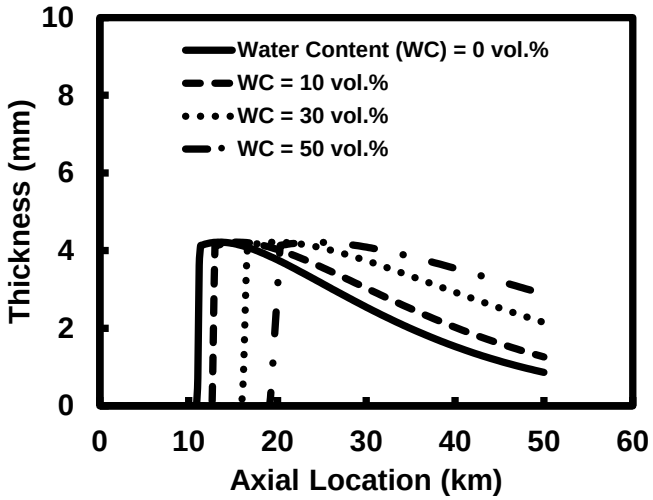

Figure 5-11: Predictions of axial deposit thicknesses in a field pipeline with varying water volume fractions in the feed

Two observations can be made from Figure 5-11. First, the water phase significantly delays the onset of wax deposition and second, deposit thickness increases with increasing water volume fraction. These two observations will now be explained separately.

As the water volume fraction of the feed varies from 0 vol.% to 50 vol.%, the onset location of wax deposition is shifted downstream by almost 10 km. This observation can be explained by the change in the oil temperature at wall with varying water volume fraction. Figure 5-12 shows the predicted wall temperature at different water volume fractions.

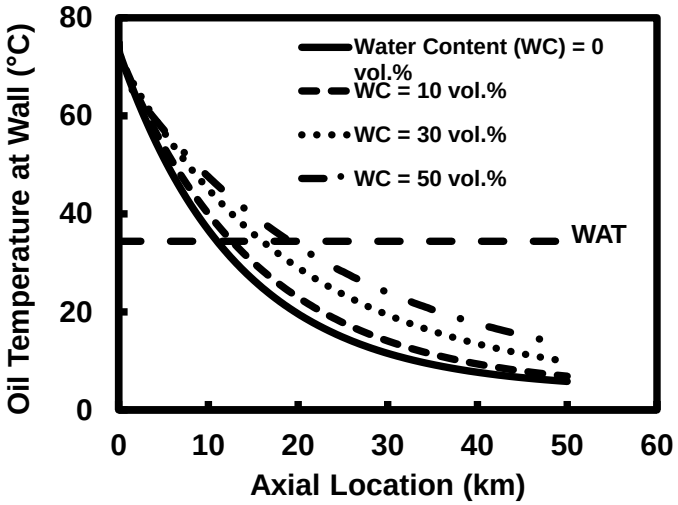

Figure 5-12: Axial oil temperature at wall with varying water volume fractions

As can be seen from Figure 5-12, the wall temperature in the axial direction decreases at a slower rate with an increased water volume fraction in the feed. Hence, the water phase acts as a heat carrier and retards the decrease of wall temperature with axial position. Therefore, the wall temperature reaches the wax appearance temperature at an axial location further from the entrance, thus shifting the onset of wax deposition towards downstream.

In addition to the delay in the onset of wax deposition, the local deposit thickness increases with the increasing water volume fraction. This trend at first appears to be counter-intuitive! The increase in deposit thickness with increasing water volume fraction can be explained by inspecting the heat flux from the oil to the ambient surroundings. The correlation between the deposition rate and the heat flux can be established via the following derivation shown in Equation (5-26)

$$\text{growth rate: } \frac{\mathrm{d}\delta}{\mathrm{d}t} \sim J_{\text{wax}} = -D_{\text{wo}} \frac{\partial C_{\text{wax}}}{\partial r}\Big|_{\text{wall}}$$

$$J_{\text{wax}} = -D_{\text{wo}} \frac{\mathrm{d}C_{\text{wax}}}{\mathrm{d}T}\Big|_{T_{\text{wall}}} \cdot \frac{\partial T}{\partial r}\Big|_{\text{wall}} \text{ (valid with instantaneous bulk precipitation)}$$

$$= -D_{\text{wo}} \frac{\mathrm{d}C_{\text{wax}}}{\mathrm{d}T}\Big|_{T_{\text{wall}}} \cdot k_{\text{oil}} \frac{\partial T}{\partial r}\Big|_{\text{wall}} \cdot \frac{1}{k_{\text{oil}}} \tag{5-26}$$

$$= D_{\text{wo}} \frac{\mathrm{d}C_{\text{wax}}}{\mathrm{d}T}\Big|_{T_{\text{wall}}} \cdot h_{\text{extn}} (T_{\text{wall}} - T_{\text{ambient}}) \frac{1}{k_{\text{oil}}}$$

$$= D_{\text{wo}} \frac{\mathrm{d}C_{\text{wax}}}{\mathrm{d}T}\Big|_{T_{\text{wall}}} \cdot \frac{1}{k_{\text{oil}}} \cdot Q_{\text{oil to ambient}}$$

As can be seen from Equation (5-26), the deposition rate increases with increasing heat flux from the oil to the surrounding sea water, $Q_{\text{oil to ambient}}$. As the wall temperature, T_{wall}, increases with increasing water volume fraction, so does the heat flux to the surrounding sea water: $Q_{\text{oil to ambient}} = h_{\text{extn}}(T_{\text{wall}}-T_{\text{ambient}})$. Thus, the local deposition rate increases with water volume fraction. It should be noted that the deposit thickness decreases with increasing water volume fraction in the lab scale simulation while the deposit thickness increases with increasing water volume fraction in this field scale simulation. The opposite trends of the deposit thickness as a function of water volume fraction will now be analyzed.

In lab scale simulations, a large external heat transfer coefficient (on the order of 1 kW/m^2/K) is used to represent the intensive cooling by forced convection of a coolant stream around the hot oil flow. The thermal resistance of the oil flow is larger than the thermal resistance of the coolant stream. Consequently, the overall thermal resistance to heat loss from the oil to the coolant is dominated by the thermal resistance of the oil flow. *As a result, the increase in the viscosity of the oil-water flow with increasing water volume fraction causes a corresponding increase in the overall thermal resistance and retards the heat loss, leading to a decrease in deposition rate in lab scale simulations*. In a field scale simulation, a small external heat transfer coefficient (on the order of 0.01 kW/m^2/K) was used to represent the cooling by sea water. As a result, the overall thermal resistance of heat loss from a field scale pipeline is dominated by the

thermal resistance of the surrounding sea water and the increase in the fluid viscosity by water does not impact heat transfer significantly. On the other hand, the water phase generates a large temperature driving force for heat transfer by raising the interface temperature due to the high heat capacity of the water. *This increase leads to a higher heat loss rate and therefore higher deposition rate at higher water volume fraction in field scale simulations*. The opposite trends in the deposit thickness with varying water volume fraction predicted with lab scale and field scale simulations challenge the relevance of lab scale experiments on water-in-oil dispersed phase flow performed previously[69–71].

5.F.3 Case Study 3: The Effect of Droplet Size on Wax Deposition

It should be noted that no investigation, theoretical or experimental, has been performed to understand the effect of droplet size on wax deposition rate owing to the lack of a fundamental wax deposition model. Previous elementary modeling studies consider the water and oil mixture as one pseudo-fluid and therefore cannot resolve the effect of droplet size on wax deposition. In order to provide insights to the effect of droplet size on wax deposition rate, we now perform two wax deposition simulations by assuming a droplet diameter of 1mm and 1μm respectively. The Chilton-Colburn approach was used for the bulk precipitation kinetics. The pipe dimensions, operating conditions and fluid properties were summarized in Appendix M. Figure 5-13 shows the comparison between the wax deposition rates predicted with the two different assumed droplet sizes.

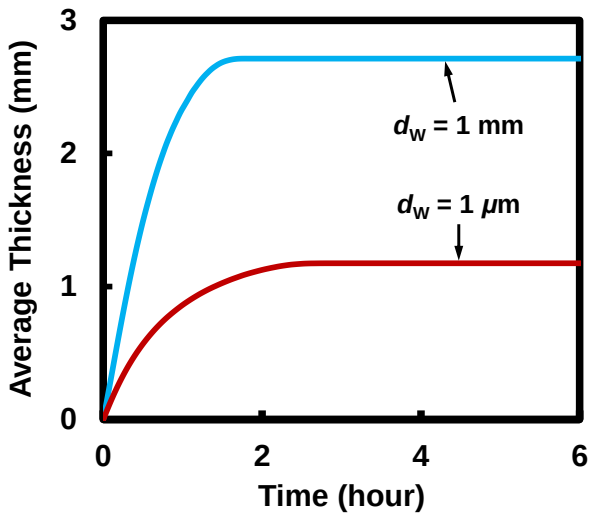

Figure 5-13: Comparison between deposit thickness predictions generated with an assumed droplet diameter of 1mm and an assumed droplet diameter of 1 μm

Two observations can be made from Figure 5-13

- The plateau of the wax deposit thickness predicted with a droplet diameter of 1 mm is higher than that predicted with a droplet diameter of 1μm.
- The rate that the thickness approaches the plateau value is higher for droplet diameter of 1 mm compare to that of a droplet diameter of 1 μm.

These two observations are due to the different roles of droplet size on heat and mass transfer respectively. Firstly, the thickness reaches a plateau value when the interface temperature reaches the WAT due to the insulation provided by the deposit layer. As the droplet size decreases, it is easier for water to supply heat to the oil phase and raise the oil phase temperature. As a result, at smaller droplet sizes, the interface temperature reaches the WAT more rapidly and with a thinner deposit layer. The reduced deposition rate with decreasing water droplet size can be understood by inspecting the characteristics wax flux generated with different water droplet diameter. The definition of the characteristic wax flux was first proposed by Huang et al. in order to explain the effect of operating temperature on wax deposition[27]. Equation (5-27) gives the wax flux used in this investigation.

$$J_{\text{wax}} = D_{\text{eff}} \left(\frac{C_{\text{wax,bulk}} - C_{\text{wax,wall}}}{r_{\text{interface}}} \right) \tag{5-27}$$

Note that the molecular diffusivity of wax, D_{wo}, in Huang et al.'s original definition is replaced with the effective diffusivity, D_{eff}, in order to account for the hindered diffusion of wax due to dispersion of water droplets. Table 5-2 summarizes the important parameters in the calculation of the characteristic wax flux.

Table 5-2: Comparison of the parameters for the characteristic mass flux associated with different assumed droplet diameters

	d = 1 μm	d = 1 mm
T_{oil} (°C)	45	45
T_{wall} (°C)	18	12
(C_{bulk}-C_{wall}) (wt.%)	4.86	5.13
$D_{eff,wall}$ ($\times 10^{-10}$ m^2/s)	0.27	0.49
J_{wax} ($\times 10^{-10}$ wt.%/m^2/s)	260	490

As can be seen from Table 5-2, the concentration driving forces, (C_{bulk}-C_{wall}), predicted with different droplet diameters are virtually the same, while the effective diffusivity increases by a factor of approximately two when the droplet diameter increases from 1 micron to 1 millimeter. This impact of the change in effective diffusivity on wax deposition rate has not been previously investigated or reported in literature. Another simulation was performed with a droplet diameter at 1 millimeter and the method of volume averaging for the diffusivity calculation. It was observed that the initial deposition rate varies from 3.0 mm/hr to 1.8 mm/hr when the method of volume averaging is used. It should be noted that this ~40% underprediction is sometimes acceptable when generating a first estimation of the wax deposition rate during the design phase of field development. The method of ensemble averaging is of better physical basis while the method of volume averaging can also be used for engineering applications as a first estimation.

5.G Conclusions

In this study, a wax deposition model in water-in-oil dispersed flows was developed. Two approaches for heat transfer calculations, i.e., the pseudo-single phase approach (PSP) and the Eulerian-Eulerian approach (E-E), were introduced and compared. The following characteristics were observed for the two heat transfer models:

- E-E approach is suitable for cases with high external heat transfer coefficient and coarse droplets.
- PSP model is suitable for cases with low external heat transfer coefficient or fine droplets.

It was pointed out that mass transfer modeling is not necessary when the solubility approach is used for bulk precipitation kinetics. When the Chilton-Colburn approach is used for the bulk precipitation kinetics, two methods for mass transfer modeling can be used depending on the relative sizes of the droplet and the mass transfer boundary layer. The following mass transfer characteristics were discovered from mass transfer analysis:

- When the droplet size is much smaller than the mass transfer boundary layer, the effect of water droplets on mass transfer can be accounted for by using an effective diffusivity calculated using the Maxwell-Garnett equation.
- When the droplet size is comparable/larger than the mass transfer boundary layer thickness, droplets cannot fit into the boundary layer. Therefore, the hindrance of molecular diffusion is less profound than the case with fine droplets. The effective diffusivity can be calculated by a novel method of ensemble averaging.

With these enhancements in the heat and mass transfer calculations, wax deposition modeling was performed with both lab and field scale operating conditions to understand the different roles

of the water phase on wax deposition. The following impacts of the water phase on the wax deposition characteristics were discovered.

- In lab scale simulations, wax deposition rate decreases with increases water volume fraction in the bulk because of the expansion of thermal and mass transfer boundary layer associated with the increase in the fluid viscosity when water is dispersed in oil.
- On the contrary, in field scale simulations, wax deposition rate increases with increasing water volume fraction in the feed as the water phase preserves temperature and concentration driving forces for deposition due to its high heat capacity.
- The wax deposition rate also decreases with decreasing droplet diameter. When the droplet size is comparable or larger than that of the mass transfer boundary layer, the mass transfer within the boundary layer is not hindered as profoundly as when the droplet size is much smaller than the boundary layer thickness.

Chapter 6

Entrapment of Water Droplets in Wax Deposits from Water-in-Oil Dispersion and Its Impact on Deposit Build-up

6.A Introduction

Water and oil commonly co-exist in the production stream from petroleum reservoirs[62]. The production stream is mainly composed of hydrocarbons and with low water content at early stages of well production because hydrocarbons usually lie above the aquifer and flow out of the well before water. The water content of the production stream usually increases over time[99]. Moreover, at the terminal stages of well production, the well is flooded with water, resulting in a significant amount of water in the production stream[100–102]. Wells with water contents higher than 90% can still produce an economically valuable amount of oil[103]. During pipeline transportations of the crude, co-existence of water and oil in the production stream can generate complex multiphase flow patterns, including water-in-oil dispersed flow[70,104], oil-in-water dispersed flow[105,106], annular flow[107], stratified flow[64], etc. Crude oil usually contains natural surfactants such as resins and asphaltenes[65–68]. Mixing of water and oil in presence of these natural surfactants by turbulence eddies promotes the formation of water-in-oil dispersion, making it a common multiphase flow regime in oil production. In the water-in-oil dispersed flow pattern, the oil phase is in contact with the pipe wall. As a result, wax deposition can occur when the temperature of the inner pipe wall is below the wax appearance temperature[69,70,104]

Wax deposition poses severe risks to off-shore assets. The presence of dispersed water droplets can affect the wax deposition characteristics. Bruno et al, Couto et al., Panacharoensawad and Sarica and Zhang et al[69–71,80]. performed wax deposition experiments with cold finger or flow loop apparatus using crude oils. It was observed that wax deposition rate decreases with increasing water content in the bulk. Similar trend in the effect of water on wax deposition rate was also observed by Kasumu and Mehrotra[108]. Wang et al. and Quan et al. observed non-monotonic variation in the deposition rate with increasing water content[104,109]. The investigators explained the non-monotonic variation in the wax deposition rate based on a combination of diffusion and gelation mechanism. Wang et al. further advanced the understanding of the gelling deposition mechanism on wax deposition and proposed an algebraic model to calculate deposition rate based on this mechanism[110].

Different from wax deposition from single phase oil flow, it was observed that the deposits formed from water-in-oil dispersed flow could contain water droplets[69,70,104]. It should be noted that entrapment of water droplets in the deposit *significantly* alters the rheological properties of the deposit, including yield stress[111], storage/loss modulus and thixotropy[112]. For example, it was observed that incorporation of water droplets in the deposit microstructure lowered the deposit yield stress[111]. Among the impact of water droplets on the rheological properties of the deposit, the change in the deposit yield stress has the most relevant influence on wax deposition characteristics as a lowered yield stress makes the deposit prone to slough-off by the shear stress imposed by the flow[8]. Without the consideration for deposit slough-off, existing wax deposition models will over-predict the deposit growth rate and lead to unnecessarily conservative scheduling of the costly pigging operation. The yield stress of the deposit varies with the water content of the deposit[112–114]. As a result, knowledge of the water content of the deposit is

essential for the estimation of deposit yield stress and assessment for the probability of slough-off of wax deposit. Unfortunately, the characterization of deposit water content has not received due attentions in previous experimental campaigns to study wax deposition from water-in-oil two phase flow[69,70,104,108]. Figure 6-1 summarizes previous reports of the water volume fraction of the deposit generated with water-oil mixtures[69,104].

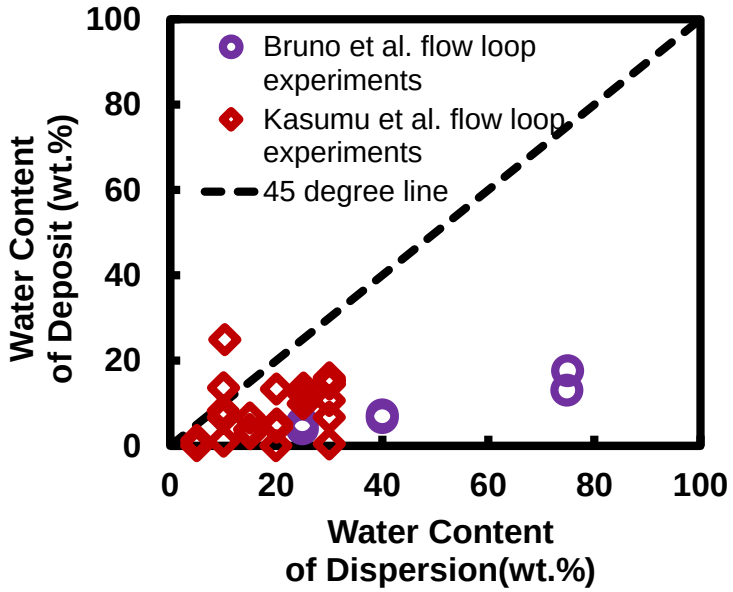

Figure 6-1: Summary of reported characterizations of the water content in the deposit in comparison with the water content of the dispersion[69,104]

As can be seen from Figure 6-1, *no* obvious correlation between the water contents of the bulk liquid and the deposit has been observed in previous experimental investigations. Interestingly, in some experiments[69,104], the deposits contain virtually no water while the water content of the bulk can be as high as 40 wt.%. Because of the existing inconsistencies reported in the water contents of deposits formed from water-in-oil dispersions, a fundamental understanding of the entrapment of water droplets during the deposition process is still lacking.

A comprehensive characterization of the water content and the droplet size distribution of the deposit is reported in this study. Based on this characterization, the inconsistencies in the

reported deposit water content[69,104] are resolved. In addition, the slough-off of wax deposits due to the entrapment of water droplets was demonstrated with a flow loop apparatus.

6.B Experimental

6.B.1 Model Oils

Two waxy model oils, Oils 1 and 2 were prepared and used as the oil phases for the experiments. The compositions, wax contents and wax appearance temperatures (WAT) of these two model oils were summarized in Table 6-1. The WAT's of the model oils were measured by cooling the model oils in a rheometer and monitoring the viscosity. The WAT is defined as the temperature below which the viscosity-temperature trajectory deviates from an Arrhenius temperature dependence.

Table 6-1: Summary of the formulations of the two waxy model oils used in this study

Model Oil	Solvent	Wax	Wax Content (wt.%)	WAT (°C)
1	Crystal Plus 70T Mineral Oil	Wax A: 327204 Aldrich, melting point 53°C-57°C	3	20
2		Wax B: 411663 Aldrich, melting point ≥ 65°C	5	38

The solvent used in both model oils is the Crystal Plus 70 T mineral oil purchased from STE Oil Company. The basic physical properties of this mineral oil are shown in Table 6-2[77].

Table 6-2: Basic physical properties of the solvent in the model oils

Density at 20 °C (g/mL)	0.857
Viscosity at 40°C (c.P.)	10.2
Averaged Molecular Weight (g/mol)	311

Figure 6-2 shows the carbon number distributions of the waxes in the two model oils. The carbon number distributions were measured by an Agilent Technogolies 6890 N high temperature gas chromatograph (HTGC).

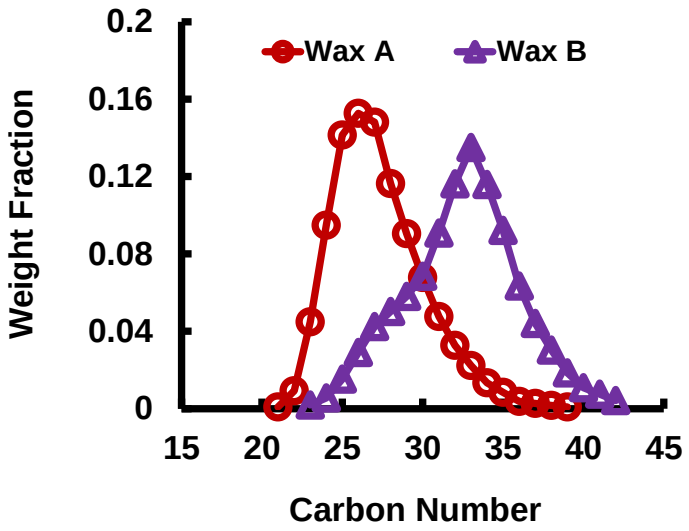

Figure 6-2: Carbon number distributions of the waxes used in the preparation of model oils

The first wax, wax A, with a lighter carbon number distribution between the two waxes was used to generate a model oil with a WAT (20 °C) lower than room temperature (25 °C). With this model oil, the water droplets in the deposit can be inspected easily at room temperature without the interference from precipitated wax particles as wax molecules remain dissolved at room temperature.

The second wax, wax B, with the heavier carbon number distribution was used to generate a model oil with a WAT (38°C) higher than room temperature (25 °C) to induce stabilization of water-in-oil dispersion with suspended wax particles. Such stabilization by suspended wax particles is critical to allow for the characterization of droplet size distribution of dispersions with low surfactant dosages.

6.B.2 Preparation of Model Emulsion

The mineral oil used in this study is free of natural surfactants such as resins and asphaltenes contained by crude oils. Consequently, synthesized surfactants were added to the model oil in order to facilitate emulsification. The surfactant used to generate the emulsion/dispersion is a 9:1 (based on mass) mixture of sorbitan monooleate (SPAN 80) and sodium di-2-

ehtylhexylsulfosuccinate (AOT). According to previous experimental studies[89], the water-in-oil mixtures generated with a surfactant concentration higher than 0.5wt.% (based on the total mass of oil and water) present long-term stability against phase separation. Therefore, these mixtures will be called "emulsion" from this point onward. Preliminary experiments in this investigation show that the water-in-oil mixtures with a surfactant concentration in the range between 0.1 wt.% and 0.5 wt.% undergo rapid phase separation when kept stationary while can be homogenized with stirring in the cold finger apparatus or with pumping in the flow loop apparatus. Because of the significantly different bulk stability characteristics compared to the stable emulsions, these mixtures with low surfactant dosages will be called "dispersion" from this point onward. In order to prepare emulsion/dispersion for wax deposition experiments in the cold finger apparatus/flow loop, the oil phase was prepared by first dissolving various amount of the surfactant mixture (0.1wt.% to 1.0wt.% based on the total mass of oil and water) in the model oils. In the cold finger apparatus, emulsification/dispersion of water was achieved by adding deionized (DI) water with a volume fraction varying from 10% to 70% to the oil phase at a temperature above the WAT while under intensive mixing with a mechanical stirrer. In the flow loop apparatus, the emulsion/dispersion was prepared by addition of DI water to the reservoir containing oil followed by circulation of the water-oil mixture in the flow loop apparatus until the pressure drop reading across the test section reaches a steady level.

6.B.3 Cold Finger Wax Deposition Experiments

Figure 6-3 shows a schematic drawing of the cold finger apparatus.

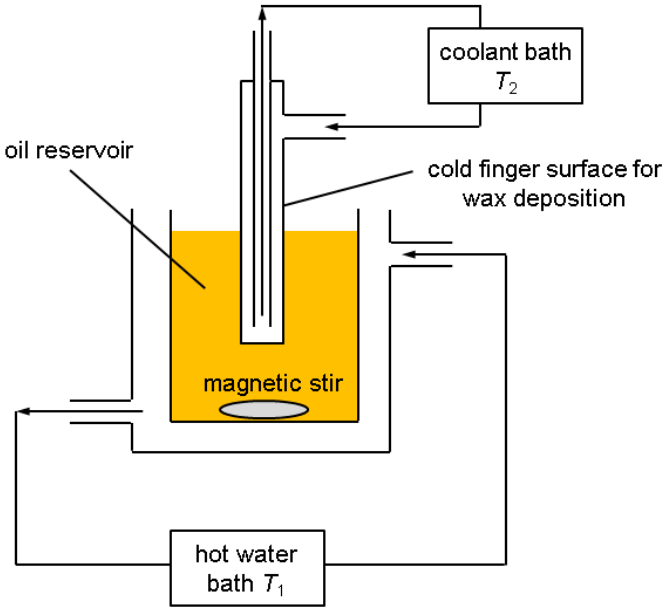

Figure 6-3: A schematic drawing of the cold finger apparatus

In order to prepare for a wax deposition experiment with the cold finger apparatus, the temperatures of the reservoir as well as the cold finger were first adjusted to the desired set points T_1 and T_2, ($T_1 > T_2$ and $T_2 <$ WAT) by setting the temperatures of two thermal baths. Once the desired set points were reached, the cold finger was inserted into the water-oil mixture in the reservoir containing waxy emulsion/dispersion to start wax deposition.

6.B.4 Flow Loop Experiments

Flow loop wax deposition experiments were performed under ambient pressure with the newly built Michigan Flow Loop. Figure 6-4 shows a schematic drawing of the flow loop apparatus.

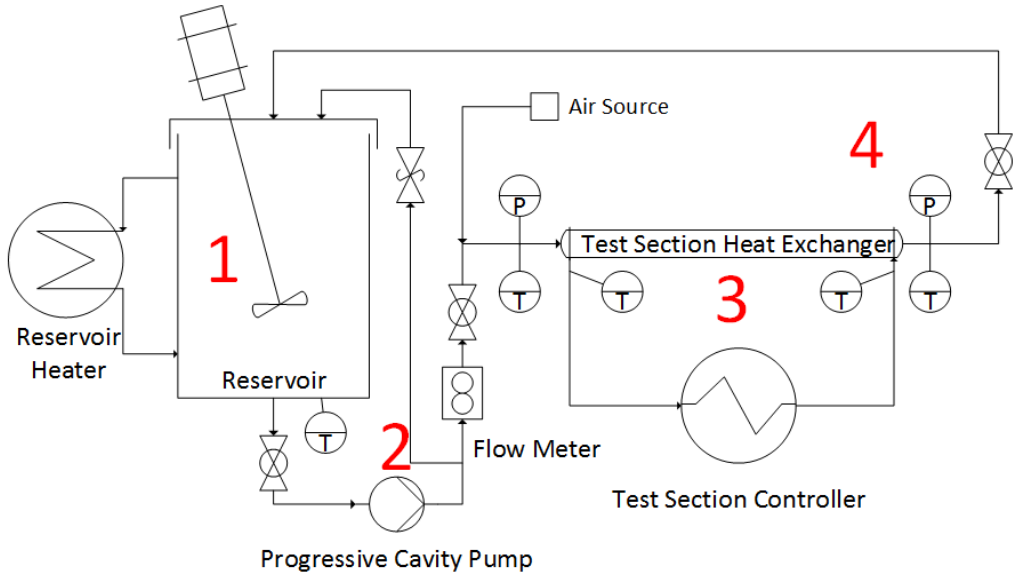

Figure 6-4: A schematic drawing of the Michigan Flow Loop; labeled sections refer to: 1) conditioning system, 2) pumping system, 3) testing system and 4) data acquisition system

The flow loop apparatus consists of four key parts: the conditioning system, the pumping system, the testing system and the data acquisition system. The flow loop test section is a double pipe heat exchanger with an inner diameter of 0.4 inch and a length of 4 feet. A hot waxy oil/water-in-oil mixture and a cold coolant streams flow in a counter-current configuration to generate wax deposition. Thermal couples are installed at the inlet and outlet of the test section to monitor the temperatures of the waxy oil/water-in-oil mixture and the coolant at these locations. Pressure transducers are installed at the inlet and the outlet of the test section in order to monitor the build-up of pressure drop due to deposit formation. The test section can be detached from the flow loop apparatus for sampling of wax deposit at the end of wax deposition experiments. In order to perform wax deposition experiments, wax and surfactants were dissolved in the mineral oil in the reservoir. Water-in-oil dispersion was prepared by addition of water into the reservoir followed by circulation of the water-in-oil mixture in the flow loop apparatus at the desired flow rate. It should be noted that only "model oil 2" was used for the flow loop wax deposition

experiments as the wax deposition rate achieved with “model oil 1” is unreasonably low due to its low wax content and wax appearance temperature.

6.B.5 Characterization for Water Content and Droplet Size Distribution

In order to measure the water content of the deposit, the deposit sample was first dissolved in a 1:1 (based on volume) mixture of toluene and acetone. The water content was then measured with a Mettler Toledo V20 Volumetric Karl-Fischer Titrator.

Two techniques were used to characterize the droplet size distribution. An optical microscope was used to characterize the droplet size distribution of stable emulsions generated with a surfactant dosage higher than 0.5wt.% as well as the deposits generated from stable emulsions. In order to carry out this characterization, a liquid film of the sample was prepared by placing a drop on a glass slide followed by compressing with a cover slide. The microstructures of the emulsion and deposit were inspected by a Nikon Eclipse E600 microscope. A 50×objective lens and a 10× eyepiece were attached to the microscope. A Sony ACV-D7 CCD camera was used to take photos. With model oil 1, the wax particles dissolve in the oil phase at room temperature. Without the interference from wax particles, the droplet size distribution can be measured based on the micrographs using image-processing software, ImageJ. For dispersions generated with a lower surfactant concentration (0.1wt.% to 0.2wt.%), phase separation occurs rapidly in absence of wax particles. Therefore, the droplet size distribution can only be characterized in presence of wax particles, which retard phase separation. As a result, such characterization is only possible with the deposits generated with model oil 2 whose WAT is significantly higher than the room temperature. Unfortunately, suspended wax particles then cause the micrographs of the dispersion/deposit to become hazy. As a result, a non-optical method is necessary for the characterization of droplet size distribution for the water-in-oil dispersions and the deposit

generated from dispersions. The DOSY-NMR technique[78,81,115] is used for this characterization. DOSY-NMR measures the ^{1}H signal attenuation with increasing pulse field gradient, which is due to the Brownian motion of H_2O molecules. This signal attenuation becomes more profound if the Brownian motion of the molecules generates a large mean square displacement. As a result, Brownian motions of water molecules enclosed by a coarse droplet will lead to a smaller signal attenuation compared to the Brownian motions of molecules enclosed by a fine droplet as the boundaries of droplets limit the mean square displacement of the Brownian motions. Based on this principle, the measured signal attenuation can be used to back-calculate the droplet size distribution. The DOSY-NMR experiments in this investigation were performed on a 400 MHz Varian MR400 NMR spectrometer at the University of Michigan NMR facility.

6.B.6 Characterization of the Yield Stresses of Waxy Gels and Waxy Emulsion Gels

The yield stresses of the waxy gels/waxy emulsion gels were measured with an AR2000 controlled stress rheometer. The yield stress tests were performed with model oil 2 and the corresponding stable emulsions (with a surfactant concentration of 1wt.%) with water contents of 10, 30, 50 and 70 vol.%. These emulsions were generated with a Scilogex D160 homogenizer. Before testing for the yield stress, a gel was first formed in the geometry gap of the rheometer by cooling of the waxy model oil/emulsion from ~10 °C above its WAT to ~30°C below its WAT. The evolution of the storage and loss moduli were probed with an oscillatory stress of 1 Pa and an oscillatory frequency of 0.1 Hz during cooling of the sample. The gelation temperature was defined as the cross-over point between the storage modulus – temperature and the loss modulus – temperature trajectories. The shear stress imposed on the gel was then increased at a ramp rate of 20 Pa/min and the viscosity was monitored during this stress ramp test. The shear stress at

which the viscosity decreases drastically is defined as the yield stress of the gel, as shown in Figure 6-5.

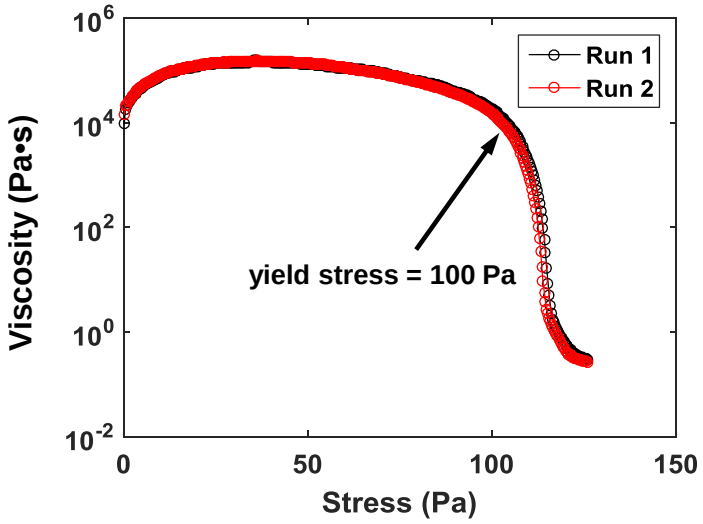

Figure 6-5: Determination of the yield stress of a waxy gel/waxy emulsion gel based on the viscosity-stress trajectory

For the yield stress tests, a serrated bottom plate was mounted on top of the smooth bottom plate and a serrated 40 mm plate was used as the top geometry. Use of such serrated surfaces prevents slippage between the sample and the bottom plate/top geometry and improves the reproducibility of the tests. As can be seen from Figure 6-5, excellent reproducibility in the yield stress measurements can be achieved with the serrated bottom plate and top geometry.

6.C Cold Finger Experiments

Cold finger wax deposition experiments were first performed to investigate the entrapment of water droplets in the deposit. Table 6-3 summarizes the experimental runs and the variables investigated.

Table 6-3: Cold finger experimental matrix

Group 1: Investigate of the ***effect of bulk water content*** and the ***time-evolution*** of deposit water content

Experiments in this group were performed under ambient pressure, an oil reservoir temperature of 15 °C and a finger temperature of 5°C

Experimental Run No.	Water Content in the Bulk (vol.%)	Surfactant Loading (wt.%)	Duration (hr)
1-4	10,30,50,70	1	1/12
5-8			1/4
9-12			1/2
13-16			1
17-20			2

Group 2: Investigate the effect of ***bulk droplet size*** on the deposit water content

Experiments in this group were performed under ambient pressure, an oil reservoir temperature of 50 °C and a finger temperature of 5°C

Experimental Run No.	Water Content in the Bulk (vol.%)	Surfactant Loading (wt.%)	Duration (hr)
21	50	0.1	1/2
22		0.15	
23		0.2	
24		0.5	
25		1	

6.C.1 Water Content and Droplet Size Distribution of Wax Deposits from Stable Water-in-Oil Emulsion (with Model Oil 1) in a Cold Finger

Cold finger wax deposition experiments were first performed with a stable water-in-oil emulsion using model oil 1 with varying Water Contents (WC) from 10 (WC = 10) to 70 vol.% (WC = 70). For WC = 10 and WC = 30 emulsions, the deposition experiments were performed under stirring while the experiments with WC 50 and WC 70 were performed under stationary conditions as stirring is not possible owing to the high viscosity of these emulsions with high water contents. Figure 6-6 shows the comparison between the water contents of the water-in-oil emulsion in the cold finger and the deposit.

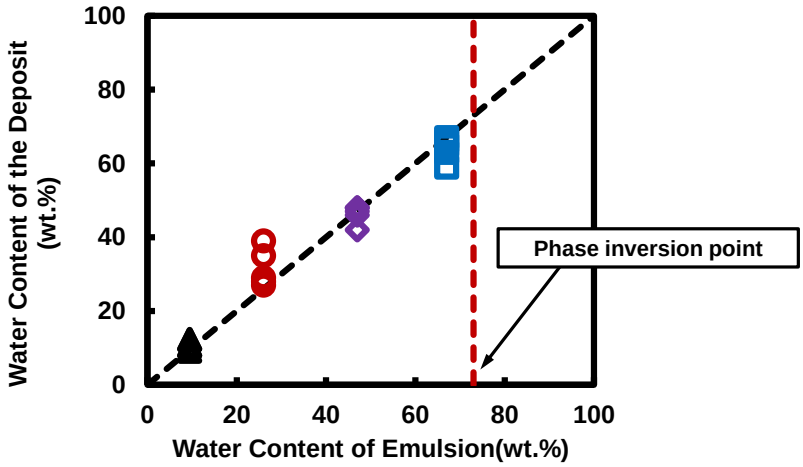

Figure 6-6: Comparison between the water content in the deposit with that in the emulsion[iv]

As can be seen from Figure 6-6, the deposit water content equals that of the bulk for all experiments performed with stable water-in-oil emulsions before phase inversion occurs. In order to determine the phase inversion point, the viscosities of the water-in-oil emulsion with various water contents were measured. The phase inversion point was determined as the water content where a maximal viscosity is observed.

Figure 6-6 suggests that the deposit water content can be as high as that of the emulsion, i.e., the emulsion water content is the upper bound of the deposit water content. This upper bound is reported here for the first time. None of the previous experimental investigations was able to establish this upper bound[69,104].

All previous experimental investigations reported deposits with a lower water content than that of the bulk[69,104]. Moreover, no apparent correlation was observed between the deposit and bulk water content. Consequently, in order to support the experimental findings in this study, the

[iv] Different data points at the same bulk water content represent deposit water contents obtained with various deposition durations of 5 minutes, 15 minutes, 30 minutes, 60 minutes and 120 minutes.

droplets in the deposit were inspected using an optical microscope. Figure 6-7 shows the micrograph of the deposit and the emulsion.

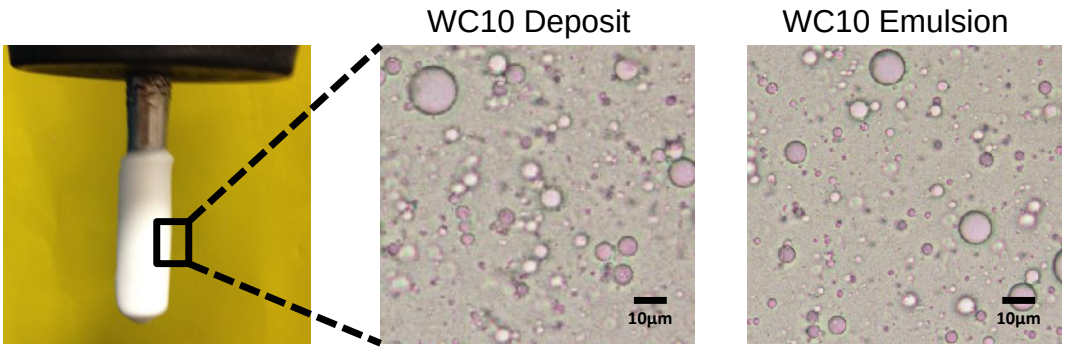

Figure 6-7: Comparison between the microstructures of deposit and emulsion

As can be seen from Figure 6-7, water droplets remain dispersed in both the emulsion and the deposit. Figure 6-8 shows the comparison between the droplet size distribution of the deposit and that of the emulsion extracted from image analysis based on micrographs.

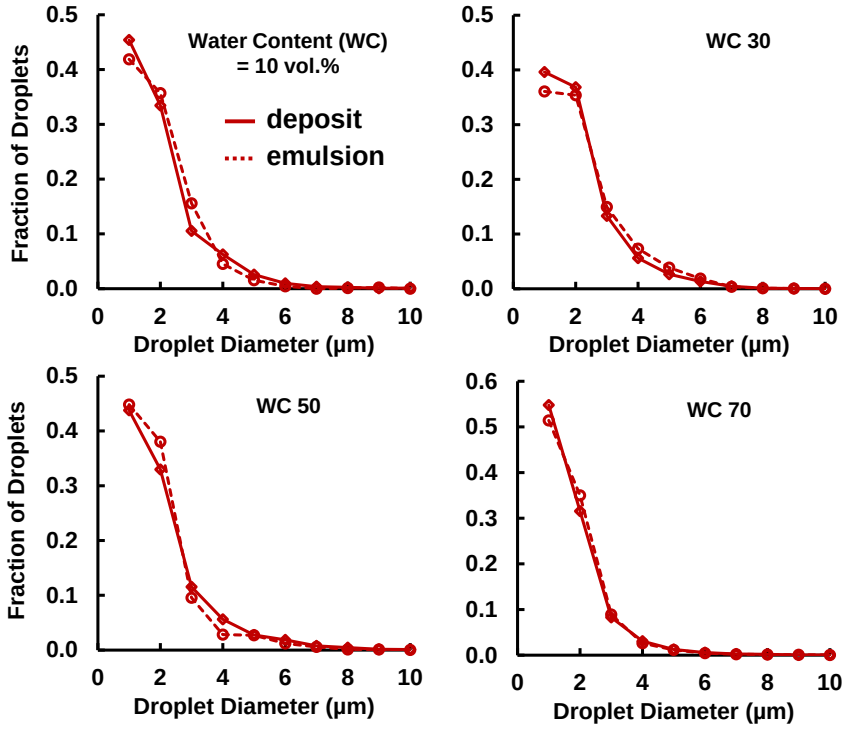

Figure 6-8: Comparison between the droplet size distributions of the deposit and the emulsion

As can be seen from Figure 6-8, the droplet size distributions in the deposit and in the emulsion are virtually the same.

The results shown in Figure 6-8 are the first reported comparisons of droplet size distribution in the deposit and in the emulsion. Identical water contents and droplet size distributions of the deposit and emulsion suggest that water droplets are entrapped "in-situ" in the void space enclosed by the interlocking network of wax particles during deposit formation.

6.C.2 Time Evolutions of the Water Content and Droplet Size Distribution from Stable Water-in-Oil Emulsion in a Cold Finger

Wax deposition is a long-term process that can occur over a time period on the order of weeks. During the process of wax deposition, it has been shown that the deposit thickness as well as the deposit wax content increase over time[21,34,116,117]. However, the time evolution of the water content in wax deposit has not been well understood. Consequently, cold finger wax deposition experiments were then performed with various durations in order to understand the time evolution of the water content and droplet size distribution. Figure 6-9 shows an example of the increases in the deposit weight and wax content over a 2-hour period, confirming deposit growth and aging.

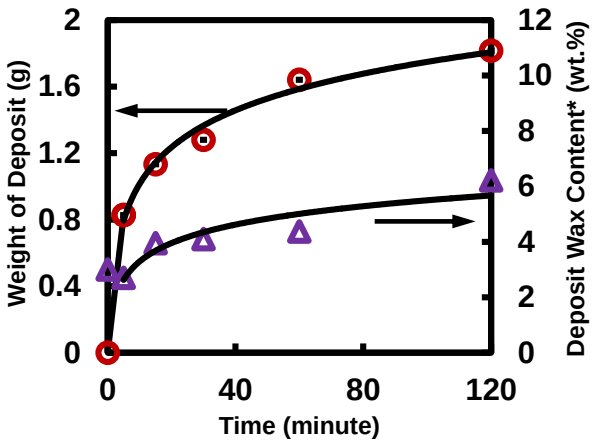

Figure 6-9: Time evolution of the deposit weight and wax content with a water content of 10 vol.%[v]

[v] Deposit wax content is defined as $m_{wax}/(m_{wax}+m_{deposit})$ and the mass of water is not included.

Figure 6-10 (a) shows the evolution of deposit water content over a deposition period of 2 hours. The theoretical water content was calculated based on the amount of oil and water added to the reservoir at the beginning of the wax deposition. Figure 6-10 (b) shows the evolution of deposit droplet size distribution over the same deposition period.

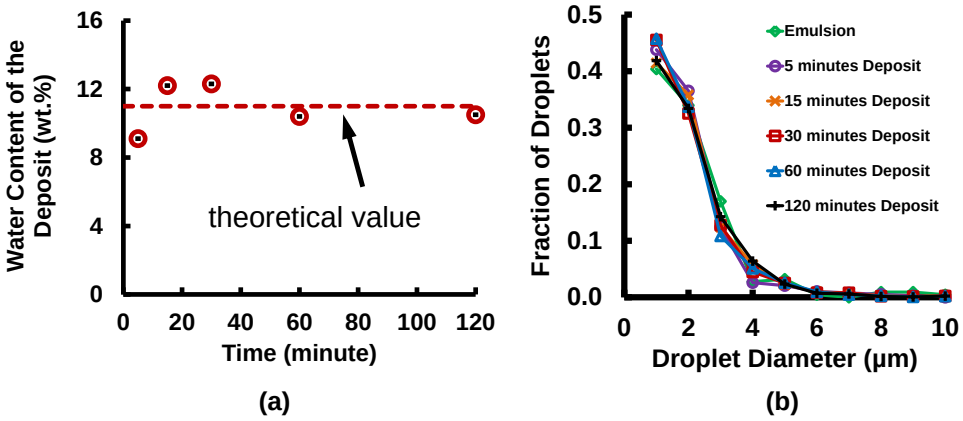

Figure 6-10: Time evolutions of (a) water content and (b) droplet size distribution of the deposit generated from emulsion with a water content of 10 vol.%

As can be seen from Figure 6-10, the deposit water content as well as the droplet size distribution remain constant during the process of deposit growth. Constant water content during wax deposition was also observed from tests performed with higher water contents (30 vol.%, 50 vol.% and 70 vol.%), shown in Figure 6-11.

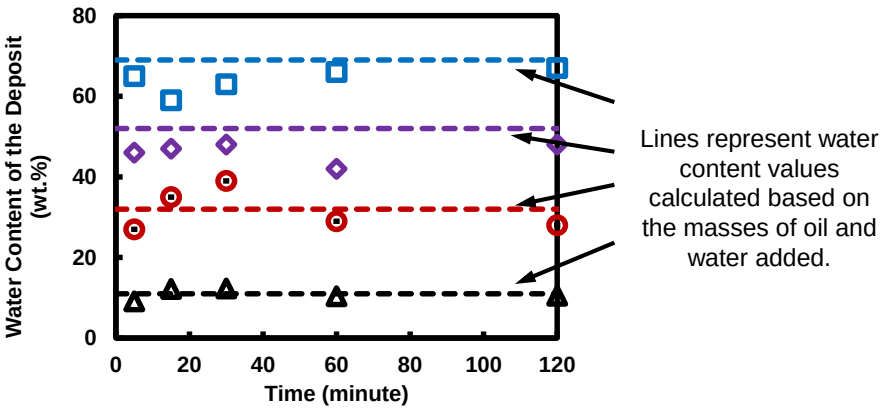

Figure 6-11: Time evolution of water contents of the deposits generated from emulsions with water contents of 10, 30, 50 and 70 vol.%

The evolution of the deposit water content and droplet size distribution with time, shown in Figure 6-10 and Figure 6-11 respectively, reveal the mechanism of droplets entrapment by the deposit. That is, the deposit water content and the deposit droplet size distribution do not vary with time, suggesting the water droplets are entrapped "in-situ" in the deposit solid matrix.

6.C.3 Effect of Droplet Size on the Entrapment of Water during Wax Deposition (with Model Oil 2) in a Cold Finger

In order to explain the different characteristics of the deposit water content observed in this investigation (deposit water content equals the bulk water content) with the observations in literature (deposit water content does not correlate with the bulk water content), we hypothesize that the deposit water content depends on the droplet size of the bulk. Intuitively, droplets smaller than the void space of the deposit solid matrix can be entrapped by deposition. Wax deposition experiments with various droplet size were then performed to test this hypothesis. The size of the water droplets in the bulk was varied by varying the surfactant loading within a range of 0.1 wt.% to 1.0 wt.%. It should be noted that with low surfactant dosages (< 0.5wt.%), the resulting water-in-oil dispersions undergo rapid phase separation when kept stationary. Therefore, model oil 2 with a WAT above the room temperature was used for this investigation of the effect of droplet size on the entrapment of water during wax deposition. Because the WAT of model oil 2 is above the room temperature, wax particles precipitate and act as barriers against flocculation and coalescence of water droplets, retarding phase separation and allowing for droplet size characterization.

Figure 6-12 shows the variation of the water content of the deposit as a function of surfactant loading. Recall that the water-in-oil mixtures prepared with surfactant concentrations at 0.5 wt.% and 1 wt.% are termed as "water-in-oil emulsions" as they present long-term stability

against phase separation. The water-in-oil mixtures prepared with surfactant concentrations below 0.5 wt.% are termed as "water-in-oil dispersions" as they undergo rapid phase separation when kept stationary.

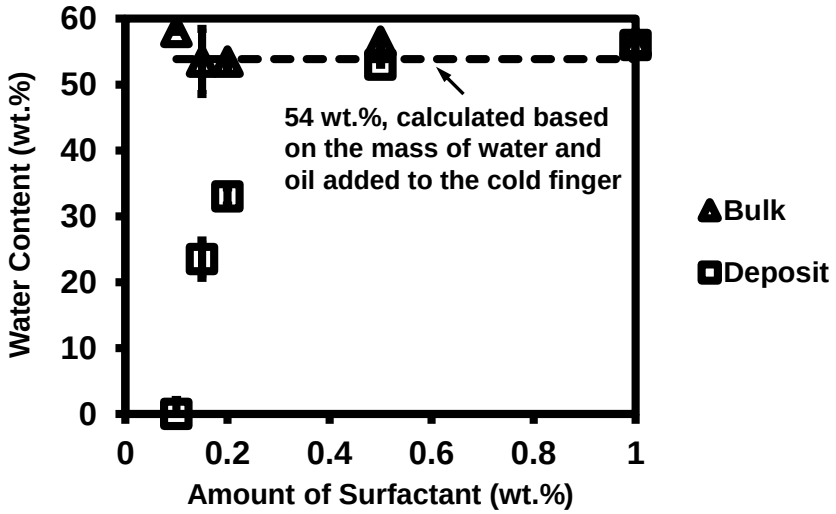

Figure 6-12: Effect of surfactant concentration on the water content of the deposit generated from an emulsion or dispersion with water content of 50 vol.% (54 wt.%)

As can be seen from Figure 6-12, regardless of the surfactant concentration, the water content of the bulk always equals the water content calculated based on the amount of water and oil added to the cold finger. Based on this observation, it can be conclude that although surfactant concentrations below or equal to 0.2 wt.% are not sufficient to generate stable emulsions, mixing provided by the stir plate can maintain homogeneous dispersions during wax deposition experiments. It can also be observed from Figure 6-12 that the water content of the deposit increases with increasing surfactant concentration. When the surfactant concentration increases to as high as 0.5 wt.%, the deposit water content equals that of the emulsion as measured by Karl-Fisher titration. The droplet size of the dispersion decreases with increasing surfactant concentration as the surfactant lowers the interfacial tension between oil and water, making it easier for fine droplets to form. Therefore, it may be deduced that the water content of the deposit increases with decreasing droplet size in the bulk, i.e., fine droplets are easier to be

incorporated in the deposit than coarse droplets. If this hypothesis holds, the droplet size distribution of the deposit should be smaller than that of the dispersion. In order to test this expectation, we proceeded to measure the droplet size distributions of the deposit and the emulsion/dispersion. The droplet size distribution has to be measured with the DOSY-NMR technique as the conventional microscopy experiments are not applicable owing to the following reason. Measuring droplet size distribution with conventional microscopic experiments requires melting of suspended wax particles. Unfortunately, with the low surfactant dosages (0.1 wt.% - 0.2 wt.%) in the oil phase, phase separation occurs rapidly upon melting of wax particles. DOSY-NMR does not require the wax particles to be melted for droplet size distribution characterizations. Solid wax particles can then act as barriers to flocculation/coalesce of water droplets and retards phase separation, shown in Figure 6-13.

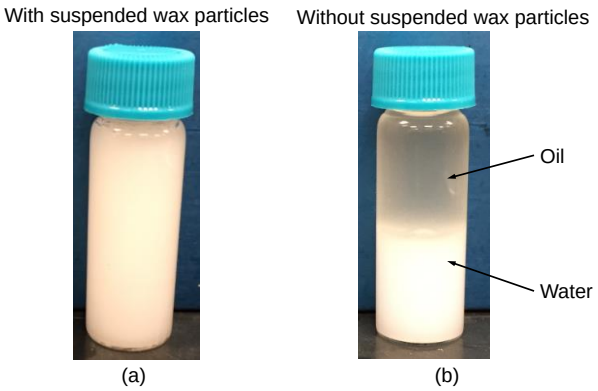

Figure 6-13: Bulk appearance of water-in-oil dispersion prepared with a low surfactant dosage at 0.1 wt.% after kept stationary for 30 minutes: (a) bulk stability of water-in-oil dispersion in presence of suspended wax particles and (b) rapid phase separation of oil and water in absence of wax particles

DOSY-NMR measures the droplet size based on ^{1}H signal attenuation under pulse field gradient due to the Brownian motion of water molecules in the droplet. Brownian motions of the water molecules enclosed by fine droplets are expected to generate a smaller signal attenuation than that generated by water molecules enclosed by coarse droplets. In order to demonstrate the effect of droplet diameter on the ^{1}H signal attenuation, DOSY-NMR measurements were taken

for a stable emulsion prepared with a surfactant concentration of 0.5wt.%, a dispersion with a surfactant concentration of 0.2wt.% and DI water. Figure 6-14 shows the comparison between the acquired $^{1}H_2O$ proton NMR signal attenuations from these three samples.

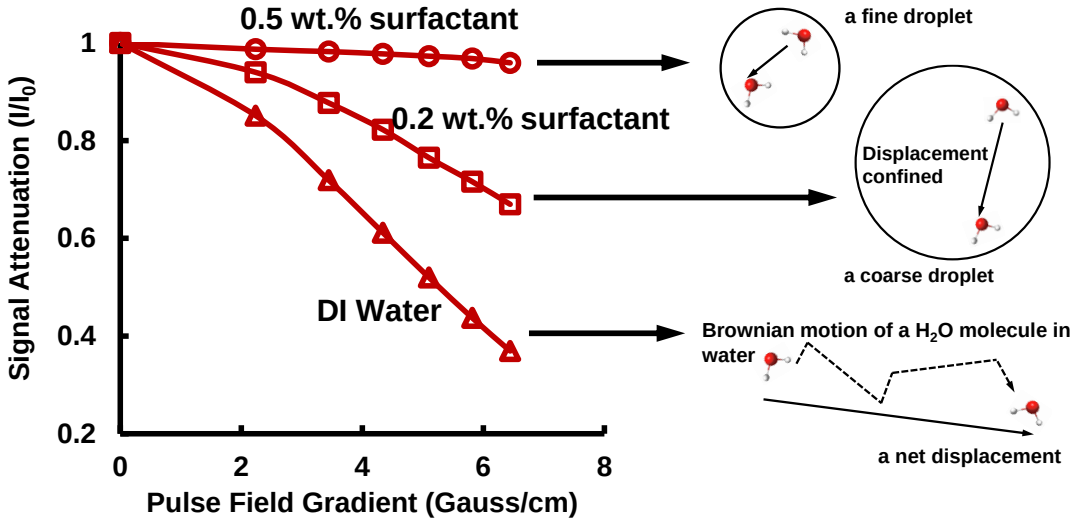

Figure 6-14: An illustration of the effect of droplet diameter on the ^{1}H signal attenuation of the H_2O molecules enclosed by droplets

As can be seen from Figure 6-14, the minimal signal attenuation was observed with the emulsion sample prepared with a surfactant concentration of 0.5 wt.%, indicating a finer droplet diameter than the dispersion prepared with a surfactant concentration of 0.2 wt.%. The DI water sample generates the largest signal attenuation as the Brownian motions of the water molecules are not restricted by any boundary at all. The measured NMR signal attenuation can then be used to back-calculate the droplet size distribution.

Figure 6-15 shows the measured signal attenuation of the water molecules in the emulsion/dispersion and deposit formed with four different surfactant concentration: 0.5wt.%, 0.2wt.%, 0.15wt.% and 0.1 wt.%.

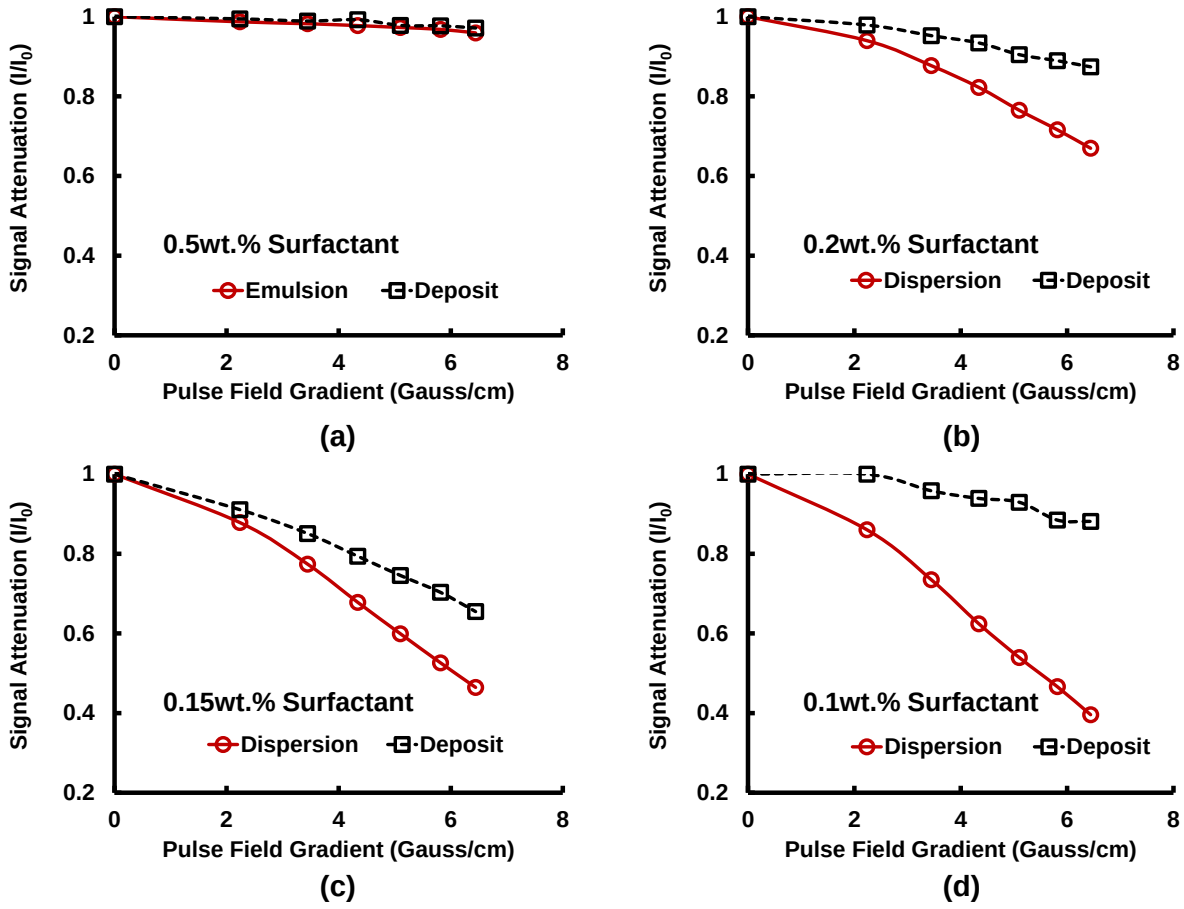

Figure 6-15: Comparisons between the ^{1}H signal attenuations of H_2O molecules in the emulsion/dispersion and deposits under pulse field gradients

As can be seen from Figure 6-15 (a), the ^{1}H signal attenuations of the water molecules in the emulsion and in the deposit generated with a surfactant concentration of 0.5wt.% are virtually the same, indicating identical droplet size in the emulsion and the deposit. The signals obtained from the deposit samples always decrease at a slower rate with increasing pulse field gradient when the surfactant concentration is less than or equal to 0.2 wt.%, as seen in Figure 6-15 (b)-(d), qualitatively suggesting that the deposit droplet size is smaller than the bulk droplet size. Figure 6-16 shows the quantitative droplet size distribution of the emulsion/dispersion and deposits back-calculated from the measured signal attenuations.

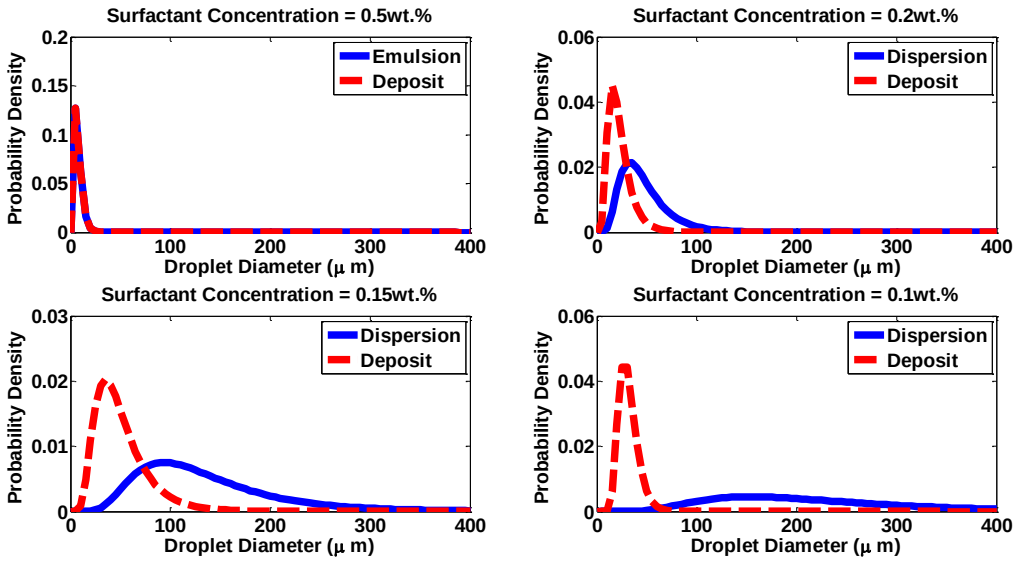

Figure 6-16: Comparison between the droplet size distributions of the emulsions/dispersions and the deposits generated from the corresponding emulsions/dispersions

As can be seen from Figure 6-16, the droplet size distribution of the deposit is smaller and narrower than or equal to that of the dispersion in all experimental runs, supporting our initial hypothesis that fine droplets are more easily incorporated in the deposit than coarse droplets. Moreover, the size of the droplets that can be incorporated in the deposit is usually smaller than ~100 microns.

Recall that no obvious correlation between the water content of the bulk and that of the deposit was observed in previous studies while we have observed same water contents of the bulk and deposit. This inconsistency can now be explained: at low surfactant dosages, coarse droplets are generated but cannot be trapped by deposit formation, leading to a lower water content of the deposit than that of the oil. It should be noted that the droplet size of a dispersion formed with a particular crude oil depends on the intrinsic emulsifying power of the natural surfactants contained by this crude oil.

6.D Role of Water Droplets on the Shearing and Sloughing of Waxy-Emulsion Gels

Entrapment of water droplets in the deposit significantly lowers its yield stress, as is denoted by the blue circles in Figure 6-17. It was first suspected that the lowered yield stress of the waxy emulsion gel is due to the addition of surfactants. However, follow-up experiments indicated that the addition of surfactant to a concentration of up to 1 wt.% has negligible impact on the yield stress of the gel, as is denoted by the red triangle in Figure 6-17.

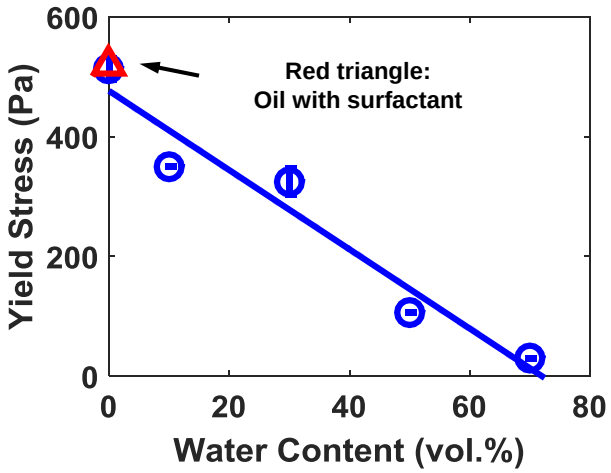

Figure 6-17: Effect of water content of the waxy emulsion gel on the yield stress of the gel

As can be seen from Figure 6-17, the yield stress of the waxy emulsion gel decreases with increasing water content of the gel. The waxy emulsion gel at a water content of 70 vol.% has a yield stress (30 Pa) that is less than 10% that of the waxy gel free of water (510 Pa). These two gels also have distinct appearances after breakage, shown in Figure 6-18.

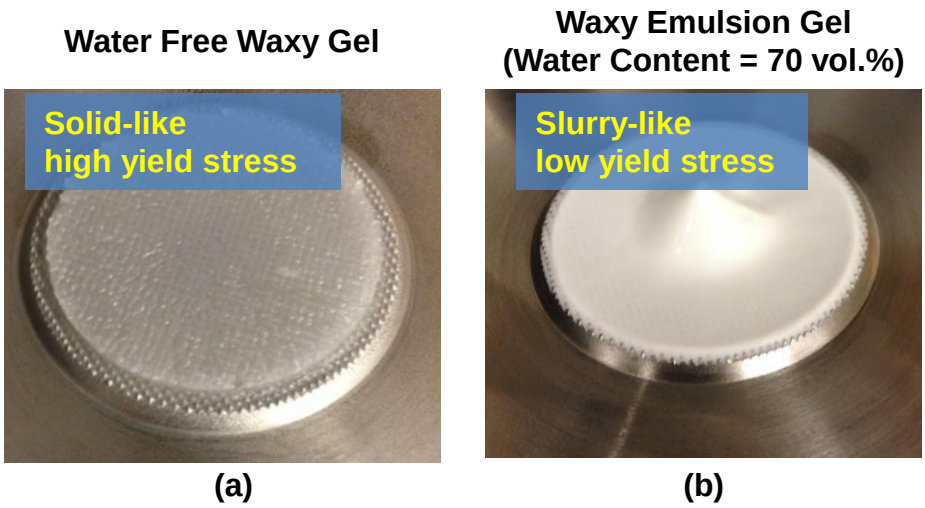

Figure 6-18: Appearances of the water free waxy gel and waxy emulsion gel after gel breakage

As can be seem from Figure 6-18 (a), the water free waxy gel appears to be mostly solid-like with debris broken from the edge of the gel. On the contrary, the emulsion gel with a water content of 70 vol.% becomes slurry-like after gel breakage, as is seen in Figure 6-18 (b).

A lowered yield stress can cause the deposit to become prone to be "sloughed off" by the shear stress imposed by the fluid flow, leading to a significantly lower wax deposit build-up predicted by conventional wax deposition models. The "sloughing-off" of wax deposit containing water droplets in the deposit was also investigated with a flow loop apparatus in the section 6.E below.

6.E Flow Loop Wax Deposition Experiments

Wax deposition experiments were performed with water-in-oil dispersion (prepared at a surfactant concentration of 0.1wt.%). Figure 6-19 shows the pressure-time trajectory for wax deposition experiments carried out with water content of the bulk at 10 vol.%. In the experimental runs performed with and without water in the bulk, the Reynolds number associated with the pipe flow is approximately 300. In other words, wax deposition experiments were performed in laminar flow regime.

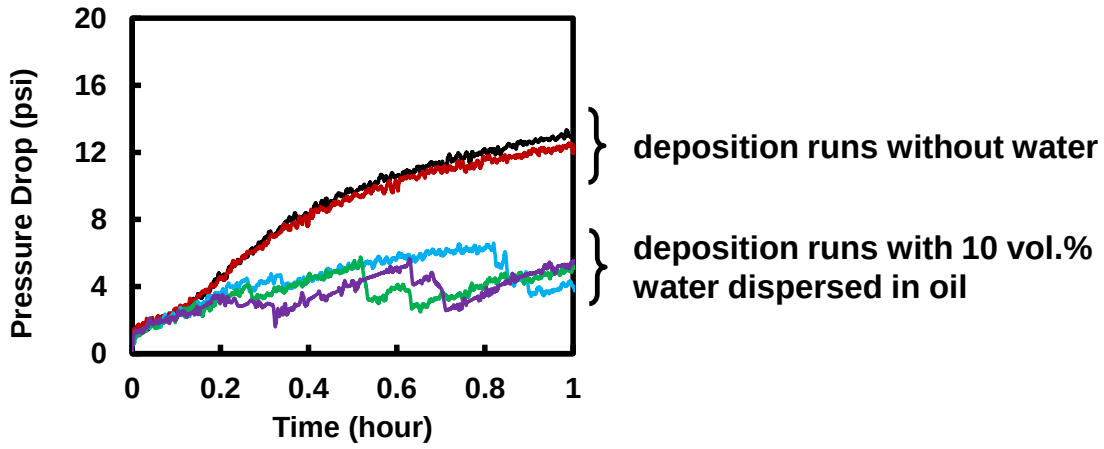

Figure 6-19: Pressure-time trajectories for wax deposition experiments with various water contents of the bulk at the following operating conditions: T_{oil} = WAT+5°C, temperature of the coolant stream, $T_{coolant}$ = WAT-30°C and oil flow rate Q_{oil} = 0.2 m^3/hr

As can be seen from the experiments with water-in-oil dispersion, the pressure drop increases due to deposit build-up and then decreases abruptly multiple times during the experiment. These abrupt drops in the pressure transducer reading serve as the first evidence of deposit slough-off. In order to confirm this slough-off phenomenon, we also meticulously inspected the times at which these rapid drops in pressure transducer occurred and looked for other evidence that suggest "slough-off". It was discovered that the thermal couple readings at the test section outlet decreased immediately after each and every decrease in the pressure transducer reading, shown in Figure 6-20.

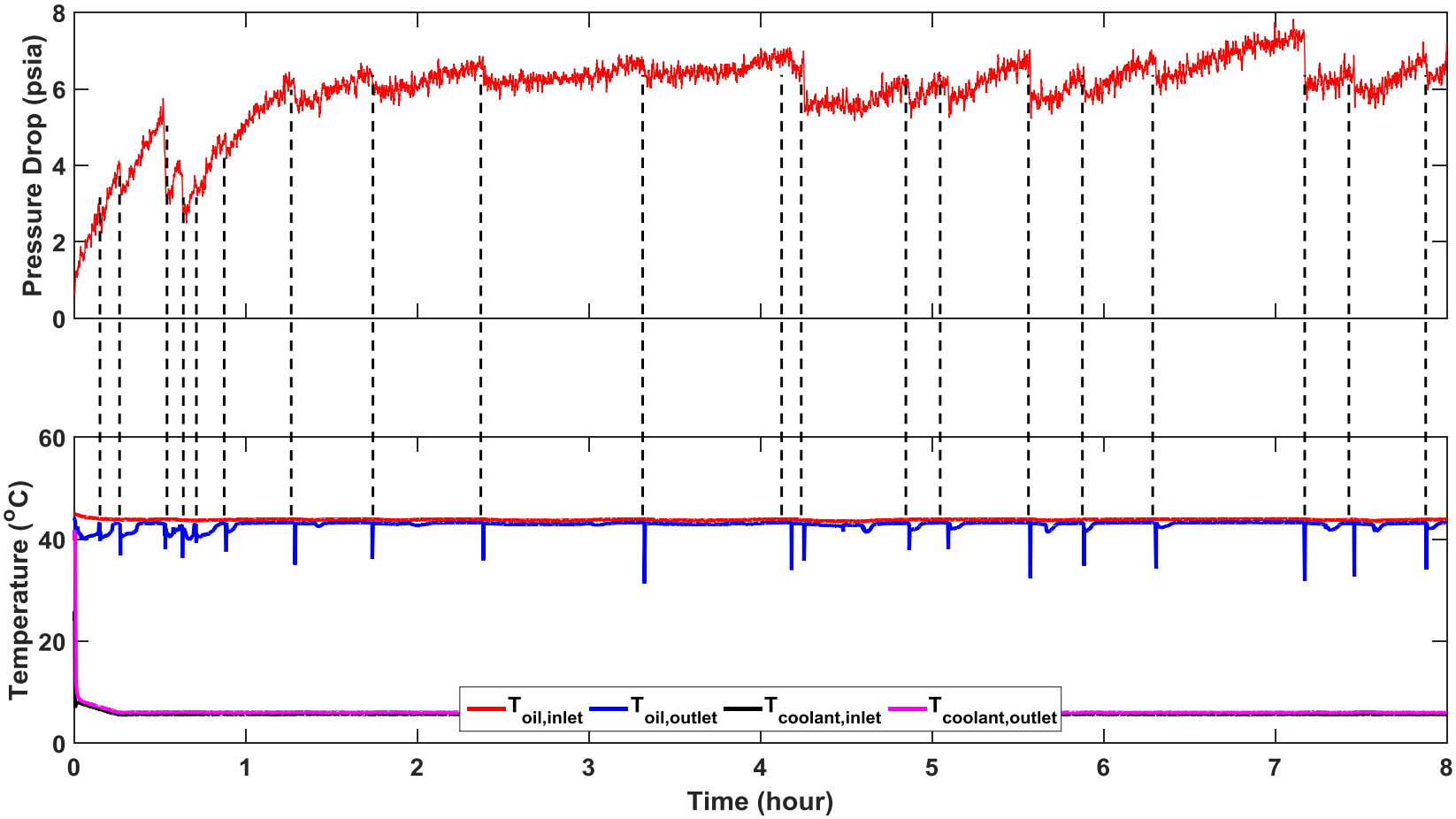

Figure 6-20: Correlation between the abrupt decreases in the pressure transduser and outlet thermal couple readings supports the hypothesis that deposit sloughed off under imposed shear

This correlation between the drop in pressure and temperature readings indicates that a small piece of deposit was first sloughed off from the cold pipe wall/deposit-fluid interface, leading to less restriction of the pipe flow and a corresponding decrease in the pressure drop. This debris then traveled with the fluid flow and eventually reached the outlet thermal couple. The contact of the wax deposit debris with the thermal couple causes a decrease in the thermal couple reading because this debris is removed from the cold wall and is at a lower temperature than the bulk. It should be noted that no such correlated drops in the pressure transducer and thermal couple readings were observed for single phase wax deposition experiments, shown in Figure 6-21.

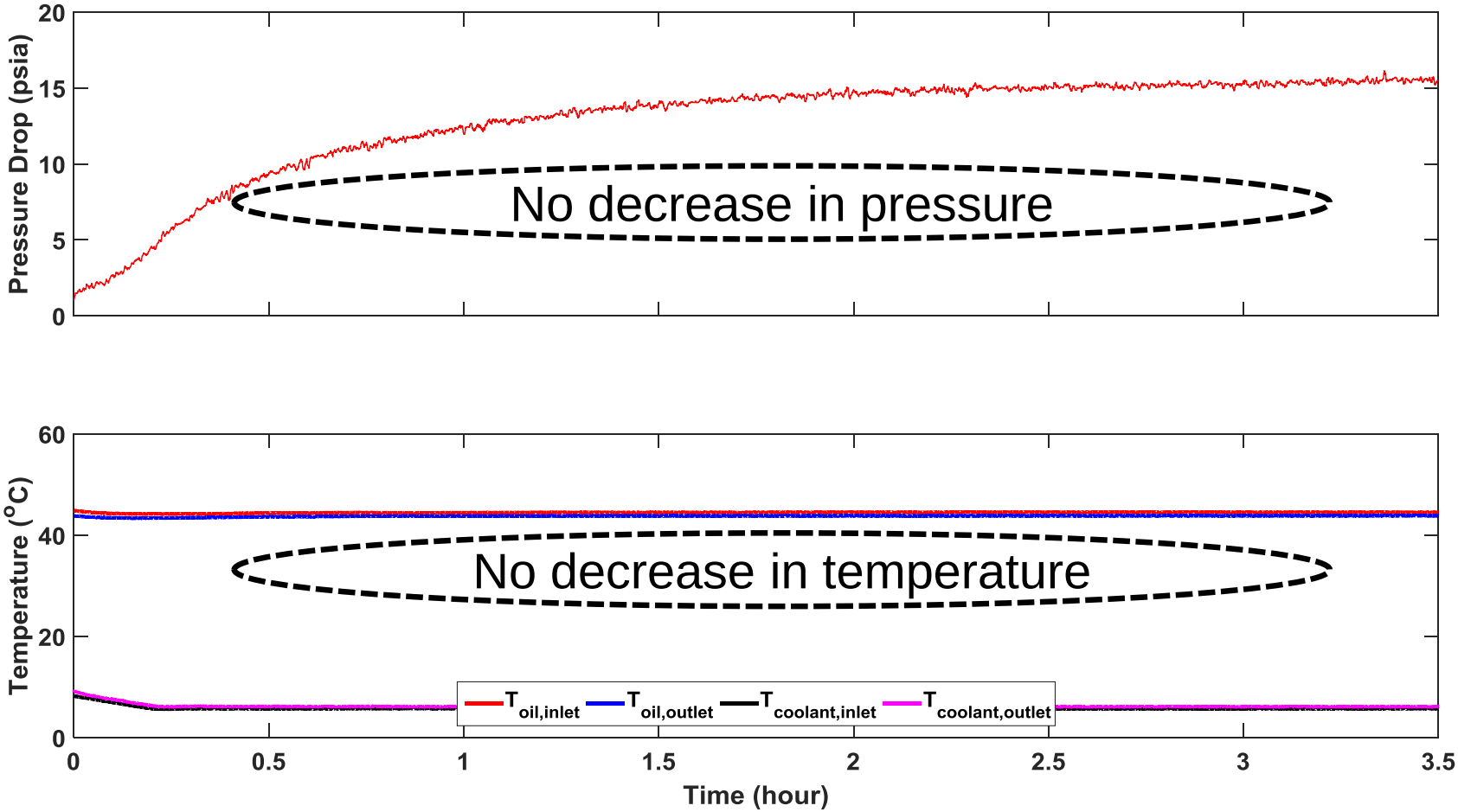

Figure 6-21: Pressure drop and thermal couple readings during a single-phase wax deposition experiments with the following operating conditions: T_{oil} = WAT+5°C, temperature of the coolant stream, $T_{coolant}$ = WAT-30°C and oil flow rate Q_{oil} = 0.2 m^3/hr

The simultaneous drops in the pressure and the outlet temperature confirm slough-off. It should be noted that characterization of the deposit shows a water content of as low as 5 wt.%, suggesting a small amount of water can drastically lower the yield stress of the deposit and make it prone to slough-off.

6.F Conclusions

In this investigation, we presented the most comprehensive characterization of the entrapment of water droplets in the wax deposit during wax deposition from water-in-oil emulsion/dispersion. This characterization resolves inconsistencies in the deposit water content measurements in literature. The key findings in this investigation are:

- The upper limit of the deposit water content equals the water content of the bulk.
- When the water droplets of the dispersion are coarse, the deposit will contain virtually no water even with a bulk water content of as high as 50 vol.%.
- Comparison between the bulk and deposit droplet size distributions suggests that only the droplets smaller than 100 microns in diameter can be incorporated in the deposit.

In addition, based on the rheological characterizations as well as flow loop experiments, the following roles of the dispersed water phase on wax deposit build up are reported.

- Incorporation of the water droplets in the deposit leads to a significant decrease in the deposit yield stress.
- This decrease in the deposit yield stress causes deposit to become prone to be sloughed off during deposit build up, leading to a lower overall deposition rate.

Figure 6-22 highlights the key points addressed in this investigation.

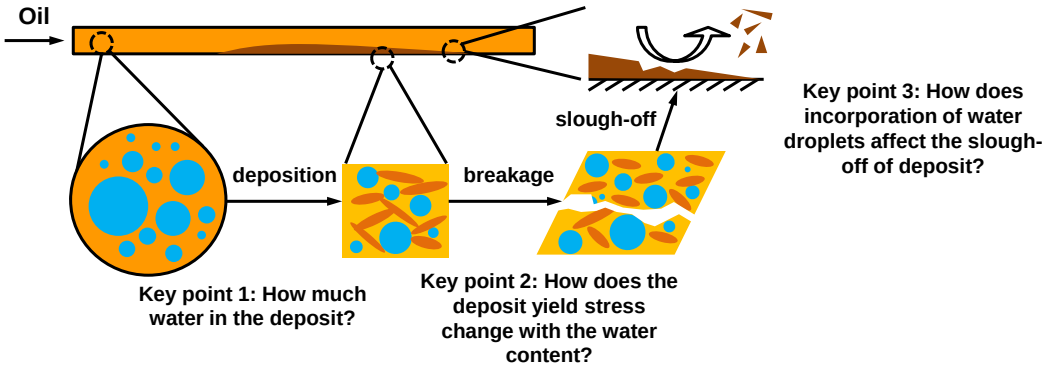

Figure 6-22: Highlights of the key points addressed in this investigation: 1) incorporation of the water droplets in the deposit, 2) lowered yield stress of deposit due to incorporation of water droplets and 3) slough-off of deposit due to the lowered yield stress

We may expect that with a crude oil rich in natural surfactants, the wax deposit formed from water-in-crude oil dispersion/emulsion can contain a large number of fine droplets and become prone to slough-off.

Without the consideration for deposit slough-off, existing wax deposition models can significantly over-predict the deposit growth rate, resulting in conservative design. This over-prediction is likely to occur when the crude oil of interest contains a large amount of natural surfactants. The deposits formed with such crude oils are then expected to entrap a large amount of water droplets, leading to frequent sloughing. It should be noted that the slough-off of wax deposit is random. Modeling of such stochastic process is beyond the scope of the current investigation. Such modeling campaign likely requires advanced techniques in probability theory.

Chapter 7

Wax Deposition Modeling with Considerations of non-Newtonian Characteristics: Application on Field Scale Pipeline

7.A Introduction

7.A.1 Wax Deposition in Subsea Pipelines

During subsea oil transportation, the crude oil is cooled by the sea water. Dissolved wax molecules contained by the crude oil will precipitate when the temperature of the fluid is below the wax appearance temperature (WAT). Precipitation of wax is expected to be the most profound at the pipe wall where the lowest temperature is encountered among all radial locations, generating a radial concentration gradient of the dissolved wax and a net flux of dissolved wax towards the wall. Radial diffusion of wax molecules causes wax to deposit on the inner pipe wall, reducing the effective pipe diameter and posing severe risks to oil production. To remove the wax deposit, pigging operations need to be performed. It should be noted that frequent pigging will generate significant operational costs while insufficient pigging will lead to thick and hard deposit that is impossible to remove[8]. Therefore, determination of a proper pigging frequency is crucial to the subsea oil production. Determination of a proper pigging frequency relies on wax deposition and aging rates predicted by wax deposition models. Continuing efforts have been dedicated to improving wax deposition modeling capabilities, especially upscaling from laboratory-scale predictions to field applications.

7.A.2 Non-Newtonian Characteristics of Waxy Crude Oil

A dynamic yield stress and shear thinning characteristics can be observed for waxy crude oil when the temperature is below the WAT. Such unique non-Newtonian characteristics originate from the precipitation of wax at temperatures below the WAT and the resulting wax-in-oil suspension. The complex rheology of waxy crude oil below the WAT has been extensively studied[54,118–121]. These investigations show that various constitutive equations, including the Cross model[122], the Casson model[123] and the Herschel-Bulkley model[123], can usually be used to fit the non-Newtonian flow curves of waxy crude oils. Furthermore, it has been found that the non-Newtonian rheology of waxy crude oil has a significant impact in the modeling of pipeline restart[124,125]. Unfortunately, the role of non-Newtonian fluid characteristics of waxy crude oil in wax deposition modeling is not well-understood. The next subsection discusses the steps involved in wax deposition modeling and the potential roles of non-Newtonian fluid characteristics in these steps.

7.A.3 Wax Deposition Modeling Considering non-Newtonian Fluid Mechanics

A wax deposition model consists of three steps: 1) hydrodynamic calculations, 2) heat and mass transfer calculations which then allow for 3) the calculation of deposit thickness. The hydrodynamic calculation predicts the pressure drop along the pipeline. Pressure drop predictions can be used to compare with the measured pressure drop in experiments/field operations to benchmark the wax deposition model. In addition, hydrodynamic calculations predict the radial velocity profile and the eddy momentum diffusivity to be used in the subsequent heat and mass transfer calculations. Heat and mass transfer calculations simulate the heat loss from oil to the surroundings and the radial molecular diffusion of wax, followed by calculations of deposit growth and aging. These steps in the wax deposition modeling algorithm

need to be enhanced to capture the non-Newtonian characteristics of waxy crude oil. Benallal et al. and Zheng et al. first attempted to model wax deposition with non-Newtonian fluid mechanics in laminar flow regime[126,127]. In this investigation, we analyzed non-Newtonian turbulent characteristics to enable turbulent applications such as industrial scale pipe flow.

The following section, i.e., Section 7.B, discusses two existing numerical techniques, including Large Eddy Simulation (LES) and Reynolds-Averaged Navier Stokes (RANS) simulation, for

- Hydrodynamic modeling to calculate the shear stress at wall/deposit-fluid interface as well as the radial velocity profile and eddy diffusivities.
- Heat and mass transfer modeling

Predictions from the theoretically advanced LES are used as benchmarks to assess the more commonly used RANS. It was found that RANS cannot be used to model non-Newtonian turbulent flow.

In Section 7.C, we will develop a method to model hydrodynamics, heat and mass transfer by adapting the law of the wall method. The predictions from the modified law of the wall agree well with those from LES. Section 7.D discusses the modeling of wax deposit formation based on first principles of the rheology of waxy oil. Finally, the wax deposition model developed by combining findings from Sections 7.B - 7.D will be applied to simulate deposit build-up in a real-world field pipeline, discussed in Section 7.E.

7.B Hydrodynamic Modeling with Non-Newtonian Characteristics

The hydrodynamic calculations will predict the pressure drop, the radial velocity profile as well as the eddy momentum diffusivity. The pipeline pressure drop, or equivalently, the shear stress at the pipe wall/deposit-fluid interface is a critical parameter for pipeline design. Moreover, as will be discussed in Section 7.D, the prediction of the deposit growth rate is achieved by

comparing the shear stress imposed by the fluid and the dynamic yield stress of the deposit. In the laminar flow regime, the wall shear stress of both Newtonian and non-Newtonian fluids can be analytically derived as a function of the pipe diameter, the flow rate and the rheological parameters of the fluid of interest. However, transportation of crude oil in subsea pipelines usually occurs in turbulent flow regime. Therefore, it is imperative to establish reliable methods to calculate the wall shear stress for industrial scale field pipeline transporting waxy crude oils. At temperatures above the wax appearance temperature, a waxy crude oil behaves as a Newtonian fluid and the calculation of wall shear stress for Newtonian turbulent pipe flow can be readily achieved using a friction factor correlation such as the one by Blasius[128], shown in Equation (7-1).

$$f_D = 0.316\,\mathrm{Re}^{-1/4} \tag{7-1}$$

$f_D =$ Darcy friction factor

$\mathrm{Re} =$ Reynolds number

The wall shear stress can then be calculated using the friction factor shown in Equation (7-2)

$$\tau_{\text{wall/interface}} = f_D \frac{\rho_{\text{oil}} U^2}{8} \tag{7-2}$$

$\tau_{\text{wall/interface}} =$ shear stress imposed by the fluid at wall/deposit-fluid interface,(Pa)

$\rho_{\text{oil}} =$ density of the oil,(kg/m^3)

$U =$ superficial velocity of the oil,(m/s)

Unfortunately, methods to calculate the wall shear stress of turbulent non-Newtonian pipe flows are not well established[129]. The most common approach is to calculate the shear stress at the wall based on friction factors correlations. However, friction factor correlations are available only for non-Newtonian fluids whose flow curves follow simple rheological models such as the power law model[130] and the Herschel-Bulkley model[131]. The complexity of the rheological behavior of a waxy crude oil can be beyond these classical rheological models[118,132]. Friction factor correlations for non-Newtonian fluids with complex rheological behaviors do not exist at

this time. In addition, different friction factor correlations can give drastically different predictions for the wall shear stress, even for the same non-Newtonian fluid. Under extreme conditions, the prediction of the wall shear stress obtained from one correlation can be twice as high as the prediction from another correlation[129]. Therefore, it is imperative to develop reliable methods to model the hydrodynamics of non-Newtonian turbulent pipe flow.

The turbulent characteristics of non-Newtonian pipe flow can be modeled from first principles with Direct Numerical Simulation (DNS). This simulation can be achieved by numerically solving the Navier-Stokes equations, shown in Equation (7-3).

$$\rho_{\text{oil}} \frac{\partial \mathbf{U}}{\partial t} + \mathbf{U} \cdot \nabla \mathbf{U} = -\nabla p + \nabla \cdot \tau = -\nabla p + \nabla \cdot \mu \left[\nabla \mathbf{U} + (\nabla \mathbf{U})^T \right] \tag{7-3}$$

t = time,(s)

$\mathbf{U}$ = the velocity vector,(m/s)

p = pressure,(Pa)

τ = stress tensor,(Pa)

μ = viscosity of the oil,$(Pa \cdot s)$

The viscosity of the fluid can be described by a non-Newtonian constitutive equation, such as the Herschel-Bulkley equation shown in Equation (7-4).

$$\mu = \frac{\tau_y + K |\dot{\gamma}|^n}{|\dot{\gamma}|} \tag{7-4}$$

τ_y = dynamic yield stress,(Pa)

K = consistency,$(Pa \cdot s^n)$

$|\dot{\gamma}|$ = strain rate magnitude (s^{-1})

n = flow index

It should be noted that in order to resolve the motions of turbulent eddies, the size of the computational grid needs to be smaller than the size of the turbulent eddies. For an industrial pipeline, the Reynolds number can be on the order of 10^6. The size of the smallest eddies associated with this Reynolds number will be on the order of 10^{-3} m. Consequently, resolution of all the turbulent eddies in a 10-km industrial scale pipeline with an inner diameter of 12 in. will

require a computational mesh with as many as 10^{12} computational cells. Simulation with such computational intensity is not feasible. As a result, DNS is usually prohibitive in engineering applications, e.g., wax deposition modeling in subsea pipelines, due to the computational intensity. In comparison with DNS, large eddy simulation (LES) is more promising to be adapted to model the turbulence characteristics in industrial scale pipelines owing to its relatively more tolerable computational intensity. In LES, only the turbulent eddy motions larger than the computational cell size are resolved, thereby significantly reducing the computational intensity and cost of LES. With the existing computational power, LES is the best available approach to investigate the turbulence characteristics for non-Newtonian pipe flow at field scale. However, the computational intensity associated with LES still does not allow it to be applied on the entire pipeline with a length scale of kilometers. Therefore, we will first perform LES for sections of a field scale pipeline (NOT the entire pipeline) in order to gain insights on the turbulent characteristics of non-Newtonian pipe flow. We will then use LES to evaluate the turbulent characteristics predicted by more computationally efficient approaches for hydrodynamic modeling including Reynolds Average Navier Stokes (RANS) method and methods based on the law of the wall to see if they can be used.

7.B.1 Large Eddy Simulation (LES)

In this section, we will perform large eddy simulation (LES) to uncover the turbulent characteristics of the non-Newtonian oil flow in an industrial scale pipeline. The findings from LES will be compared with the predictions from the more commonly used Reynolds Average Navier Stokes (RANS) method to assess if the RANS method can be used to account for the non-Newtonian fluid mechanics in wax deposition modeling.

7.B.1.a LES Governing Equations

LES does not resolve all the turbulent eddies in the flow field but just the large ones. In order to do so, the pressure and velocity first undergo a filtering operation defined according to Equation (7-5).

$$\bar{\phi}(\mathbf{x}) = \frac{1}{V}\int_{\mathrm{V}} \phi(\mathbf{x}')\mathrm{d}\mathbf{x}', \quad \mathbf{x}' \in \mathbf{V} \tag{7-5}$$

$\bar{\phi}$ = the filtered variable of interest,
e.g., pressure, velocity, temperature, concentration
V = volume of the computational cell,(m^3)
$\mathbf{x}'$ = position vector pointing from the origin to the location of interest,(m)
$\mathbf{V}$ = space enclosed by the computational cell,(m^3)

The filter operation calculates the volume average of the variable of interest over the computational cell. The mass and momentum balances were then constructed with the filtered variables as the independent variables. The filtered mass balance is shown in Equations (7-6). It should be noted that the equation was expressed in the Einstein tensor notation for brevity.

$$\frac{\partial \rho_{\mathrm{oil}}}{\partial t} + \frac{\partial}{\partial x_i}\left(\rho_{\mathrm{oil}}\overline{U_i}\right) = 0 \tag{7-6}$$

$x_i (i = 1,2,3)$ = the three spatial directions,(m)
$\overline{U_i} (i = 1,2,3)$ = filtered velocity components in the three directions,(m/s)

The momentum balance is shown in Equation (7-7).

$$\frac{\partial}{\partial t}\left(\rho_{\mathrm{oil}}\overline{U_i}\right) + \frac{\partial}{\partial x_j}\left(\rho_{\mathrm{oil}}\overline{U_i}\,\overline{U_j}\right) = \frac{\partial}{\partial x_j}\left[\mu(\bar{\dot{\gamma}})\left(\frac{\partial \overline{U_i}}{\partial x_j} + \frac{\partial \overline{U_j}}{\partial x_i}\right)\right] - \frac{\partial \bar{p}}{\partial x_i} - \frac{\partial \tau_{ij}}{\partial x_j} \tag{7-7}$$

$\bar{p}$ = filtered pressure,(Pa)
τ_{ij} = sub grid scale (SGS) stress components,(Pa)

7.B.1.b Input Parameters for LES

Subsea pipelines are usually with the length scale of tens of kilometers. Along the length of a subsea pipeline, the temperature of the fluid can change by as much as 50°C, leading to a drastic

change in the volume fraction of solid wax of the fluid along the axial direction. Consequently, the rheological parameters of the fluid can vary significantly along the pipe from upstream to downstream locations. In order to demonstrate this unique development of the hydrodynamics along the subsea pipeline associated with the change in the local rheological parameters, LES were performed at five difference axial locations. To generate rheological parameters for these five simulations, a preliminary simulation was first conducted with the pipeline dimensions and operating conditions shown in Table 7-1.

Table 7-1: Summary of input parameters for LES hydrodynamic simulation in a field pipeline section

Diameter, D (m)	0.3048
Length, L (m)	1.524 (L = 5D)
Velocity (m/s)	0.75
Total flow rate, Q (m^3/hr)	196.9
Viscosity at Inlet (c.P.)	1.76
Reynolds number (based on viscosity at the inlet)	111702

The Newtonian fluid mechanics approach is used in this preliminary simulation in order to estimate the solid volume fraction in the bulk and the rheological parameters associated with the local solid wax volume fraction. In the complete wax deposition model presented later in the manuscript, the heat/mass transfer simulations are integrated with non-Newtonian hydrodynamic simulations.

LES were performed with rheological parameters taken at five different axial positions with different bulk temperatures shown in Figure 7-1.

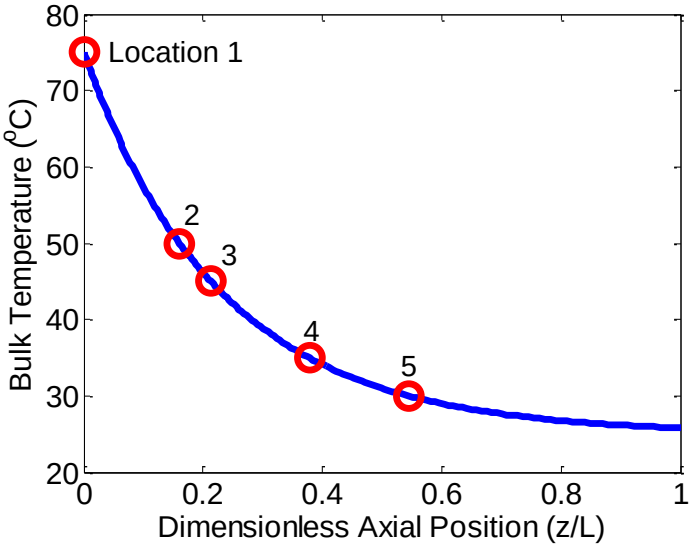

Figure 7-1: Axial bulk temperature profile evolution and locations at which the rheological parameters are used for LES hydrodynamic simulations

We begin the analysis by using the Herschel-Bulkley model for the LES. The rheological parameters in the Herschel-Bulkley equation, namely the dynamic yield stress, τ_y, the consistency, *K*, and the flow index, *n* were obtained based on the measured viscosity – temperature curves at various shear rates, shown in Figure 7-2.

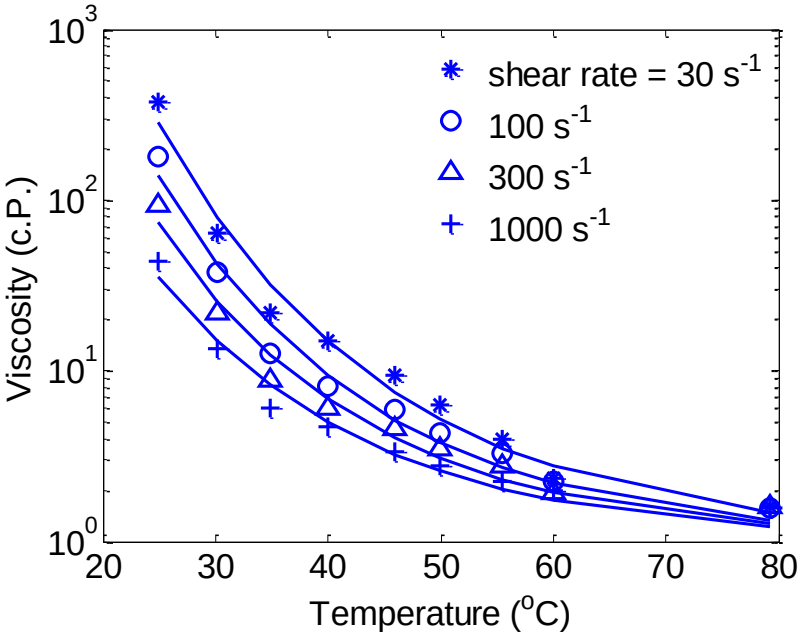

Figure 7-2: Typical crude oil viscosity – temperature curves measured at various shear rates[59]

The Herschel-Bulkley model parameters at a particular temperature were obtained by fitting the viscosity measurements at this temperature under various shear rates using the Herschel-Bulkley equation. The fitted parameters at the aforementioned 5 axial locations are shown in Table 7-2.

Table 7-2: Summary of Herschel-Bulkley model parameters used for hydrodynamic simulations at different axial pipeline locations

Location	Temperature (°C)	τ_y (Pa)	K (Pa×s^n)	n
1	75	0 (Newtonian)	0.002	1.00
2	50	0.09	0.004	0.94
3	45	0.15	0.007	0.91
4	35	0.81	0.035	0.81
5	30	2.22	0.094	0.76

7.B.1.c Computational Specifications

The LES was implemented with a commercial computational fluid dynamic software, FLUENT 16. The computational mesh represents a 1.5-meter-long section of pipeline with an inner diameter of 0.305 m. In order to reduce the required length of the computational domain to achieve fully-developed turbulent flow, a pair of periodic boundary conditions was used at the inlet and outlet of the computational domain. The entire computational mesh contains 7,000,000 computational cells. Fine computational mesh grids were used in the vicinity of the pipe wall. A transient LES with a time step of 4 milliseconds was performed to model the evolution of the fluctuating velocity field. With this time step, it will take 2.5 hours to simulate 1 residence time (~ 2s) using 48 CPU's in parallel. It usually takes a simulation with 5 residence times to reach a statistical steady state after which 5 additional residence times were simulated to collect statistics. Therefore, each simulation to obtain time-averaged velocity profile and pressure drop in a 1.5-m pipe section will require 25 hours. This computational time required to model a 1.5-m pipe section prohibits the direct scale-up of LES to industrial scale wax deposition modeling

where the pipeline is usually several kilometers in length. Detailed procedures to perform LES is included in Appendix O.

It should be noted that the viscosity defined by the Herschel-Bulkley model approaches infinity as the shear rate approaches zero. As a result, this mathematical singularity can cause divergence in the CFD solver. In order to overcome this numerical challenge, the Herschel-Bulkley-Papanastasiou model[133] shown in Equation (7-8), was used instead of the conventional Herschel-Bulkley model.

$$\mu = \frac{\tau_y}{\dot{\gamma}}\left[1-\exp(-m\dot{\gamma})\right] + K\dot{\gamma}^{n-1} \tag{7-8}$$

This model preserves the non-Newtonian characteristics by the conventional Herschel-Bulkley model but continuously approaches an upper bound $m\tau_y$ instead of infinity as the shear rate approaches zero. In this simulation, the constant m is set to be 10^4s[133].

7.B.2 Numerical Results from LES at Axial Locations 1 – 3: Turbulent Flow

It should be noted that the crude oil is Newtonian at the inlet, i.e., location 1, as the inlet temperature is higher than the wax appearance temperature. Flow characteristics, such as velocity profile and pressure drop for Newtonian pipe flow have been extensively investigated and are readily available[128]. Using the parameters at location 1 listed in Table 7-2, we compared the pressure drop as well as the velocity profile predicted by LES and RANS and confirmed that the LES was correctly implemented. These comparisons were included in Appendix P in the supporting information.

At locations 2 and 3, the flow is expected to be non-Newtonian as the temperature is below the WAT at these two locations and thus, wax particles will form, causing the fluid to become non-

Newtonian. The LES results from locations 2 and 3 are qualitatively identical. We will now analyze the velocity profile predicted with rheological properties at location 3 as an example. Figure 7-3 shows an instantaneous velocity profile plotted at a cut-plane along the axial direction.

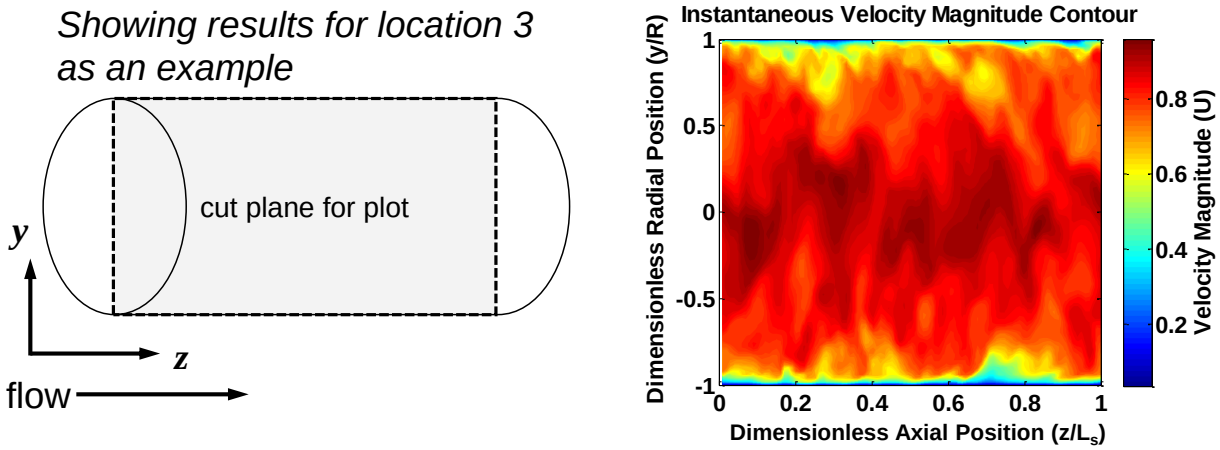

Figure 7-3: A snapshot of the instantaneous velocity magnitude generated from turbulent non-Newtonian pipe flow simulation performed with rheological parameters at location 3

As can be seen from Figure 7-3, the velocity field fluctuates spatially, indicating that a non-Newtonian turbulent flow regime is encountered at this location. As one approaches the centerline, the shear stress decreases and can potentially be lower than the local dynamic yield stress of the fluid[134]. It was previously speculated that a plug could form around the centerline. Based on Figure 7-3, it can be seen that the instantaneous shear rate fluctuation constantly breaks up the fluid microstructure near the centerline and therefore preventing this central plug from forming.

In comparison with LES, RANS is more computationally economical and commonly used for turbulent modeling[135,136]. Therefore, it is of interest to evaluate whether RANS can be used to calculate the velocity and turbulent diffusivity profiles of non-Newtonian turbulent pipe flow. Different from LES, RANS simulation solves the time-averaged Navier Stokes equation, shown in Equation (7-9).

$$\rho_{\text{oil}}\left\langle U_j\right\rangle\frac{\partial\left\langle U_i\right\rangle}{\partial x_j}=-\frac{\partial\left\langle p\right\rangle}{\partial x_i}+\frac{\partial}{\partial x_j}\left\langle\mu\left(\frac{\partial U_i}{\partial x_j}+\frac{\partial U_j}{\partial x_i}\right)\right\rangle-\frac{\partial}{\partial x_j}\rho_{\text{oil}}\left\langle U_i{}'U_j{}'\right\rangle \tag{7-9}$$

$\left\langle U_i\right\rangle(i=1,2,3)=\text{time}-\text{averaged velocity component in three spatial directions},(m/s)$

$\left\langle p\right\rangle=\text{time-averaged pressure},(Pa)$

$\rho_{\text{oil}}\left\langle U_i{}'U_j{}'\right\rangle=\text{Reynolds stress},(Pa)$

It should be noted that the time-averaged strain rate is used to calculate the strain rate-dependent viscosity in the RANS governing equations because RANS only tracks time-averaged quantities. Therefore, the calculation for viscosity is different in LES and RANS simulation. Figure 7-4 shows the comparison between the viscosity calculated with LES and RANS simulation.

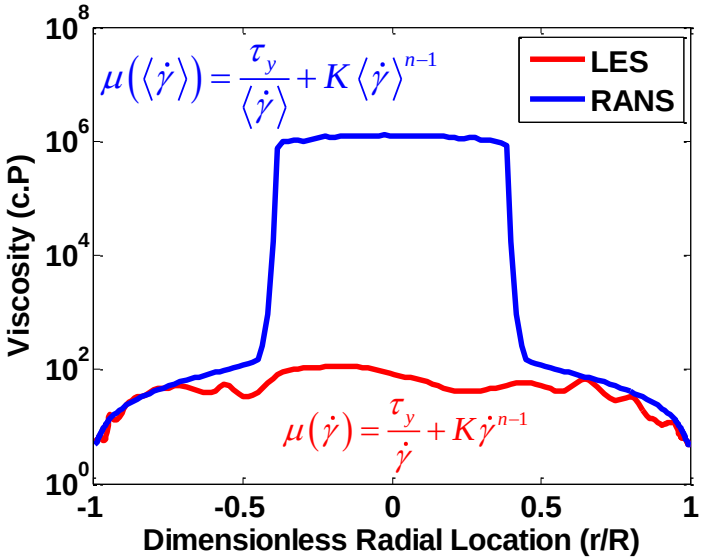

Figure 7-4: Comparison between the instantaneous viscosities predicted by LES and the time-averaged viscosity predicted by RANS

As can be seen from Figure 7-4, the RANS simulation predicts a plug with an extremely high viscosity in the central region of the pipe. It should be noted that the prediction of a plug is a numerical artifact because the RANS approach cannot resolve the instantaneous fluctuating strain rate in the central region. Consequently, RANS can significantly underestimate the intensity of turbulent mixing during heat and mass transfer simulation, leading to un-reliable predictions for the temperature and concentration profiles. In order to demonstrate this

shortcoming of RANS, RANS is used to solve the heat/mass transfer governing equation shown in Equation (7-10) and the predicted radial temperature/concentration profile was compared with the prediction from LES. Detailed implementations of RANS and LES to numerically solve Equation (7-10) are included in Appendix Q.

$$\frac{\partial \phi}{\partial t} + \frac{\partial}{\partial x_j}\left(U_j \phi\right) - \frac{\partial}{\partial x_j}\left(\Gamma \frac{\partial \phi}{\partial x_j}\right) = 0 \qquad (7\text{-}10)$$

ϕ = temperature or wax concentration

Γ = thermal or mass diffusivity,(m^2 / s)

Figure 7-5, shows the predicted radial temperature/concentration profile by RANS and LES.

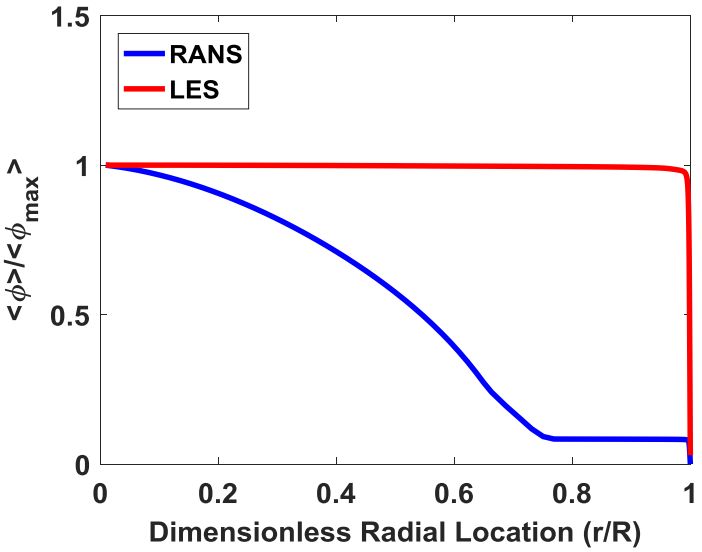

Figure 7-5: Predicted radial profile of temperature/concentration with RANS and LES

As can be seen from Figure 7-5, the prediction by RANS differs significantly from that by LES. It can be observed that RANS predicts a large gradient near the central region of the pipe flow due to the under-estimation of the effective diffusivity in this region.

A dimensionless number, Δ, characterizing the relative rate of convective and diffusive transfer, defined in Equation (7-11), was also calculated based on the temperature/concentration profiles predicted by RANS and LES, respectively. Note that Δ is identical to the Nusselt number in the context of heat transfer and Sherwood number for mass transfer.

$$\Delta = \frac{h_{\text{int}} D}{\Gamma} = \frac{-\frac{\partial \phi}{\partial r}|_{\text{wall}} \; D}{\phi_{\text{bulk}} - \phi_{\text{wall}}} \tag{7-11}$$

$\Delta \equiv$ Nu, Nusselt number for heat transfer,

$\Delta \equiv$ Sh, Sherwood number for mass transfer

h_{int} = internal convective transfer coefficient,(m/s)

D = pipe diameter,(m)

r = radial coordinate,(m)

ϕ_{bulk} = temperature/concentration in the bulk

ϕ_{wall} = temperature/concentration at wall

The calculated values of Δ are summarized in Table 7-3.

Table 7-3: Summary of the Δ values associated with the internal heat/mass transfer predicted by LES and RANS

LES	823
RANS	80

As can be seen from Table 7-3, for the non-Newtonian case with the RANS method, the predicted Δ value is significantly lower, indicating under-estimation of the heat/mass transfer in the central region due to the artificial plug. As a result, RANS cannot be used for heat/mass transfer modeling.

7.B.3 Numerical Results from LES Simulation at Axial Locations 4 and 5: Transition from Turbulent to Laminar Flow

Figure 7-6 shows the instantaneous steady state radial velocity profile obtained with rheological properties at location 5.

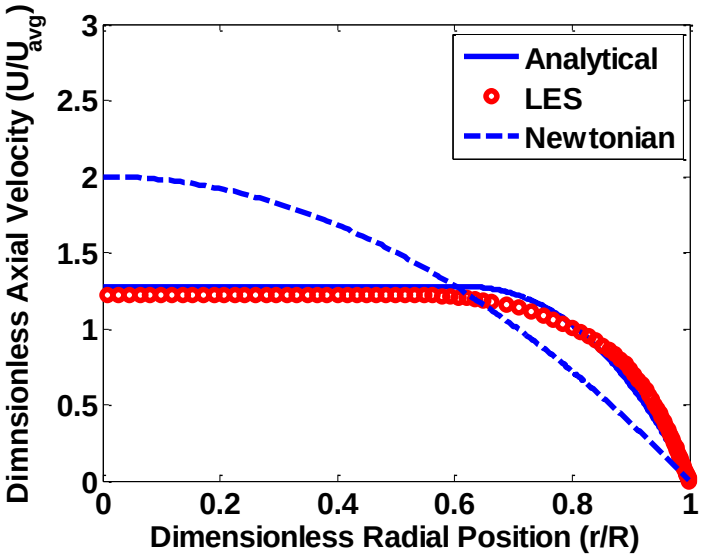

Figure 7-6: Comparison between the analytical and numerical velocity profiles of Herschel-Bulkley fluid with a laminar velocity profile expected for Newtonian pipe flow

It can be observed from Figure 7-6 that the velocity profile at axial location 5 is non-fluctuating, indicating that the flow field has become laminar at this downstream location. The significant amount of solid wax in the bulk at this location leads to a high viscosity in the bulk, dampening the turbulent eddies and causing transition from turbulent to laminar flow. In order to support this claim, the dampening of the turbulent kinetic energy of a fluid packet traveling along the centerline is included in Appendix R. Moreover, the non-fluctuating velocity profile predicted by LES corresponds well with the analytical solutions for the radial velocity profile of laminar Herschel-Bulkley fluid pipe flow. It should be noted that a plug is predicted in the center region of the pipe. Different from the artificial "plug" predicted due to numerical artifacts associated with RANS, this plug in laminar flow can be observed in laminar pipe flow experiments[137].

It should be noted that being able to capture the transition from turbulent to laminar flow along the axial direction is critical in the modeling of heat and mass transfer as turbulent flow has significant lower heat/mass transfer resistance than laminar flow.

In order to understand the impact of flow regime prediction on heat and mass transfer modeling, two heat transfer simulations were performed with 1) Newtonian viscosity model and 2) non-Newtonian viscosity model. Table 7-4 shows the parameters used in these two simulations.

Table 7-4: Input parameters for heat transfer simulation with Newtonian and non-Newtonian approach

	Case 1	Case 2
Viscosity Model	Arrhenius	non-Newtonian
Diameter, D (m)	0.3048	
Length, L (m)	1.524 (L = 5D)	
Velocity (m/s)	0.75	
Inlet Temperature (°C)	30	
Ambient Temperature (°C)	5	
External Heat Transfer Coefficient ($W/m^2/K$)	20	
Predicted Internal Heat Transfer Coefficient ($W/m^2/K$)	460	60

The conventional wax deposition model predicts a turbulent flow regime with the Newtonian viscosity-temperature dependence calculated using a form of the Arrhenius equation. However, the actual viscosity of the wax-in-oil suspension is significantly higher than the value calculated by the Arrhenius temperature dependence, as the Arrhenius temperature dependence does not account for the effect of suspended solid on viscosity. Due to the underestimation of the viscosity with the Arrhenius equation, conventional wax deposition models fail to predict the correct (i.e., laminar) flow regime. The internal heat transfer coefficient associated with the turbulent flow predicted from Case 1 using Newtonian fluid mechanics is 460 $W/m^2/K$ while that from a laminar flow in Case 2 is 60 $W/m^2/K$. We note that an approximately 700 % over-estimation in the internal heat transfer coefficient is observed by neglecting the transition from turbulent to laminar using non-Newtonian fluid mechanics discussed above. This over-estimation can translate into an over-estimation in the rate of heat transfer. As a result, it is essential to incorporate the modeling of non-Newtonian fluid mechanics in wax deposition modeling.

7.C A Computationally Efficient Method for Hydrodynamic Modeling to be Used in Wax Deposition Modeling

As was discussed in the previous section, neither LES nor RANS can be applied to model wax deposition in a pipeline. LES is unacceptably time consuming and RANS can generate numerical artifacts. Therefore, it is imperative to develop a reliable and computationally efficient method to predict the wall shear stress, velocity, temperature and concentration profiles to be used to predict wax deposition. This desired method should be able to capture the flow characteristics uncovered by LES simulations, recapitulated below:

- A flow pattern that can transit from turbulent to laminar flow due to the increase in viscosity.
- A plug in the near center line region that can be expected in the laminar flow regime while this plug is likely to be broken up by turbulent eddies in the turbulent flow regime.
- In the turbulent flow regime, a laminar boundary layer that can be observed in the vicinity of the wall while the local velocity fluctuates with time outside this boundary layer.

We now propose a reliable and computationally efficient method to perform hydrodynamic, heat and mass transfer modeling of non-Newtonian pipe flow. This method consists of three steps:

- Prediction of flow regime
- Calculation of velocity profile
- Calculation of turbulent diffusivity for heat and mass transfer modeling

These three steps which will be discussed individually in the three subsections to follow.

7.C.1 Prediction of Flow Regime

Chilton and Stainsby developed a friction factor correlation that can predict the wall shear stress of Herschel-Bulk pipe flows based on the fluid rheological parameters, the pipeline diameter and the flow rate[131], shown in Equation (7-12).

$$f_{HB} = 0.079\left[\frac{R_{HB}}{n^2(1-X)^4}\right]^{-0.25} \tag{7-12}$$

$$R_{HB} = \frac{\rho_{oil} UD}{\mu_w\left(\frac{3n+1}{4n}\right)\left(\frac{1}{1-aX-bX^2-cX^3}\right)}$$

$$X = \frac{\tau_y}{\tau_{wall}}, a = \frac{1}{2n+1}, b = \frac{2n}{(n+1)(2n+1)}, c = \frac{2n^2}{(n+1)(2n+1)}$$

f_{HB} = friction factor for a Herschel-Bulkley fluid

R_{HB} = Reynolds number for a Herschel-Bulkley fluid

μ_{wall} = viscosity of oil at wall,$(Pa \cdot s)$

This friction factor correlation is first utilized to predict the flow regime. The transition point is defined as the intersection of the wall shear stress – mean velocity relationship generated by assuming laminar and turbulent flows respectively. The rheological parameters taken at location 5 of the pipeline were used to generate an example for the flow pattern prediction, shown in Figure 7-7.

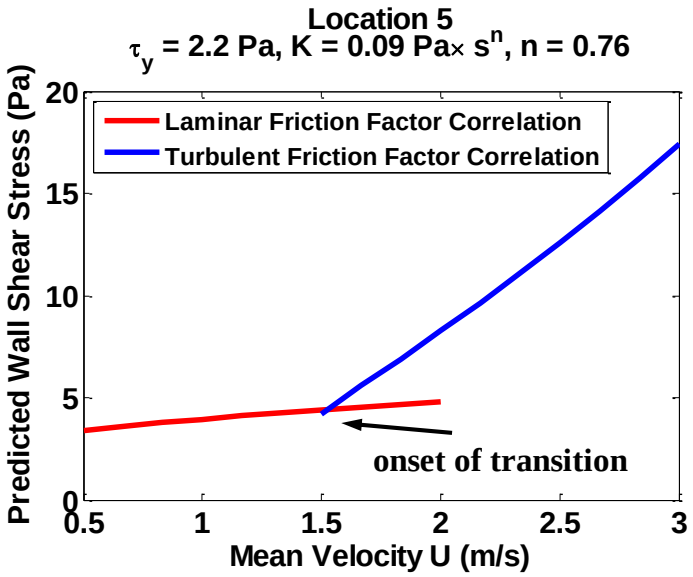

Figure 7-7: Prediction of wall shear stress based on the laminar and turbulent Chilton-Stainsby friction factor correlations and the definition of the onset for turbulent-laminar transition

A sensitivity analysis was also performed to understand the effect of rheological parameters, τ_y, *n* and *K* on the prediction of laminar turbulent transition. It was found that the transition occurs at a higher mean velocity with larger values of τ_y, *K* and with smaller values of *n*. Details with respect to this sensitivity analysis is included in Appendix S.

Table 7-5 shows the flow pattern predictions (Laminar or Turbulent) based on the Chilton-Stainsby friction factor correlation as well as predictions by LES.

Table 7-5: Predictions of flow regime with LES and Chilton-Stainsby (C-S) friction factor correlation

Location	Flow Pattern		Axial Location (% Total Length)
	LES	C-S	
1	Turbulent	Turbulent	0
2	Turbulent	Turbulent	16
3	Turbulent	Turbulent	21
4	Laminar	Laminar	38
5	Laminar	Laminar	55

7.C.2 Calculation of Velocity Profile

For the laminar flow regimes, an analytical solution for the velocity profile and pressure drop can be obtained. Therefore, we will now focus on developing a computationally efficient approach

for the hydrodynamic modeling of turbulent flow. In this subsection, we will explore modifications of the conventional law of the wall that are necessary in order for it to be applicable to non-Newtonian pipe flow. The conventional law of the wall can be expressed with the following Equations (7-13) to (7-14).

$$U_z^+ = \begin{cases} y^+ & y^+ \le 5 \\ 5\ln y^+ - 3.05 & 5 < y^+ \le 30 \\ 2.5\ln y^+ + 5.5 & y^+ \ge 30 \end{cases} \tag{7-13}$$

$$U_z^+ = \frac{U_z}{\sqrt{\tau_w / \rho_{oil}}}, y^+ = \frac{y}{\nu}\sqrt{\frac{\tau_w}{\rho_{oil}}} \tag{7-14}$$

$U_z = \text{axial velocity magnitude}, (m/s)$

$y = \text{distance from the wall}, (m)$

$\nu = \text{kinematic viscosity of oil}, (m^2/s)$

The conventional law of the wall is derived based on the idea that:

- A thin laminar sublayer exists in the immediate vicinity of the wall within which velocity changes drastically. In the laminar layer, the shear stress is mainly contributed by viscous stresses.
- Outside this laminar layer velocity fluctuation is significant and the shear stress is mainly contributed by Reynolds stress.

In order to check these two assumptions for non-Newtonian turbulent flow, a representative instantaneous radial velocity profile is generated from LES performed with non-Newtonian turbulent flow, shown in Figure 7-8.

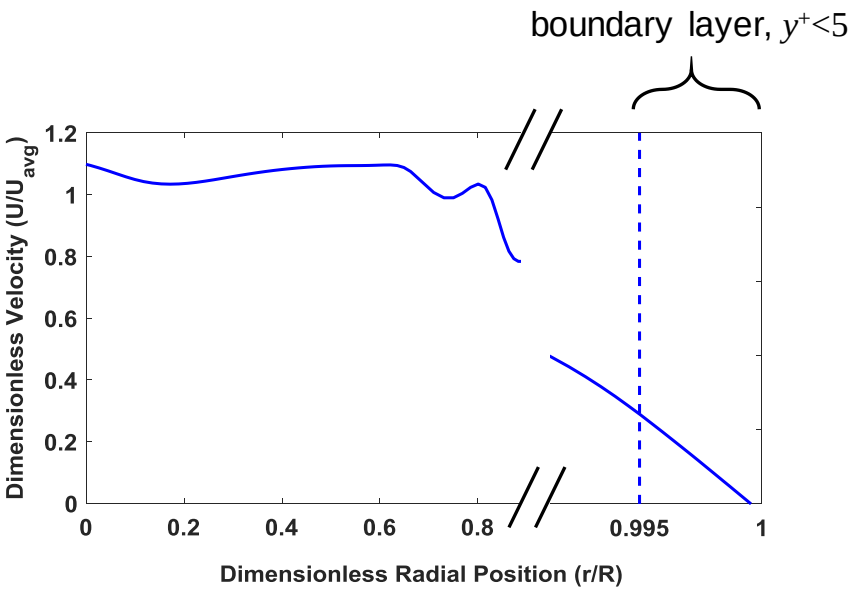

Figure 7-8: A representative instantaneous radial velocity profiles for a turbulent non-Newtonian pipe flow

As can be seen from Figure 7-8, these two qualitative turbulence characteristics are preserved in the non-Newtonian turbulent pipe flow with the laminar-like boundary sublayer in the vicinity of the pipe wall and a turbulent core in the central region of the flow.

Consequently, we can analogously derive a modified law of the wall for non-Newtonian turbulent flow. It should be noted that in the laminar sublayer, the shear stress equals viscous stress. Therefore, velocity profile of non-Newtonian flow obeys the conventional law of the wall in the laminar region if the viscosity at wall ($r = R$) is used in place of the Newtonian viscosity in the definition for the dimensionless distance-to-wall, shown in Equation (7-15).

$$y^+ = \frac{y}{\nu_w}\sqrt{\frac{\tau_w}{\rho_{oil}}} \tag{7-15}$$

$$\nu_w = \text{kinematic viscosity at wall}, (m^2/s)$$

The conventional law of the wall with this modified definition of the dimensionless distance-to-wall, y^+ will be implemented to predict the velocity profile of non-Newtonian turbulent pipe flow. In order to initiate this prediction, the wall shear stress or equivalently the pressure gradient needs to be predicted. As is shown in Appendix T, it was verified that reliable wall

shear stress/pressure gradient predictions for non-Newtonian pipe flow can be achieved with the Chilton-Stainsby friction factor correlation. Figure 7-9 shows the dimensionless radial velocity profile predicted by the modified law of the wall and LES.

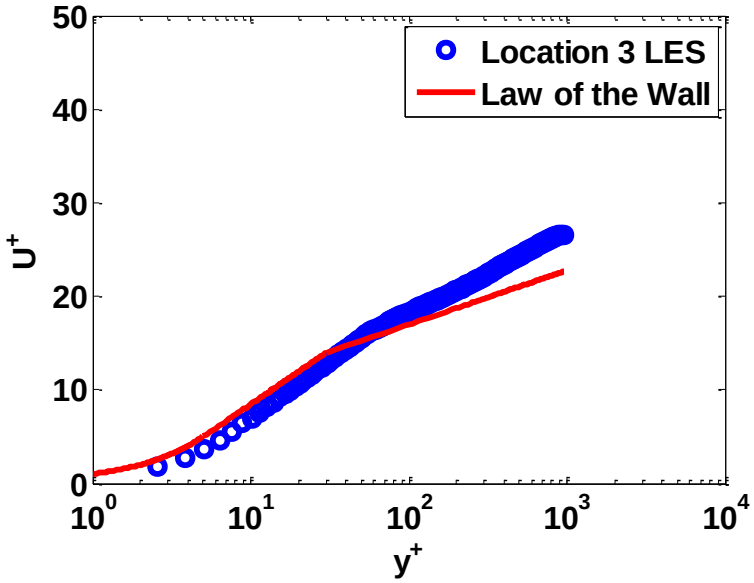

Figure 7-9: Comparison between the dimensionless velocity profiles predicted by LES and that by the law of the wall

As can be seen from Figure 7-9, the dimensionless radial velocity profile predicted by LES corresponds well with the law of the wall in the laminar region as well as the buffer region but deviates in the outer region. This small deviation is potentially due to the fact viscosity increases as the distance to the wall distance increases[138].

Figure 7-10 shows the predicted velocity profiles by LES and the law of the wall.

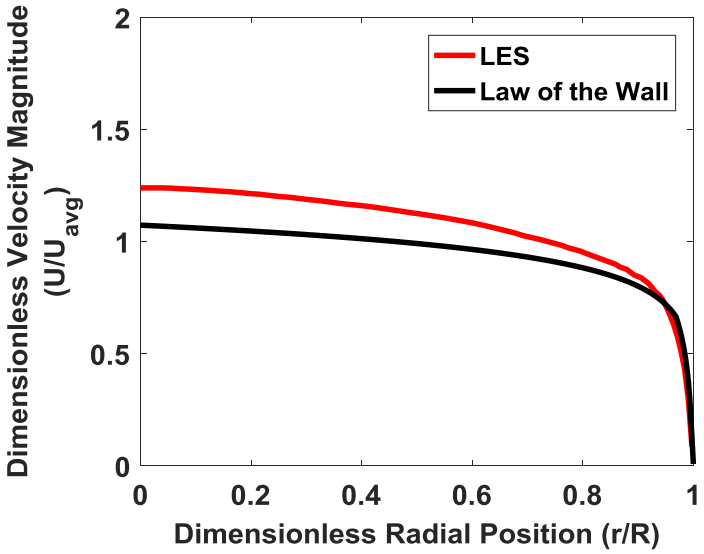

Figure 7-10: Predicted radial velocity profiles by LES and the Law of the Wall

As can be seen from Figure 7-10, the radial velocity profile predicted by the law of the wall only differs from LES predictions by ~10%, showing that the law of the wall method is reliable to generate predictions for the velocity profile to be used in heat and mass transfer modeling.

In this section, we developed a rapid method to perform hydrodynamic modeling in order to generate input parameters for the heat and mass transfer modeling. The key findings from this section were summarized below:

- The flow regime of non-Newtonian pipe flow can be readily predicted by the Chilton-Stainsby correlation.
- The modified law of the wall can generate reliable predictions for the radial velocity profile.

7.C.3 Calculation of Turbulent Diffusivity for Heat and Mass Transfer Modeling

Solving the heat/mass transfer equation is a critical step in wax deposition modeling. In order to generate reliable predictions for the temperature and concentration profiles, the turbulent heat/mass diffusivity needs to be calculated accurately. As was shown in Section 7.B.2, RANS fails to predict the correct temperature and concentration profiles as it significantly under-

predicts the turbulent diffusivities. The turbulent heat/mass diffusivity depends on the turbulent momentum diffusivity, shown in Equations (7-16) and (7-17), as the mixing of heat and mass is caused by turbulent eddy motions.

$$\frac{\varepsilon_M}{D_{wo}} = \frac{Sc}{Sc_T}\frac{\nu_T}{\nu_w} \tag{7-16}$$

$$\frac{\varepsilon_H}{\alpha} = \frac{Pr}{Pr_T}\frac{\nu_T}{\nu_w} \tag{7-17}$$

ε_M = eddy mass diffusivity, (m^2 / s)
D_{wo} = molecular diffusivity of wax in oil, (m^2 / s)
Sc = Schmidt number
Sc_T = turbulent Schmidt number
ε_H = eddy thermal diffusivity, (m^2 / s)
α = material thermal diffusivity of oil, (m^2 / s)
Pr = Prandtl number
Pr_T = turbulent Prandtl number
ν_T = turbulent diffusivity, (m^2 / s)

The modified law of the wall was again used to calculate the turbulent momentum diffusivity, shown in Equations (7-18)

$$\frac{\nu_T}{\nu_w} = \begin{cases} \left(\kappa y^+\right)^2\left[1-\exp\left(-\frac{y^+}{A}\right)\right]^2 & y^+ \le 5 \\ \left(\kappa y^+\right)^2\left[1-\exp\left(-\frac{y^+}{A}\right)\right]^2\frac{5}{y^+} & 5 < y^+ \le 30 \\ \left(\kappa y^+\right)^2\left[1-\exp\left(-\frac{y^+}{A}\right)\right]^2\frac{2.5}{y^+} & y^+ \ge 30 \end{cases} \tag{7-18}$$

with $\kappa = 0.4, A = 26$

Figure 7-11 shows the predict temperature/concentration profile using the modified law of the wall.

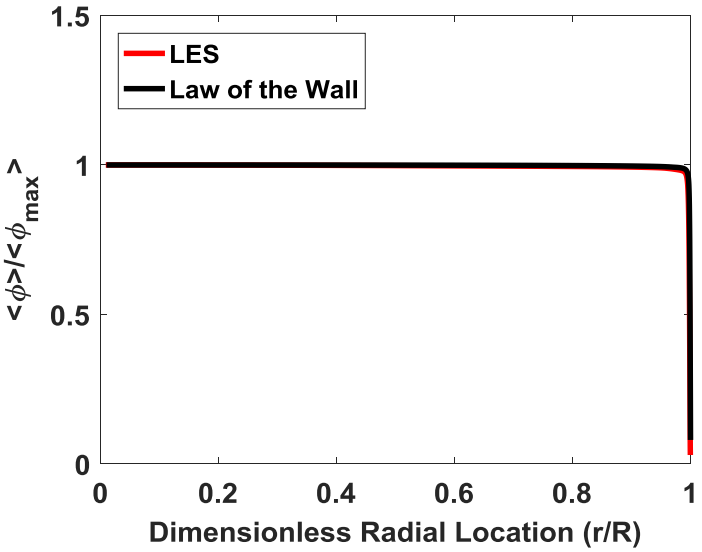

Figure 7-11: Predicted radial profile of temperature/concentration with the Law of the Wall and LES

As can be seen from Figure 7-11, the temperature/concentration profile predicted by law of the wall is virtually identically with that predicted by LES, indicating that the law of the wall is appropriate for the calculation of turbulent diffusivity to be used in heat/mass transfer modeling. In order to compare results from the law of the wall and LES to further validate the law of the wall method, the important dimensionless number, Δ, characterizing the relative rate of convective and diffusive transfer, defined in Equation (7-11) and repeated below, is again calculated based on the temperature/concentration profiles predicted by the law of the wall and LES.

$$\Delta = \frac{h_{\text{int}} D}{\Gamma} = \frac{-\frac{\partial \phi}{\partial r}|_{\text{wall}} D}{\phi_{\text{bulk}} - \phi_{\text{wall}}}$$

For heat transfer, Δ is the Nusselt Number and for mass transfer Δ is the Sherwood Number. The calculated values of Δ based on LES and the law of the wall are summarized in Table 7-6.

Table 7-6: Summary of the Δ values associated with the internal heat/mass transfer

LES	823
Law of the Wall	1116

As can be seen from Table 7-6, the Δ values predicted from LES and the law of the wall agree well with each other.

In summary, the modified law of the wall discussed in this section is appropriate for hydrodynamic, heat and mass transfer modeling for non-Newtonian turbulent pipe flow. The algorithm based on the modified law of the wall to be incorporated in wax deposition model is summarized in Figure 7-12 below.

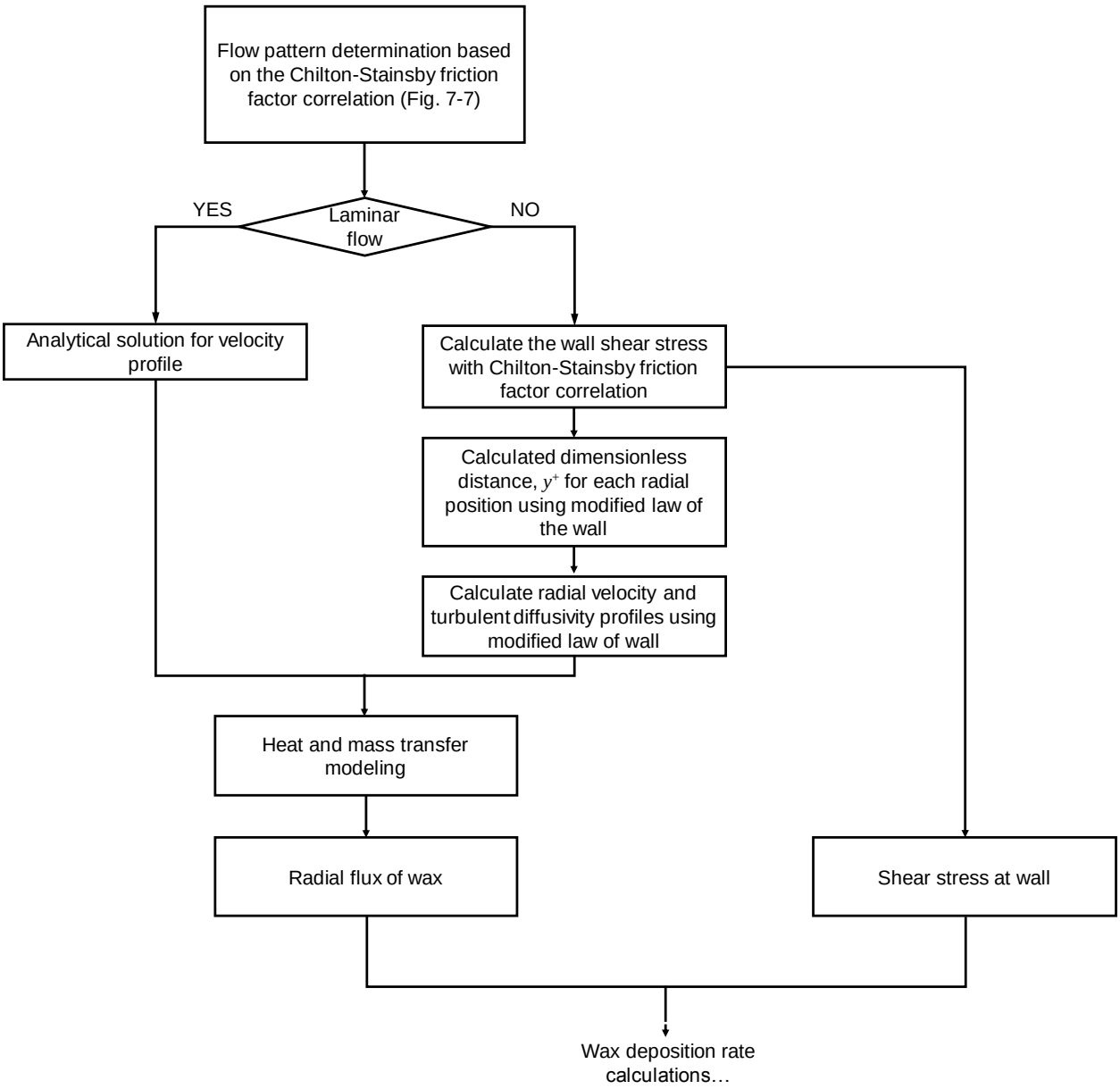

Figure 7-12: Summary of the hydrodynamic, heat and mass transfer modeling algorithm developed based on the law of the wall

It should be noted that Figure 7-12 includes another advancement in the wax deposition modeling, i.e., accounting for the effect of shear stress at wall on the calculation of deposition rate, which will be discussed in detail in the following section.

7.D Modeling of Gelation in the Immediate Vicinity of the Wall/Deposit-Fluid Interface

Conventional wax deposition models simulate deposit growth solely based on the molecular diffusion mechanism. Wax deposition is initiated by the precipitation of wax molecules at the wall ($t = 0^+$) / deposit-fluid interface ($t > 0$) when the surface temperature is below the wax appearance temperature (WAT). Precipitation of wax generates a radial concentration gradient and a net diffusive flux of dissolved wax molecules to the cold solid surface. A fraction of the dissolved wax molecules reaching the deposit-fluid interface precipitate and form an interlocking network with entrapped oil, leading to deposit growth[21]. The rest of the wax molecules continue to diffuse into the existing deposit layer, causing an increase in the wax content of the deposit[21]. Modeling efforts have been mostly concentrated on the calculation of radial diffusion of wax molecules towards the pipe wall ($t = 0^+$) / deposit-fluid interface ($t > 0$) and the internal diffusion of wax molecules into the deposit, as these variables are essential for the calculation of the growth rate of wax deposit, shown in Equation (7-19).

$$\rho_{\text{wax}}\Omega_{\text{wax}}\frac{\mathrm{d}\delta}{\mathrm{d}t} = J_{\text{wax,to interface}} - J_{\text{wax,into the deposit}} \tag{7-19}$$

ρ_{wax} = density of the wax,(kg/m^3)
Ω_{wax} = volume fraction of solid wax in the gel
δ = deposit thickness,(m)
$J_{\text{wax,to interface}}$ = wax diffusive flux to the interface,$(kg/m^2/\text{s})$
$J_{\text{wax,into the deposit}}$ = wax diffusive flux into the deposit,$(kg/m^2/s)$

In existing wax deposition models, the solid volume fraction of the depositing layer, Ω_{wax}, is either assumed to be a constant or determined empirically. As a result, existing models cannot capture the variation of deposit solid wax volume fraction with changing operating conditions,

such as the imposed shear stress by the fluid and fail to predict the correct deposit growth rate and solid fraction at high and low oil flow rates[14].

Multiple experimental evidences suggest that the deposit solid volume fraction increases with increasing shear stress imposed by the fluid. Singh et al. measured the gelation temperature of a model wax-in-oil mixture under various shear stress and cooling rate with a controlled stress rheometer[139]. In Singh et al.'s study, the gelation temperature is defined as the point when the loss and storage modulus equals each other. It was discovered that the gelation temperature of the oil of interest decreases with increasing imposed shear stress, suggesting that a larger amount of solid has precipitated at gelation under higher shear stress. In addition to rheometric characterizations, the variation of the solid content in the deposit was also observed from flow loop wax deposition experiments[39]. Figure 7-13 shows the deposit composition obtained from two flow loop wax deposition experiments with similar diffusive fluxes of dissolved wax, but with different oil and wall temperatures.

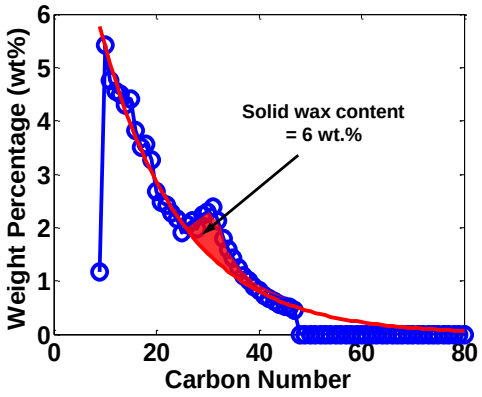

T_{oil} = 15.3 °C
$T_{coolant}$ = 5.0 °C
Predicted T_{wall} = 7°C
Theoretical flux J_{wax} = 2.2 × 10^{-5} kg/m^2/s
t = 4.1 days
Q = 5 m^3/hr (τ_w = 1.3 Pa)
D = 52.5 mm
Thickness = 7.4 mm

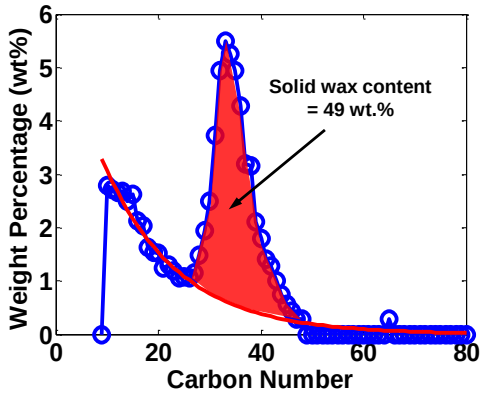

T_{oil} = 20.2 °C
$T_{coolant}$ = 10.0 °C
Predicted T_{wall} = 14.8°C
Theoretical flux J_{wax} = 2.3 × 10^{-5} kg/m^2/s
t = 2.9 days
Q = 21 m^3/hr (τ_w = 16 Pa)
D = 52.5 mm
Thickness = 0.6 mm

Figure 7-13: Comparison between the deposit solid wax contents from two runs with similar concentration driving forces but drastically different wall shear stresses

As can be seen from Figure 7-13, despite the similar mass flux of dissolved wax between the two experimental runs, the compositions of the solid deposits in these two experiments are drastically different. A deposit layer forms when its dynamic yield stress exceeds the shear stress imposed by the flow. As the dynamic yield stress of the deposit increases with the solid content of the deposit, the deposit formed at the higher flow rate (high wall shear stress) contains a significantly larger amount of solid wax than the deposit formed at the lower flow rate.

Both rheometric and flow loop experiments suggest that the deposit solid content can vary significantly with shear stress. Despite the overwhelming experimental evidence suggesting that the deposit solid content changes with imposed shear stress, it has remained unclear how the solid volume fraction of the depositing layer can be modeled rigorously. We now introduce a rigorous method to model the formation of a gel deposit and predict the solid volume fraction of the depositing layer based on first principles of rheology.

The solid wax-in-oil suspension in the immediate vicinity of the wall gradually develops a yield stress (τ_y) as the solid volume fraction, Ω_{wax}, increases due to molecular diffusion of wax towards the wall and into the deposit. The wax-in-oil suspension in the immediate vicinity of the wall cease to flow when the yield stress, τ_y of the suspension exceeds the shear stress (τ_s) imposed by the fluid flow. Figure 7-14 provides an illustration of the process of gelation described above associated with the mathematical implementations.

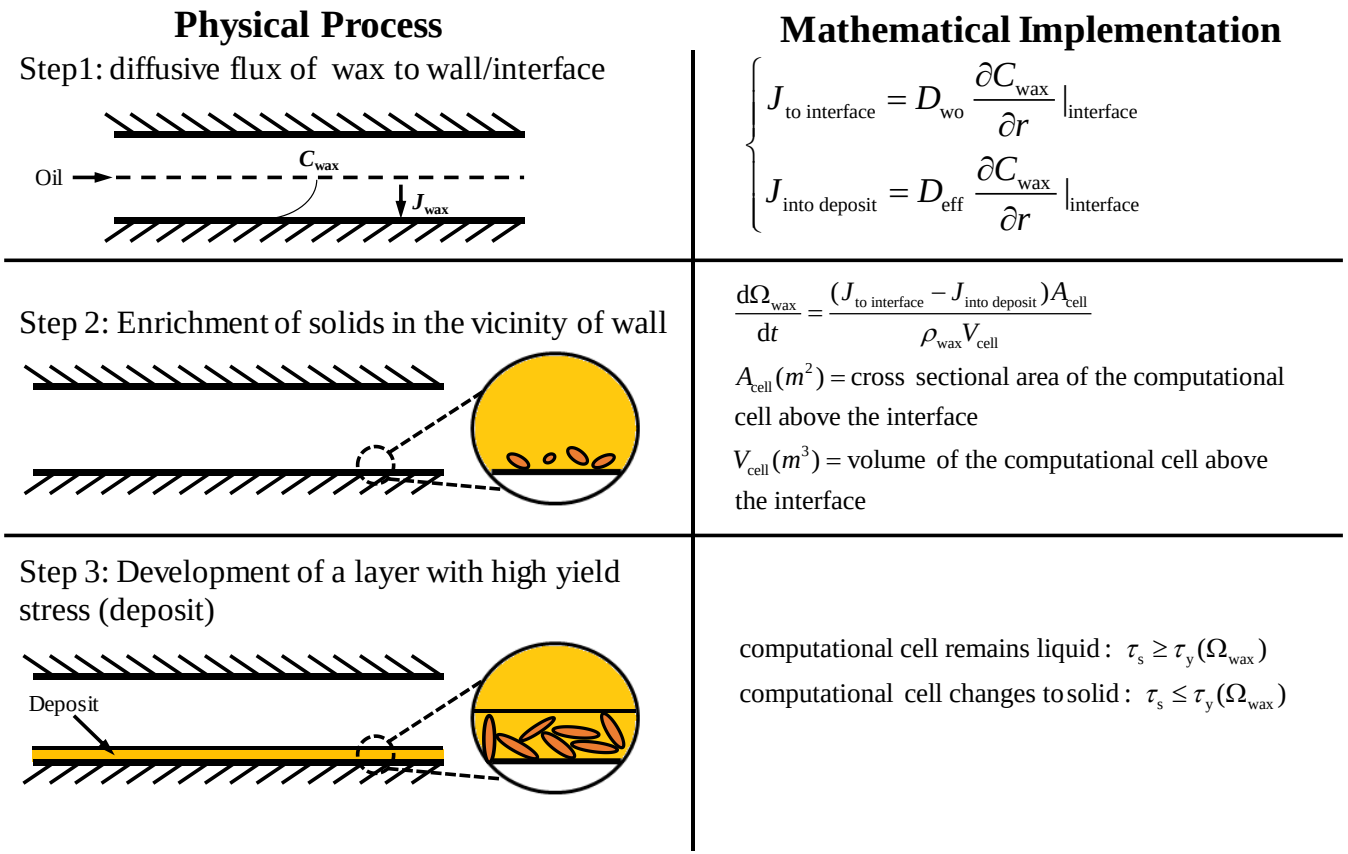

Figure 7-14: Illustration of gelation process in the immediate vicinity of the wall and the mathematical implementation

Figure 7-15 (a) shows the predicted increase of the solid volume fraction in the oil in the immediate vicinity of the wall in a field scale simulation. In order to calculate the change of dynamic yield stress as a function of time, the solid volume fraction at each time step shown in Figure 7-15 (a) is entered into the relationship between the dynamic yield stress and the solid volume fraction. The relationship between the dynamic yield stress and the solid volume fraction was obtained by fitting of the viscosity-temperature curves measured at different shear rates using the Herschel-Bulkley equation. The increase in the dynamic yield stress of the wax-oil suspension is shown in Figure 7-15 (b). This field scale simulation will be described in detail in the following Section 7.E.

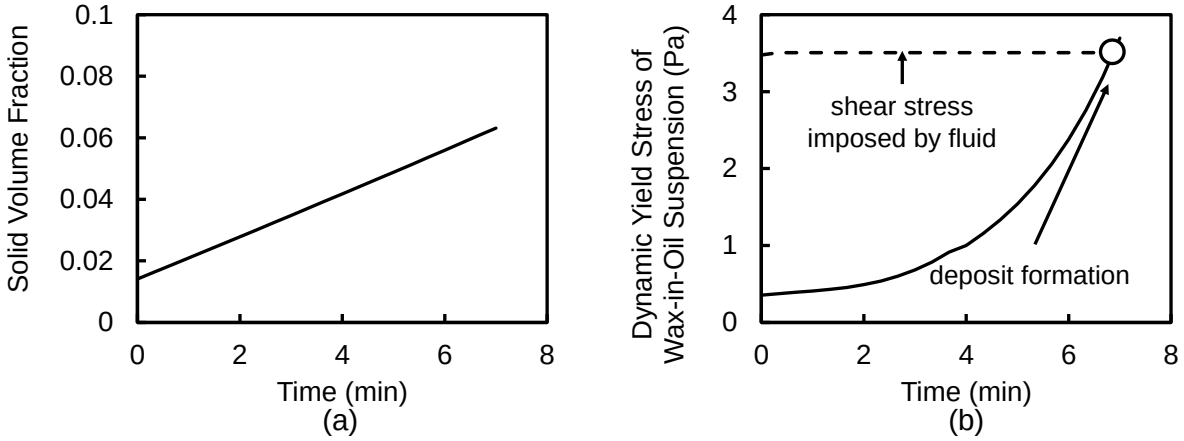

Figure 7-15: (a) Evolution of solid volume fraction in the immediate vicinity of the wall (b) evolution of dynamic yield stress of wax-in-oil suspension in the immediate vicinity of the wall to the point of deposit formation

As can be seen from Figure 7-15 (a), the solid volume fraction of in the immediate vicinity of the wall continuously increases as time elapses due to accumulation of solid wax, leading to a continuous increase in the dynamic yield stress of the solid-liquid suspension, shown in Figure 7-15 (b). This layer gels to form a deposit when the dynamic yield stress reaches or exceeds the shear stress imposed by the fluid at the interface of ~ 3.5 Pa.

At this point, the modeling of hydrodynamics, heat and mass transfer as well as the deposit formation were enhanced with non-Newtonian fluid mechanics. In the following section, the enhanced wax deposition model will be applied on a real-world field scale pipeline.

7.E Application of the Enhanced Wax Deposition Model on a Field Scale Pipeline

The enhanced wax deposition model is applied to predict wax deposition in a real-world field scale pipeline offshore of Indonesia[59]. This pipeline transports waxy crude oil from a central processing platform to floating production storage offloading. The subsea pipeline has an inner diameter of 12 inch and a length of 23 km. The pressure drop across the entire pipeline is monitored over the production period. It was observed that wax deposition causes the pressure drop to increase from ~ 200 psi to ~ 300 psi over a production period of 7 days[59]. Detailed description of this field as well as the monitored operating variables, such as flow rate, temperature, and pressure drop can be found in the article by Singh et al[59]. The simulation parameters and configurations are summarized in Appendix U in the supporting information. The wax deposition model was first used to calculate the pressure drop along the pipeline without wax deposit attached to the pipe wall. The calculated pressure drop, 180 psi, corresponds well with the pressure drop recorded right after pigging, ~200 psi, thereby validating the hydrodynamic calculation. The heat transfer simulation predicts an average outlet temperature of 30°C, which corresponds well with the field observation of an outlet temperature varying from 27 °C to 29 °C during production[59]. Wax deposition modeling was then performed after the hydrodynamic and heat transfer calculations were validated by comparison between predictions and field observations. Figure 7-16 (a) shows the predicted pressure drop – time

trajectory by assuming two limiting scenarios for the bulk precipitation kinetic constant, i.e., the Chilton-Colburn approach[139] and the solubility approach[96].

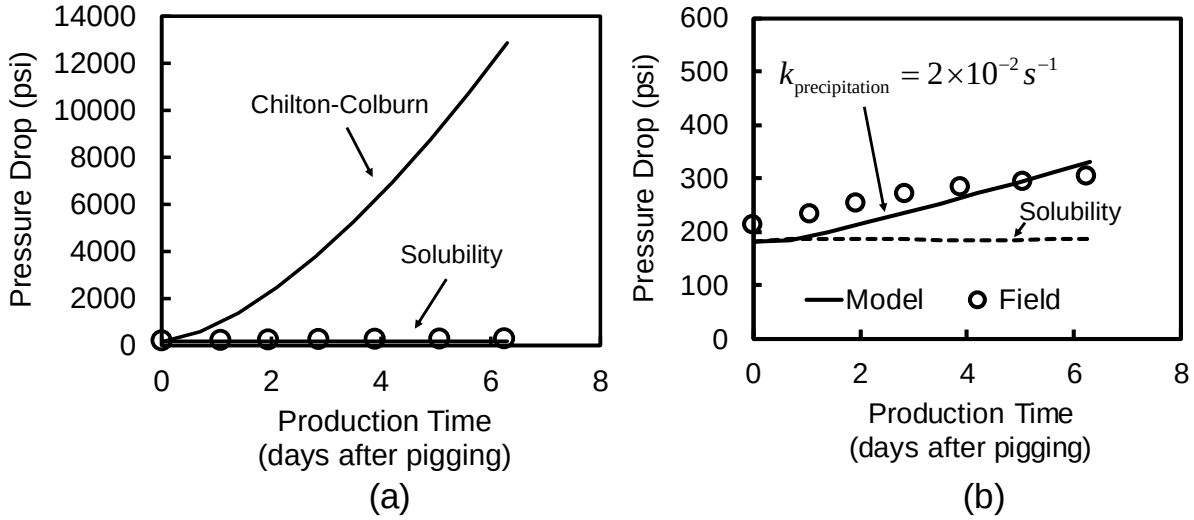

Figure 7-16: Comparison between the predicted pressure drop evolutions with that observed in field

As can be seen from Figure 7-16 (a), the Chilton-Coburn analogy significantly over-predicts the pressure drop build-up rate while the solubility method is more representative for the bulk precipitation kinetics in this field scale simulation. The bulk precipitation kinetic constant was adjusted to achieve agreement between the predicted pressure drop – time trajectory and that observed in the field, shown in Figure 7-16 (b). As can be seen from Figure 7-16 (b), the predicted pressure drop matches the observed pressure drop evolution with an adjusted bulk precipitation kinetic constant of $2\times10^{-2}s^{-1}$. This value is consistent with the range of bulk precipitation kinetic constant reported by Lee et al., i.e., 10^{-2}-$1s^{-1}$[113]. It is noticed that the predicted starting pressure drop is slightly lower (10 %) than the observed pressure drop. This discrepancy is likely due to the fact that a certain amount of wax deposit remains attached to the pipeline after the pigging, therefore leading to a higher pressure drop right after the pigging than the pressure drop associated with a completely bare pipeline. This enhanced wax deposition

model is the first model that can generate reasonable field predictions from first principles of fluid mechanics, transport and rheology. The enhanced wax deposition model predicts a wax content of 24 wt.%, which corresponds well with the wax content of the pig return deposit, i.e., 27±2 wt.%. Table 7-7 summarized the comparisons between predictions and field observations.

Table 7-7: Summary of non-Newtonian model predictions and field observations

	Prediction	Field observation
Pressure drop right after pigging (psi)	180	200
Pressure drop with Newtonian approach	160	200
Pipeline outlet temperature (°C)	30	27-29
Deposit wax content (wt.%)	24	27±2

As can be seen from Table 7-7, excellent agreement between the model predictions and field observations of pressure drop, temperature as well as the wax content presented in this section indicate that the enhanced wax deposition model can provide wax deposit predictions with a high level of confidence. If the Newtonian approach is used to predict the pressure drop right after pigging, a more severe under-prediction can be observed, shown in Table 7-7. Figure 7-17 shows the predicted average wax deposit thickness over the entire length of the pipeline as well as the axial deposit thickness profile.

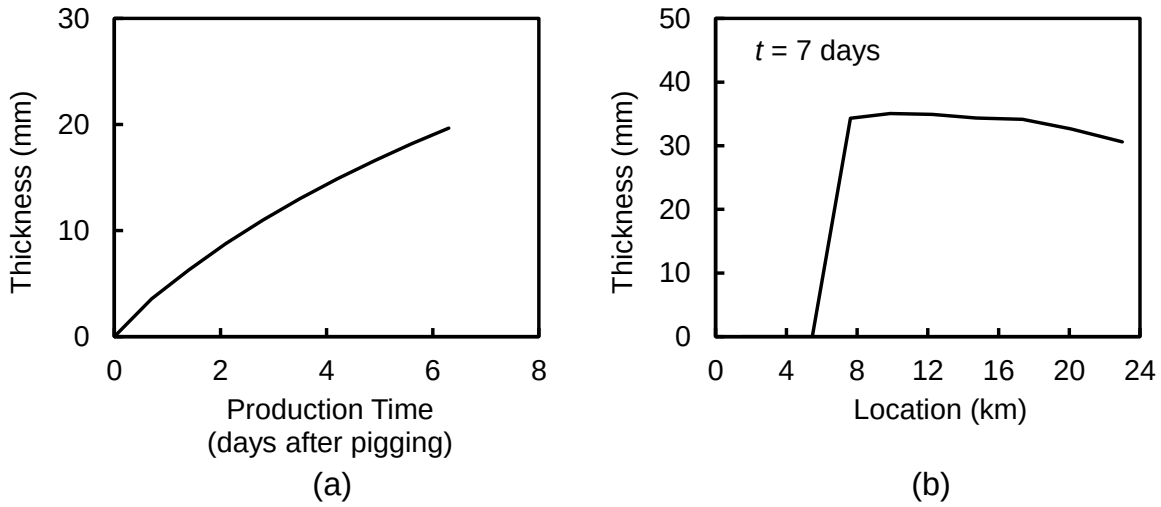

Figure 7-17: (a) Predicted average deposit thickness evolution over a production period of 7 days (b) Predicted axial deposit thickness profile after 7 days of production

It should be noted that predictions such as those shown in Figure 7-17 are virtually impossible to measure in a field scale pipeline. Therefore, such insights on the average deposit thickness evolution and the axial deposit thickness profile are extremely valuable for pigging design. In order to highlight the difference between the Newtonian and non-Newtonian wax deposition models, the change of pressure drop as a function of time as well as the axial deposit thickness profile were generated with the Newtonian wax deposition model, shown in Figure 7-18. It should be noted that exact same input parameters, except the viscosity, used for wax deposition modeling with the non-Newtonian modelwerealso used in the Newtonian model. An Arrhenius temperature dependency was used for the viscosity in the Newtonian model without the consideration for the increase in viscosity due to suspended solid.

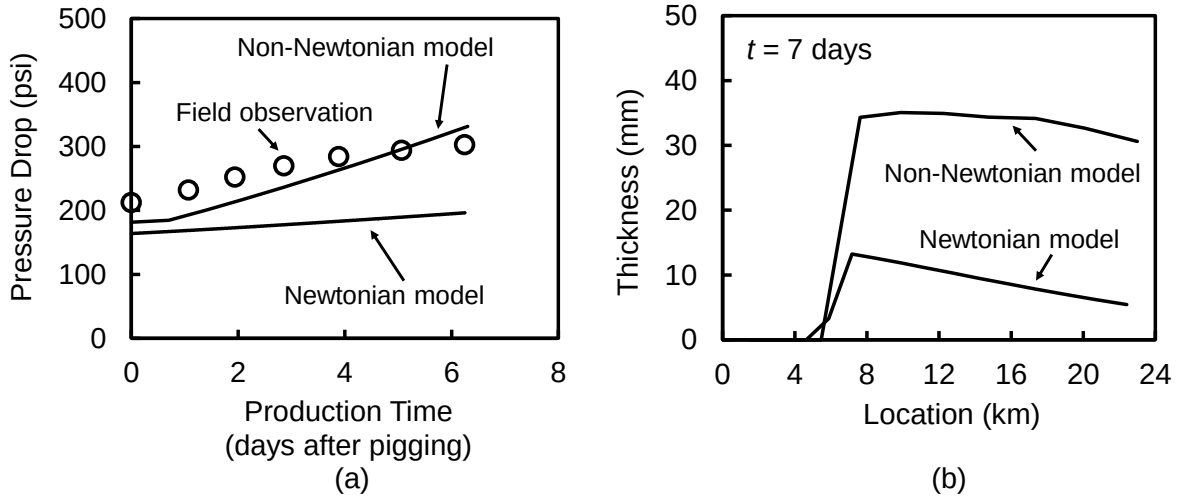

Figure 7-18: (a) Comparison between the pressure drop-time trajectories predicted by non-Newtonian and Newtonian approaches; (b) Comparison between the axial deposit thickness profile predicted by non-Newtonian and Newtonian approaches

As can be seen from Figure 7-18 (a), the Newtonian model significantly under-estimates the pressure drop increase over time due to the under-estimation in the viscosity. Misinterpretation of this under-estimation of the pressure drop build-up generated from the Newtonian model can lead to overoptimistic assessment of the wax deposition risk. As can be seen from Figure 7-18 (b), the Newtonian model also significantly under-predicts the deposit thickness. This under-

estimation is due to the fact that the Newtonian model assumes the solid fraction of the deposit to be always greater than total wax content of the oil, i.e., 17 wt.% for this particular crude while based on analysis from rheology, it only takes ~ 6 wt.% of solid wax to immobilize the wax-in-oil suspension and form a deposit.

7.F Conclusions

In this investigation, we assessed the role of non-Newtonian characteristics on wax deposition modeling. Non-Newtonian hydrodynamics as well as heat and mass transfer modeling were investigated with large eddy simulations (LES). With LES, the effects of non-Newtonian turbulent characteristics on hydrodynamics as well as heat and mass transfer models were studied from first principles. The computational cost of applying LES to model wax deposition in a field scale pipeline was calculated. It was discovered that LES is too computationally intensive for the modeling of wax deposition in a field scale pipeline. The option of using common turbulent modeling technique, i.e., RANS, for wax deposition modeling in industrial scale pipeline was explored. Comparison between LES predictions and Reynolds Average Navier Stokes (RANS) predictions revealed that commonly used RANS models lead to numerical artifacts in the hydrodynamic and transport modeling results. Based on the insights provided by LES, computationally efficient and reliable methodologies, i.e., the modified law of the wall for the calculations of velocity profile, temperature and concentration profiles were developed to enhance hydrodynamic, heat and mass transfer calculations in existing wax deposition models. The key findings from the hydrodynamic modeling as well as heat and mass transfer modeling using the three simulation techniques, i.e., LES, RANS and the law of the wall are summarized as follows:

- The previously suspected plug in the central region of the flow is constantly destroyed by turbulent eddies
- Transition of turbulent flow to laminar flow can occur as the fluid flows and cools along pipeline.
- The computational cost of using LES for wax deposition modeling an industrial scale pipeline is intolerable.
- RANS generates numerical artifacts in both velocity profile prediction and temperature/concentration profile predictions due to its limitation that it cannot resolve the instantaneous fluctuating shear rates near the central region of the flow.
- The modified law of the wall approach can generate rapid and accurate predictions for the velocity profile, temperature and concentration profiles. Therefore, the modified law of the wall approach is used for wax deposition modeling.

The enhanced wax deposition model is applied to predict wax deposition in a real-world field scale pipeline. The wax deposition model generates reliable predictions for the increase of pressure drop due to deposit build-up over time, the temperature at the outlet of the pipe as well as the wax content of the deposit. The good agreement between the model predictions and field observations validate that the predictions by this enhanced model is of high confidence and reliability.

Chapter 8

Conclusions

8.A Wax Deposition from Single Phase Oil Flows

8.A.1 Prediction of the Compositions of Wax Deposits

A theoretically rigorous methodology by combining thermodynamic modeling and heat and mass transfer modeling was developed to predict the compositions of wax deposits. It was discovered that the composition of a wax deposit is governed by the difference among the concentration driving forces of the molecular diffusion of different precipitating and deposit paraffin components. It was generalized that the deposit formed under a high wall temperature is more enriched in heavy normal alkanes as these alkanes consist of the first fraction to precipitate when the wall temperature drops below the wax appearance temperature.

8.A.2 Wax Deposition Modeling Considering the non-Newtonian Fluid Mechanics

A novel wax deposition model was developed to account for the impacts of non-Newtonian fluid mechanics of waxy crude oil on the modeling of hydrodynamics, heat and mass transfer. In addition, the deposit formation is modeled as a gelation process. It was discovered that common computational fluid dynamics techniques, such as large eddy simulation and Reynolds-Averaged Navier-Stokes equations are not applicable for the modeling of wax deposition in field scale pipelines. A modified law of the wall is applicable for this particular engineering application.

The novel model can predict the pressure drop increase as well as the wax content of the deposit collected by pigging in a real-world field scale pipeline.

8.B Wax Deposition from Oil-Water Two Phase Flows

8.B.1 Wax Deposition from Water-Oil Stratified Flow

Wax deposition characteristics in water/oil stratified flow were investigated by flow loop wax deposition experiments. It was discovered that the stratified water phase reduces the pipe wall surface area available for deposition by preventing the contact between oil and the pipe wall. The water phase has negligible impacts on the heat and mass transfer aspects of wax deposition while the wall shear stress of the oil phase decreases with increasing water volume fraction in the bulk, leading to increased deposit thickness as the water volume fraction increases.

8.B.2 Wax Deposition from Water-Oil Dispersed Flow

The impacts of the dispersed water phase on the heat transfer, mass transfer and deposit rheology were analyzed comprehensively. Different heat transfer characteristics were observed in lab scale and field scale wax deposition processes. The water phase retards the heat loss by increasing the viscosity of the fluid flow under lab scale conditions, leading to decreased deposition rate with increasing water volume fraction in the fluid. On the other hand, under field scale conditions, the water phase preserves the concentration driving force for wax deposition due to its high heat capacity, causing more severe wax deposition in presence of the water phase. The water phase retards the mass transfer of wax molecules by acting as barriers to diffusion. This inhibitive effect on molecular diffusion can be modeled with fundamental equations for the transport process in porous media. Water droplets can be entrapped by the deposit during wax deposition. The amount of water trapped in a deposit depends not only on the water volume fraction of the bulk but also the droplet size. Smaller droplets are easier to be entrapped while

droplets larger than 100 microns in diameter will not be entrapped. Entrapment of water droplets significantly lowers the deposit yield stress and causes it to slough-off under imposed shear.

Chapter 9Future Directions

This thesis work advanced our understanding of wax deposition processes in both single-phase oil flow and water-oil two phase flow. Along with experimental investigations, enhanced wax deposition models have been developed in order to enable reliable predictions of wax deposition rate in field scale pipelines. Such predictions are of great value during the conceptual design phase of field development where judgmental calls are to determine 1) whether significant wax deposition/gelation risk will be encountered, 2) whether economical wax treatment program can be implemented to remediate the wax risks and eventually 3) whether the field development is profitable considering the wax risks and necessary treatment programs.

Besides the insights generated from this thesis, the following several projects can be pursued.

- Characterization of paraffin precipitation kinetics
- Wax deposition modeling in oil-gas two phase flows
- Modeling the effect of wax inhibitors/pour point depressants on wax deposition and pipeline restart
- Computer-aided design of wax remediating chemistries

Progress in these areas can not only generate interests and advancements in the scientific community but also lead to significant industrial impacts.

9.A Paraffin Precipitation Kinetics

The precipitation kinetic constant of wax molecules is a critical input parameter to wax deposition models as predictions from wax deposition models are sometimes sensitive to this parameter. Consequently, the wax deposition rate predictions can have large uncertainties due to the unknown bulk precipitation kinetic constant. Unfortunately, no experimental method has been developed to measure this parameter. As a result, the precipitation kinetic constant remains as a tuning parameter in wax deposition models. The uncertainties of the predictions from wax deposition models can be greatly reduced if the precipitation kinetic constant could be experimentally characterized or estimated to some extent. Lopes-da-Silva et al. characterized the kinetics of the structural development of wax-in-oil suspension during cooling using a rheometer and attempted to correlate the rate of structural development to the rate of precipitation via fitting of the experimental data to the Avrami model[140]. The development of a microscopic structure of the wax-in-oil suspension is indeed caused by precipitation of wax. However, the observed rate of structural development of wax-in-oil suspension not only depends on the rate of precipitation but also depend on the thixotropic characteristics of the oil[118]. Therefore, the measured rate of structural development in a rheometric experiment is a convoluted net effect from both precipitation and thixotropy and does not necessarily represent the true precipitation kinetics. Compared to rheometric experiments, differential Scanning Calorimetry (DSC) technique is a more promising experimental method to study the rate of crystallization of materials as it monitors the heat release associated with precipitation[141]. In order to observe the kinetics of precipitation/crystallization with a DSC instrument, it is required that the rate of cooling that can be achieved by the DSC apparatus be more rapid than the rate of precipitation/crystallization. Due to this limitation, DSC has only been commonly used to study the precipitation kinetics of

polymers, whose rates of precipitation are relatively low[141]. For example, Blaine has successfully determined the precipitation rate law and rate constants of polypropylene[141]. The rapid precipitation rate of waxes due to their relatively short chain lengths compared to polymers can make it challenging to achieve the required cooling power for the study of wax precipitation kinetics.

Besides experimental techniques to study wax precipitation kinetics, simulation techniques have been developed to predict the rate of precipitation[142–147]. For example, Waheed et al. simulated the crystal growth of n-eicosane[142] and Yi et al. simulated the crystal growth of n-octane[146]. It should be noted that both simulations were performed based on a single component system composed solely of the paraffin of interest. In order words, these investigations simulated the crystallization process of molten n-eicosane and n-octane respectively. However, precipitation/crystallization of waxes from crude oils occurs from a solution composed of n-alkanes covering a wide range of carbon numbers as solutes and iso-, cyclic-paraffins or aromatic hydrocarbons as solvents. Therefore, the systems studied by Waheed et al. and Yi et al. are not satisfying representations of crude oils. The main challenge in the simulation of precipitation/crystallization is the modeling of nucleation as this simulation process requires the computer model to access a "rare" event with low probability. As can be imagined, the modeling of nucleation will become more challenging if the developed methods were directly extrapolated to model wax precipitation from crude oils because wax is usually at a much lower concentration in a crude oil compare to the reported single component system where the concentration of the alkane is unity. Consequently, the probability of a computer model to generate a nucleus will be significantly limited, making the program unacceptably computational intensive. Therefore,

more advanced computational techniques are required to predict the rate of precipitation of waxes from crude oils.

9.B Wax Deposition Modeling in Oil-Gas Two Phase Flow

Oil-gas multiphase flow is commonly encountered in oil production. However, existing wax deposition modeling methodology for oil-gas multiphase flow is highly empirical[148]. The only existing oil-gas two phase flow wax deposition model by Matzain calculates the deposit growth rate based on the diffusive mass flux of wax towards the fluid-deposit interface but uses as many as three adjustable parameters to account for the effects of flow pattern and shear on wax deposition rate. A model with this many tuning parameters can easily over-fit the experimental data. Additionally, empirical adjustments were applied to off-set the error in the calculated convective heat and mass transfer coefficients of the oil-gas two phase flow using Sieder-Tate correlation which is originally developed based on single-phase turbulent flow. Although this elementary model can be tuned to match experimental data, its predicative power is extremely limited. A rigorous wax deposition model for oil-gas two phase flow should start with a thermal dynamic simulation of the vapor-liquid equilibrium to predict the relative amount of gas and oil in the pipeline, followed by predictions of the flow pattern. It was experimentally observed that various flow patterns can form during oil-gas two phase flow depending on the superficial velocities of oil and gas[149]. The wax deposition characteristics are drastically different among different oil-gas flow patterns and therefore require case-by-case analysis. Computational Fluid Dynamics (CFD) techniques are promising to provide insights to the heat and mass transfer characteristics associated with different oil-gas two phase flow patterns. Duan et al. applied CFD techniques to simulate heat and mass transfer as well as wax deposition in oil-gas stratified flow[150]. Such approach can be extended to other important oil-gas two phase flow patterns, such

as stratified-wavy flow, intermittent flow, annular flow etc. The heat and mass transfer characteristics obtained from CFD simulations can be condensed in the form of a correlation for the convective heat/mass transfer coefficient, which can then be used in wax deposition modeling to generate wax deposition predictions. Figure 9-1 shows a conceived algorithm for an oil-gas two phase flow wax deposition model.

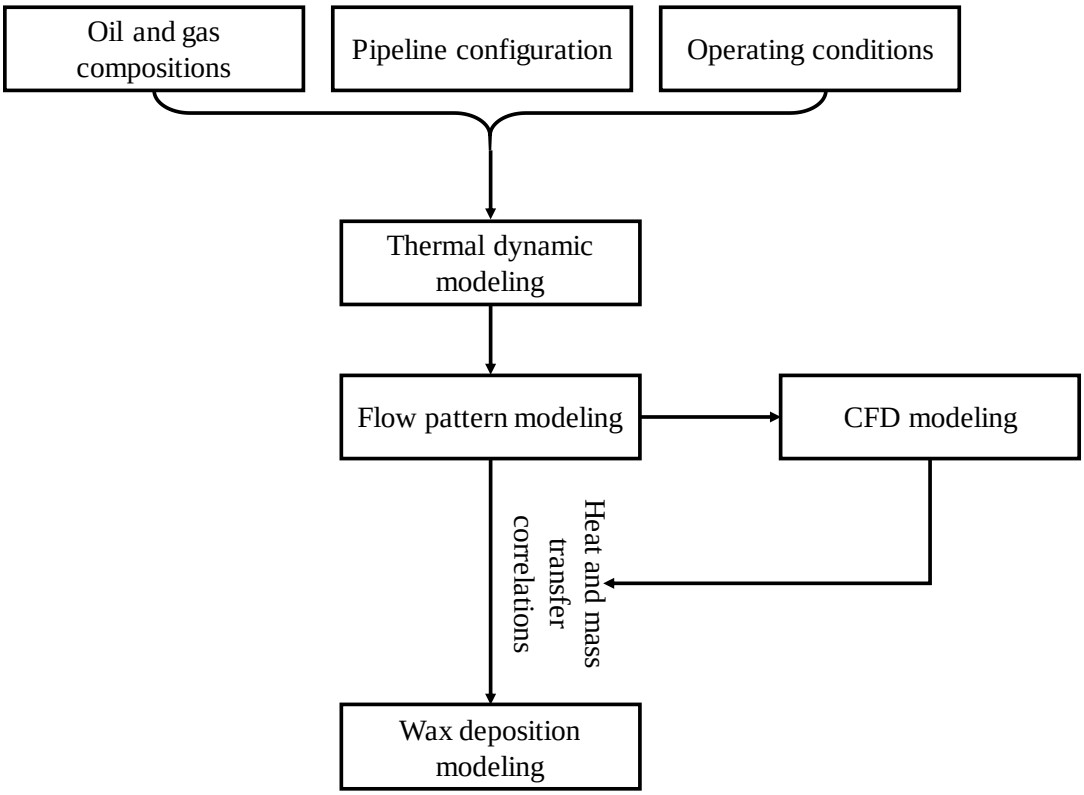

Figure 9-1: A conceived algorithm for oil-gas two phase flow wax deposition model

9.C Effects of Polymeric Inhibitors on Wax Deposition/Pipeline Restart

Investigations on wax inhibition have been carried out extensively with the hope to discover chemicals that can improve the flow properties of wax oil and reduce wax deposition rate. Pedersen and Rønningsen discovered that the addition of wax inhibitors lowers the wax appearance temperature (WAT) and viscosity of the waxy oil[151]. Jennings and Weispffennig performed cold finger wax deposition experiments in order to assess the impact of wax inhibitors on wax deposition rate[10]. It was observed that the wax deposition rate decreases in presence of

wax inhibitors. Recently, Hoffmann and Amundsen conducted flow loop wax deposition experiments in presence of wax inhibitors[152]. A reduction of 60% to 90% in the deposit thickness was observed. Chi et al. performed additional flow loop wax deposition experiments in presence of wax inhibitors and observed similar reduction in the wax deposition rate upon addition of wax inhibitors[153]. Despite the extensive investigations on the effect of wax inhibitor on wax deposition using cold finger and flow loop apparatus, it is unclear how the results from laboratory testing can be scaled-up to estimate the reduction in wax deposition rate in the field. To date, selection of wax inhibitors largely depends on laboratory cold finger wax deposition experiments and experiences from seasoned field engineers. Therefore, there is an imperative need to incorporate the effect of wax inhibitors in wax deposition modeling to predict the wax deposition rate in presence of wax inhibitors under field conditions. It was speculated that wax inhibitors alter the precipitation characteristics, i.e., the wax appearance temperature and the wax precipitation curve, leading to reduction in wax deposition rates[151]. However, emerging experimental evidence suggests that wax inhibitors only cause minimal changes in the wax precipitation characteristics[154] and the minimal change cannot quantitatively explain the significant reduction in wax deposition rate. On the other hand, it was observed that the wax inhibitors cause drastic changes in the microstructure of the solid network of the wax-in-oil suspension. Figure 9-2 shows the low temperature microstructure of a waxy crude oil before and after treated with maleic anhydride co-polymer.

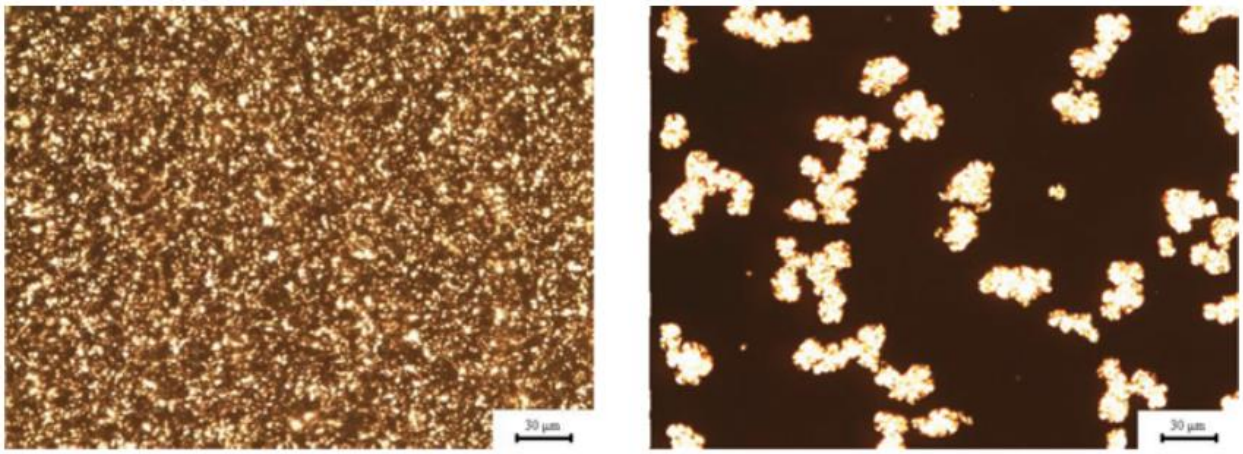

Figure 9-2: (a) Microstructure of Changqing waxy crude oil below the wax appearance temperature; (b) Microstructure of Changqing waxy crude oil doped with maleic anhydride copolymer[154]

As can be seen from Figure 9-2 that the microstructure changes from a volume-spanning network to groups of distantly distributed agglomerates. This change in microstructure is likely due to the fact that polymeric inhibitors co-crystallize with alkane molecules and prevent wax crystals from forming an interlocking network. The change in the microstructure of the wax-in-oil suspension leads to drastic changes in the rheological properties, including the apparent viscosity and pour point, of the oil[154]. As a result, efforts to predict the effect of wax inhibitors on wax deposition should be focused on incorporating the effect of the wax inhibitors on oil rheology into the wax deposition model. The second-generation wax deposition model presented in Chapter 7 is likely a good starting point for this research campaign.

In addition to wax deposition, pipeline gelation and restart is also a severe flow assurance challenge originated from wax precipitation. Occasionally, oil flow in the pipeline needs to be temporarily stopped due to maintenance needs. Gelation of the remaining waxy oil can occur in the pipeline if the ambient temperature is lower than the pour point of the oil. The gelled waxy oil behaves like a Bingham plastic with a yield stress. In order to restart the oil flow, a pressure

drop is applied across the gelled pipe section in order to overcome the yield stress of the waxy gel and induce gel breakage, mathematically represented by Equation (9-1).

$$\Delta p \geq \frac{4L}{D}\tau_y \tag{9-1}$$

Δp = pressure drop across the gelled pipe section,(Pa)
L = length of the gelled pipe section,(m)
D = pipe radius,(m)
τ_y = yield stress of the waxy gel,(Pa)

In real-world field operation, the crude oil is usually treated with wax inhibitors. It was observed that wax inhibitors significantly reduce the yield stress of a waxy gel[155]. Therefore, application of polymeric wax inhibitors is promising to facilitate gel breakage and pipeline restart. Furthermore, it was discovered that the gel-break process is not instantaneous[114], complicating the design for restart process. Researchers have developed mathematical models to simulate the time-dependent yielding of waxy gel in a pipeline[124,156]. Incorporation of the effect of wax inhibitors on the thixotropic rheology of waxy gel in these mathematical models can generate more representative predictions of the pipeline restart process in the field.

9.D "Smart" Design of Polymeric Wax Inhibitors/Pour Point Depressants

Polymeric wax inhibitors and pour point depressants usually contains two molecular moieties: a paraffin-like moiety and a non-paraffin like polar moiety. Several classical polar moieties include esters, vinyl acetates, maleic anhydrides and acrylonitriles[154]. Such molecular structures are designed to induce co-crystallization between the paraffin-like portion of the wax inhibitor and wax while the polar moieties disrupt the molecular alignment in the crystal structure due to the low affinity between these moieties and alkane molecules. During experimentation, it was observed that certain waxes respond to certain wax inhibitors/pour point depressants while are not responsive to other chemical treatments[157]. Despite the variety of available wax

inhibitor/pour point depressant chemistries, a widely effective chemistry is still lacking. Some tough-to-treat waxy crude oils do not respond to any available wax inhibitor/pour point depressant chemistry. Therefore, novel wax inhibitor/pour point depressant chemistries need to be developed.

Instead of a "brute-force" approach where numerous polymer molecules are synthesized and tested for wax inhibition and pour point depression efficacy in crude oils, computer simulations can be utilized to guide the design of polymeric wax inhibitors/pour point depressants. Duffy and Rodger simulated the effect of poly(octadecyl acrylate) on wax inhibition. It was discovered by computer simulation that the polymer molecules create defects in the crystal structure and thereby slowing crystal growth[158]. Jang et al. studied wax inhibition by comb-like polymers with molecular dynamics simulations. It was discovered that the comb-like polymer prefers the interactions with oil solvent and as a result, perturb the wax crystal structure when incorporated in the crystal matrix, leading to wax inhibition[159]. With more and more able computers, such simulation can be performed rapidly. Instead of physically synthesizing molecules via chemical reactions, promising polymer candidates as wax inhibitors/pour point depressants can be designed with computer simulations and their interaction with alkane molecules can be predicted.

In addition to conventional polymeric wax inhibitors/pour point depressants, hybrid wax inhibitors are currently being developed. One typical hybrid wax inhibitor/pour point depressants has been developed by mounting active polymer molecules onto nano-sized silica particles[160,161]. This hybrid wax inhibitor/pour point depressant is easier to handle due to its solid nature compared to conventional polymers which usually need to be dissolved in a large amount

of organic solvent before field applications. In some cases, the hybrid wax inhibitor/pour point depressants out-performs the polymeric inhibitor/pour point depressants[161].

Design of wax inhibitors/pour point depressants have been focused on achieving molecular interaction between the inhibitor and paraffin in order to disrupt the microstructure of wax crystals. However, it has been observed that aromatic moieties in the polymer structure can interact with the polar fractions of the crude oils, e.g., asphaltenes and resins to achieve better wax inhibition/pour point depression performance[162,163]. Consequently, the design of the next-generation wax inhibitor/pour point depressant chemistry should aim for interactions with not only wax molecules but also aromatic molecules in the crude oil to achieve synergistic wax inhibitor/pour point depression.

Appendices

Appendix A

Analysis of the Pseudo-Steady State Assumption Implemented in Heat Transfer Modeling

In order to determine the radial and axial temperature profile of the oil flow, the heat transfer equation, shown in Equation (A-1), needs to be solved numerically.

$$\frac{\partial T}{\partial t} + V_z \frac{\partial T}{\partial z} = \frac{1}{r} \frac{\partial}{\partial r} \left(r \varepsilon_{\text{eff,T}} \frac{\partial T}{\partial r} \right) \tag{A-1}$$

It should be noted that Equation (A-1) is applicable when the pipe diameter is much smaller than the pipe length. In the Michigan Wax Predictor (MWP), it is assumed that the temperature profile of the flow is always close to the steady state profile, i.e., at pseudo-steady state. As a result, the temperature profile is determined by solving the steady state heat transfer equation, shown in Equation (A-2), where the time-dependent term is neglected.

$$V_z \frac{\partial T}{\partial z} = \frac{1}{r} \frac{\partial}{\partial r} \left(r \varepsilon_{\text{eff,T}} \frac{\partial T}{\partial r} \right) \tag{A-2}$$

It should be noted that the wax deposit formed on the inner pipe wall acts as an insulation layer that retards heat loss from the oil flow to the surrounding. Therefore, the temperature profile depends on the deposit thickness. Moreover, the deposit thickness increases as time elapses. Consequently, in order for the pseudo-steady state assumption to be valid, it is required that the time scale for the temperature profile to achieve steady states is significantly shorter than the time scale of deposit build-up.

The time scale for the temperature profile to reach steady state depends on time scales of both advection and conduction, shown in Equations (A-3) and (A-4).

$$t_{\text{advection}} \sim \frac{L}{V_z} \tag{A-3}$$

$$t_{\text{conduction}} \sim \frac{R^2}{\varepsilon_{\text{eff,T}}} \tag{A-4}$$

We will now estimate these two time scales based on the typical parameter values, e.g., pipe radius, oil flowrate, etc. in a field pipeline. Table A-1 provides the typical values for the parameters of interest in a field scale wax deposition simulation.

Table A-1: Representative values for the parameters used in field scale wax deposition modeling

Variables	Values in intuitive units	Values in SI units
Pipeline length, L	10 km	10^4 m
Superficial velocity, V_z	1 m/s	1 m/s
Pipe radius, R	10 in.	10^{-1} m
Effective thermal diffusivity, $\varepsilon_{\text{eff,T}}$	10^{-7} m^2/s	10^{-7} m^2/s

The time scales for advection and conduction can be calculated as shown in Equations (A-5) and (A-6), respectively.

$$t_{\text{advection}} \sim 10^4 s \tag{A-5}$$

$$t_{\text{conduction}} \sim 10^5 s \tag{A-6}$$

Note that the time scale for conduction is much longer than the time scale for advection, i.e., advection is much more rapid than conduction. Therefore, the time it takes for the temperature profile to reach steady state depends on the time it takes for the fluid packet to travel from the pipeline inlet to the outlet. This finding can be validated by numerically solving the unsteady state advection-conduction equation using the Crank-Nicolson scheme and monitoring the temperature profile evolution over time. Figure A-1 shows the evolution of the axial temperature

profile along the inner pipe wall obtained using parameters in the field scale pipeline modeling performed from Chapter 7. It should be noted that at t = 0, the hot oil at 75°C has not yet entered the pipe and thus, the temperature of the entire pipe wall equals the ambient temperature of 25 °C regardless of the axial position.

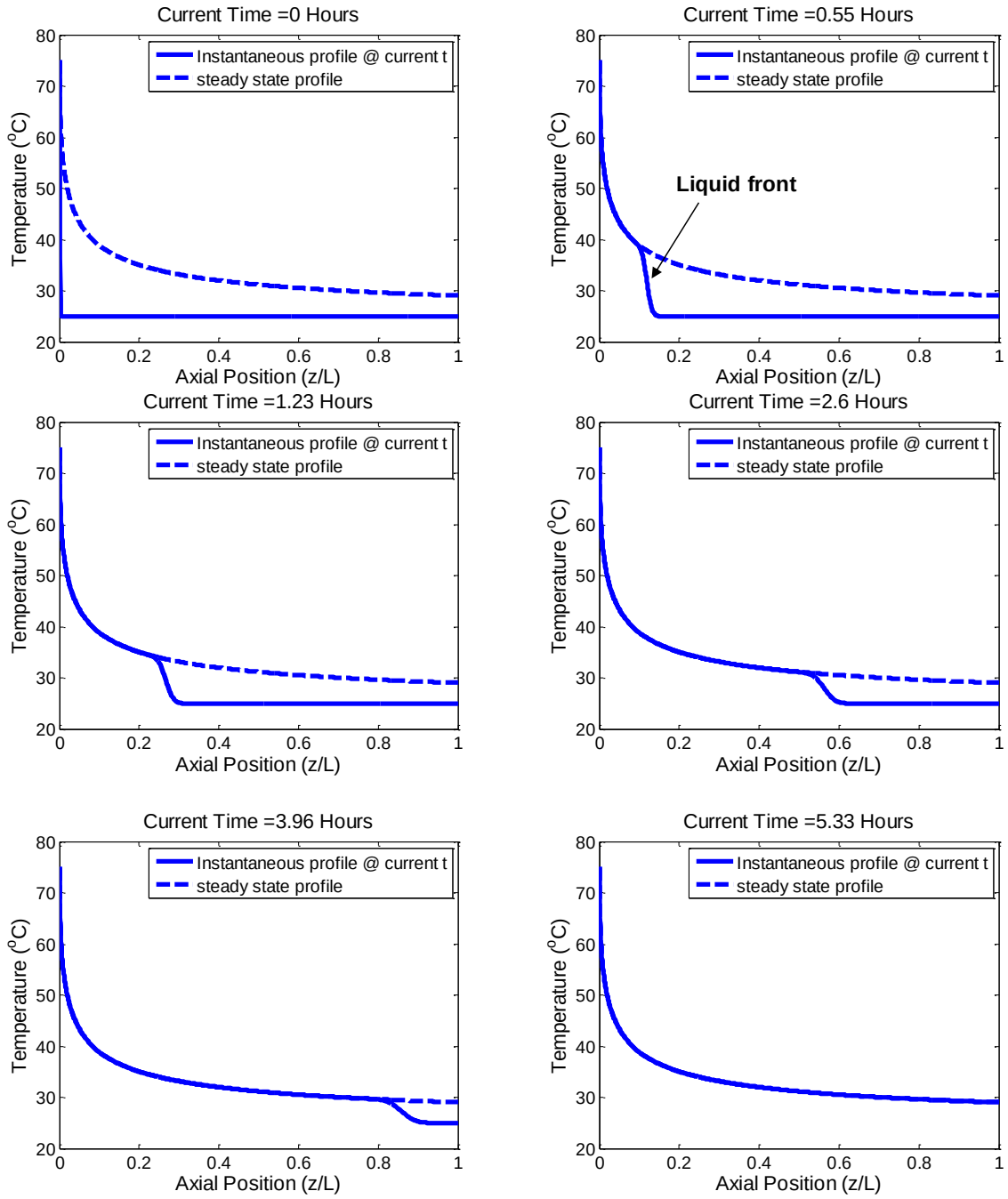

Figure A-1: Change of axial temperature profile along the pipe wall as a function of time.

As can be seen from Figure A-1, the development of the axial temperature profile is limited by the advancement of the liquid front.

In order for the pseudo-steady state assumption to be valid, it is required that the time scale for the temperature profile to reach steady state is significantly shorter than the time scale for deposit formation. In this case, it is required that the time scale for deposit formation is much longer than 10^4s.

Here we use the time it takes for the deposit thickness to grow by 1% of the pipe radius, defined in Equation (A-7), as a characterization for the time scale of deposit formation.

$$t_{\text{deposition}} \sim \frac{\rho_{\text{deposit}} \left(0.01R\right) \Omega_{\text{wax}}}{J_{\text{wax}}} [=] \frac{kg/m^3 \cdot m}{kg/(m^2/s)} = s \tag{A-7}$$

The three parameters, ρ_{deposit}, R and Ω_{wax} (the solid mass fraction of the depositing layer) in the numerator take typical values as shown in Equations (A-8) - (A-10).

$$\rho_{\text{deposit}} \sim 10^3 kg/m^3 \tag{A-8}$$

$$R \sim 10^{-1} m \tag{A-9}$$

$$\Omega_{\text{wax}} \sim 10^{-1} \tag{A-10}$$

The flux of wax reaching the pipe wall to generate deposit can be estimated as shown in Equation (A-11).

$$J_{\text{wax}} = -D_{\text{wo}} \left(\frac{\partial C_{\text{wax}}}{\partial r} \right)_{\text{wall}} = \left(-10^{-10} \frac{m^2}{s} \right) \cdot \left(-1000 \frac{kg/m^3}{m} \right) = 10^{-7} \frac{kg}{m^2 \cdot s} \tag{A-11}$$

As a result, the time scale for deposit formation can be estimated as shown in Equation (A-12).

$$t_{\text{deposition}} = \frac{10^3 \times \left(0.01 \times 10^{-1}\right) \times 10^{-1}}{10^{-7}} = 10^6 s \tag{A-12}$$

Note that the time scale of deposit formation is 100 times that of the time scale for the temperature profile to reach steady state. In other words, it takes one hundred times longer for the deposit thickness to grow by 1% radius than for the temperature profile to reach steady state.

Therefore, it is appropriate to assume that the deposit thickness remains constant when solving for the temperature profile.

Appendix B

Equations used by Coutinho's Model to Calculate Liquid Phase Equilibrium Concentration

The phase distribution of n-alkane depends on the difference in Gibbs free energy between the solid and the liquid phases. Coutinho model calculates the Gibbs free energy difference using Equation (B-1)

$$\Delta G_{\text{liquid}\rightarrow\text{solid}} = \frac{\Delta H_m}{RT_m}\left(\frac{T_m}{T}-1\right)+\frac{\Delta H_{tr}}{RT_{tr}}\left(\frac{T_{tr}}{T}-1\right)-\frac{\Delta Cp_{m,i}}{R}\left(\frac{T_{m,i}}{T}-\ln\frac{T_{m,i}}{T}-1\right) \quad \text{(B-1)}$$

Using the Gibbs free energy difference, the distribution of n-alkane molecules between the solid and liquid phases can be calculated according to Equation (B-2).

$$\Delta G_{\text{liquid}\rightarrow\text{solid}} = -RT\ln\frac{s\gamma^S}{x\gamma^L} \quad \text{(B-2)}$$

As can be seen from Equation (B-2), Coutinho model takes into consideration of solid and liquid phase non-idealities and thus corrects the concentration terms in Equation (B-2) by multiplication with the activity coefficients.

Coutinho's model calculates the liquid phase activity coefficients based on Flory-free volume theory which accounts for the entropy effects due to molecule size difference as well as the free-volume effects. Equations (B-3)-(B-4) show the calculation of liquid phase activity coefficient.

$$\ln\gamma_i^L = \ln\frac{\phi_i}{x_i}+1-\frac{\phi_i}{x_i} \quad \text{(B-3)}$$

$$\phi_i = \frac{x_i (V_i^{1/3} - V_{wi}^{1/3})^{3.3}}{\Sigma x_j (V_j^{1/3} - V_{wj}^{1/3})^{3.3}} \quad \text{(B-4)}$$

Coutinho model has two variations with different approaches to simulate the solid phase non-idealities: the Wilson model and the UNIQUAC model. According to the study by Coutinho et al., Wilson model and UNIQUAC model provide similar prediction of wax precipitation characteristics. The advantage of the UNIQUAC model is that it can predict the formation of multiple solid phases. However, the formation of multiple solid phases has no effect on the deposit CND because the deposit CND is determined for the deposit as a whole. On the other hand, thermodynamic modeling with the UNIQUAC model is more computationally demanding because the compositions of multiple solid phases have to be calculated. Consequently, Wilson model is used in this study for the calculation of solid phase activity coefficient.

Equations (B-5)-(B-8) show the calculation of solid phase activity coefficient using Wilson model.

$$\ln \gamma_i^S = -\ln(\Sigma_j \Lambda_{ij} x_j) + 1 - \Sigma_j \frac{\Lambda_{ji} x_j}{\Sigma_k \Lambda_{jk} x_k} \quad \text{(B-5)}$$

$$\Lambda_{ij} = \exp(-\frac{\lambda_{ij} - \lambda_{ii}}{RT}) \quad \text{(B-6)}$$

$$\lambda_{ii} = -\frac{1}{3}(\Delta H_{sub,i} - RT) \quad \text{(B-7)}$$

$$\lambda_{ij} = \alpha_{ij} \min(\lambda_{ii}, \lambda_{jj}) \quad \text{(B-8)}$$

Combining the Coutinho model with the MWP, one can calculate the inlet and wall concentration of each component and can thus study the deposit CND by performing deposition modeling of each component.

Appendix C

Procedures Used to Obtain the "True" Precipitated Solid Phase Composition

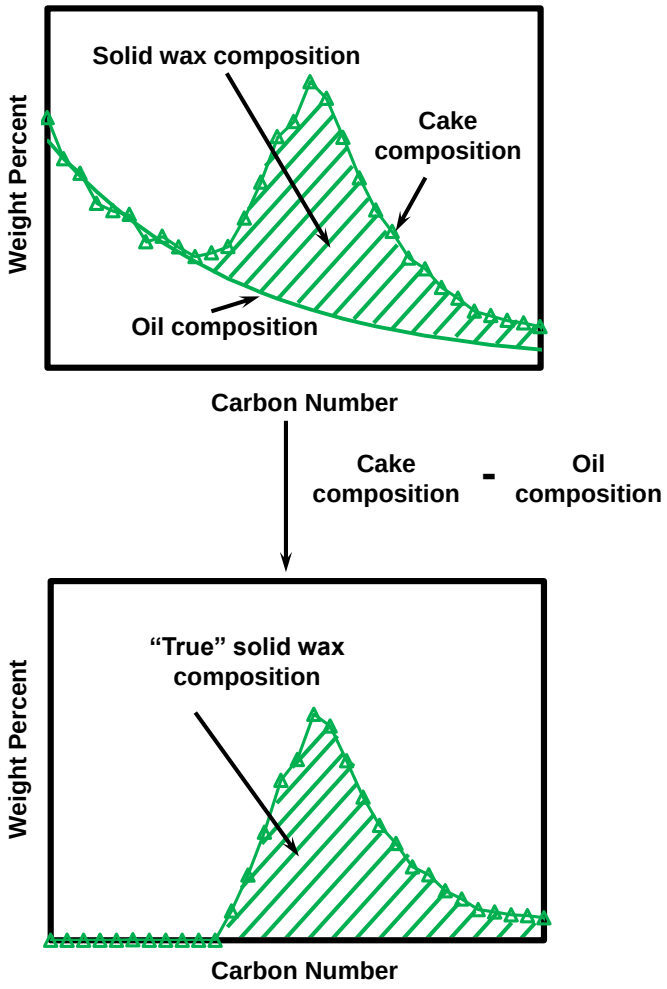

Figure C-1: The procedure to obtain precipitated solid phase composition by subtracting the oil composition from the cake composition

Appendix D

Equations for Hydrodynamic Calculations in the Michigan Wax Predictor (MWP)

For laminar flow regime, the radial velocity profile is parabolic and can be calculated based on the effective pipe diameter and the superficial velocity of the flow as shown in Equation (D-1).

$$V_z(r) = 2V_{avg}\left[1-\left(\frac{r}{r_{interface}}\right)^2\right] \tag{D-1}$$

For turbulent flow regime

$$y^+ = \frac{y}{\nu}\sqrt{\frac{\tau_w}{\rho}} = \left(1-\frac{r}{r_{interface}}\right)\frac{\mathrm{Re}}{2}\sqrt{\frac{f}{8}} \tag{D-2}$$

$$f = \frac{0.305}{\mathrm{Re}^{0.25}} \tag{D-3}$$

$$V_z^+ = \begin{cases} y^+ & y^+ \le 5 \\ 5\ln y^+ - 3.05 & 5 < y^+ \le 30 \\ 2.5\ln y^+ + 5.5 & y^+ \ge 30 \end{cases} \tag{D-4}$$

$$V_z = V_z^+\sqrt{\frac{\tau_w}{\rho}} \tag{D-5}$$

The dimensionless distance, y^+, is first calculated based on the kinematic viscosity of the water-in-oil dispersion and the shear stress at wall. The universal velocity profile is then used to calculate the dimensionless velocity, V_z^+. The dimensionless velocity is then converted to the actual velocity, V_z^+.

Appendix E

Derivation for the Formula to Calculate the Heat Transfer Coefficient between Oil and Water

The heat flow from the water phase to the oil phase can be calculated according to Equation (E-1).

$$Q_{W\to O} = hA_{interface}(T_W - T_O) \tag{E-1}$$

The interfacial area of all the water droplets can be calculated with Equation (E-2).

$$A_{interface} = N4\pi r_W^2 \tag{E-2}$$

The number of water droplets within the control volume, *N*, at a water volume fraction of ϕ_w can be calculated using Equation (E-3).

$$N \sim \frac{\phi_W}{\frac{4}{3}\pi r_W^3} \tag{E-3}$$

The convective heat transfer coefficient between oil and water can be calculated based on the Nusselt number of flow around sphere, shown in Equation (E-4).

$$h = \frac{k_O \mathrm{Nu}}{d_W} \tag{E-4}$$

The Nusselt number under such flow condition can be calculated based on the Reynolds number of the flow and the Prandtl number defined based on the physical properties of the oil phase, shown in Equation (E-5).

$$\mathrm{Nu} = \frac{h d_{\mathrm{W}}}{k_{\mathrm{O}}} = 2.0 + 0.6\,\mathrm{Re}_{\mathrm{W}}^{1/2}\,\mathrm{Pr}^{1/3} \approx 2.0 \tag{E-5}$$

It should be noted that the velocity of the oil phase and the dispersed water phase is small due to the high viscosity of the oil phase. Consequently, the Reynolds number in Equation (E-5) defined based on the velocity difference between the two phases is virtually zero.

Substituting Equations (E-2) - (E-4) into Equation (E-1) leads to the following equation to calculate the heat transfer rate between oil and water

$$\begin{aligned} Q_{\mathrm{W}\to\mathrm{O}} &= \frac{2k_{\mathrm{O}}}{d_{\mathrm{W}}} \frac{\phi_{\mathrm{W}}}{\frac{4}{3}\pi r_{\mathrm{W}}^3} 4\pi r_{\mathrm{W}}^2 (T_{\mathrm{W}} - T_{\mathrm{O}}) \\ &= \frac{12 k_{\mathrm{O}} \phi_{\mathrm{W}} (T_{\mathrm{W}} - T_{\mathrm{O}})}{d_{\mathrm{W}}^2} \end{aligned} \tag{E-6}$$

Therefore, the heat transfer coefficient between the oil and water phases can be defined according to Equation (E-7).

$$h_{\mathrm{inter}} = \frac{12 k_{\mathrm{O}} \phi_{\mathrm{W}}}{d_{\mathrm{W}}^2} \tag{E-7}$$

For a dispersion with a water droplet size described with a probability density function $P(d_{\mathrm{w}})$, the heat transfer rate from water to oil in a control volume can be written as the total heat transfer rate from each individual droplet, shown in Equation (E-8).

$$Q_{\mathrm{W}\to\mathrm{O}} = \Sigma_{\text{all droplets}} h(d_{\mathrm{W}})(T_{\mathrm{W}} - T_{\mathrm{O}}) A_{\mathrm{W}} \tag{E-8}$$

Substituting the calculation for the heat transfer coefficient between oil and water droplets, i.e., Equation (E-4) in to Equation (E-8) leads to Equation (E-9).

$$\begin{aligned} Q_{\mathrm{W}\to\mathrm{O}} &= \Sigma_{\text{all droplets}} h(d_{\mathrm{W}})(T_{\mathrm{W}} - T_{\mathrm{O}}) A_{\mathrm{W}} \\ &= \Sigma_{\text{all droplets}} \frac{2k_{\mathrm{O}}}{d_{\mathrm{W}}} (T_{\mathrm{W}} - T_{\mathrm{O}}) \pi d_{\mathrm{W}}^2 \\ &= \Sigma_{\text{all droplets}} 2k_{\mathrm{O}} (T_{\mathrm{W}} - T_{\mathrm{O}}) \pi d_{\mathrm{W}} \\ &= 2k_{\mathrm{O}} (T_{\mathrm{W}} - T_{\mathrm{O}}) \pi \Sigma_{\text{all droplets}} d_{\mathrm{W}} \end{aligned} \tag{E-9}$$

The summation can be replaced by an integral given that there is a large number of droplets in the control volume, shown in Equation (E-10).

$$\Sigma_{\text{all droplets}} d_{\text{W}} = \int_0^{\infty} NP(d_{\text{W}}) d_{\text{W}} \mathrm{d}d_{\text{W}} \tag{E-10}$$

In addition, the number of droplets can be related to the water volume fraction of the control volume through Equation (E-11).

$$\int_0^{\infty} NP(d_{\text{W}}) \frac{1}{6} \pi d_{\text{W}}^3 \mathrm{d}d_{\text{W}} \sim \phi_{\text{W}} \tag{E-11}$$

$$N \sim \frac{\phi_{\text{W}}}{\int_0^{\infty} P(d_{\text{W}}) \frac{1}{6} \pi d_{\text{W}}^3 \mathrm{d}d_{\text{W}}} \tag{E-12}$$

Substituting Equations (E-10) and (E-12) into (E-9) leads to

$$Q_{\text{W}\to\text{O}} = 12 k_{\text{O}} (T_{\text{W}} - T_{\text{O}}) \phi_{\text{W}} \frac{\int_0^{\infty} P(d_{\text{W}}) d_{\text{W}} \mathrm{d}d_{\text{W}}}{\int_0^{\infty} P(d_{\text{W}}) d_{\text{W}}^3 \mathrm{d}d_{\text{W}}} \tag{E-13}$$

Therefore, the interphase heat transfer coefficient between water and oil can be defined according to Equation (E-14).

$$h_{\text{inter}} = 12 k_{\text{O}} \phi_{\text{W}} \frac{\int_0^{\infty} P(d_{\text{W}}) d_{\text{W}} \mathrm{d}d_{\text{W}}}{\int_0^{\infty} P(d_{\text{W}}) d_{\text{W}}^3 \mathrm{d}d_{\text{W}}} \tag{E-14}$$

Appendix F

Parameters Used in the Field Scale and Lab Scale Simulations to Generate Temperature Profile Predictions

The viscosity of the oil used in the field scale simulation is described by Equation (F-1).

$$\mu_{\mathrm{O}}(Pa{\cdot}s) = \mu_0 \exp\left(\frac{E_A}{T(K)+273.15}\right), E_A = 1191K, \mu_0 = 1.1\times10^{-4}\,Pa{\cdot}s \qquad \text{(F-1)}$$

The viscosity of the emulsion used in the simulation is described by Equation (F-2)[164].

$$\mu_{\mathrm{E}}(Pa{\cdot}s) = \mu_{\mathrm{O}} \exp\left(5\phi_{\mathrm{W}}\right)\left(1-3\phi_{\mathrm{W}}+5.5\phi_{\mathrm{W}}^2\right) \qquad \text{(F-2)}$$

Other input parameters used in the field scale simulation are summarized in Table F-1.

Table F-1: Input parameters for field scale heat transfer simulation

Length (km)	20
Diameter (mm)	324
Total flow rate (m^3/hr)	570
Water volume fraction	0.5
Inlet temperature (°C)	75
Coolant temperature (°C)	4
External heat transfer coefficient (W/m^2/K)	20

The viscosity of the oil used in the lab scale simulation is described by Equation (F-3).

$$\mu_{\mathrm{O}}(Pa{\cdot}s) = \mu_0 \exp\left(\frac{E_A}{T(K)+273.15}\right), E_A = 1990K, \mu_0 = 3.1\times10^{-6}\,Pa{\cdot}s \qquad \text{(F-3)}$$

Equation (F-2) was used to describe the viscosity of the water-in-oil emulsion in the lab scale simulation as well.

Other input parameters used in the lab scale simulation is shown in Table F-2.

Table F-2: Input parameters for lab scale heat transfer simulation

Length (m)	5.5
Diameter (mm)	52.5
Total flow rate (m^3/hr)	15
Water volume fraction	0.5
Inlet temperature (°C)	25
Coolant temperature (°C)	15
External heat transfer coefficient (W/m^2/K)	1000

Appendix G

Heat Transfer Modeling with the Rectangular Channel

Panacharoensawad et al. performed water-in-oil flow experiments in a rectangular channel[70,95]. Several pairs of adjacent thermal couples were installed beneath the channel and in the perpendicular direction to the flow. Based on the readings from two paired thermal couples and the distance between them, the heat flux from the oil-water mixture to the coolant can be calculated. Other details concerning this apparatus can be found in ref. 70 and 95. This investigation provides a comprehensive characterization of the heat transfer from water-in-oil dispersed flow to coolant. As a result, heat transfer modeling was performed on this laboratory flow channel in order to assess the performance of the pseudo-single phase and the Eulerian-Eulerian approaches. It should be noted that governing equations should be set up in the Cartesian coordinates for this heat transfer modeling as the flow channel is rectangular. The operating conditions used for this simulation are included in Table G-1.

Table G-1: Input parameters for heat transfer modeling on the rectangular channel

Channel Length (m)	0.8
Channel Height (cm)	1.46
Channel Width (cm)	4.51
Bulk Superficial Velocity (m/s)	0.94
Water Volume Fraction	0.35
Inlet Temperature (°F)	105
Coolant Temperature (°F)	84
External Heat Transfer Coefficient ($kW/m^2/K$)	8.6

Figure G-1 shows the measured heat fluxes at different axial locations along the deposition cell in comparison with the predictions generated with different heat transfer modeling approaches.

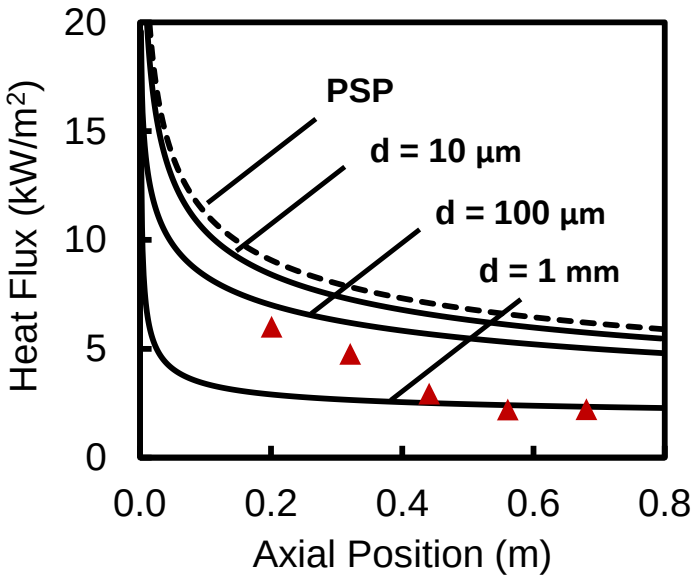

Figure G-1: Comparison between the predicted heat fluxes (solid and dashed curves) with various assumed droplet diameter and a fixed water volume fraction of 0.35 with experimental measurements (▲) obtained from a rectangular flow channel

As can be seen from Figure G-1, using a pseudo-single phase approach over-estimates the heat fluxes at all axial locations. In order to use the Eulerian-Eulerian approach, the droplet size distribution needs to be characterized experimentally. Unfortunately, the droplet size distribution of the water-in-oil dispersion was not measured when this experiment was performed as the investigators of this study were *not* aware that the droplet size distribution would become an important input parameter for wax deposition modeling at that time. As a result, a sensitivity analysis on the droplet diameter was performed in order to generate a first assessment of the

Eulerian-Eulerian approach. As can be seen from Figure G-1, a reasonably good match between the experimental measurements and predictions can be achieved with the Eulerian-Eulerian approach by assuming a droplet diameter of 1 mm.

Appendix H

Prediction of Wax Concentration Profile around Water Droplets in Absence of Bulk Precipitation

The concentration profile of wax molecules around the water droplets was simulated by assuming no bulk precipitation. The computational domain as well as the boundary conditions are shown in Figure H-1.

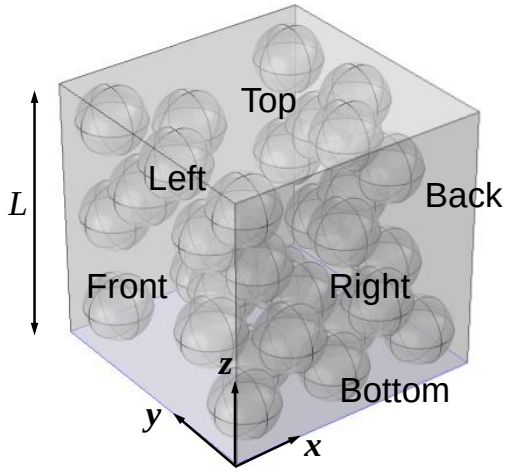

Governing Equation:

$$0 = \nabla^2 \theta_{wax}$$

Spheres represent water droplets.

Boundary conditions
Top: θ_{wax} (dimensionless concentration) = 1
Bottom: θ_{wax} = 0 (dimensionless concentration)
Left and Right: periodic boundary condition
Front and Back: periodic boundary condition
Water-oil interface: no-flux normal to the surface

Figure H-1: Schematics of the control volume as well as the governing equations and boundary conditions used to simulate the wax concentration profile in absence of bulk precipitation

Figure H-2 shows the simulated diffusion pathway of wax molecules with various water volume fraction in the bulk.

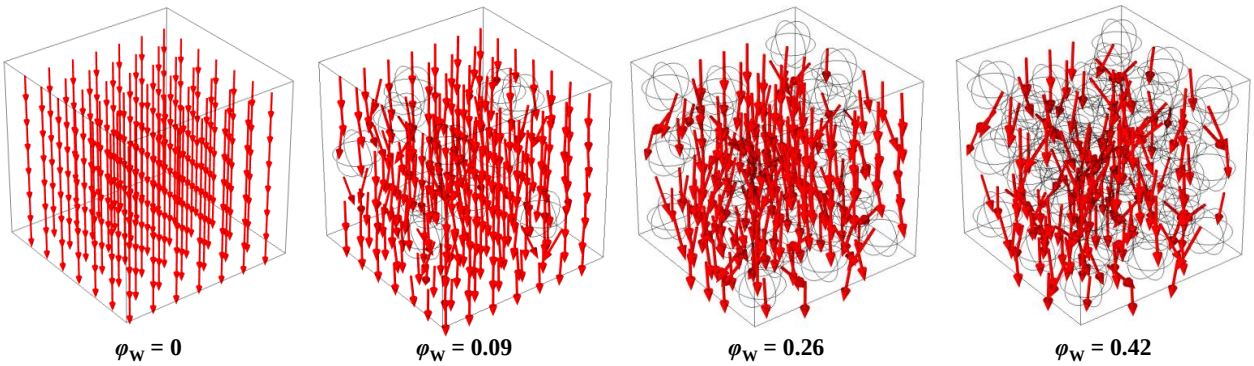

Figure H-2: The simulated diffusion pathways (red arrows) of wax molecules in presence of water droplets at different volume fractions

As can be seen from Figure H-2, the diffusion pathway of wax molecules become more and more tortuous as the water volume fraction increases, leading to a lower effective diffusivity. The decrease of effective diffusivity with increasing water volume fraction is analyzed in the main body of the manuscript.

Appendix I

Prediction of the Diffusivity Reduction Parameter in the Method of Ensemble Averaging

The concentration profile of wax molecules around the water droplets was simulated by assuming no bulk precipitation. The computational domain as well as the boundary conditions are shown in Figure I-1.

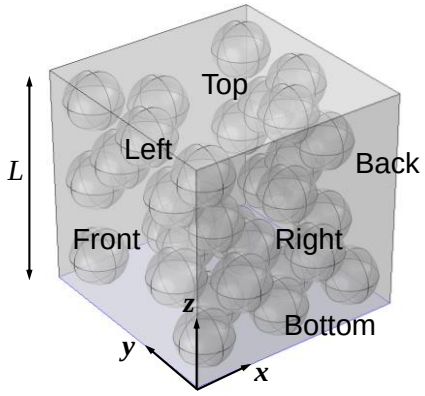

Spheres represent water droplets.

Governing Equation:

$$V_z \frac{\partial C_{\text{wax}}}{\partial z} + \frac{\partial}{\partial y}\left[-\left(\varepsilon_M + D_{\text{wo}}\right)\frac{\partial C_{\text{wax}}}{\partial y} \right] + k_{\text{precipitation}}\left(C_{\text{wax}} - C_{\text{wax,eq}}\right) = 0$$

Boundary conditions
Constant concentrations calculated from preliminary macroscopic modeling are imposed on top and bottom of the control volume.
Periodic boundary conditions are imposed on the left and right surfaces.
The wax concentration profile calculated from preliminary macroscopic modeling is imposed on the front surface.
No-flux boundary conditions are imposed on droplet-oil interfaces.
The equilibrium concentration profile is calculated based on the temperature profile predicted by the macroscopic simulation.

Figure I-1: Schematics of the control volume as well as the governing equations and boundary conditions used to predict the diffusivity reduction parameter in the method of ensemble average

Appendix J

Wax Concentration Profile around Water Droplets with Instantaneous Bulk Precipitation Kinetics

The concentration profile of wax molecules around the water droplets was simulated by assuming an instantaneous bulk precipitation kinetics. The computational domain as well as the boundary conditions are shown in Figure J-1. The mass transfer simulation was performed in a cubic control volume instead of the entire pipeline. Such simulation does not require overwhelming computational power and is sufficient to demonstrate the effect of instantaneous bulk precipitation kinetics on the wax concentration profiles.

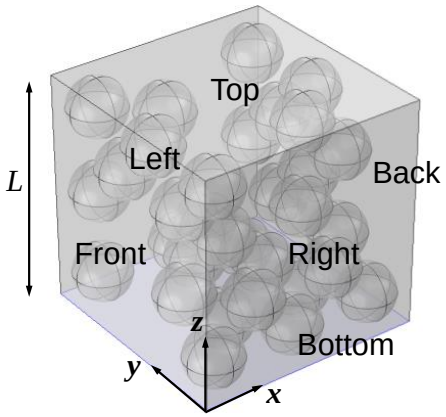

Governing Equation:

$$0 = \nabla^2 \theta_{wax} - \Phi(\theta_{wax} - \theta_{wax,eq})$$

$$\Phi = \frac{k_{precipitation} d_w^2}{D_{wo}}$$

$\Phi \to \infty$ as $k_{precipitation} \to \infty$

$\Phi = 10^{20}$ used in numerical simulation

Spheres represent water droplets.

Boundary conditions
Top: θ_{wax} (dimensionless concentration) = 1
Bottom: θ_{wax} = 0 (dimensionless concentration)
Left and Right: periodic boundary condition
Front and Back: periodic boundary condition
Water-oil interface: no-flux normal to the surface
The equilibrium concentration, $\theta_{wax,eq}$, varies linearly from 1 to 0 as one moves from the top surface to the bottom surface.

Figure J-1: Schematics of the control volume as well as the governing equations and boundary conditions used to simulate the wax concentration profile in presence of instantaneous bulk precipitation kinetics

The predicted concentration profile as well as the equilibrium concentration profile is compared in Figure J-2.

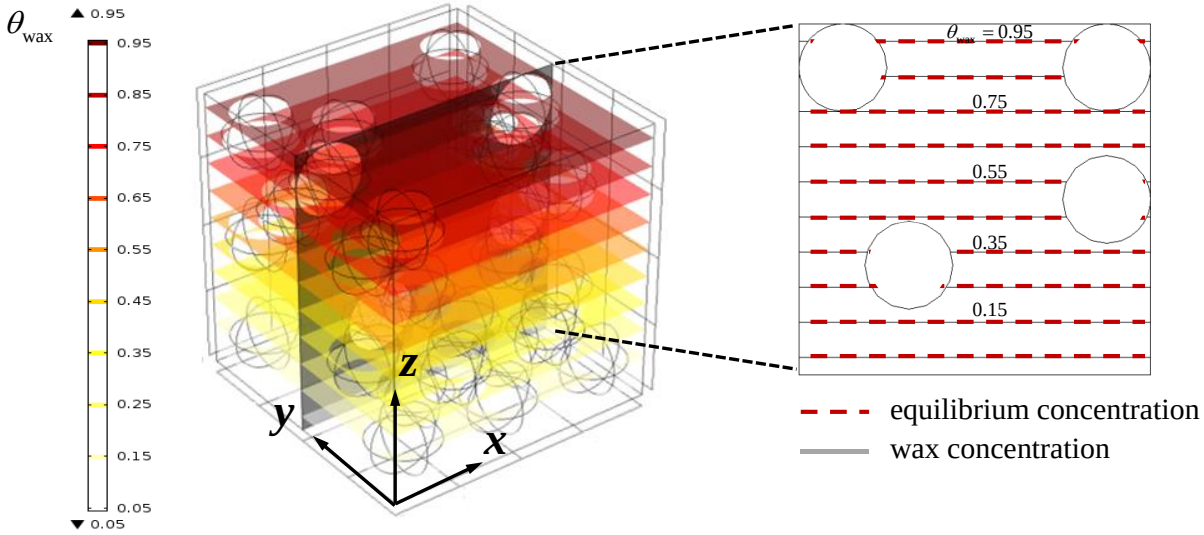

(a) 3D wax concentration contour

(b) Wax concentration contour on the cut plane marked in black

Figure J-2: 3D and 2D concentration contours of wax molecules in presence of instantaneous bulk precipitation

As can be seen from Figure J-2, the wax concentration profile and the equilibrium concentration profile are identical in presence of instantaneous bulk precipitation kinetics.

Appendix K

Input Parameters for the Case Study of the Effect of Water Volume Fraction on Laboratory Scale Wax Deposition

The viscosity of the oil used in the simulation is described by Equation (K-1).

$$\mu_{\mathrm{O}}(Pa{\cdot}s) = \mu_0 \exp\left(\frac{E_A}{T(K)+273.15}\right), E_A = 1191K, \mu_0 = 1.1\times10^{-4}\,Pa{\cdot}s \qquad \text{(K-1)}$$

The viscosity of the emulsion used in the simulation is described by Equation (K-2)[164].

$$\mu_{\mathrm{E}}(Pa{\cdot}s) = \mu_{\mathrm{O}} \exp\left(5\phi_{\mathrm{W}}\right)\left(1-3\phi_{\mathrm{W}}+5.5\phi_{\mathrm{W}}^2\right) \qquad \text{(K-2)}$$

The solubility curve of the crude oil used in this simulation is fitted to a polynomial function shown in Equation (K-3).

$$C_{\mathrm{wax}}(\mathrm{wt.frac.}) = -4.9\times10^{-6}T(^oC)^2 + 4.8\times10^{-4}T + 2.1\times10^{-2} \qquad \text{(K-3)}$$

Other input parameters used in simulation are summarized in Table K-1.

Table K-1: Input parameters for the modeling of the lab scale wax deposition case study

Length (m)	2.4
Diameter (mm)	41
Total flow rate (m^3/hr)	5.63
Water volume fraction	Varying
Inlet temperature (°C)	27
Coolant temperature (°C)	10
External heat transfer coefficient (W/m^2/K)	2500

Appendix L

Input Parameters for the Case Study of the Effect of Water Volume Fraction on Field Scale Wax Deposition

Table L-1: Summary of operating conditions in a field scale pipeline

Length (km)	50
Diameter (mm)	324
Total flow rate (barrel per day)	86000
Water volume fraction	varying
Inlet temperature (°C)	75
Sea bed temperature (°C)	4
External heat transfer coefficient ($W/m^2/K$)	20
Duration (days)	180

Appendix M

Input Parameters for the Case Study on the Effect of Droplet Size on Wax Deposition

The viscosity of the oil used in the simulation is described by Equation (M-1).

$$\mu_{\mathrm{O}}(Pa{\cdot}s) = \mu_0 \exp\left(\frac{E_A}{T(K)+273.15}\right), E_A = 3180K, \mu_0 = 4.3\times10^{-7}\,Pa{\cdot}s \qquad \text{(M-1)}$$

The viscosity of the emulsion used in the simulation is described by Equation (M-2)[164].

$$\mu_{\mathrm{E}}(Pa{\cdot}s) = \mu_{\mathrm{O}} \exp(5\phi_{\mathrm{W}})(1-3\phi_{\mathrm{W}}+5.5\phi_{\mathrm{W}}^2) \qquad \text{(M-2)}$$

The solubility curve of the crude oil used in this simulation is fitted to a polynomial function shown in Equation (M-3).

$$C_{\mathrm{wax}}(\mathrm{wt.frac.}) = 8.6\times10^{-5}T(^oC)^2 - 2.1\times10^{-3}T + 1.3\times10^{-2} \qquad \text{(M-3)}$$

Other input parameters used in the simulation are summarized in Table M-1.

Table M-1: Input parameters for the modeling of the lab scale wax deposition case study

Length (m)	1.2
Diameter (mm)	10.2
Total flow rate (m^3/hr)	0.22
Water volume fraction	0.5
Inlet temperature (°C)	45
Coolant temperature (°C)	5
External heat transfer coefficient (W/m^2/K)	620

Appendix N

Determination of the Phase Inversion Point of Water-Oil Mixture

The viscosities of the water- oil mixture at various water contents were measured at 5 °C with a shear rate of $1s^{-1}$. The water content at which a maximal viscosity was observed was defined as the phase inversion point. The change of viscosity as a function of water content is shown in Figure N-1.

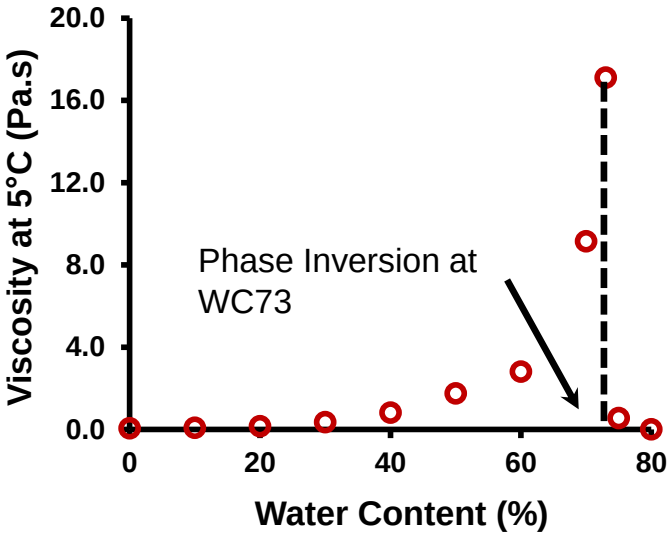

Figure N-1: Change of viscosity of the water-oil mixture as a function of water content

Appendix O

Steps to Perform Large Eddy Simulations (LES)

In order to initiate the LES calculations with a fluctuating velocity profile, a steady state Reynolds Averaged Navier Stokes (RANS) simulation is first performed with the $k-\varepsilon$ model and the fluid properties at the inlet of the pipeline. The RANS simulation was performed for 3000 iterations to achieve a converged steady state velocity profile and turbulence characteristics. A locally fluctuating divergence-free velocity field was then generated with the method developed by Smirnov et al.[165] based on the turbulence characteristics predicted by the RANS simulation. The turbulence intensity of the fluctuating velocity field is estimated to be ~5%, which is a typical value for fully developed turbulent flow with the corresponding Reynolds number. The calculation of the turbulence intensity is shown below.

The turbulence intensity, *I*, can be calculated with Equation (O-1).

$$I = \frac{u'}{U} \tag{O-1}$$

where u' is the root-mean-square of the turbulent velocity fluctuation defined by Equation (O-2). Note that the Einstein notation is used for brevity.

$$u' = \sqrt{\frac{1}{3}\left(u_i'\right)^2} \tag{O-2}$$

U is the mean velocity calculated by Equation (O-3).

$$U = \sqrt{U_i^2} \tag{O-3}$$

The volume averaged turbulence intensity was calculated by the following volume integral.

$$\bar{I} = \frac{\int_v I \mathrm{d}V}{\int_v \mathrm{d}V} \tag{O-4}$$

The volume averaged turbulence intensity is ~5%.

For fully developed turbulent pipe flow, the turbulent intensity can also be estimated using Equation (O-5).

$$I = 0.16\,\mathrm{Re}^{-1/8} \tag{O-5}$$

The turbulent intensity in this case estimated with Equation (O-5) is shown in Equation (O-6)

$$\begin{aligned} I &= 0.16\,\mathrm{Re}^{-1/8} \\ &= 0.16\left(\frac{\rho DU}{\mu}\right)^{-1/8} \\ &= 0.16\left(\frac{860\times 0.3048\times 0.75}{0.00176}\right)^{-1/8} \\ &= 4\% \end{aligned} \tag{O-6}$$

The turbulent intensity estimated with the well-established empirical correlation corresponds well with that calculated in CFD simulation.

Appendix P

Validation of the Implementation of LES

Using the parameters at location 1, the pressure gradient obtained from the LES at this location is 13 Pa/m, which is consistent with the prediction from Newtonian friction factor correlation, 14 Pa/m. The statistical steady state radial velocity profile obtained from LES simulation was then compared with the velocity profile generated from a RANS simulation, and is shown in Figure P-1.

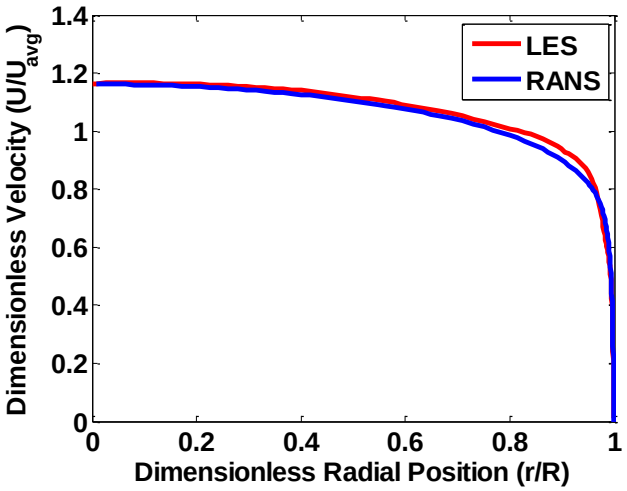

Figure P-1: Predicted time-averaged radial velocity profiles from LES and RANS simulations

Additionally, in the wall region, the results correspond well with the law of the wall, shown in Figure P-2.

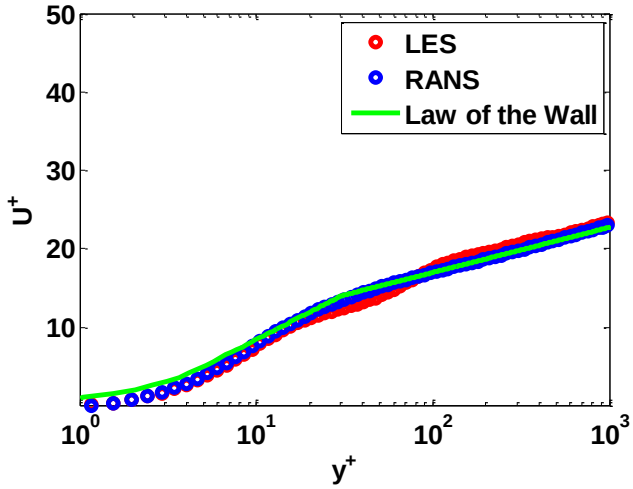

Figure P-2: Radial velocity profiles from LES and RANS compared with the law of the wall

The comparisons shown in Figure P-1 and Figure P-2 suggest that the LES is correctly implemented.

Appendix Q

Governing Equations for Heat and Mass Transfer Modeling Using LES and RANS

In order to implement a LES for heat and mass transfer, the transport equation is first filtered to calculate the volume average of the variable over the computational cell, shown in Equation (Q-1).

$$\rho_{\text{oil}} \frac{\partial \bar{\phi}}{\partial t} + \frac{\partial}{\partial x_j}\left(\overline{\rho_{\text{oil}} U_j \phi}\right) - \frac{\partial}{\partial x_j}\left(\overline{\Gamma \frac{\partial \phi}{\partial x_j}}\right) = 0 \qquad \text{(Q-1)}$$

The filter operation is emphasized by the overbar on the variables. The filtered non-linear convection term, $\overline{U_j \phi}$ is then decomposed into the resolved components, $\overline{U_j} \cdot \bar{\phi}$ and the unresolved component, defined according to Equation (Q-2).

$$\sigma_j \equiv \rho_{\text{oil}} \overline{U_j \phi} - \rho_{\text{oil}} \overline{U_j} \cdot \bar{\phi} \qquad \text{(Q-2)}$$

σ_j represents the intensity of mixing of heat or mass by the turbulent eddies that are smaller than the cell size. This term is calculated based on the "gradient-diffusion" hypothesis[166], which suggests that the rate of heat or mass transfer due to turbulent eddies is directly proportional to the gradient of temperature or concentration with a turbulent diffusivity as the proportionality constant. This mathematical implementation is shown in Equation (Q-3).

$$\sigma_j = -\Gamma_{\mathrm{T,SGS}} \frac{\partial \bar{\phi}}{\partial x_j} \tag{Q-3}$$

The turbulent diffusivity, $\Gamma_{\mathrm{T,SGS}}$, is then calculated with an empirical correlation shown in Equations (Q-4).

$$\nu_{\mathrm{T,SGS}} / \Gamma_{\mathrm{T,SGS}} \simeq 0.85 \tag{Q-4}$$

$\nu_{\mathrm{T,SGS}}$ = the eddy momentum diffusivity associated with the subgrid scale turbulent eddies,(m^2 / s)

Combining Equations (Q-1)- (Q-3) yields Equation (Q-5)

$$\rho_{\mathrm{oil}} \frac{\partial \bar{\phi}}{\partial t} + \rho_{\mathrm{oil}} \frac{\partial}{\partial x_j} \overline{U_j} \cdot \bar{\phi} - \frac{\partial}{\partial x_j} \left[\left(\Gamma + \Gamma_{\mathrm{T,SGS}} \right) \frac{\partial \bar{\phi}}{\partial x_j} \right] = 0 \tag{Q-5}$$

Equation (Q-5) will now be numerically solved to generate the solution profiles for temperature and concentration in non-Newtonian turbulent fluids. The time-averaged solution profile is then determined based on the instantaneous solution profiles.

Conventional CFD techniques such as RANS are commonly used to simulate heat and mass transfer in turbulent flow. In RANS simulations, the time-averaged transport equation shown in Equation (Q-6) is solved. We will also perform RANS simulation with the non-Newtonian fluid and demonstrate the limitation of RANS applications on non-Newtonian flows.

$$\rho_{\mathrm{oil}} \frac{\partial \langle \phi \rangle}{\partial t} + \rho_{\mathrm{oil}} \frac{\partial}{\partial x_j} \langle U_j \rangle \cdot \langle \phi \rangle - \frac{\partial}{\partial x_j} \left[\left(\Gamma + \Gamma_{\mathrm{T}} \right) \frac{\partial \langle \phi \rangle}{\partial x_j} \right] = 0 \tag{Q-6}$$

$\langle \phi \rangle$ = time-averaged temperature/concentration

In this investigation, the conventional $k - \varepsilon$ RANS model is used. Based on this RANS model, the turbulent diffusivity of heat and mass can be estimated based on the momentum diffusivity, according to Equation (Q-7).

$$\nu_{\mathrm{T}} / \Gamma_{\mathrm{T}} \simeq 0.85 \tag{Q-7}$$

ν_{T} = turbulent momentum diffusivity,(m^2 / s)

where the momentum diffusivity can be calculated based on the turbulent kinetic energy as well as the turbulent kinetic energy dissipation rate, according to Equation (Q-8).

$$\nu_{\mathrm{T}} = 0.09\frac{k^2}{\varepsilon} \tag{Q-8}$$

k = turbulent kinetic energy per unit mass,(m^2 / s^2)

ε = turbulence dissipation rate,(m^2 / s^3)

Figure Q-1 shows the temperature/concentration profile in Newtonian turbulent flow predicted by RANS and LES.

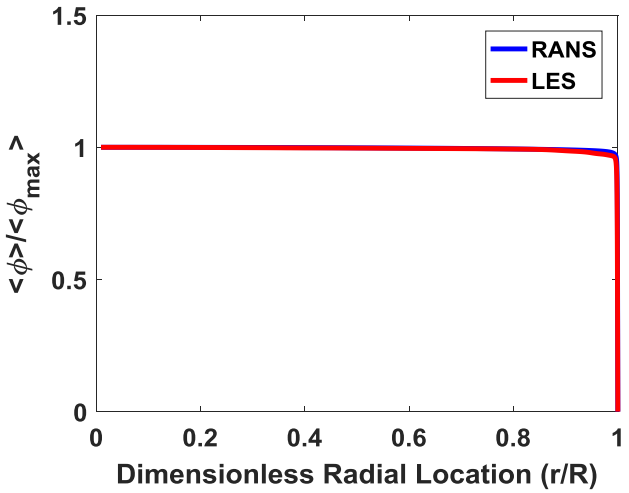

Figure Q-1: Predicted radial profile of temperature/concentration with RANS and LES

As can be seen from Figure Q-1, excellent agreement between the RANS and LES predictions is achieved, indicating that both methods are implemented correctly.

Appendix R

Time Evolution of the Turbulent Kinetic Energy Leading to Turbulent-to-Laminar Transition

The turbulent kinetic energy of a fluid packet at the centerline (r = 0), defined in Equation (R-1), calculated at locations 1, 3 and 5 was monitored as a function of time, shown in Figure R-1.

$$TKE = \frac{U_i'^2}{2} = \frac{\left(U_i - \langle U_i \rangle\right)^2}{2} \text{ calculated at } r = 0(\text{centerline}) \qquad \text{(R-1)}$$

U_i = instantaneous velocity calculated by LES,(m/s)

$\langle U_i \rangle$ = statistical steady state velocity calculated by LES,(m/s)

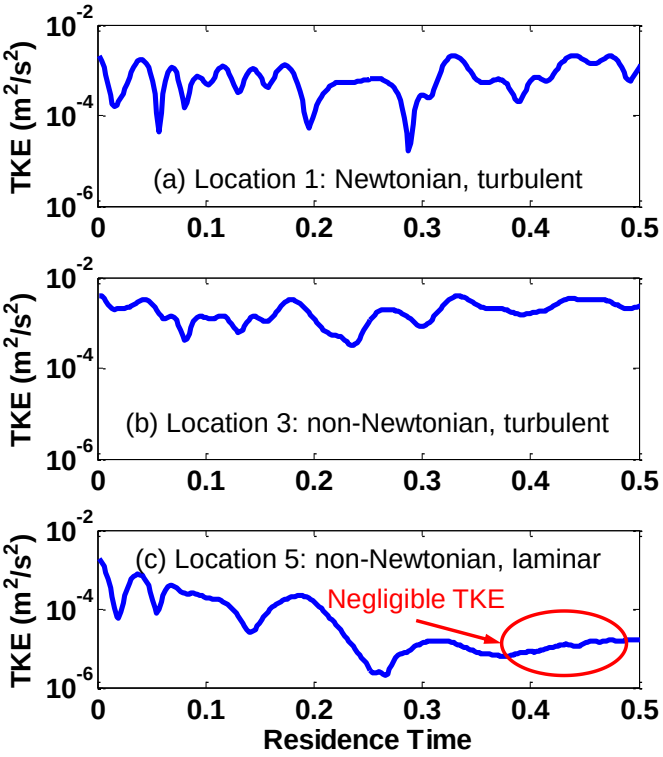

Figure R-1: Time-evolution of turbulent kinetic energy (TKE) at the centerline

The turbulent kinetic energy continuously oscillates near approximately 10^{-3} m^2/s^2 at locations 1 and 3, shown in Figure R-1(a) and (b). As can be seen in Figure R-1(c), the turbulent kinetic energy is dampened over the residence time as the fluid moves down the pipe and eventually reaches a negligible level for the case at location 5.

Appendix S

Effects of Rheological Parameters on Flow Regime Transition

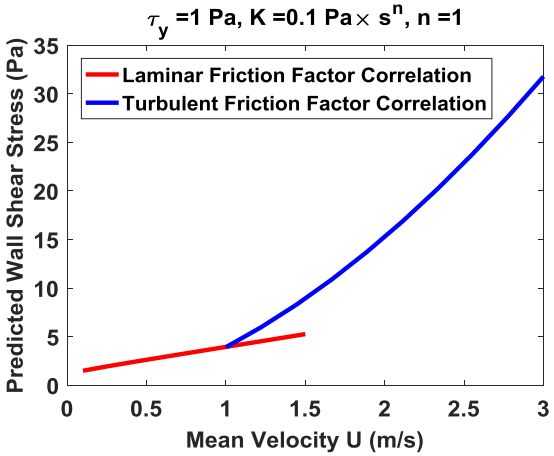

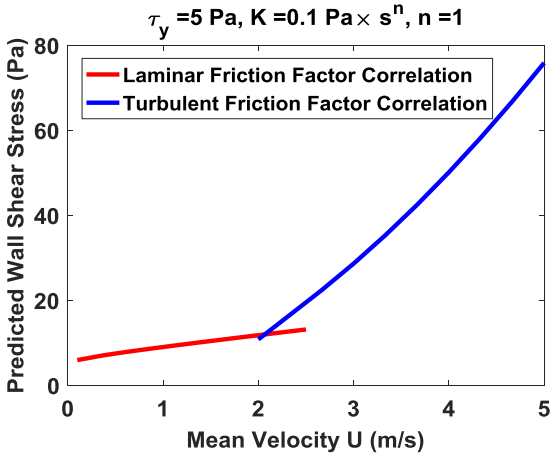

The laminar to turbulent transition occurs at a higher mean velocity as τ_y increases.

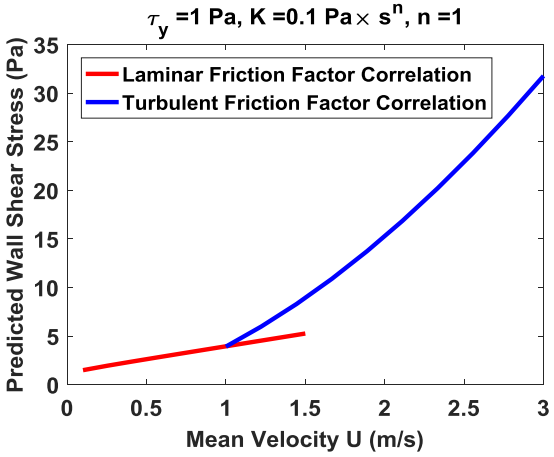

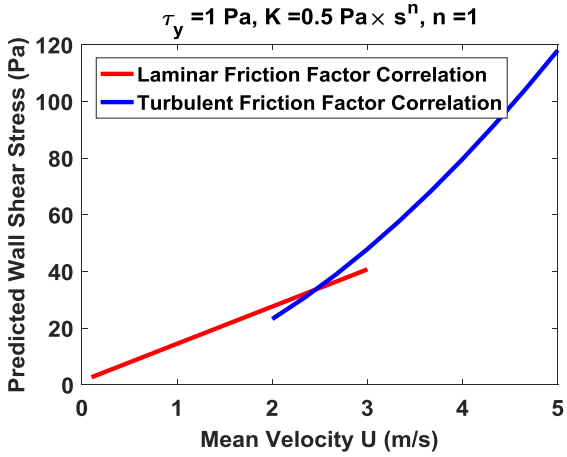

The laminar to turbulent transition occurs at a higher mean velocity as K increases.

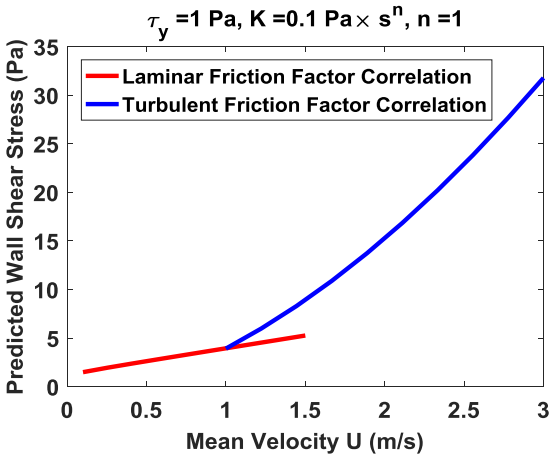

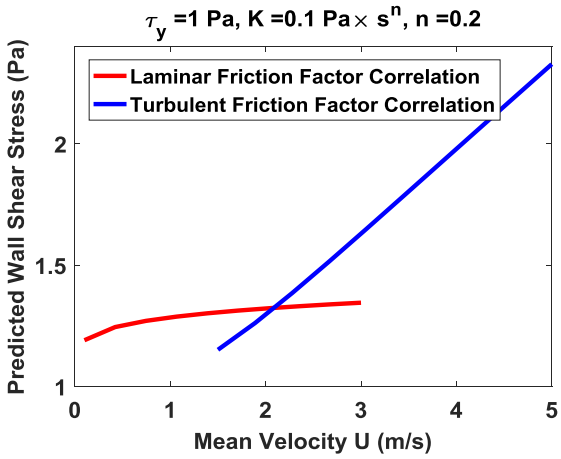

The laminar to turbulent transition occurs at a higher mean velocity as n decreases.

Appendix T

Validation of the Pressure Gradient Prediction from the Chilton-Stainsby Correlation

Figure T-1 summarizes the predicted pressure gradient by LES and the Chilton-Stainsby friction factor correlation.

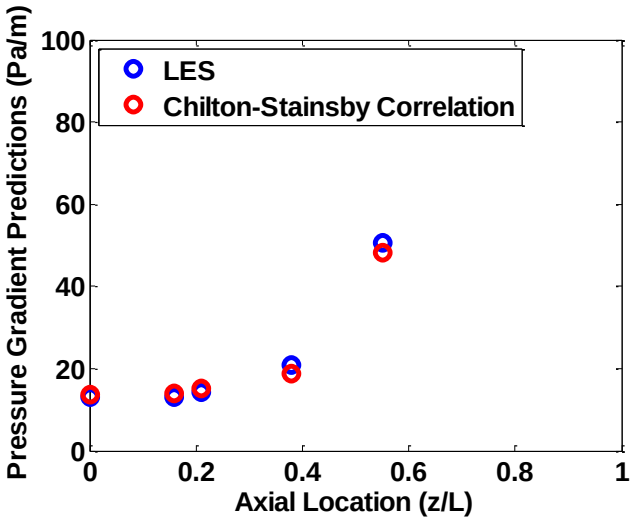

Figure T-1: Comparison between the pressure gradient predictions by LES and Chilton-Stainsby correlation

As can be seen from Figure T-1, the Chilton-Stainsby friction factor correlation can achieve consistent predictions with that from a more advanced modeling technique, i.e., LES.

Appendix U

Input Parameters for Field Scale Wax Deposition Simulation

The input parameters are listed in Table U-1.

Table U-1: Input parameters for field scale wax deposition simulation

Inner diameter, D (m)	0.305
Length, L (km)	23
Total flow rate, Q (m^3/hr)	364.0
Inlet temperature (°C)	75
Ambient temperature (°C)	25
External heat transfer coefficient (W/m^2/K)	22
Oil/Wax density (kg/m^3)	800
Oil/Wax heat capacity (J/kg/K)	2100
Oil/Wax thermal conductivity (W/m/K)	0.2
Wax aspect ratio	10

Bibliography

(1) World energy consumption https://en.wikipedia.org/wiki/World_energy_consumption (accessed Feb 20, 2017).

(2) Crude Oil Production https://www.eia.gov/dnav/pet/pet_crd_crpdn_adc_mbblpd_a.htm (accessed Feb 20, 2017).

(3) Singh, P. Gel deposition on cold surfaces, University of Michigan, 2000.

(4) Paso, K.; Senra, M.; Yi, Y.; Sastry, A. M.; Fogler, H. S. *Ind. Eng. Chem. Res.* **2005**, *44* (18), 7242.

(5) Venkatesan, R.; Nagarajan, N. R.; Paso, K.; Yi, Y.-B.; Sastry, a. M.; Fogler, H. S. *Chem. Eng. Sci.* **2005**, *60* (13), 3587.

(6) Kök, M. V.; Letoffe, J. M.; Claudy, P. *J. Therm. Anal. Calorim.* **2007**, *90* (3), 827.

(7) Holder, G. A.; Winkler, J. *J. Inst. Pet.* **1965**, *51*, 228.

(8) Venkatesan, R. The Deposition and Rheology of Organic Gels, University of Michigan, 2004.

(9) Short Story of a Long Pipeline - Cairn India - Raychem STS https://www.youtube.com/watch?v=Cgkb25pxFro&t=33s (accessed Feb 20, 2017).

(10) Jennings, D. W.; Weispfennig, K. *Energy and Fuels* **2006**, *20* (6), 2457.

(11) Niesen, V. G. The Real Cost of Subsea Pigging http://www.epmag.com/archives/features/3332.htm (accessed Feb 20, 2017).

(12) Newberry, M. E. *J. Pet. Technol.* **1984**, *36* (5), 779.

(13) Lee, H. S. Computational and Rheological Study of Wax Deposition, University of Michigan, 2008.

(14) Huang, Z. Application of The Fundamentals of Heat and Mass Transfer to The Investigation of Wax Deposition in Subsea Pipelines, University of Michigan, 2011.

(15) Daqin Oil Province http://www.cnpc.com.cn/en/operatediol/201405/f96f221bb538428f9b1b7f4869c8f576.shtml (accessed Feb 20, 2017).

(16) The Mangala and Bhagyam oil fields http://www.oilandgastechnology.net/upstream-news/mangala-bhagyam-oil-fields (accessed Feb 20, 2017).

(17) House, D. Utah's challenge: Get its waxy crude oils flowing http://archive.sltrib.com/story.php?ref=/sltrib/money/53886364-79/utah-crude-oil-waxy.html.csp (accessed Feb 20, 2017).

(18) Coutinho, J. a. P.; Edmonds, B.; Moorwood, T.; Szczepanski, R.; Zhang, X. *Energy & Fuels* **2006**, *20* (3), 1081.

(19) Burger, E. D.; Perkins, T. K.; Striegler, J. H. *J. Pet. Technol.* **1981**, *33* (6), 1075.

(20) Majeed, A.; Bringedal, B.; Overa, S. *Oil Gas J.* **1990**, *88* (25), 63.

(21) Singh, P.; Venkatesan, R.; Fogler, H. S.; Nagarajan, N. *AIChE J.* **2000**, *46* (5), 1059.

(22) Gluyas, J. G.; Underhill, J. R. *Geol. Soc. London, Mem.* **2003**, *20* (1), 327.

(23) Lee, H. S.; Singh, P.; Thomason, W. H.; Fogler, H. S. *Energy & Fuels* **2008**, *22* (1), 480.

(24) Lindeloff, N.; Krejbjerg, K. *Energy & Fuels* **2002**, *16* (4), 887.

(25) Ramirez-Jaramillo, E.; Lira-Galeana, C.; Manero, O. *Pet. Sci. Technol.* **2004**, *22* (7–8), 821.

(26) Huang, Z.; Lee, H. S.; Senra, M.; Fogler, H. S. *AIChE J.* **2011**, *57* (11), 2955.

(27) Huang, Z.; Lu, Y.; Hoffmann, R.; Amundsen, L.; Fogler, H. S. *Energy & Fuels* **2011**, *25* (11), 5180.

(28) Lu, Y.; Huang, Z.; Hoffmann, R.; Amundsen, L.; Fogler, H. S. *Energy & Fuels* **2012**, *26* (7), 4091.

(29) Edmonds, B.; Moorwood, T.; Szczepanski, R.; Zhang, X. *Energy & Fuels* **2008**, *22* (11), 729.

(30) Wang, Q.; Sarica, C.; Chen, T. T. X. *J. Energy Resour. Technol.* **2005**, *127* (4), 302.

(31) Senra, M. J. Assessing the Role of PolyDispersity and Cocrystallization on Crystallizing n-Alkane in n-alkane Solutions, University of Michigan, 2009.

(32) Bai, C.; Zhang, J. *Energy & Fuels* **2013**, *27* (2), 752.

(33) Svendsen, J. A. *AIChE J.* **1993**, *39* (8), 1377.

(34) Creek, J. .; Lund, H. J.; Brill, J. P.; Volk, M. *Fluid Phase Equilib.* **1999**, *158–160*, 801.

(35) Huang, Z.; Senra, M.; Kapoor, R.; Fogler, H. S.; Lee, H. S. *AIChE J.* **2011**, *57* (11), 841.

(36) Hayduk, W.; Minhas, B. *Can. J. Chem. ...* **1982**, *60* (2), 295.

(37) Erickson, D. D.; Niesen, V. G.; Brown, T. S. *Proc. SPE Annu. Tech. Conf. Exhib.* **1993**.

(38) Daridon, J. *Energy & Fuels* **2001**, *15* (14), 730.

(39) Hoffmann, R.; Amundsen, L. *Energy & Fuels* **2010**, *24* (2), 1069.

(40) Han, S.; Huang, Z.; Senra, M.; Hoffmann, R.; Fogler, H. S. *Energy & Fuels* **2010**, *24* (3), 1753.

(41) Green, D. W. *Perry's Chemical Engineers' Handbook, 8th Edition*; McGraw-Hill: New York, 2008.

(42) Hansen, J. H.; Fredenslund, A.; Lyngby, D.-; Pedersen, K. S. *AIChE J.* **1988**, *34* (12), 1937.

(43) Coto, B.; Coutinho, J. A. P.; Martos, C.; Robustillo, M. D.; Espada, J. J.; Peña, J. L. *Energy & Fuels* **2011**, *25* (3), 1153.

(44) Singh, P.; Youyen, A.; Fogler, H. S. *AIChE J.* **2004**, *47* (9).

(45) Dauphin, C.; Daridon, J. .; Coutinho, J.; Baylère, P.; Potin-Gautier, M. *Fluid Phase Equilib.* **1999**, *161* (1), 135.

(46) Pauly, J.; Dauphin, C.; Daridon, J. L. *Fluid Phase Equilib.* **1998**, *149* (1–2), 191.

(47) Pauly, J.; Daridon, J.-L.; Coutinho, J. a. P. *Fluid Phase Equilib.* **2004**, *224* (2), 237.

(48) Padgett, P. W.; Hefley, D. G.; Henriksen, A. *Ind. Eng. Chem. Res.* **1926**, *18* (8), 832.

(49) Visintin, R. F. G.; Lapasin, R.; Vignati, E.; D'Antona, P.; Lockhart, T. P.; Antona, P. D. *Langmuir* **2005**, *21* (14), 6240.

(50) Abdallah, D. J.; Weiss, R. G. *Langmuir* **2000**, *16* (10), 352.

(51) Ranningsen, H. P.; Bjamdal, B. *Energy & Fuels* **1991**, *5* (6), 895.

(52) Senra, M.; Scholand, T.; Maxey, C.; Fogler, H. S. *Energy & Fuels* **2009**, *23* (12), 5947.

(53) Kane, M.; Djabourov, M.; Volle, J.; Lechaire, J.; Frebourg, G. *Fuel* **2003**, *82*, 127.

(54) Kané, M.; Djabourov, M.; Volle, J.-L. *Fuel* **2004**, *83* (11–12), 1591.

(55) Wardhaugh, L. T.; Boger, D. V. *AIChE J.* **1991**, *37* (6), 871.

(56) Ronningsen, H. P. *J. Pet. Sci. Eng.* **1992**, *7*, 177.

(57) Vignati, E.; Piazza, R.; Visintin, R. F. G.; Lapasin, R.; D'Antona, P.; Lockhart, T. P. *J. Phys. Condens. Matter* **2005**, *17* (45), S3651.

(58) Hoffmann, R.; Johnson, G. W. *Flow Meas. Instrum.* **2011**, *22* (5), 351.

(59) Singh, A.; Lee, H.; Singh, P.; Company, C.; Sarica, C. In *Offshore Technology Conference*; Offshore Technology Conference: Houston, Texas, USA, 2011.

(60) Noville, I.; Naveira, L. In *SPE Latin America and Caribbean Petroleum Engineering Conference*; Society of Petroleum Engineers: Mexico City, Mexico, 2012; pp 1–12.

(61) Zheng, S.; Zhang, F.; Huang, Z.; Fogler, H. S. *Energy & Fuels* **2013**, *27* (12), 7379.

(62) Mohamed, A. M. O.; Elgamal, M.; Said, R. . *Sensors Actuators A* **2006**, *125* (2), 133.

(63) Shi, H.; Cai, J.; Jepson, W. P. *J. Energy Resour. Technol.* **2001**, *123* (4), 270.

(64) Hoffmann, R.; Amundsen, Lene; Huang, Z.; Zheng, S.; Fogler, H. S. *Energy & Fuels* **2012**, *26*, 3416.

(65) Czarnecki, J.; Tchoukov, P.; Dabros, T.; Xu, Z. *Can. J. Chem. Eng.* **2013**, *91* (8), 1365.

(66) McLean, J. D.; Kilpatrick, P. K. *J. Colloid Interface Sci.* **1997**, *189* (2), 242.

(67) Schorling, P.-C.; Kessel, D. .; Rahimian, I. *Colloids Surfaces A Physicochem. Eng. Asp.* **1999**, *152* (1–2), 95.

(68) Xia, L.; Lu, S.; Cao, G. *J. Colloid Interface Sci.* **2004**, *271* (2), 504.

(69) Bruno, A.; Sarica, C.; Chen, H.; Volk, M. In *2008 SPE Annual Technical Conference and Exhibition*; Society of Petroleum Engineers: Denver, Colorado, USA, 2008.

(70) Panacharoensawad, E.; Sarica, C. *Energy & Fuels* **2013**, *27* (9), 5036.

(71) Couto, G. H.; Chen, H.; Dellecase, E.; Sarica, C.; Volk, M. In *2006 Offshore Technology Conference*; Offshore Technology Conference: Houston, Texas, USA, 2008.

(72) Sarica, C.; Panacharoensawad, E. *Energy & Fuels* **2012**, *26* (7), 3968.

(73) Holz, M.; Heil, Stefan, R.; Sacco, A. *Phys. Chem. Chem. Phys.* **2000**, *2*, 4740.

(74) Stejskal, E. O.; Tanner, J. E. *J. Chem. Phys.* **1965**, *42* (1), 288.

(75) Claridge, T. D. *High-Resolution NMR Techniques in Organic Chemistry*, 2nd ed.; Elsevier, 2014.

(76) Reddy, S. R.; Fogler, H. S. *J. Colloid Interface Sci.* **1981**, *79* (1), 105.

(77) Delgado-Linares, J. G. J. G.; Majid, A. a. a.; Sloan, E. D.; Koh, C. a.; Sum, A. K. *Energy & Fuels* **2013**, *27* (8), 4564.

(78) Opedal, N. V. der T.; Sørland, G.; Sjöblom, J. *Open-Access J. Basic Princ. Diffus. Theory, Exp. Appl.* **2009**, *9* (7), 1.

(79) Jonsson, B.; Wennerstrom, H.; Nilsson, P. G.; Linse, P. *Colloid Polym. Sci.* **1986**, *264* (1), 77.

(80) Zhang, Y.; Gong, J.; Ren, Y.; Wang, P. *Energy & Fuels* **2010**, *24* (2), 1146.

(81) Aichele, C. P.; Chapman, W. G.; Rhyne, L. D.; Subramani, H. J.; House, W. V. *Energy & Fuels* **2009**, *23* (13), 3674.

(82) *FLUENT User Guide*; 2004.

(83) *ANSYS CFX-Solver Modeling Guide*; 2009.

(84) Oosthuizen, P. H.; Naylor, D. *An Introduction to Convective Heat Transfer Analysis*; WCB/McGraw Hill: New York, 1999.

(85) Chang, J.; Wang, G.; Gao, J.; Zhang, K.; Chen, H.; Yang, Y. *Powder Technol.* **2012**, *217*, 50.

(86) Choi, H. S.; Meier, D. *Heat Mass Transf.* **2012**, *48* (9), 1513.

(87) Hamzehei, M.; Rahimzadeh, H. **2009**, 3177.

(88) Yusuf, R.; Halvorsen, B.; Melaaen, M. C. *Chem. Eng. Sci.* **2011**, *66* (8), 1550.

(89) Zheng, S.; Fogler, H. S. *Ind. Eng. Chem. Res.* **2014**, *54* (16), 4420.

(90) Grace, H. P. *Chem. Eng. Commun.* **1982**, *14* (3–6), 225.

(91) Hinze, J. O. *AIChE J.* **1955**, *1* (3), 289.

(92) Brauner, N.; Moalem, D. **1992**, *18* (I), 123.

(93) Cai, J.; Li, C.; Tang, X.; Ayello, F.; Richter, S.; Nesic, S. *Chem. Eng. Sci.* **2012**, *73*, 334.

(94) Maxwell, C. A. *Treatise on Electricity and Magnetism*, 3rd ed.; Dover Publications, Inc.: New York, 1954.

(95) Panacharoensawad, E. Wax Deposition under Two-Phase Oil-Water Flowing Conditions, The University of Tulsa, 2012.

(96) Venkatesan, R.; Fogler, H. S. *AIChE J.* **2004**, *50* (7), 1623.

(97) Alder, B. J.; Wainwright, T. E. *J. Chem. Phys.* **1957**, *27* (5), 1208.

(98) Wood, W. W.; Jacobson, J. D. *J. Chem. Phys.* **1957**, *27* (1957), 1207.

(99) Bailey, B.; Crabtree, M.; Tyrie, J.; Elphick, J.; Kuchuk, F.; Romano, C.; Roodhart, L. *Oilf. Rev.* **2000**, *12*, 30.

(100) Craig Jr., F. F. *The Reservoir Engineering Aspects of Waterflooding*, Vol.3.; SPE Monograph Series: Richardson, Texas, 1971.

(101) Whillhite, G. P. *Waterflooding*, Vol. 3.; Society of Petroleum Engineers, 1986.

(102) Rose, S. C.; Buckwalter, J. F.; Woodhall, R. J. *The Design Engineering Aspects of Waterflooding*, Vol. 11.; Society of Petroleum Engineers: Richardson, Texas, 1989.

(103) Controlling excess water production http://petrowiki.org/Controlling_excess_water_production#cite_note-r1-1 (accessed Jan 1, 2016).

(104) Wang, P.; Wang, W.; Gong, J.; Zhou, Y.; Yang, W. *J. Energy Resour. Technol.* **2013**, *135* (4), 42902.

(105) Abdurahman, N. H.; Rosli, Y. M.; Azhari, N. H.; Hayder, B. a. *J. Pet. Sci. Eng.* **2012**, *90–91*, 139.

(106) Vilasau, J.; Solans, C.; Gómez, M. J.; Dabrio, J.; Mújika-Garai, R.; Esquena, J. *Colloids Surfaces A Physicochem. Eng. Asp.* **2011**, *389* (1–3), 222.

(107) Ghosh, S.; Mandal, T. K.; Das, G.; Das, P. K. *Renew. Sustain. Energy Rev.* **2009**, *13* (8), 1957.

(108) Kasumu, A. S.; Mehrotra, A. K. *Energy & Fuels* **2013**, *27* (4), 1914.

(109) Quan, Q.; Wang, W.; Wang, P.; Zhou, Y.; Gong, J. *Pet. Sci. Technol.* **2015**, *33* (5), 520.

(110) Wang, Z.; Liu, Y.; Li, J.; Zhuge, X.; Zhang, L. *Energy & Fuels* **2016**, *30* (6), 4570.

(111) Oh, K.; Deo, M. D. *Fuel* **2011**, *90* (6), 2113.

(112) Sun, G.; Zhang, J.; Li, H. *Energy and Fuels* **2014**, *28*, 3718.

(113) Magda, J. J.; El-Gendy, H.; Oh, K.; Deo, M. D.; Montesi, A.; Venkatesan, R. *Energy & Fuels* **2009**, *23* (3), 1311.

(114) Paso, K.; Silset, A.; Sørland, G.; Goncalves, M. de A. L.; Sjöblom, J. **2009**, No. 4, 471.

(115) Packer, K. .; Rees, C. *J. Colloid Interface Sci.* **1972**, *40* (2), 206.

(116) Lashkarbolooki, M.; Seyfaee, A.; Esmaeilzadeh, F.; Mowla, D. *Energy & Fuels* **2010**, *24* (2), 1234.

(117) Seyfaee, A.; Lashkarbolooki, M.; Esmaeilzadeh, F.; Mowla, D. *J. Dispers. Sci. Technol.* **2011**, *32* (3), 312.

(118) Dimitriou, C. J.; McKinley, G. H. *Soft Matter* **2014**, *10* (35), 6619.

(119) Dimitriou, C. J.; McKinley, G. H.; Venkatesan, R. *Energy and Fuels* **2011**, *25* (7), 3040.

(120) Pedersen, K. S.; Rønningsen, H. P. *Energy & Fuels* **2000**, *14* (7), 43.

(121) Marchesini, F. H.; Alicke, A. A.; De Souza Mendes, P. R.; Ziglio, C. M. *Energy and Fuels* **2012**, *26* (5), 2566.

(122) Cross, M. M. *J. Colloid Sci.* **1965**, *20* (5), 417.

(123) Larson, R. G. *The Structure and Rheology of Complex Fluids*, 1st ed.; Oxford University Press, 1998.

(124) Kumar, L.; Paso, K.; Sjöblom, J. *J. Nonnewton. Fluid Mech.* **2015**, *223*, 9.

(125) Kumar, L.; Zhao, Y.; Paso, K.; Grimes, B.; Sjöblom, J.; Lawrence, C. *AIChE J.* **2015**, *61* (8), 2657.

(126) Benallal, A.; Maurel, P.; Agassant, J.-F.; Darbouret, M.; Avril, G.; Peuriere, E.; François, J.; Darbouret, M.; Avril, G.; Peuriere, E. *SPE Annu. Tech. Conf. Exhib.* **2008**, 1.

(127) Zheng, S.; Saidoun, M.; Mateen, K.; Palermo, T.; Ren, Y.; Fogler, H. S. In *Proceedings of Offshore Technology Conference (OTC)*; Offshore Technology Conference: Houston, Texas, USA, 2016.

(128) Wilkes, J. O. *Fluid Mechanics for Chemical Engineers, 2nd Edition*; Prentice Hall, 2005.

(129) Heywood, N. I.; Cheng, D. C.-H. *Trans. Inst. Meas. Control* **1984**, *6* (1), 33.

(130) Dodge, D. W.; Metzner, A. B. *AIChE J.* **1959**, *5* (2), 189.

(131) Chilton, R. A.; Stainsby, R. *J. Hydraul. Eng.* **1998**, *124* (5), 522.

(132) Palermo, T.; Tournis, E. *Ind. Eng. Chem. Res.* **2015**, *54* (16), 4526.

(133) Papanastasiou, T. C. *J. Rheol. (N. Y. N. Y).* **1987**, *31* (5), 385.

(134) Masalova, I.; Malkin, A. Y.; Slatter, P.; Wilson, K. *J. Nonnewton. Fluid Mech.* **2003**, *112*, 101.

(135) Wu, B. *Water Res.* **2010**, *44* (13), 3861.

(136) Wu, B.; Chen, S. *Biotechnol. Bioeng.* **2008**, *99* (3), 700.

(137) Poumaere, A.; Moyers-González, M.; Castelain, C.; Burghelea, T. *J. Nonnewton. Fluid*

Mech. **2014**, *205*, 28.

(138) Rudman, M.; Blackburn, H. M. **2006**, *30*, 1229.

(139) Singh, P.; Fogler, H. S. S.; Nagarajan, N. *J. Rheol. (N. Y. N. Y).* **1999**, *43* (6), 1437.

(140) Lopes-da-Silva, J. A.; Coutinho, J. A. P. *Energy and Fuels* **2007**, *21* (19), 3612.

(141) Blaine, R. L. *Therm. Anal. Rheol.* 1.

(142) Waheed, N.; Lavine, M. S.; Rutledge, G. C. *J. Chem. Phys.* **2002**, *116* (5), 2301.

(143) Yi, P.; Rutledge, G. C. *J. Chem. Phys.* **2011**, *135* (2).

(144) Waheed, N.; Engineering, B. S. C.; Rutledge, G. C.; Supervisor, T.; Blankschtein, D. Molecular Simulation of Crystal Growth in Alkane and Polyethylene Melts, MIT, 1997.

(145) Shimizu, T.; Yamamoto, T. *J. Chem. Phys.* **2000**, *113* (8), 3351.

(146) Yi, P.; Locker, C. R.; Rutledge, G. C. *Macromolecules* **2013**, *46* (11), 4723.

(147) Yi, P.; Rutledge, G. C. *J. Chem. Phys.* **2009**, *131* (13), 134902.

(148) Matzain, A. Multiphase Flow Paraffin Deposition Modeling, The University of Tulsa, 1999.

(149) Apte, M. S.; Matzain, A.; Zhang, H.-Q.; Volk, M.; Brill, J. P.; Creek, J. L. *J. Energy Resour. Technol.* **2002**, *124* (3), 180.

(150) Duan, J.; Liu, H.; Guan, J.; Hua, W.; Jiao, G.; Gong, J. *AIChE J.* **2016**, *62* (7), 2550.

(151) Pedersen, K. S.; Rønningsen, H. P. *Energy & Fuels* **2003**, *17* (2), 321.

(152) Hoffmann, R.; Amundsen, L. *J. Pet. Sci. Eng.* **2013**, *107*, 12.

(153) Chi, Y.; Daraboina, N.; Sarica, C. *AIChE J.* **2016**, *62* (11), 4131.

(154) Yang, F.; Zhao, Y.; Sjöblom, J.; Li, C.; Paso, K. G. *J. Environ. Plan. Manag.* **2007**, *50* (4), 517.

(155) Ashbaugh, H. S.; Guo, X.; Schwahn, D.; Prud'homme, R. K.; Richter, D.; Fetters, L. J. *Energy and Fuels* **2005**, *19* (1), 138.

(156) Davidson, M. R.; Dzuy Nguyen, Q.; Chang, C.; Rønningsen, H. P. *J. Nonnewton. Fluid Mech.* **2004**, *123* (2–3), 269.

(157) Gawas, K.; Krishnamurthy, P.; Wei, F.; Acosta, E.; Jiang, Y. *Soc. Pet. Eng.* **2015**.

(158) Duffy, D. M.; Rodger, P. M. *J. Phys. Chem. B* **2002**, *106*, 11210.

(159) Jang, Y. H.; Blanco, M.; Creek, J.; Tang, Y.; Goddard, W. a. *J. Phys. Chem. B* **2007**, *111* (46), 13173.

(160) Yang, F.; Paso, K.; Norrman, J.; Li, C.; Oschmann, H.; Sjöblom, J. *Energy and Fuels* **2015**, *29* (3), 1368.

(161) He, C.; Ding, Y.; Chen, J.; Wang, F.; Gao, C.; Zhang, S.; Yang, M. *Fuel* **2016**, *167*, 40.

(162) Zhao, H.; Xu, J.; Li, T.; Wang, T.; Wei, X.; Wang, J.; Xu, Y.; Li, L.; Guo, X. *Energy and Fuels* **2016**, *30* (7), 5398.

(163) Cao, K.; Zhu, Q. J.; Wei, X. X.; Yao, Z. *Energy and Fuels* **2015**, *29* (2), 993.

(164) Oil emulsions http://petrowiki.org/Oil_emulsions (accessed Mar 6, 2016).

(165) Smirnov, a.; Shi, S.; Celik, I. *J. Fluids Eng.* **2001**, *123* (2), 359.

(166) Pope, S. B. *Turbulent Flows*; Cambridge University Press, 2000.